Alma Mater Studiorum – Università di Bologna

FACULTY OF ENGINEERING

DEPARTMENT OF ELECTRICAL, ELECTRONIC AND INFORMATION ENGINEERING "GUGLIELMO MARCONI" – DEI

XXV Ph.D. Course in Electrotechnical Engineering
ELECTRICAL ENERGY ENGINEERING (09/E2)
ELECTRIC POWER SYSTEMS (ING-IND/33)

Evaluation of Human Exposure to Magnetic Fields Generated by Electric Power Systems in Complex Configurations

Ph.D. Thesis

by

EFFROSYNI KANDIA

Tutor	*Coordinator*
Prof. Eng. Giovanni Mazzanti	*Prof. Eng. Domenico Casadei*

Bologna 2013

ABSTRACT

The international growing concern for the human exposure to magnetic fields generated by electric power lines has unavoidably led to imposing legal limits. Respecting these limits, implies being able to calculate easily and accurately the generated magnetic field also in complex configurations. Twisting of phase conductors is such a case. The consolidated exact and approximated theory regarding a single-circuit twisted three-phase power cable line has been reported along with the proposal of an innovative simplified formula obtained by means of an heuristic procedure. This formula, although being dramatically simpler, is proven to be a good approximation of the analytical formula and at the same time much more accurate than the approximated formula found in literature. The double-circuit twisted three-phase power cable line case has been studied following different approaches of increasing complexity and accuracy. In this framework, the effectiveness of the above-mentioned innovative formula is also examined. The experimental verification of the correctness of the twisted double-circuit theoretical analysis has permitted its extension to multiple-circuit twisted three-phase power cable lines. In addition, appropriate 2D and, in particularly, 3D numerical codes for simulating real existing overhead power lines for the calculation of the magnetic field in their vicinity have been created. Finally, an innovative 'smart' measurement and evaluation system of the magnetic field is being proposed, described and validated, which deals with the experimentally-based evaluation of the total magnetic field *B* generated by multiple sources in complex three-dimensional arrangements, carried out on the basis of the measurement of the three Cartesian field components and their correlation with the field currents via multilinear regression techniques. The ultimate goal is verifying that magnetic induction intensity is within the prescribed limits.

Στους γονείς μου

και στον Αλέξανδρό μου

CONTENTS

CHAPTER 1

CHAPTER 2

CHAPTER 3

CHAPTER 4

CHAPTER 5

CHAPTER 6

CHAPTER 7

CHAPTER 1

INTRODUCTION

Within the past years there has been very significant growth of man-made, extremely low frequency (ELF) magnetic fields at frequencies of 50 and 60 Hz predominantly from electric energy generation, transmission, distribution and use. Man-made ELF fields are many orders of magnitude greater than the naturally arising fields at 50 and 60 Hz. Within all organisms are endogenous electromagnetic fields and currents that play a role in the complex mechanisms of physiological control such as neuromuscular activity, glandular secretion, cell-membrane function and tissue development, growth and repair. It is not surprising that, because of the role of electromagnetic fields and currents in so many basic physiological processes, questions arise concerning possible effects of artificially produced fields on biological systems. With advances in technology and the ever increasing need for electric energy, human exposure to 50/60 Hz magnetic fields has increased to the point that valid questions are raised concerning safe limits of such exposure. Public concern is growing and in many countries regulatory and advisory agencies have been requested to evaluate possible adverse effects of ELF electromagnetic fields on human health.

Exposure standards have been developed internationally, that provide adequate protection against all known adverse effects of exposure to EMF. The guidelines developed by the International Commission on Non Ionizing Radiation Protection (ICNIRP) [1] are widely recognized and have formed the basis for national regulations in several countries. European Union has also established a common framework [2], [3] for giving the general public a high level of protection against the potential harmful effects of exposure to electromagnetic fields, particularly by limiting exposure to sources of non-ionizing radiation. However, social concerns for hypothesized long-term effects of chronic exposure to low-level EMF have created a demand for precautionary measures beyond the standards for recognized, acute effects.

As far as Italy is concerned, the limits currently in force for magnetic fields generated by 50 Hz power lines are set by [4]:

→ The exposure limit: 100 µT (rms value). This limit must never be exceeded in case of general public exposure.

→ The attention value: 10 μT (rms value). This limit is a cautionary measure, adopted in children's playgrounds, residential dwellings, school premises and in areas where people are staying for 4 hours or more per day, in order to protect against any possible long-term effects that might be related to power frequency (50 Hz) magnetic fields. The attention value is the median of values recorded over 24 hours, under normal operational conditions.

→ The quality objective: 3 μT (rms value). This limit is adopted for the purpose of minimizing progressively the exposures to magnetic fields generated by 50 Hz power lines and is applied in designing new power lines in the neighborhood of children's playgrounds, residential dwellings, school premises, and in areas where people are staying for 4 hours or more per day, as well as in planning developments in the proximity of existing electric power lines and installations, including the categories mentioned above. The quality objective is the median of values recorded over 24 hours, under normal operational conditions.

The above considerations have stimulated the search for methods of arranging the conductors of power lines in such a way that the surrounding magnetic fields will be greatly reduced. Focusing on power distribution cables, a solution adopted for practical reasons when laying the cables and that has proved to be very effective also in mitigating the magnetic field is twisting the phase conductors. Practical reasons and field mitigation effectiveness have made twisted three-phase cables the standard solution for medium voltage (MV) and low voltage (LV) power cables in the electric power distribution networks. In turn, at the distribution level both overhead and underground twisted three-phase cables are overwhelming traditional overhead lines with bare conductors, for many reasons, e.g.:

- Buildings are spreading over larger and larger areas, thereby making the use of traditional overhead lines possible over less and less broad areas;
- Overhead cables are often replacing traditional overhead lines also in rural areas, in order to reduce fault rate and maintenance of the lines;
- twisted cables are becoming more and more popular with the growing spread of renewable sources, since underground twisted three-phase cable lines are the preferred solution for connecting wind-generators and photovoltaic systems to the distribution grid, due to their very low environmental impact.

All this has unavoidably led to the ever increasing use of twisted three-phase cables.

The calculation of the low-frequency magnetic field in the vicinity of a three-wire twisted cable carrying three-phase current, even if it is drastically reduced, is essential for the evaluation of its impact near sensitive receptors and also for the calculation of the distance corresponding to a maximum limit value of the rms magnetic induction

[4], [5]. This calculation problem has been discussed in literature since 1937, when Buchholz gave an analytical solution for the twisted pair in form of an infinite series containing modified Bessel functions in [6] and [7]. Later on, several studies have been made and published, dealing mostly with approximations to the rather bulky series-type solution, some keeping only the dominant first term of the series [8] - [10] and others attempting direct ways of approximation [11]. Most recently, this issue has been treated analytically in [12] - [23] and particularly in [14] and [15] by Pettersson et al., who presented a complete and exact theory of the power-frequency magnetic field emitted by a twisted three-phase configuration and also provided experimental results for demonstrating the correctness of the analytical solution.

As already mentioned, the exact formula for the calculation of the magnetic field generated by a three-phase twisted configuration uses an infinite-term series of modified Bessel functions of the first and second kind and their derivatives in a reference system with cylindrical coordinates [14] - [15]. In the literature an approximate formula also exists that, for distances comparable to the pitch of the helix, gives results not far from those of the exact formula for distances exceeding, say, 1 m from the axis of the helix, and is in fact often used in these conditions. On the contrary, as the field-point approaches the twisted three-phase arrangement, the approximate formula results in steeply-increasing errors and the exact formula is recommended. Note that distances close to the conductors are of major interest in the case of MV and LV cables: indeed, such cables – in the form of overhead or underground power lines – often cross densely populated areas and are sometimes integrated within inhabited buildings; moreover, when the current rms value is relatively low then the generated level of the magnetic field is significant only in areas close to the conductors.

In this PhD Thesis, via an heuristic procedure, an innovative simplified formula for the rms magnetic induction is obtained which is much simpler than the rigorous analytical one and provides a much smaller relative error compared to the approximated one from the literature, especially for small distances from the helix axis [24] - [27]. The effectiveness of the innovative expression is evaluated by carrying out some numerical simulations relevant to a typical MV cable in order to compare the results provided by the exact and the approximate formulae from the literature with those obtained via the innovative simplified formula.

Subsequently, due to the increasing interest of utilities worldwide in double-circuit twisted overhead, as well as underground, cable lines, the theoretical treatment of a double-circuit twisted cable line was effectuated, following different approaches of increasing complexity and accuracy, all based on the superposition of the effects of each single-circuit twisted three-phase cable. Resorting to the correct vectorial approach, the total magnetic field is calculated as the vector sum of the two fields generated by each twisted cable using the exact expressions of the three field components generated by each cable, consisting in the above-described series of

Bessel functions. The objective difficulties derived from this calculus – such as knowing the precise geometrical arrangement of the three phases or being sure of the constancy of the pitch of the single helix and also of the constancy of the perfect parallelism of the two helixes – make the resulting formula far more complex than that relevant to one single three-phase twisted cable. As a second and rather necessary step for the purpose of simplicity, based on the "worst case assumption", the rms magnetic field B generated by a double-circuit twisted cable line is calculated as the algebraic sum of the two total fields from the single-circuits, each computed via the exact, the approximated from the literature and the innovative simplified formula, thereby providing the most conservative value of B that serves as an upper reference limit for exposure evaluation [28] - [32]. The analytic theory is supported by numerical evaluation as well as experimental results by actual measurements in situ.

Finally, the calculation of the magnetic field is further extended to a multiple-circuit twisted cable line, again following both the exact vectorial and the "worst case" approach where the field from each cable circuit is computed via both the exact and the innovative simplified formula, thereby providing the most conservative value of B. The effectiveness of the simplified formula for the case of a triple-circuit twisted cable lines is also proven by the simulation of some practical case-studies related to MV triple-circuit twisted cable lines [33].

The calculation of the magnetic field generated by overhead power lines, [34] - [51], was also treated in this PhD Thesis for the sake of creating appropriate bi- and tri-dimensional numerical codes. The bi-dimensional calculation of the magnetic field in the vicinity of overhead power lines overestimates the field since it does not consider the catenary form of the line and effectuates the calculation at the point of maximum exposure, i.e. at the mid-span between two adjacent towers. Doing so, the two-dimensional numerical codes for the calculation of magnetic field provide isolines of magnetic induction at 100 μT, 10 μT and 3 μT that spread over wider areas compared to the real ones, leading to a reduction in beneficial construction space. On the other hand, the tri-dimensional calculation of the magnetic field examines the real geometrical configuration of the power line, providing thus, results closer to the real ones.

In the framework of determining the general public exposure to magnetic fields from complex 3D arrangements of the field sources from power systems – particularly overhead transmission and distribution lines – measurement and evaluation systems of the magnetic field generated are needed that can provide reliable and accurate indications. Such arrangements occur more and more frequently in the vicinity of residential and industrial areas, where overhead and underground lines of different voltage rating and geometry, as well as more or less wide substations, often lie close to each other. The final part of this Thesis proposes an innovative measurement and evaluation system capable of matching this need. The innovative "smart" measurement device measures and also records the rms values of the magnetic field components B_x,

B_y and B_z as a function of time (unlike the usual magnetic field measuring devices that record and store only the rms value of total magnetic induction field B) for subsequent analytical processing. The three-dimensional magnetic field measurement device has been entirely created, calibrated and characterized in the laboratory [52] - [56], and has been tested with success by experimental campaigns in the field in the presence of multiple current sources. The innovative evaluation system uses multilinear regression algorithms developed in Matlab® environment for correlating the measurement results of B_x, B_y and B_z at a given field point to the relevant values of time-varying currents enabling, in this way, the extrapolation of the rms value of the total magnetic field to any combination of source currents of interest [57] - [59]. The best performances of that innovative measurement and evaluation system have been published [60], [61] and discussed.

CHAPTER 2

SINGLE - CIRCUIT TWISTED THREE - PHASE CABLE LINES

2.1 THE EXACT FORMULATIONS

2.1.1 Single Wire Helix

According to the Biot-Savart law, the magnetic flux density vector of a helical line source carrying current I is given by the line integral

$$B = \frac{\mu_0 I}{4\pi} \int \frac{d\vec{r} \times \left(r - \vec{r}' \right)}{\left| r - \vec{r}' \right|^3} \tag{2.1}$$

along the helix, where μ_0 is the permeability of the free space ($\mu_0 = 4\pi 10^{-7}$ H/m), $\vec{r}$ is the field point, $\vec{r}'$ is the source point variable, p is the helix pitch and α is the helix radius (see Fig. 2.1).

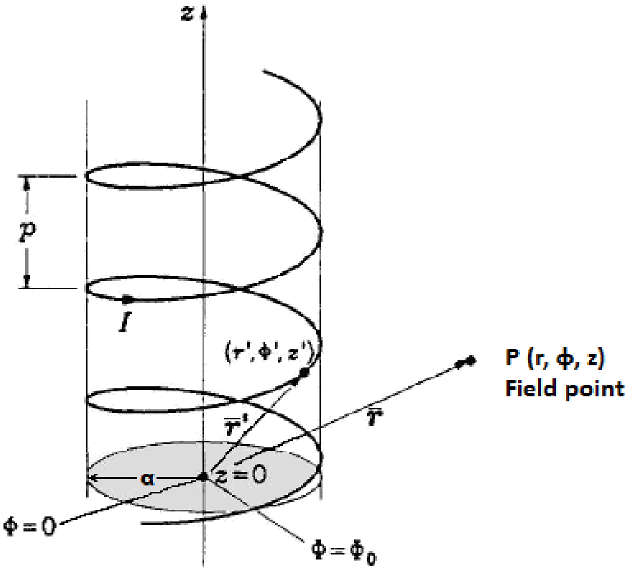

Figure 2.1: *Helical line current (after [15]).*

This integral cannot be calculated analytically in a direct manner. However, the integrand can be series expanded in terms whose integrals can be given in the form of Bessel functions.

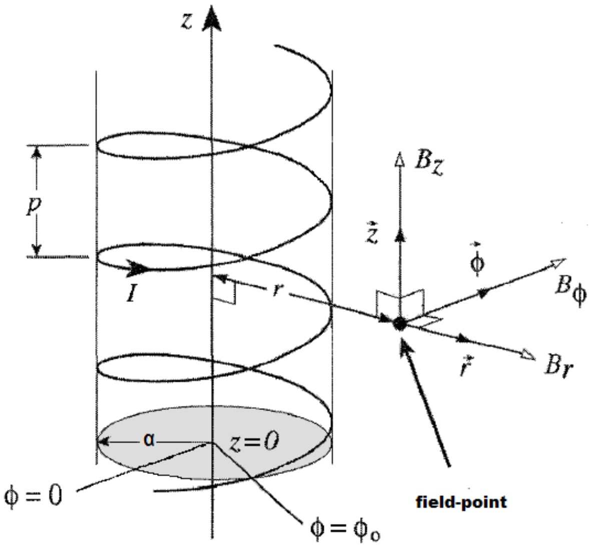

Figure 2.2: *Field components generated by a one-wire helix, expressed in cylindrical coordinates (after [14]).*

The exact theory regarding this configuration consists in calculating the magnetic field in cylindrical coordinates r, φ and z (respectively radial, azimuthal and axial, see Fig. 2.2), using the following expressions for the components B_r, B_φ, e B_z of the magnetic induction field [15]:

$$B_r = \frac{\mu_0 I\alpha}{\pi r^2}(kr)^2 \sum_{n=1}^{\infty} nI'_n(nk\alpha)K'_n(nkr)\sin[n(\phi-\phi_0-kz)] \tag{2.2.a}$$

$$B_\phi = \frac{\mu_0 I}{2\pi r} + \frac{\mu_0 I\alpha}{\pi r^2}(kr)\sum_{n=1}^{\infty} nI'_n(nk\alpha)K_n(nkr)\cos[n(\phi-\phi_0-kz)] \tag{2.2.b}$$

$$B_z = -\frac{\mu_0 I\alpha}{\pi r^2}(kr)^2 \sum_{n=1}^{\infty} nI'_n(nk\alpha)K_n(nkr)\cos[n(\phi-\phi_0-kz)] \tag{2.2.c}$$

where $k=2\pi/p$ and $I_n(z)$, $K_n(z)$ are the modified Bessel functions of first and second kind of order n, and $I_n'(z)$, $K_n'(z)$ their derivatives.

For very large distances, the three Bessel function sums may be shown to go to zero much faster than the inverse $-r$ term of B_φ, so that the only field component ultimately left will be $\mathrm{B}_\phi = \mu_0 I/2\pi r$ which is the field of an infinitely long straight conductor carrying current I. That means that the field from a single conductor does not vanish simply by twisting it.

For $p \to 0$, the current distribution will approach a purely azimuthal surface current on the cylinder surface. In this case, all three field components vanish, which is expected from the solenoids theory where the field is concentrated to the inner of the cylinder.

2.1.2 Two Wire Helix

Without loss of generality, by setting $\varphi_0 = 0$ for the conductor carrying current I and $\varphi_0 = \pi$ for the conductor carrying current $-I$, the field from each of the helices is given by eqs. (2.2.a), (2.2.b) and (2.2.c) and the total field is found by summation. Thus as the even order terms will cancel pairwise while the odd will double, the following expressions derive [15]:

$$B_r = 2\frac{\mu_0 I\alpha}{\pi r^2}\gamma^2\sum_n^{\infty} nI'_n(n\eta)K'_n(n\gamma)\sin[n(\phi - kz)] \qquad (2.3.a)$$

$$B_\phi = 2\frac{\mu_0 I\alpha}{\pi r^2}\gamma\sum_n^{\infty} nI'_n(n\eta)K_n(n\gamma)\cos[n(\phi - kz)] \qquad (2.3.b)$$

$$B_z = -2\frac{\mu_0 I\alpha}{\pi r^2}\gamma^2\sum_n^{\infty} nI'_n(n\eta)K_n(n\gamma)\cos[n(\phi - kz)] \qquad (2.3.c)$$

where the summations range over n = 1, 3, 5. For sinusoidal current of angular velocity ω, I is to be replaced by $\hat{I}\sin(\omega t)$, where $\hat{I}$ is the peak value.Up to sign, the expressions will also hold as they stand for the effective values of the B-components with I denoting the effective value of the current.

2.1.3 Three Wire Helix

For the three-phase case-study the conductor arrangement in a transverse plane will form an equilateral triangle since the three coaxial helices have equal radii. Therefore, let us number the wires as i=1,2,3 and set $\alpha_i=(i-1)2\pi/3$, $\phi_i=(i-1)2\pi/3$ and $I_i = \hat{I}\sin(\omega t + \alpha_i)$, where α_i are the phase angles of the three helices and ϕ_i are the location parameters of the three helices.Term-wise addition of the three fields yields after some elementary calculations using the auxiliary geometric relations

$$\sum_{i-1}^{3}\sin(\omega t + a_i)\sin[n(\phi - \phi_i - kz)] = \mp\frac{3}{2}\cos(\omega t \pm n\Phi) \qquad (2.4.a)$$

$$\sum_{i-1}^{3}\sin(\omega t + a_i)\cos[n(\phi - \phi_i - kz)] = \frac{3}{2}\sin(\omega t \pm n\Phi) \qquad (2.4.b)$$

with $\Phi = \phi - kz$

for n = 1,2,4,5,7... and zero for n = 3,6,9..., where the upper sign applies for n = 2,5,8... and the lower for n = 1,4,7....

Thus, the time-dependent field components are [15]:

$$B_r = \frac{3}{2}\frac{\mu_0 \overset{\frown}{I}\alpha}{\pi r^2}\gamma^2 \sum_n (\mp n) I_n'(n\eta) K_n'(n\gamma)\cos(\omega t \pm n\Phi) \tag{2.5.a}$$

$$B_\phi = \frac{3}{2}\frac{\mu_0 \overset{\frown}{I}\alpha}{\pi r^2}\gamma \sum_n n I_n'(n\eta) K_n(n\gamma)\sin(\omega t \pm n\Phi) \tag{2.5.b}$$

$$B_z = -\frac{3}{2}\frac{\mu_0 \overset{\frown}{I}\alpha}{\pi r^2}\gamma^2 \sum_n n I_n'(n\eta) K_n(n\gamma)\sin(\omega t \pm n\Phi) \tag{2.5.c}$$

The effective values of the field components can be seen to be given by [15]:

$$B_r = \frac{3}{2} B_0 \gamma^2 \left[\sum_n \sum_m (\mp n)(\mp m) I_n'(n\eta) I_m'(m\eta) K_n'(n\gamma) K_m'(m\gamma) \cos(\pm n \mp m)\Phi \right]^{1/2} \tag{2.6.a}$$

$$B_\phi = \frac{3}{2} B_0 \gamma \left[\sum_n \sum_m nm I_n'(n\eta) I_m'(m\eta) K_n(n\gamma) K_m(m\gamma) \cos(\pm n \mp m)\Phi \right]^{1/2} \tag{2.6.b}$$

$$B_z = \frac{3}{2} B_0 \gamma^2 \left[\sum_n \sum_m nm I_n'(n\eta) I_m'(m\eta) K_n(n\gamma) K_m(m\gamma) \cos(\pm n \mp m)\Phi \right]^{1/2} \tag{2.6.c}$$

with

$$B_0 = \frac{\mu_0 I \alpha}{\pi r^2} \tag{2.7}$$

where the index and sign rules of above apply and I denotes the effective value of the current.

2.1.4 Simplification of the Three Wire Helix Case

Considering an imagined helix of pitch *p* through the field-point (see Fig. 2.3 after [14]) and using the helical coordinates *r* (radial), *b* (binormal) and *s* (tangential) the field can be described by only two components, i.e. the radial component B_r and the binormal component B_b, since the tangential component B_s is zero.

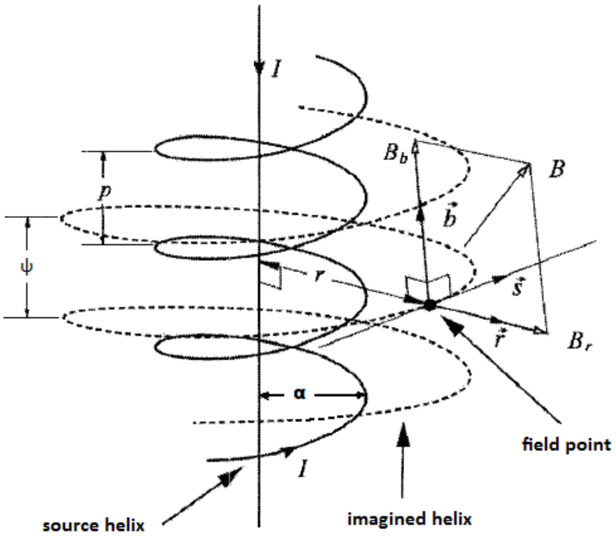

Figure 2.3: *Field components in helical coordinates (after [14]).*

The relation between the two reference systems is given by

$$B_s = B_z \sin\psi + B_\phi \cos\psi \tag{2.8.a}$$

$$B_b = B_z \cos\psi - B_\phi \sin\psi \tag{2.8.b}$$

with $\psi = \tan^{-1}(kr)$ the pitch angle of the field-point helix.

Now, cancelling the single term $\mu_0 I/2\pi r$ of B_φ by applying an imagined return current on the cylinder axis, the time dependent field-vector components can be written as follows [14]:

$$B_r = B_0\gamma^2 \sum_{n=1}^{\infty} nI'_n(n\eta)K'_n(n\gamma)\sin(n\Phi)\sin(\omega t) \tag{2.9.a}$$

$$B_b = -B_0\gamma\sqrt{1+\gamma^2} \sum_{n=1}^{\infty} nI'_n(n\eta)K_n(n\gamma)\cos(n\Phi)\sin(\omega t) \tag{2.9.b}$$

where $B_0 = \mu_0 I_p \alpha / \pi r^2$, $\eta = k\alpha$, $\gamma = kr$, $\Phi = \phi - \phi_0 - kz$ and I_p is the peak value of the sinusoidal current $i(t) = I_p \sin\omega t$ of angular frequency ω.

For the three-phase case-study we number the wires by i=1,2,3 and set $I_i = \hat{I}\sin(\omega t + \alpha_i)$, $\alpha_i=(i-1)2\pi/3$, $\phi_i=(i-1)2\pi/3$, where α_i are the phase angles of the three helices and ϕ_i are the location parameters of the three helices.

Term-wise addition of the three fields yields after calculations using the auxiliary geometric expressions (2.4) and the following results represent the time-dependent field components [14]:

$$B_r = \frac{3}{2}\frac{\mu_0 I_p \alpha}{\pi r^2}\gamma^2 \sum_n (\mp n) I_n'(n\eta) K_n'(n\gamma)\cos(\omega t \pm n\Phi) \qquad (2.10.a)$$

$$B_b = -\frac{3}{2}\frac{\mu_0 I_p \alpha}{\pi r^2}\gamma\sqrt{1+\gamma^2} \sum_n n I_n'(n\eta) K_n(n\gamma)\sin(\omega t \pm n\Phi) \qquad (2.10.b)$$

where $\Phi = \phi - kz$ and the summations range over n = 1, 2, 4, 5, 7... i.e. all positive integers except n = 3, 6, 9...; the upper sign applies for n = 2, 5, 8... and the lower for n = 1, 4, 7...

The rms values of the components and of the total field B are given by [14]:

$$B_r = \frac{3}{2} B_0 \gamma^2 \left[\sum_n \sum_m (\mp n)(\mp m) I_n'(n\eta) I_m'(m\eta) K_n'(n\gamma) K_m'(m\gamma)\cos(\pm n \mp m)\Phi \right]^{1/2} \qquad (2.11.a)$$

$$B_b = \frac{3}{2} B_0 \gamma \sqrt{1+\gamma^2} \left[\sum_n \sum_m nm I_n'(n\eta) I_m'(m\eta) K_n(n\gamma) K_m(m\gamma)\cos(\pm n \mp m)\Phi \right]^{1/2} \qquad (2.11.b)$$

$$B = \frac{3}{2} B_0 \gamma^2 \left\{ \sum_n \sum_m nm I_n'(n\eta) I_m'(m\eta) \left[(\mp 1)(\mp 1) K_n'(n\gamma) K_m'(m\gamma) + \frac{1+\gamma^2}{\gamma^2} K_n(n\gamma) K_m(m\gamma) \right] \cos(\pm n \mp m)\Phi \right\}^{1/2} \qquad (2.12)$$

Formulae (2.11) - (2.12) can be applied to the special case of an untwisted configuration (with η→0, γ→0 and p→∞) using the small argument approximations for the Bessel functions:

$$I_n(\eta) = \frac{(n/2)^n}{n!}, \quad K_n(\gamma) = \frac{1}{2}\frac{(n-1)!}{(\gamma/2)^n} \quad \text{with } \eta,\gamma \ll 1 \qquad (2.13)$$

The result is [14]:

$$B_r = \frac{3}{2} B_0 \left\{ \sum_n \sum_m \left(\frac{\alpha}{r}\right)^{n+m-2} \frac{1}{4} (\mp 1)(\mp 1)\cos(\pm n \mp m)\Phi \right\}^{1/2} \qquad (2.14.a)$$

$$B_b = \frac{3}{2} B_0 \left\{ \sum_n \sum_m \left(\frac{\alpha}{r}\right)^{n+m-2} \frac{1}{4} \cos(\pm n \mp m)\Phi \right\}^{1/2} \qquad (2.14.b)$$

$$B = \frac{3}{2} B_0 \left\{ \sum_n \sum_m \left(\frac{\alpha}{r} \right)^{n+m-2} \frac{1}{4} \left[(\mp 1)(\mp 1) + 1 \right] \cos(\pm n \mp m)\Phi \right\}^{1/2} \tag{2.15}$$

2.2 THE APPROXIMATE FORMULATION FROM THE LITERATURE

For certain values of parameters $\alpha$and p, the first term of the series expansions will be so dominant that it can serve as an approximation of the whole sum for proper values of the variable r. One important example of such a situation is when the configuration has a loose twist ($\alpha << p$) and the field-point is far from the axis of the helix ($r >> p$, hence $\gamma >> 1$). In this case the total field reduces to [14], [15]:

$$B = \frac{3}{2} B_0 \gamma^2 I_n'(\eta) \left[K_1{}^2(\gamma) + \frac{1+\gamma^2}{\gamma^2} K_1{}^2(\gamma) \right]^{1/2} \tag{2.16}$$

Using the small argument approximation $I_n'(\eta)=1/2$, holding for $\eta \to 0$, and the large argument approximation $K_1(\gamma) \approx -K_1'(\gamma) \approx \sqrt{2/(\pi\gamma)}\ \mathrm{e}^{-\gamma}$ holding for $\gamma >> 1$, one obtains from eq. (2.16) [14], [15]:

$$B \approx {}^{3}\!/_{4} F \sqrt{2} B_0 \tag{2.17}$$

where F is the so-called “twist factor” [14], [15]:

$$F = \sqrt{\pi/2}\ \gamma^{3/2}\ \mathrm{e}^{-\gamma} \tag{2.18}$$

Formulae (2.17) - (2.18) illustrate that the field reduction involved by twisting the conductors is expressed by the twist factor F. For example, for distance to pitch ratios, r/p, equal to 1 and 2, F is equal to 0.037 and 0.0002 respectively. Thus, a dramatic decay of field with distance is observed.

2.3 THE SIMPLIFIED INNOVATIVE FORMULATION

An unavoidable preliminary step was to implement in Matlab$^{\mathrm{TM}}$ environment both the approximate (eq. (2.17)) and the exact (eq. (2.12)) expressions, so as to reproduce the literature values of magnetic field reported in [14], [15]. Since the exact formula of eq. (2.12) was in turn verified satisfactorily via a sound experimental campaign illustrated in detail in [14], [15], it can be argued that the validation of the script by reproducing the literature values of magnetic field according to both the approximate (eq. (2.17)) and the exact (eq. (2.12)) expressions – is fundamental. An extensive comparison of the results provided by the implemented script with those reported in [14], [15] has been carried out in [24] - [27], not only from the viewpoint of total *B*-field, but also of radial and binormal components, and has provided excellent results.

2.3.1 Angle Φ

In search for an innovative simplified expression of the magnetic induction, it is convenient to analyze the behaviour of *B* as a function of the distance *r* only. To do so, the dependence of the total field and the relevant components on angle Φ (which indicates the angular position of the field-point in the twisted configuration) has been studied in [24], [25]. The results are depicted in Fig. 2.4 and can be summarised as follows:

1. the radial component B_r prevails in the composition of the total magnetic field *B*;
2. the radial component B_r, and therefore the total magnetic field *B*, reaches its maximum value at angles Φ=60°, Φ=180° and Φ=300°. At these angle values the azimuthal, B_φ, and the axial, B_z, components reach their minimum value;
3. the radial component B_r, and therefore the total magnetic field *B*, presents its minimum value at angles Φ=0°, Φ=120° and Φ=240°. At these angle values the azimuthal, B_φ, and the axial, B_z, components reach their maximum value.

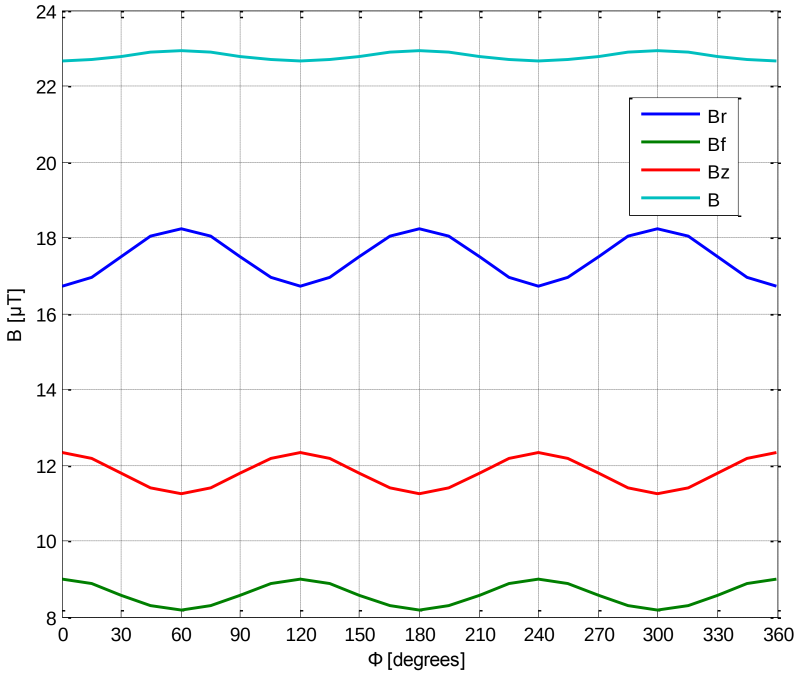

Figure 2.4: *B, B_r, B_φ, B_z vs. angle Φ (r=0.3m, I=280A, p=1.37m, α=0.02m)*

So, by setting and keeping constant $\Phi=60^o$ during the search of the innovative simplified formula, the maximum value of the total magnetic field *B* at every field point was guaranteed, providing, thus, a conservative estimation of the magnetic field.

2.3.2 Simplification of the Bessel Functions

In order to find an alternative approximate expression that simplifies the exact calculation, it is useful to set a finite maximum value for the indexes *n* and *m* of the Bessel functions in eq. (2.12).Such maximum value has to be high enough to let the approximate solution converge to the exact one, but low enough to make the approximate solution easily computable. From an analysis of the convergence of *B* it can be deduced that:

1. with increasing *n* and *m*, the approximate solution tends to the exact one;
2. the first-order approximation ($n=m=1$) corresponds to the approximate solution given by eq. (2.16). This approximation of the magnetic field does not depend on the angle Φ and seems to give a good average value of the field *B*;
3. for greater distances the speed of convergence to the exact solution increases. In particular, for distances >1 m the second-order approximation ($n=m=2$) is an excellent approximation of the exact solution. The second-order approximation results always better than the first-order one and moreover always overestimates the field compared to the exact one (which is desirable from an engineering point of view, since it is conservative).

By setting:

$$A=\left\{\sum_n\sum_m nmI'_n(n\eta)I'_m(m\eta)\left[(\mp1)(\mp1)K'_n(n\gamma)K'_m(m\gamma)+\frac{1+\gamma^2}{\gamma^2}K_n(n\gamma)K_m(m\gamma)\right]\cos(\pm n\mp m)\Phi\right\}^{1/2} \tag{2.19}$$

equation (2.12) simplifies as follows:

$$B=\frac{3}{2}B_0\gamma^2A=\frac{3}{2}\frac{\mu_0 I\alpha}{\pi}\left(\frac{2\pi}{p}\right)^2A=\frac{2.4\pi^2 I\alpha}{p^2}A \tag{2.20}$$

with $\mu_0=4\pi10^{-1}\mu\text{H/m}$ in order for *B* to result directly in μT.

The term *A* is the square root that contains the series of the Bessel functions and the rms magnetic induction *B* is directly proportional to it. Since the quantity $2.4\pi^2 I\alpha/\mathrm{p}^2$ does not depend on the distance *r*, the root *A* is the single term that determines the dependence of the magnetic field on distance *r*.

For all distances, the second-order ($n=m=2$) approximation B_2 of the exact value of magnetic induction *B*– based on the second-order approximation A_2 of the exact value of *A* – implies always a percent relative error e_2 smaller than that implied by the first-order approximation; e_2 is defined as:

$$e_2(r) = 100\frac{A_2(r) - A(r)}{A(r)} = 100\frac{B_2(r) - B(r)}{B(r)} \qquad (2.21)$$

Moreover, what is important from a practical point of view, e_2 is always low and positive. The value of A_2 derived from the second-order approximation is always greater than the exact value of A, thereby leading to a precautionary overestimation of the magnetic field. Therefore, the exact expression of the total magnetic field B can be reasonably approximated via the second-order approximation, as proved by the analysis made in [24], [25].

2.3.3 The Innovative Formula

A fundamental clue for finding the innovative formula has been gained by plotting the curve of B vs. the radial distance from the helix axis, r, in semi-logarithmic coordinates. Such dependence is nearly linear, with a slight deviation from linearity (of hyperbolic type) only for small values of r. This means that the field can be approximated with the equation of a straight line plus a hyperbolic term which vanishes rapidly by increasing r. Thus the following innovative simplified expression has been conceived:

$$\ln B = a_0^{'} + a_1^{'} r + \frac{a_2^{'}}{r^{a_3^{'}}} \qquad (2.22)$$

Subsequently, on the basis of eq. (2.20) relationship (2.22) has been reprocessed as follows:

$$\ln B \approx \ln B_2 = \ln\left(\frac{2.4\pi^2\alpha}{p^2}\right) + \ln I + \ln A_2 \approx \ln G + \ln I + \left(a_0 + a_1 r + \frac{a_2}{r^{a_3}}\right) \qquad (2.23)$$

being:

- $\ln I = f(I)$, known and trivial function of I;
- $\ln G = \ln(2.4\pi^2\alpha / p^2) = f(\alpha, p)$, known function of α, p;
- $\ln A_2 \approx a_0 + a_1 r + a_2 / r^{a_3} = f(r; \alpha, p)$, known function of r and unknown function of α, p.

B is proportional to I, so the dependence of ln$B$ on the current I is trivially expressed by using the natural logarithm of I. The dependence on helix radius and pitch is expressed partly in an exact form via the logarithm of G, where $G = 2.4\pi^2\alpha / p^2$, and partly in an approximated form via the logarithm of A_2. In this way, only the square root of A_2 is approximated and not the entire expression of the field B_2.

The unknown parameters of the innovative approximate expression (2.23) are a_0, a_1, a_2 and a_3. These parameters have been derived as a function of α and p with best-fitting techniques developed in Matlab^{TM} and aimed at minimizing the overall error on B as a function of r, under the constraint that a positive error, possibly >10%, is to be privileged. Accurate values for parameters a_1 and a_0 are essential, since they govern the linear part of the $\ln B_2$ vs. r, and for this purpose an appropriate solution has been to limit the fitting of the linear part to the interval [1.2 m; 2.0 m] instead of the entire range [0.3 m; 2.0 m]. After several tests, the value of a_2=0.1 has been set, while for parameter a_3 the value that minimizes the overall error has been chosen case by case with varying α, p according to the above requirement of a positive error not exceeding 10%.

The three-dimensional Figures 2.5 - 2.7 show the values of parameters a_0, a_1, a_3 obtained by means of the above-described best-fitting procedure as a function of $p \in$[0.8 m; 2.0 m] and $\alpha \in$[0.01 m; 0.10 m]; note that such wide intervals include most – if not all – the values of α, p that have practical interest.

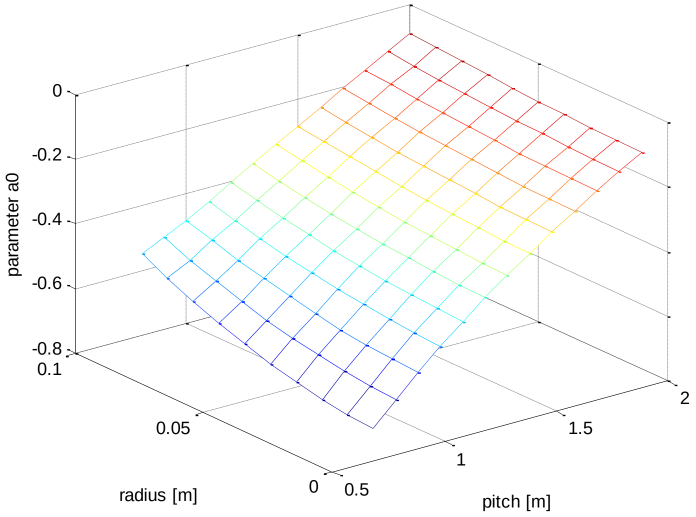

***Figure 2.5:** Parameter a_0 versus radius α and pitch p of the helix.*

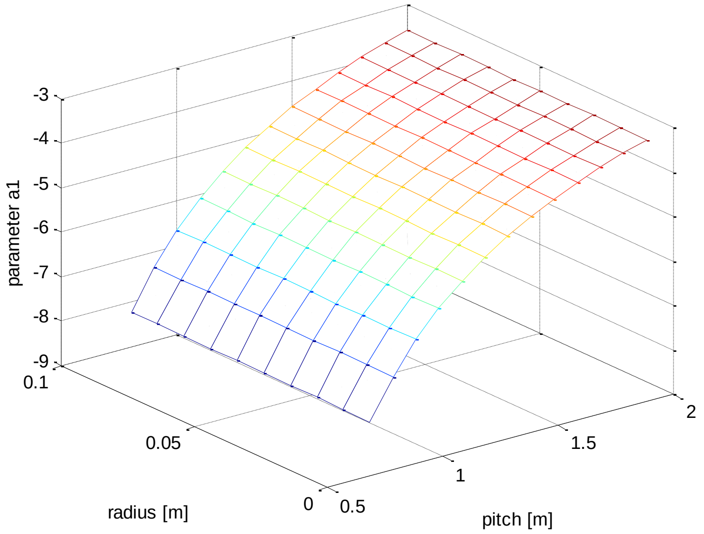

***Figure 2.6:** Parameter a_1 versus radius α and pitch p of the helix.*

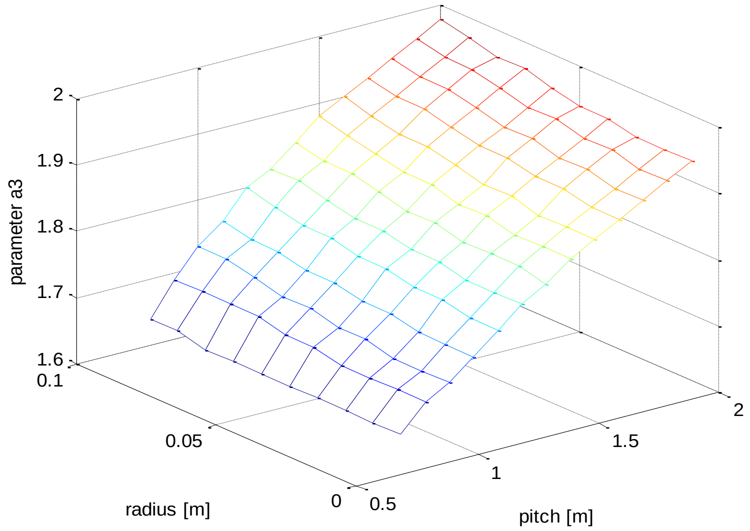

Figure 2.7: *Parameter* a_3 *versus radius α and pitch p of the helix.*

A second phase of analysis is based on the fact that the parameters a_0, a_1 and a_3 are functions of both pitch and radius of the helix [24], [25]. Therefore, using the techniques outlined above for the minimization of the error with respect to the exact formulation (eq. (2.12)), analytical approximated expressions of a_0, a_1 and a_3 have been obtained that represent the dependence of these parameters on both radius and pitch of the helix. To do so, a great number of simulations has been performed, taking again into consideration the various types of cables commercially available, each one characterized by different values of α and p, and so by different values of the parameters a_0, a_1 and a_3. All these simulations show that parameters a_0, a_1 and a_3 exhibit the following common behaviour for all the cables treated (see Appendix 1).

Parameter a_0 is a second-degree function of the pitch p, so an adequate representation of its dependence on the pitch is as follows: $a_0 = a_{00} + a_{01} \cdot p + a_{02} \cdot p^2$; parameters a_{00}, a_{01} and a_{02} are in their turn second-degree functions of the radius α. Considering all the above (Fig. 2.5) the following analytical approximated expression of a_0 as a function of p and α has been obtained:

$$\begin{aligned} a_0 = &\left[\left(12.8712 \cdot \alpha^2\right) + \left(0.2107 \cdot \alpha\right) - 0.1383\right] \cdot p^2 + \\ + &\left[\left(-48.4318 \cdot \alpha^2\right) + \left(-0.6919 \cdot \alpha\right) + 0.9094\right] \cdot p + \\ + &\left[\left(49.6932 \cdot \alpha^2\right) + \left(0.5724 \cdot \alpha\right) - 1.3991\right] \end{aligned} \tag{2.24}$$

As far as parameter a_1 is concerned, the results of all the cases of the cables treated show that the dependence of this parameter on the radius α, with p fixed, can be represented as an horizontal straight line. Thus parameter a_1 depends only on p and more precisely it is a third-degree function of the pitch p. Taking into consideration these arguments (Fig. 2.6) and minimizing the error, the following analytical approximated expression of a_1 as a function of p has been obtained:

$$a_1 = (2.1018 \cdot p^3) + (-11.6186 \cdot p^2) + (23.2879 \cdot p) - 20.4446 \tag{2.25}$$

Finally, all the cables treated show that parameter a_3 is a function of both pitch and radius of the helix (Fig. 2.7): in fact, a_3 is a first-degree function of the pitch p so it can be approximated with a straight line $a_3 = a_{30} + a_{31}\,p$, where the parameters a_{30} and a_{31} are also first-degree functions of the radius α. Minimizing the error, the following analytical expression of a_3 as a function of p and α has been obtained:

$$a_3 = \left(0.2739 \cdot \alpha + 0.2430\right) \cdot p + \left(0.1036 \cdot \alpha\right) + 1.4444 \tag{2.26}$$

At this point, the heuristic parametric analysis is concluded having established two levels of approximation of different complexity:

1. the **first level of approximation**, which consists in calculating the numerical values of parameters a_0, a_1 and a_3 for various types of twisted cables commercially available, therefore for a defined set of values for pitch and radius;
2. the **second level of approximation**, which consists in explaining the dependence of these parameters on radius and pitch of the helix by defining the approximate functional relationships based on the numerical values of a_0, a_1 and a_3 previously obtained. The advantage of the 2nd level of approximation is the analytical representation of the dependence of B on p and α, whereas its disadvantage is the greater error on the value of B because of the further level of heuristic approximation.

2.4 APPLICATIONS – SIMULATION RESULTS

The simplified innovative formula developed here is applied to a type of three-phase twisted cable frequently used in MV in Italy, named ARG7H1RX after [63], with the following main characteristics: conductor cross-section 3x120 mm^2, rated voltage 12(phase to ground)/20(phase-to-phase) kV, ampacity I=280 A, pitch p=1.37 m and radius α=0.02 m.

Regarding the considered cable used in overhead power lines, the values of B_{exact}, B_{lit}, B_{simp1}, B_{simp2} as a function of the distance r from the axis of the helix are shown in Fig. 2.8 in linear coordinates and in Table 2.1 along with the percent errors of B_{lit}, B_{simp1}, B_{simp2} with respect to B_{exact}. The error of the simplified innovative formulain in the first level of approximation is always much smaller than the error of the approximate formula from the literature, never exceeding a few % even for small values of the distance r apart a value ~10% for r=0.3 m. As to the second level of approximation, the same considerations hold, apart distances higher than, say, 1.3 m, where the absolute error of the simplified innovative formula, B_{simp2}, is practically the same as the error of the approximate formula: this is the price paid to the further level of approximation. However, in this range (and mostly elsewhere) the second level of approximation overestimates B, whereas eq. (2.17) underestimates B; hence – as the first level of approximation – also the second level provides a conservative estimate with respect to the literature approximation.

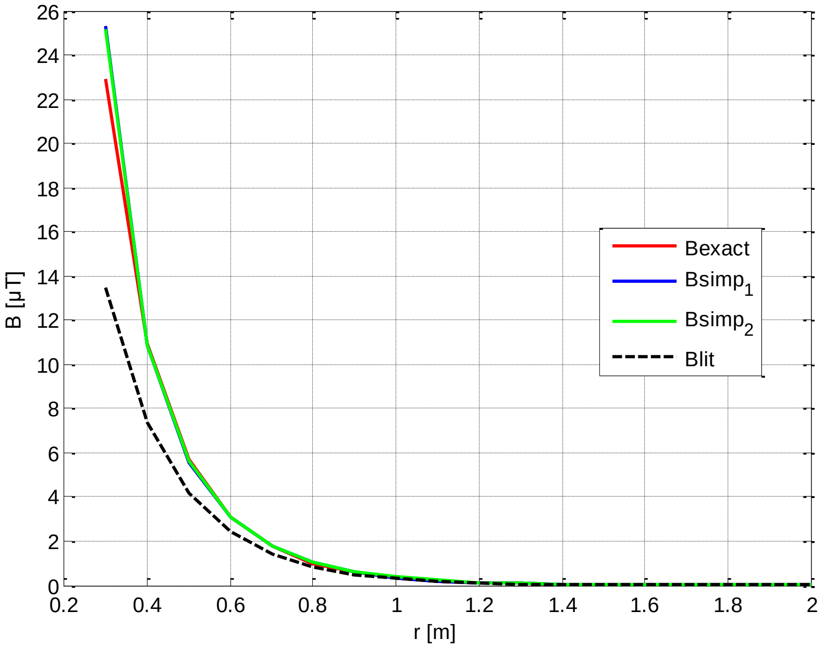

Figure 2.8: *B_{exact}, B_{lit}, B_{simp1}, B_{simp2} vs. distance r from the axis of the helix for the cable ARG7H1RX 12/20 kV 3x120 mm^2(I=280 A) in overhead line configuration in linear coordinates.*

Table 2.1: *B_{exact}, B_{lit}, B_{simp1}, B_{simp2} vs. distance r from the axis of the helix and relevant percent errors with respect to B_{exact} for the cable ARG7H1RX 12/20 kV 3x120 mm^2(I=280 A) in overhead line configuration.*

r [m]	**B_{exact} [μT]**	**B_{lit} [μT]**	**error [%]**	**B_{simp1} [μT]**	**error [%]**	**B_{simp2} [μT]**	**error [%]**
0.3	22.92	13.49	–41.15	25.34	10.56	25.17	9.81
0.4	10.94	7.385	–32.50	10.84	–0.94	10.87	-0.66
0.5	5.695	4.175	–26.68	5.553	–2.49	5.598	-1.70
0.6	3.112	2.410	–22.57	3.066	–1.47	3.103	-0.30
0.7	1.752	1.410	–19.53	1.756	0.21	1.782	1.71
0.8	1.007	0.8339	–17.21	1.026	1.91	1.045	3.71
0.9	0.5873	0.4970	–15.37	0.6071	3.38	0.6194	5.47
1.0	0.3461	0.2980	–13.90	0.3619	4.55	0.3701	6.92
1.1	0.2057	0.1796	–12.68	0.2168	5.39	0.2223	8.04
1.2	0.1231	0.1087	–11.66	0.1304	5.92	0.1339	8.83
1.3	0.0740	0.0660	–10.79	0.0786	6.16	0.0809	9.32
1.4	0.0447	0.0402	–10.05	0.0475	6.13	0.0490	9.54
1.5	0.0271	0.0246	–9.40	0.0287	5.85	0.0297	9.50
1.6	0.0165	0.0150	–8.84	0.0174	5.36	0.0180	9.24
1.7	0.0101	0.0092	–8.34	0.0105	4.67	0.0109	8.77
1.8	0.0062	0.0057	–7.89	0.0064	3.82	0.0067	8.12
1.9	0.0038	0.0035	–7.50	0.0039	2.82	0.0040	7.31
2.0	0.0023	0.0021	–7.14	0.0024	1.67	0.0025	6.36

Dealing now with the considered cable used in underground power lines at a burial depth of 0.80 m, the values of B_{exact}, B_{lit}, B_{simp1}, B_{simp2} calculated at the soil level as a function of the horizontal distance *x* from the orthogonal projection of the cable axis on the ground plane are shown in Fig. 2.9 in linear coordinates. From the viewpoint of the performances of B_{simp1} and B_{simp2} vs. B_{lit}, considerations very similar to those made for the previous case hold in this case, too. Indeed, Fig.2.9 shows clearly that the error of the simplified innovative formula, in both levels of approximation, is always much smaller than the error of the approximate formula from the literature. For very small values of *B* the curves in Fig. 2.9 tend to overlap; thus, it is better to refer to the numerical values of B_{exact}, B_{lit}, B_{simp1}, B_{simp2} and to the percent errors of B_{lit}, B_{simp1}, B_{simp2} with respect to B_{exact} reported in Table 2.2. The Table confirms that the percent errors provided by innovative eq. (2.23) in first level of approximation remain much lower - never exceeding a few % even for small values of the distance *x* and tending to 0 - than those provided by eq. (2.17) after [14], [15] and always positive.As to the second level of approximation, the errors appear slightly larger, but never exceeding 10%, and always positive, also providing a conservative estimate with respect to the literature approximation.

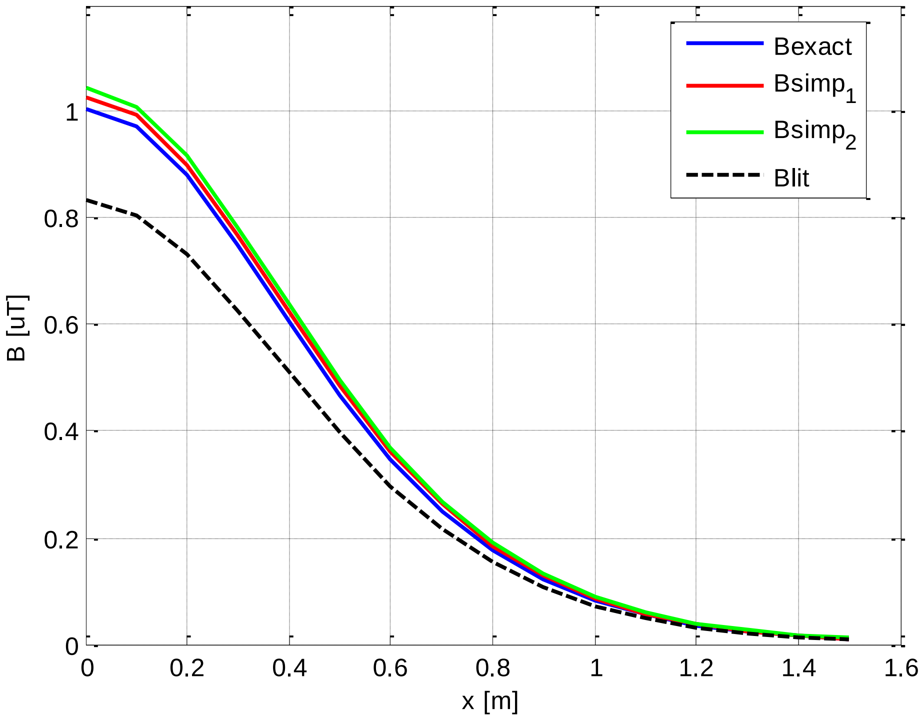

Figure 2.9: *B_{exact}, B_{lit}, B_{simp1}, B_{simp2} at ground level vs. horizontal distance x from the orthogonal projection of the cable axis on the ground plane for the cable ARG7H1RX 12/20 kV 3x120 mm^2 (I=280 A) in underground line configuration at a depth of 0.80 m in linear coordinates.*

Table 2.2: *B_{exact}, B_{lit}, B_{simp1}, B_{simp2} at ground level vs. horizontal distance x from the orthogonal projection of the cable axis on the ground plane for the cable ARG7H1RX 12/20 kV 3x120 mm^2(I=280 A) in underground line configuration at a depth of 0.80 m.*

x [m]	**B_{exact} [μT]**	**B_{lit} [μT]**	**error [%]**	**B_{simp1} [μT]**	**error [%]**	**B_{simp2} [μT]**	**error [%]**
0.0	1.007	0.8339	–17.21	1.026	1.91	1.045	3.71
0.1	0.9735	0.8073	–17.08	0.9930	2.01	1.011	3.83
0.2	0.8809	0.7336	–16.71	0.9011	2.29	0.9176	4.17
0.3	0.7499	0.6287	–16.16	0.7704	2.74	0.7852	4.70
0.4	0.6050	0.5114	–15.47	0.6250	3.31	0.6376	5.38
0.5	0.4663	0.3978	–14.69	0.4846	3.93	0.4950	6.14
0.6	0.3461	0.2980	–13.90	0.3619	4.55	0.3701	6.92
0.7	0.2492	0.2165	–13.10	0.2619	5.12	0.2683	7.66
0.8	0.1750	0.1534	–12.34	0.1848	5.59	0.1896	8.32
0.9	0.1205	0.1065	–11.62	0.1276	5.94	0.1312	8.86
1.0	0.0817	0.0727	–10.95	0.0867	6.14	0.0892	9.25
1.1	0.0546	0.0490	–10.33	0.0580	6.17	0.0598	9.48
1.2	0.0362	0.0327	–9.77	0.0384	6.04	0.0396	9.55
1.3	0.0238	0.0216	–9.25	0.0251	5.74	0.0260	9.45
1.4	0.0155	0.0141	–8.77	0.0163	5.29	0.0169	9.19
1.5	0.0101	0.0092	–8.34	0.0105	4.67	0.0109	8.77

For the same underground configuration of Fig. 2.9, the values of B_{exact}, B_{lit}, B_{simp1}, B_{simp2} are calculated 1 m above the soil level, i.e. where the human vital organs are situated, as a function of the horizontal distance *x* from the orthogonal projection of the cable axis on the plane parallel to the ground at the same height are shown in Fig. 2.10 in linear coordinates.

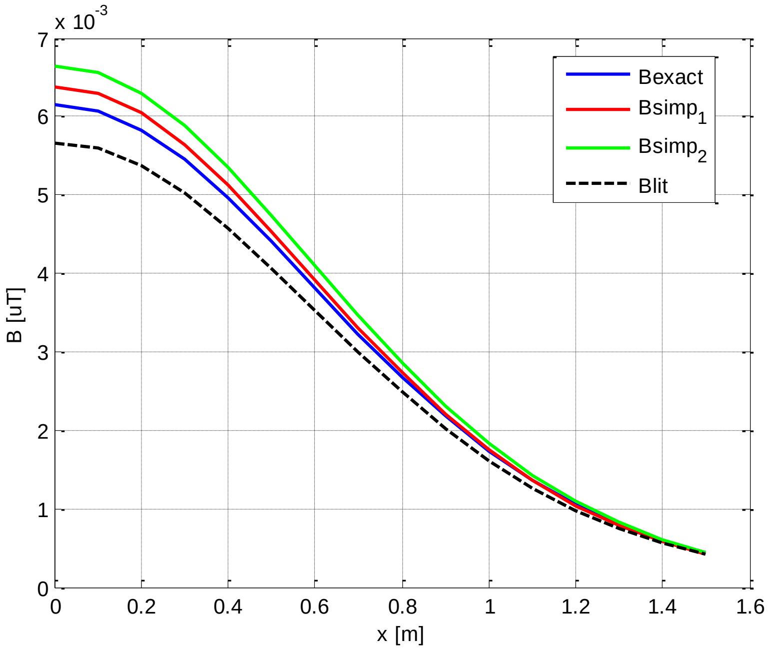

Figure 2.10: *B_{exact}, B_{lit}, B_{simp1}, B_{simp2} at 1 m height from the ground vs. horizontal distance x from the orthogonal projection of the cable axis on the ground plane for the cable ARE4H1RX 12/20 kV 3x120 mm^2 (I=280 A) in underground line configuration at a depth of 0.80 m in linear coordinates.*

The values of B are very small and the curves in Fig. 2.10 tend to overlap, although the better performances of B_{simp1} and B_{simp2}, with respect to B_{lit} remain evident; however, for a less subjective evaluation, the numerical values of B_{exact}, B_{lit}, B_{simp1}, B_{simp2} and the percent errors of B_{lit}, B_{simp1}, B_{simp2},with respect to B_{exact} are reported in Table 2.3.

Table 2.3: *B_{exact}, B_{lit}, B_{simp1}, B_{simp2} at 1 m height from the ground vs. horizontal distance x from the orthogonal projection of the cable axis on the ground plane for the cable ARE4H1RX 12/20 kV 3x120 mm^2 (I=280 A) in underground line configuration at a depth of 0.80 m.*

x [m]	**B_{exact} [μT]**	**B_{lit} [μT]**	**error [%]**	**B_{simp1} [μT]**	**error [%]**	**B_{simp2} [μT]**	**error [%]**
0.0	0.0062	0.0057	-7.89	0.0064	3.82	0.0067	8.12
0.1	0.0061	0.0056	-7.88	0.0063	3.79	0.0066	8.10
0.2	0.0058	0.0054	-7.85	0.0060	3.71	0.0063	8.04
0.3	0.0054	0.0050	-7.79	0.0056	3.58	0.0059	7.93
0.4	0.0050	0.0046	-7.71	0.0051	3.39	0.0053	7.78
0.5	0.0044	0.0041	-7.62	0.0045	3.15	0.0047	7.58
0.6	0.0038	0.0035	-7.51	0.0039	2.84	0.0041	7.33
0.7	0.0032	0.0030	-7.38	0.0033	2.47	0.0035	7.03
0.8	0.0027	0.0025	-7.24	0.0027	2.03	0.0029	6.66
0.9	0.0022	0.0020	-7.09	0.0022	1.52	0.0023	6.23
1.0	0.0017	0.0016	-6.94	0.0018	0.95	0.0018	5.74
1.1	0.0014	0.0013	-6.78	0.0014	0.30	0.0014	5.17
1.2	0.0010	0.0010	-6.62	0.0010	-0.43	0.0011	4.54
1.3	0.0008	0.0007	-6.46	0.0008	-1.22	0.0008	3.84
1.4	0.0006	0.0006	-6.30	0.0006	-2.08	0.0006	3.07
1.5	0.0004	0.0004	-6.14	0.0004	-3.01	0.0004	2.23

All the comments relevant to previous Fig. 2.9 hold in the case of Fig. 2.10 too – in particular a further reduction of the field values is observed, as expected due to the further increase of the distance between field points and field source. Also in this case, the error of the simplified innovative formula, in both levels of approximation, is always smaller than the error of the approximate formula from the literature, being limited to a few % even for small values of the distance *x* and tending to 0, but now the difference between the simplified innovative formula and the approximate formula from the literature is smaller, due to the greater distance of the field-points from the helix axis. In particular, for these distances, B_{simp1} starts to underestimate the field providing a negative error. This is due to the fact that the approximation of the exact formula has been effectuated considering interval up to 2.0 m for the linear fitting of lnB_2 vs. r. This means that after 2.0 m it is possible that the simplified formula presents different behaviour than that expected. This inconvenience is compensated by the fact that at distances higher than 2.0 m the magnetic field is so drastically reduced that results practically zero. For this reason it was chosen to approximate with as much higher precision and accuracy the magnetic field up to 2.0 m near the field source and not to focus on the effects of the field where results negligible.

The better performances of the proposed simplified innovative formula compared to the approximated formula after [14], [15] is supported by two more practical cases, based on the same type of cable ARG7H1RX, but with different conductor cross-sections with respect to the previous one, hence with different values of *p* and α. These two cases are as follows:

<u>1^{st} *case*</u>: conductor cross-section 3x70 mm^2 [63], rated voltage 12(phase to ground)/20(phase-to-phase) kV, ampacity I=200 A, p=1.24 m, α=0.018 m;

<u>2^{nd} *case*</u>: conductor cross-section 3x185 mm^2 [63], rated voltage 12(phase to ground)/20(phase-to-phase) kV, ampacity I=360 A, p=1.5 m, α=0.022 m.

As shown in Figs. 2.11 - 2.16 and Tables 2.4 - 2.9, such cases confirm that the error involved by the innovative formula with respect to the exact formulation is not only much lower than that brought about by the approximated formula from the literature, but also fairly small (say, below 10% for distances >0.3 m and mostly around a few percent) and positive, thereby implying a conservative overestimation of the field. Since – as previously highlighted – the exact formula was extensively validated experimentally in [14], [15], this proves the satisfactory behaviour of the proposed innovative simplified formula not only in comparison with the approximated formula of the literature, but also in absolute terms.

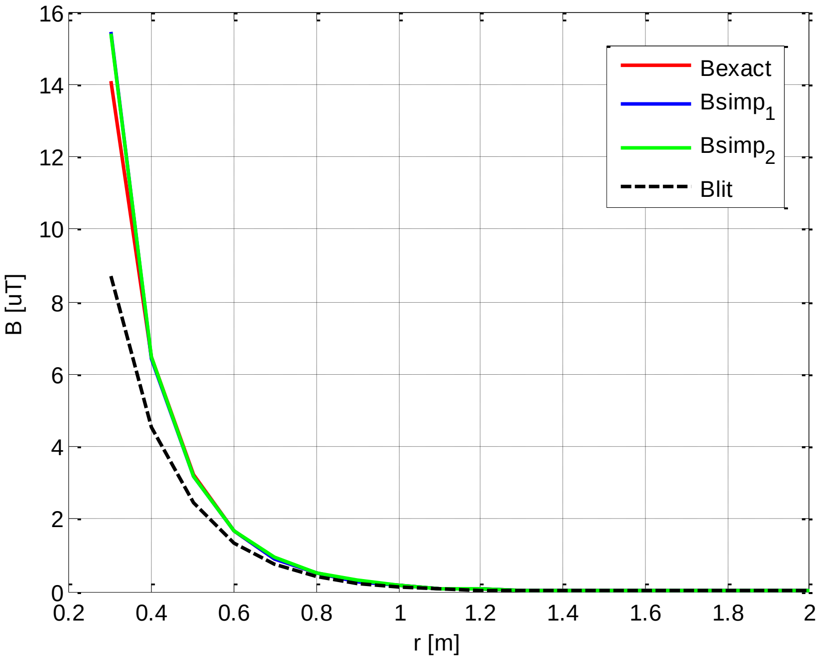

Figure 2.11: *B_{exact}, B_{lit}, B_{simp1}, B_{simp2} vs. distance r from the axis of the helix for the cable ARG7H1RX 12/20 kV 3x70 mm^2 (I=200 A) in overhead line configuration in linear coordinates.*

Table 2.4: *B_{exact}, B_{lit}, B_{simp1}, B_{simp2} vs. distance r from the axis of the helix and relevant percent errors with respect to B_{exact} for the cable ARG7H1RX 12/20 kV 3x70 mm^2(I=200 A) in overhead line configuration.*

r [m]	**B_{exact} [µT]**	**B_{lit} [µT]**	**error [%]**	**B_{simp1} [µT]**	**error [%]**	**B_{simp2} [µT]**	**error [%]**
0.3	14.06	8.718	-38.02	15.45	9.86	15.39	9.43
0.4	6.478	4.548	-29.79	6.443	-0.54	6.450	-0.44
0.5	3.240	2.451	-24.36	3.178	-1.93	3.190	-1.55
0.6	1.697	1.348	-20.55	1.681	-0.95	1.691	-0.35
0.7	0.9143	0.7519	-17.77	0.9202	0.64	0.9275	1.44
0.8	0.5023	0.4237	-15.64	0.5136	2.25	0.5185	3.22
0.9	0.2798	0.2407	-13.97	0.2900	3.64	0.2932	4.80
1.0	0.1574	0.1376	-12.62	0.1649	4.74	0.1670	6.07
1.1	0.0893	0.0790	-11.51	0.0943	5.54	0.0956	7.04
1.2	0.0510	0.0456	-10.59	0.0541	6.03	0.0549	7.70
1.3	0.0293	0.0264	-9.80	0.0311	6.24	0.0316	8.07
1.4	0.0169	0.0153	-9.13	0.0179	6.19	0.0182	8.18
1.5	0.0097	0.0089	-8.54	0.0103	5.91	0.0105	8.05
1.6	0.0057	0.0052	-8.03	0.0060	5.42	0.0061	7.71
1.7	0.0033	0.0030	-7.58	0.0034	4.74	0.0035	7.18
1.8	0.0019	0.0018	-7.17	0.0020	3.90	0.0020	6.47
1.9	0.0011	0.0010	-6.81	0.0012	2.91	0.0012	5.61
2.0	0.0007	0.0006	-6.49	0.0007	1.79	0.0007	4.61

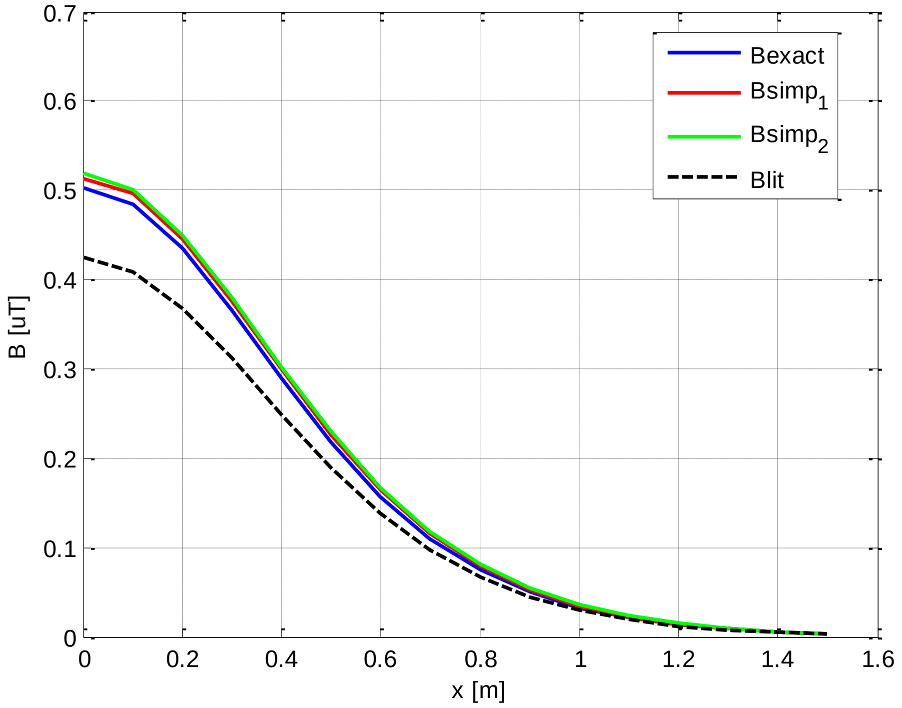

Figure 2.12: *B_{exact}, B_{lit}, B_{simp1}, B_{simp2} at ground level vs. horizontal distance x from the orthogonal projection of the cable axis on the ground plane for the cable ARG7H1RX 12/20 kV 3x70 mm^2(I=200 A) in underground line configuration at a depth of 0.80 m in linear coordinates.*

Table 2.5: *B_{exact}, B_{lit}, B_{simp1}, B_{simp2} at ground level vs. horizontal distance x from the orthogonal projection of the cable axis on the ground plane for the cable ARG7H1RX 12/20 kV 3x70 mm^2 (I=200 A) in underground line configuration at a depth of 0.80 m.*

x [m]	**B_{exact} [μT]**	**B_{lit} [μT]**	**error [%]**	**B_{simp1} [μT]**	**error [%]**	**B_{simp2} [μT]**	**error [%]**
0.0	0.5023	0.4237	-15.64	0.5136	2.25	0.5185	3.22
0.1	0.4842	0.4090	-15.52	0.4955	2.34	0.5003	3.33
0.2	0.4344	0.3684	-15.19	0.4458	2.61	0.4502	3.64
0.3	0.3648	0.3112	-14.68	0.3759	3.04	0.3798	4.11
0.4	0.2890	0.2484	-14.05	0.2993	3.57	0.3026	4.72
0.5	0.2178	0.1887	-13.35	0.2268	4.16	0.2295	5.39
0.6	0.1574	0.1376	-12.62	0.1649	4.74	0.1670	6.07
0.7	0.1101	0.0970	-11.90	0.1159	5.28	0.1174	6.72
0.8	0.0749	0.0665	-11.21	0.0791	5.72	0.0803	7.28
0.9	0.0498	0.0446	-10.55	0.0528	6.04	0.0537	7.72
1.0	0.0326	0.0293	-9.95	0.0346	6.22	0.0352	8.02
1.1	0.0210	0.0190	-9.38	0.0223	6.24	0.0227	8.17
1.2	0.0134	0.0122	-8.87	0.0142	6.10	0.0145	8.16
1.3	0.0084	0.0077	-8.40	0.0089	5.80	0.0091	7.98
1.4	0.0053	0.0049	-7.97	0.0056	5.34	0.0057	7.65
1.5	0.0033	0.0030	-7.58	0.0034	4.74	0.0035	7.18

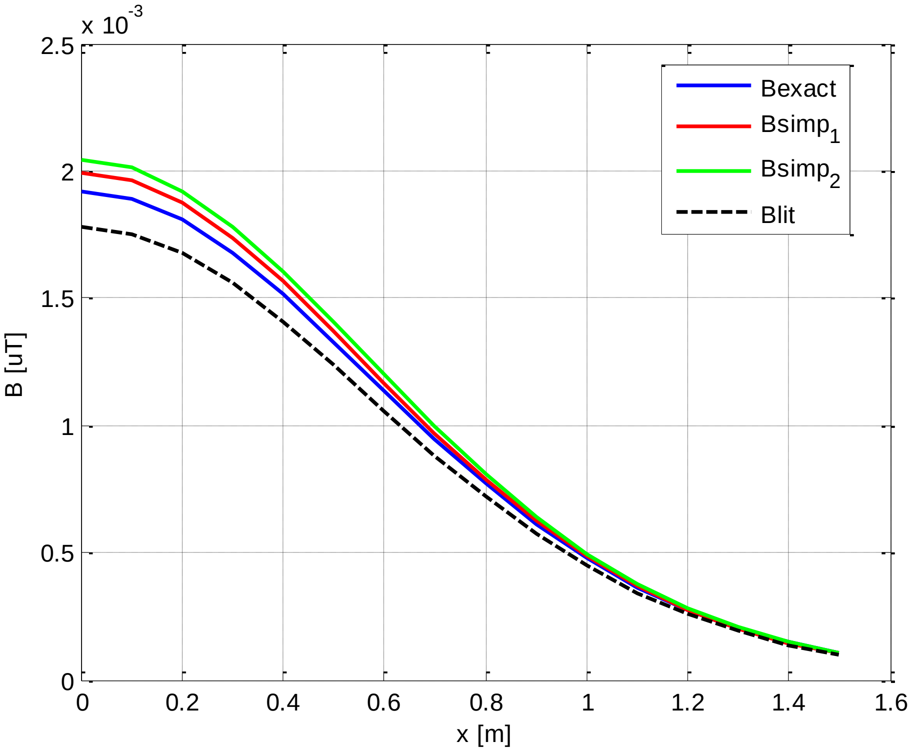

Figure 2.13: *B_{exact}, B_{lit}, B_{simp1}, B_{simp2} at 1 m height from the ground vs. horizontal distance x from the orthogonal projection of the cable axis on the ground plane for the cable ARE4H1RX 12/20 kV 3x70 mm^2 (I=200 A) in underground line configuration at a depth of 0.80 m in linear coordinates.*

Table 2.6: *B_{exact}, B_{lit}, B_{simp1}, B_{simp2} at 1 m height from the ground vs. horizontal distance x from the orthogonal projection of the cable axis on the ground plane for the cable ARE4H1RX 12/20 kV 3x70 mm^2(I=200 A) in underground line configuration at a depth of 0.80 m.*

x [m]	**B_{exact} [µT]**	**B_{lit} [µT]**	**error [%]**	**B_{simp1} [µT]**	**error [%]**	**B_{simp2} [µT]**	**error [%]**
0.0	0.0019	0.0018	-7.17	0.0020	3.90	0.0020	6.47
0.1	0.0019	0.0018	-7.16	0.0020	3.87	0.0020	6.45
0.2	0.0018	0.0017	-7.13	0.0019	3.80	0.0019	6.38
0.3	0.0017	0.0016	-7.08	0.0017	3.67	0.0018	6.27
0.4	0.0015	0.0014	-7.01	0.0016	3.48	0.0016	6.11
0.5	0.0013	0.0012	-6.92	0.0014	3.24	0.0014	5.90
0.6	0.0011	0.0011	-6.82	0.0012	2.94	0.0012	5.63
0.7	0.0009	0.0009	-6.71	0.0010	2.57	0.0010	5.31
0.8	0.0008	0.0007	-6.58	0.0008	2.14	0.0008	4.93
0.9	0.0006	0.0006	-6.45	0.0006	1.65	0.0006	4.48
1.0	0.0005	0.0004	-6.31	0.0005	1.08	0.0005	3.97
1.1	0.0004	0.0003	-6.17	0.0004	0.44	0.0004	3.39
1.2	0.0003	0.0003	-6.02	0.0003	-0.27	0.0003	2.74
1.3	0.0002	0.0002	-5.87	0.0002	-1.04	0.0002	2.03
1.4	0.0001	0.0001	-5.73	0.0001	-1.89	0.0001	1.24
1.5	0.0001	0.0001	-5.58	0.0001	-2.80	0.0001	0.39

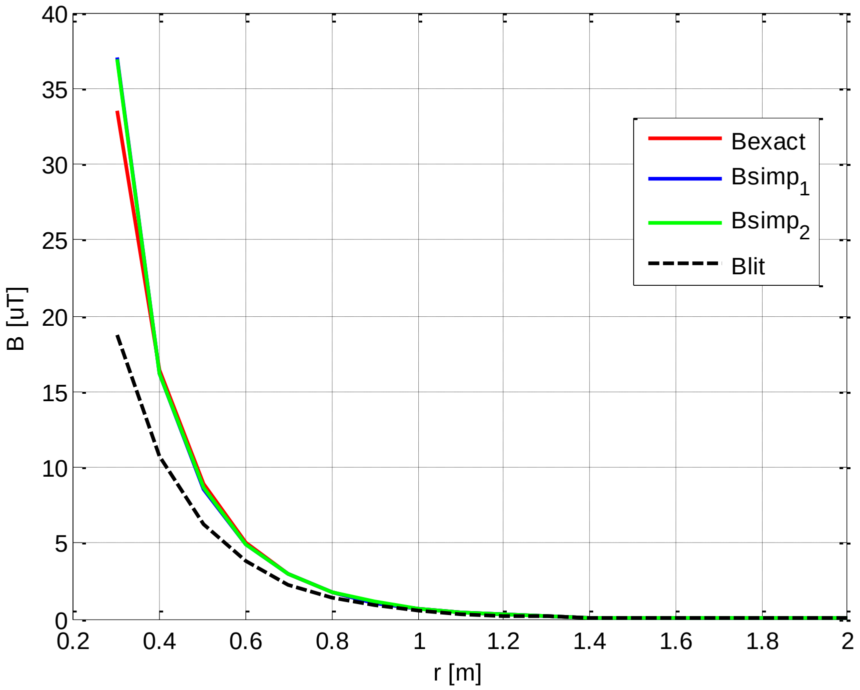

Figure 2.14: *B_{exact}, B_{lit}, B_{simp1}, B_{simp2} vs. distance r from the axis of the helix for the cable ARG7H1RX 12/20 kV 3x185 mm^2 (I=360 A) in overhead line configuration in linear coordinates.*

Table 2.7: *B_{exact}, B_{lit}, B_{simp1}, B_{simp2} vs. distance r from the axis of the helix and relevant percent errors with respect to B_{exact} for the cable ARG7H1RX 12/20 kV 3x185 mm^2 (I=360 A) in overhead line configuration.*

r [m]	**B_{exact} [μT]**	**B_{lit} [μT]**	**error [%]**	**B_{simp1} [μT]**	**error [%]**	**B_{simp2} [μT]**	**error [%]**
0.3	33.56	18.76	–44.09	37.03	10.36	36.85	9.82
0.4	16.47	10.69	–35.10	16.18	–1.73	16.22	-1.52
0.5	8.849	6.295	–28.94	8.560	–3.26	8.610	-2.70
0.6	5.004	3.776	–24.54	4.898	–2.10	4.939	-1.30
0.7	2.921	2.299	–21.27	2.912	-0.28	2.942	0.73
0.8	1.741	1.415	–18.76	1.768	1.53	1.789	2.73
0.9	1.054	0.8774	–16.77	1.087	3.11	1.101	4.48
1.0	0.6453	0.5475	–15.16	0.6735	4.36	0.6834	5.89
1.1	0.3985	0.3434	–13.84	0.4195	5.27	0.4262	6.96
1.2	0.2478	0.2163	–12.72	0.2623	5.84	0.2668	7.69
1.3	0.1549	0.1367	–11.78	0.1644	6.11	0.1675	8.10
1.4	0.0973	0.0866	–10.97	0.1032	6.09	0.1053	8.22
1.5	0.0613	0.0550	–10.26	0.0649	5.83	0.0663	8.09
1.6	0.0388	0.0351	–9.65	0.0409	5.33	0.0418	7.72
1.7	0.0246	0.0224	–9.10	0.0258	4.64	0.0264	7.15
1.8	0.0157	0.0143	–8.61	0.0162	3.77	0.0167	6.40
1.9	0.0100	0.0092	–8.18	0.0102	2.74	0.0105	5.48
2.0	0.0064	0.0059	–7.79	0.0065	1.58	0.0066	4.42

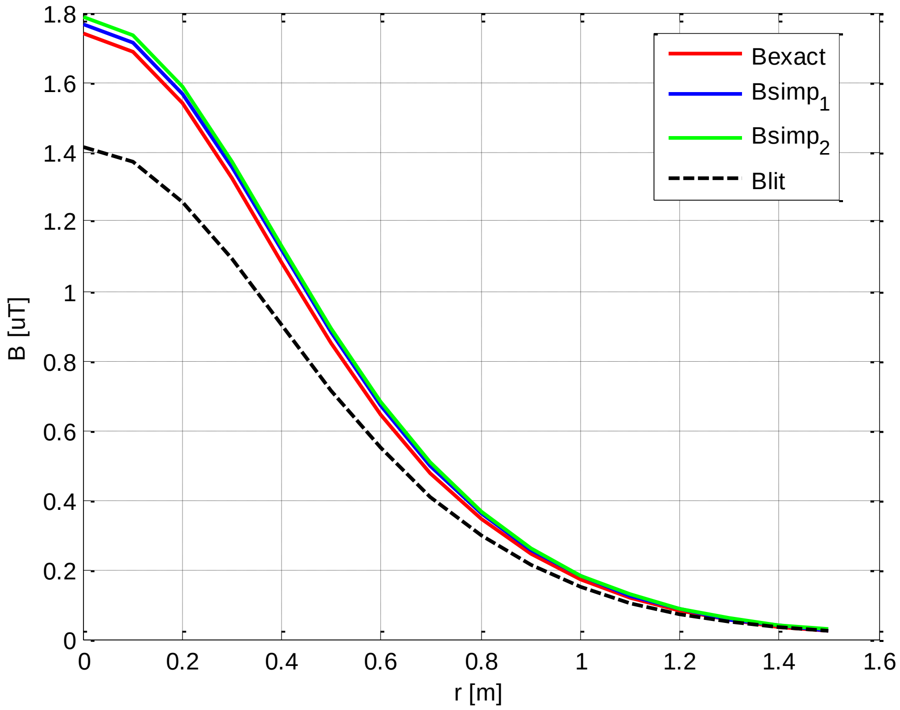

Figure 2.15: *B_{exact}, B_{lit}, B_{simp1}, B_{simp2} at ground level vs. horizontal distance x from the orthogonal projection of the cable axis on the ground plane for the cable ARG7H1RX 12/20 kV 3x185 mm^2(I=360 A) in underground line configuration at a depth of 0.80 m in linear coordinates.*

Table 2.8: *B_{exact}, B_{lit}, B_{simp1}, B_{simp2} at ground level vs. horizontal distance x from the orthogonal projection of the cable axis on the ground plane for the cable ARG7H1RX 12/20 kV 3x185 mm^2 (I=360 A) in underground line configuration at a depth of 0.80 m.*

x [m]	B_{exact} [μT]	B_{lit} [μT]	error [%]	B_{simp1} [μT]	error [%]	B_{simp2} [μT]	error [%]
0.0	1.741	1.415	-18.76	1.768	1.53	1.789	2.73
0.1	1.687	1.373	-18.62	1.715	1.64	1.735	2.85
0.2	1.537	1.257	-18.22	1.567	1.95	1.586	3.19
0.3	1.323	1.090	-17.62	1.355	2.43	1.372	3.72
0.4	1.084	0.9009	-16.87	1.117	3.03	1.131	4.39
0.5	0.8509	0.7145	-16.03	0.8823	3.69	0.8946	5.14
0.6	0.6453	0.5475	-15.16	0.6735	4.36	0.6834	5.89
0.7	0.4759	0.4078	-14.30	0.4995	4.97	0.5073	6.60
0.8	0.3431	0.2969	-13.47	0.3619	5.48	0.3679	7.22
0.9	0.2430	0.2122	-12.68	0.2572	5.86	0.2617	7.71
1.0	0.1696	0.1493	-11.95	0.1799	6.08	0.1833	8.04
1.1	0.1171	0.1039	-11.28	0.1242	6.13	0.1267	8.21
1.2	0.0800	0.0715	-10.66	0.0849	6.01	0.0866	8.20
1.3	0.0543	0.0489	-10.09	0.0574	5.72	0.0587	8.01
1.4	0.0367	0.0332	-9.57	0.0386	5.26	0.0395	7.66
1.5	0.0246	0.0224	-9.10	0.0258	4.64	0.0264	7.15

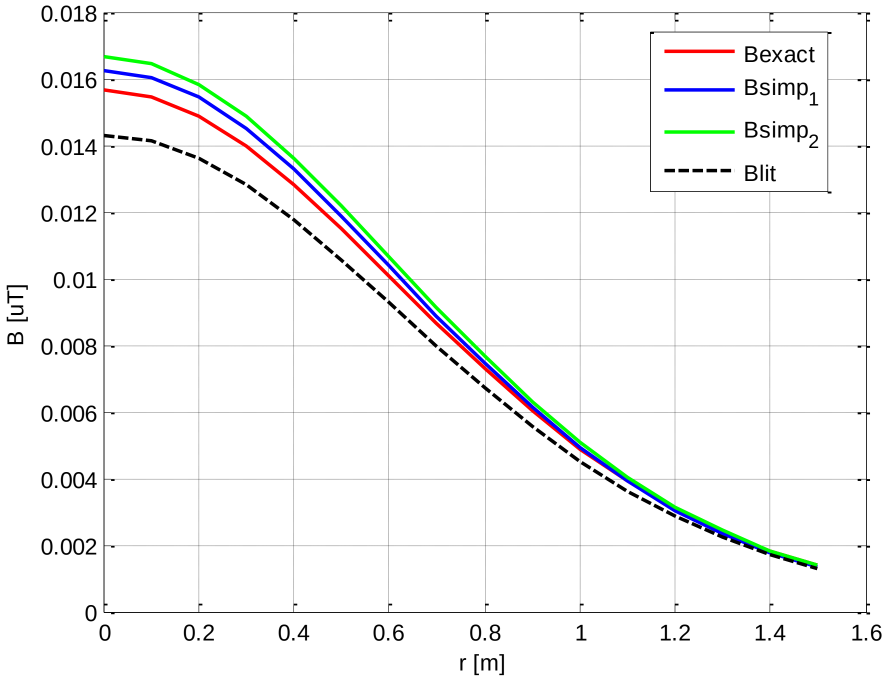

Figure 2.16: *B_{exact}, B_{lit}, B_{simp1}, B_{simp2} at 1 m height from the ground vs. horizontal distance x from the orthogonal projection of the cable axis on the ground plane for the cable ARG7H1RX 12/20 kV 3x185 mm^2(I=360 A) in underground line configuration at a depth of 0.80 m in linear coordinates.*

Table 2.9: *B_{exact}, B_{lit}, B_{simp1}, B_{simp2} at 1 m height from the ground vs. horizontal distance x from the orthogonal projection of the cable axis on the ground plane for the cable ARE4H1RX 12/20 kV 3x185 mm^2 (I=360 A) in underground line configuration at a depth of 0.80 m.*

x [m]	B_{exact} [μT]	B_{lit} [μT]	error [%]	B_{simp1} [μT]	error [%]	B_{simp2} [μT]	error [%]
0.0	0.0157	0.0143	-8.61	0.0162	3.77	0.0167	6.40
0.1	0.0155	0.0141	-8.60	0.0160	3.74	0.0164	6.37
0.2	0.0149	0.0136	-8.56	0.0154	3.66	0.0158	6.30
0.3	0.0140	0.0128	-8.50	0.0145	3.53	0.0149	6.18
0.4	0.0128	0.0118	-8.42	0.0133	3.34	0.0136	6.01
0.5	0.0115	0.0106	-8.31	0.0119	3.09	0.0122	5.79
0.6	0.0101	0.0093	-8.19	0.0104	2.77	0.0106	5.51
0.7	0.0087	0.0080	-8.05	0.0089	2.39	0.0091	5.16
0.8	0.0073	0.0067	-7.90	0.0074	1.95	0.0076	4.76
0.9	0.0060	0.0056	-7.74	0.0061	1.43	0.0063	4.28
1.0	0.0049	0.0045	-7.57	0.0049	0.84	0.0051	3.74
1.1	0.0039	0.0036	-7.40	0.0039	0.18	0.0040	3.12
1.2	0.0031	0.0028	-7.22	0.0031	-0.56	0.0031	2.43
1.3	0.0024	0.0022	-7.05	0.0023	-1.37	0.0024	1.67
1.4	0.0018	0.0017	-6.87	0.0018	-2.25	0.0018	0.84
1.5	0.0014	0.0013	-6.69	0.0013	-3.20	0.0014	-0.06

The effectiveness of the innovative expression is also evaluated with some additional numerical simulations relevant to another typical MV cable, named ARE4H1RX after [64] with the following main characteristics: conductor cross-section 3x120 mm^2, rated voltage 12(phase to ground)/20(phase-to-phase) kV, ampacity I=288 A, p=1.30 m and α=0.019 m.

As to the considered cable used in overhead power lines, the values of B_{exact}, B_{lit}, B_{simp1}, B_{simp2} as a function of the distance r from the axis of the helix are shown in Fig. 2.17 in linear coordinates and the numerical values of B_{exact}, B_{lit}, B_{simp1}, B_{simp2} and the percent errors of B_{lit}, B_{simp1}, B_{simp2} with respect to B_{exact} are reported in Table 2.10.

Figure 2.18 deals with the considered cable used in underground power lines at a burial depth of 0.80 m presenting the values of B_{exact}, B_{lit}, B_{simp1}, B_{simp2} calculated at the soil level as a function of the distance x from the axis of the cable in linear coordinates and Table 2.11 reports the numerical values of B_{exact}, B_{lit}, B_{simp1}, B_{simp2} and the percent errors of B_{lit}, B_{simp1}, B_{simp2} with respect to B_{exact}.

Finally, Fig. 2.19 shows the values of B_{exact}, B_{lit}, B_{simp1}, B_{simp2} calculated 1 m above the soil level as a function of the distance x from the cable axis in linear for the same underground configuration of Fig. 2.18, and in Table 2.12 are reported the percent errors of B_{simp1}, B_{simp2}, B_{lit} with respect to B_{exact}.

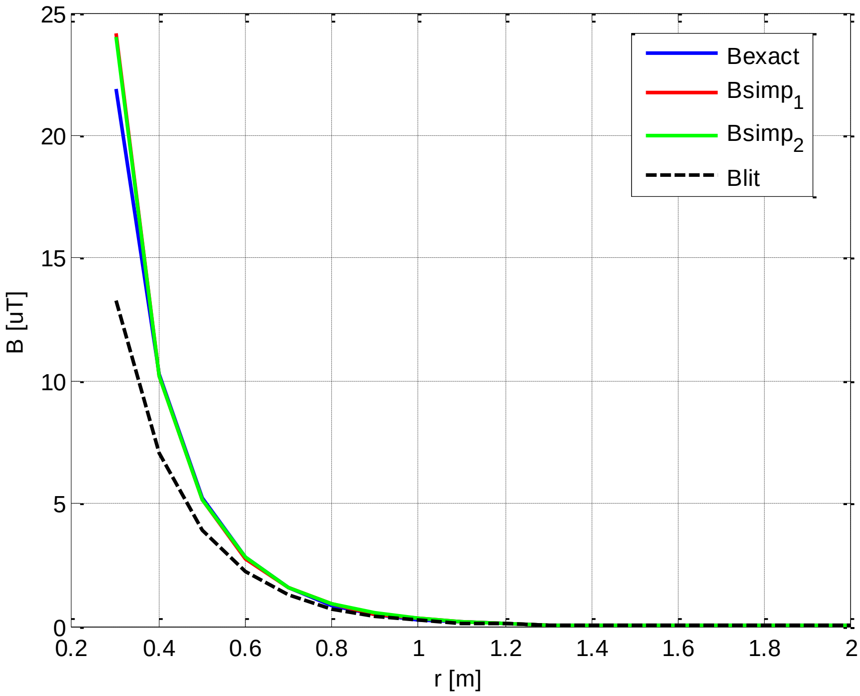

Figure 2.17: *B_{exact},B_{lit}, B_{simp1}, B_{simp2} vs. distance r from the axis of the helix for the cable ARE4H1RX 12/20 kV 3x120 mm^2 (I=288 A) in overhead line configuration in linear coordinates.*

Table 2.10: *B_{exact}, B_{lit}, B_{simp1}, B_{simp2} vs. distance r from the axis of the helix and relevant percent errors with respect to B_{exact} for the cable ARE4H1RX 12/20 kV 3x120 mm^2 (I=288 A) in overhead line configuration.*

r [m]	**B_{exact} [µT]**	**B_{lit} [µT]**	**error [%]**	**B_{simp1} [µT]**	**error [%]**	**B_{simp2} [µT]**	**error [%]**
0.3	21.88	13.24	-39.49	24.14	10.32	23.99	9.65
0.4	10.26	7.072	-31.05	10.19	-0.67	10.21	-0.46
0.5	5.232	3.901	-25.44	5.119	-2.16	5.153	-1.51
0.6	2.798	2.196	-21.49	2.765	-1.17	2.792	-0.19
0.7	1.540	1.254	-18.58	1.547	0.45	1.567	1.73
0.8	0.8650	0.7235	-16.37	0.8831	2.09	0.8965	3.64
0.9	0.4927	0.4207	-14.62	0.5100	3.52	0.5189	5.33
1.0	0.2836	0.2461	-13.21	0.2968	4.65	0.3026	6.71
1.1	0.1646	0.1447	-12.05	0.1736	5.47	0.1774	7.77
1.2	0.0961	0.0855	-11.09	0.1019	5.98	0.1043	8.52
1.3	0.0564	0.0506	-10.26	0.0599	6.20	0.0615	8.98
1.4	0.0333	0.0301	-9.56	0.0353	6.16	0.0363	9.16
1.5	0.0197	0.0179	-8.94	0.0208	5.88	0.0215	9.10
1.6	0.0117	0.0107	-8.41	0.0123	5.39	0.0127	8.81
1.7	0.0070	0.0064	-7.93	0.0073	4.70	0.0075	8.33
1.8	0.0042	0.0038	-7.51	0.0043	3.85	0.0045	7.67
1.9	0.0025	0.0023	-7.13	0.0026	2.86	0.0027	6.86
2.0	0.0015	0.0014	-6.79	0.0015	1.73	0.0016	5.91

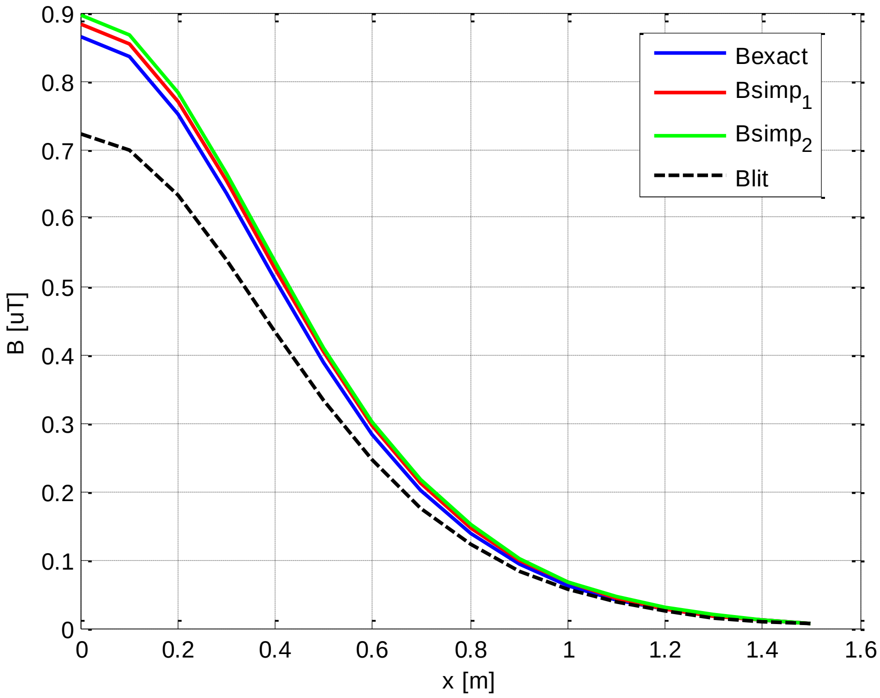

Figure 2.18: *B_{exact}, B_{lit}, B_{simp1}, B_{simp2} at ground level vs. horizontal distance x from the orthogonal projection of the cable axis on the ground plane for the cable ARE4H1RX 12/20 kV 3x120 mm^2(I=288 A) in underground line configuration at a depth of 0.80 m in linear coordinates.*

Table 2.11: *B_{exact}, B_{lit}, B_{simp1}, B_{simp2} at ground level vs. distance x from the cable axis and relevant percent errors with respect to B_{exact} for the cable ARE4H1RX 12/20 kV 3x120 mm^2(I=288 A)in underground line configuration at a depth of 0.80 m.*

x [m]	B_{exact} [µT]	B_{lit} [µT]	error [%]	B_{simp1} [µT]	error [%]	B_{simp2} [µT]	error [%]
0.0	0.8650	0.7235	-16.37	0.8831	2.09	0.8965	3.64
0.1	0.8349	0.6993	-16.25	0.8532	2.19	0.8663	3.75
0.2	0.7522	0.6326	-15.90	0.7708	2.47	0.7829	4.08
0.3	0.6359	0.5382	-15.37	0.6544	2.90	0.6651	4.59
0.4	0.5082	0.4335	-14.71	0.5258	3.45	0.5349	5.24
0.5	0.3872	0.3331	-13.97	0.4029	4.05	0.4104	5.97
0.6	0.2836	0.2461	-13.21	0.2968	4.65	0.3026	6.71
0.7	0.2011	0.1760	-12.46	0.2116	5.20	0.2160	7.42
0.8	0.1389	0.1226	-11.73	0.1468	5.66	0.1501	8.04
0.9	0.0940	0.0836	-11.05	0.0996	5.99	0.1020	8.55
1.0	0.0625	0.0560	-10.41	0.0664	6.18	0.0681	8.91
1.1	0.0411	0.0370	-9.83	0.0436	6.20	0.0448	9.12
1.2	0.0267	0.0242	-9.29	0.0283	6.07	0.0291	9.16
1.3	0.0172	0.0156	-8.79	0.0181	5.77	0.0187	9.04
1.4	0.0110	0.0100	-8.34	0.0115	5.31	0.0119	8.77
1.5	0.0070	0.0064	-7.93	0.0073	4.70	0.0075	8.33

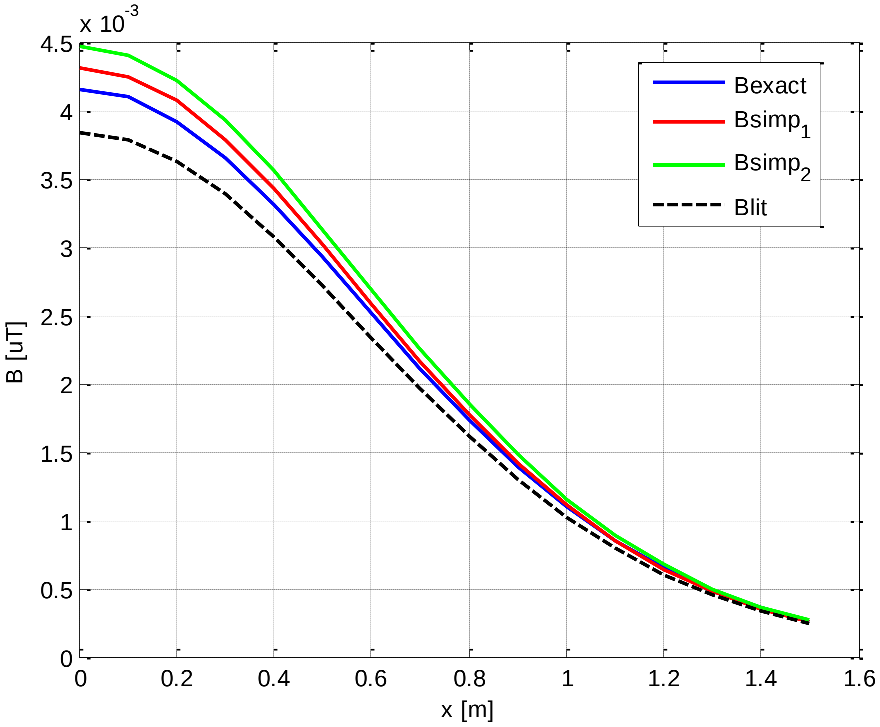

Figure 2.19: *B_{exact}, B_{lit},B_{simp1}, B_{simp2} at 1 m height from the ground vs. horizontal distance x from the orthogonal projection of the cable axis on the ground plane for the cable ARE4H1RX 12/20 kV 3x120 mm^2 (I=288 A) in underground line configuration at a depth of 0.80 m in linear coordinates.*

Table 2.12: *B_{exact}, B_{lit}, B_{simp1}, B_{simp2} at 1 m height from the ground vs. distance x from the cable axis and relevant percent errors with respect to B_{exact} for the cable ARE4H1RX 12/20 kV 3x120 mm^2(I=288 A)in underground line configuration at a depth of 0.80 m.*

x [m]	B_{exact} [µT]	B_{lit} [µT]	error [%]	B_{simp1} [µT]	error [%]	B_{simp2} [µT]	error [%]
0.0	0.0042	0.0038	-7.51	0.0043	3.85	0.0045	7.67
0.1	0.0041	0.0038	-7.50	0.0042	3.83	0.0044	7.65
0.2	0.0039	0.0036	-7.46	0.0041	3.75	0.0042	7.59
0.3	0.0037	0.0034	-7.41	0.0038	3.62	0.0039	7.49
0.4	0.0033	0.0031	-7.34	0.0034	3.43	0.0036	7.33
0.5	0.0029	0.0027	-7.25	0.0030	3.19	0.0031	7.13
0.6	0.0025	0.0023	-7.14	0.0026	2.89	0.0027	6.88
0.7	0.0021	0.0020	-7.02	0.0022	2.52	0.0023	6.57
0.8	0.0017	0.0016	-6.89	0.0018	2.08	0.0018	6.21
0.9	0.0014	0.0013	-6.75	0.0014	1.58	0.0015	5.78
1.0	0.0011	0.0010	-6.60	0.0011	1.01	0.0012	5.28
1.1	0.0008	0.0008	-6.45	0.0009	0.37	0.0009	4.72
1.2	0.0006	0.0006	-6.30	0.0006	-0.35	0.0007	4.09
1.3	0.0005	0.0005	-6.15	0.0005	-1.13	0.0005	3.39
1.4	0.0004	0.0003	-5.99	0.0003	-1.98	0.0004	2.62
1.5	0.0003	0.0002	-5.84	0.0003	-2.91	0.0003	1.79

Considerations very similar to those made for the cable ARG7H1RX 12/20 kV with conductor cross-section 3x120 mm^2 also hold in these cases. Figs. 2.17- 2.19 and Tables 2.10 - 2.12 prove once more that the error introduced by the simplified innovative formula, in the first and second level of approximation, is modest (<10%) and mostly positive, providing a conservative estimate of the field. On the other hand, the literature approximation (eq. (2.17)) brings about an error always higher, in absolute terms, than that brought about by the proposed simplified formula, and always negative, underestimating the field.

The simulations results also include the calculation of the magnetic field isolines of 1.0 μT, 3.0 μT (‘quality objective’), 5 μT, 10μT (‘attention value’) and 100 μT (‘exposure limit’) for frequently used MV cable types, and are presented in Appendix 2, facilitating the direct calculation of the distances corresponding to a maximum limit value of the rms magnetic induction generated by these cables carrying current equal at their ampacity.

2.5 CONCLUSIONS

As shown in this Chapter, the literature approximation for the calculation of the magnetic field generated by a twisted three-phase power cable carrying balanced three-phase currents provides acceptable results for large distances from the helix axis only, whereas for distances close to the conductor it exhibits large errors compared to the exact expression of the magnetic field. For this reason, a parametric heuristic analysis was performed that resulted in an innovative simplified expression of the rms magnetic induction as a function of the distance from the helix axis. This innovative expression approximates the logarithm of *B* with the equation of a straight line plus a hyperbolic term for simulating the deviation from linearity close to the helix axis.

The effectiveness of the innovative expression is evaluated through some numerical simulations relevant to two typical MV cables i.e. ARG7H1RX 12/20 kV with cross-sections 3x70 mm^2, 3x120 mm^2 and 3x185 mm^2, and ARE4H1RX with cross-section 3x120 mm^2, in order to compare the results provided by the exact and the approximate formulae from the literature with those obtained via the innovative simplified formula. The very similar results obtained from the simulations concerning the two different MV cable types have proven the satisfactory behaviour of the proposed simplified formula in comparison with the approximated formula from the literature not only for the cases treated here, but also in broader terms. Thus, it can be argued that the considerations made about the proposed simplified formula in both levels of approximation, can be regarded as valid for all cable types commonly employed in distribution networks.

In conclusion, it can be said that the innovative formula results definitely much simpler than the exact one and provides a much smaller relative error compared to the approximated one from the literature, especially for small distances from the helix axis.

CHAPTER 3

DOUBLE-CIRCUIT TWISTED THREE-PHASE CABLE LINES

3.1 THEORY

Here, both the exact and the simplified innovative formulation are extended and applied to double-circuit twisted cable lines, making the hypothesis that the currents carried by both the cables are in-phase. Because of the linearity of the medium, the study of the magnetic field from adouble-circuit twisted three-phase cable line is based on the superposition principle, which implies that the magnetic field generated by each circuit can be calculated separately at every field-point and then the two individual magnetic fields can be composed linearly. As far as this composition is concerned, different approaches of increasing complexity and accuracy will be followed.

3.1.1 Exact Vector Analysis

The exact approach to the study of the magnetic field from a double-circuit twisted three-phase cable line is based, firstly, on the conversion between the cylindrical coordinate system (see Fig. 2.2) and the Cartesian coordinate system and, subsequently, on carrying out the vector sum of the Cartesian components of the magnetic field in a “reference plane” where the field points of interest lie. This plane commonly coincides with a line section taken as orthogonal to the ground, the latter assumed as flat. For overhead cable lines – where cables hang from one pole to another at variable distances from the ground in a catenary-like shape – this section is usually the mid-span section, where the conductors are closest to the ground and hence the field is highest at the ground level. For underground cable lines, where cables in general run parallel to each other and to the ground, this section can be a particular section close to sensitive receptors.

Hence, it can be concluded that both for overhead and underground double-circuit twisted three-phase cable lines the “reference plane” for calculation is a Cartesian x–y plane assumed as orthogonal to the helix axis of both twisted three-phase cables and as matching the equation $z=0$. The helix axis – or cylindrical axis z of Fig. 2.2 - is the Cartesian z-axis; hence, the z coordinate is the same in both systems.

In order to address better the “exact” vector sum of the Cartesian components of the magnetic field for double-circuit twisted three-phase cable lines, a “reference arrangement” of the double-circuit line is firstly considered, wherethe two twisted cable circuits are attached on opposite sides of poles and placed at the same height from the ground, being *d* the horizontal distance between the two cables: for the sake ofclarity, “cable number 1”is the twisted cable located in the semi-space where $x<0$, while “cable number 2” is that located in the semi-space where $x>0$.

Fig. 3.1 shows a sketch of the chosen “reference arrangement”, as well as the radial field component, B_r, and the azimuthal field component, B_φ, generated by circuit 1 and 2 at five different equally spaced field-points lying along the *x*-axis and contained in the plane $z=0$. As a consequence of the chosen arrangement, the radial component generated by each cable at a certain field point has the direction of the straight line connecting the helix axis of each cable with that field point, whereas the azimuthal component generated by each cable is orthogonal to the radial component at every field-point. Note that the axial component, B_z, at each field-point is omitted in Fig. 3.1 since the *z*-axis is orthogonal to the plane $z=0$, as outlined in the Figure.

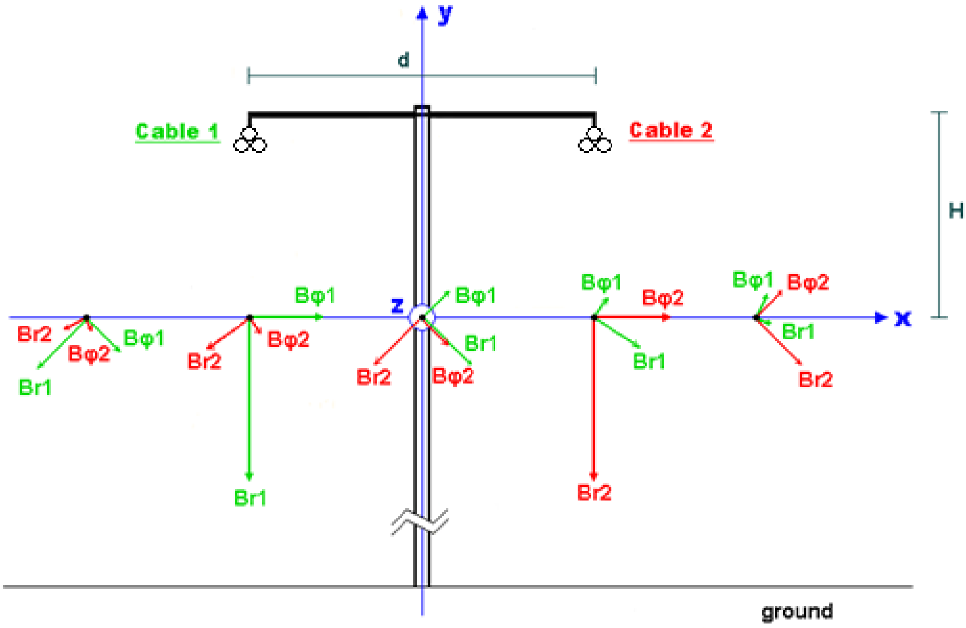

Figure 3.1: *Sketch of the “reference arrangement” of the double-circuittwisted three-phase cable line chosen as first case-study for the vector sum of the Cartesian components of the magnetic field. The relevant radial (B_r) and azimuthal (B_φ) field components generated by circuit 1 (green arrows) and 2 (red arrows) at five equally spaced field-points along the x-axis are shown.*

The magnetic field from the double-circuit, B_{DOUBLE}, is given by the following formula:

$$B_{DOUBLE} = \sqrt{B_x^2 + B_y^2 + B_z^2} \tag{3.1}$$

being
$$\begin{cases} B_x = B_{r1}\cos\theta_1 + B_{r2}\cos\theta_2 + B_{\phi 1}\cos\varphi_1 + B_{\phi 2}\cos\varphi_2 \\ B_y = B_{r1}\sin\theta_1 + B_{r2}\sin\theta_2 + B_{\phi 1}\sin\varphi_1 + B_{\phi 2}\sin\varphi_2 \\ B_z = B_{z1} + B_{z2} \end{cases} \tag{3.2}$$

where B_{r1}, B_{r2}, $B_{\varphi 1}$, $B_{\varphi 2}$ and B_{z1}, B_{z2} are the exact values of the radial, azimuthal and axial components of the magnetic field from circuit 1 and from circuit 2, respectively, while θ_1, θ_2, and φ_1, φ_2 are the angles formed by the x-axis and the radial, B_r, and azimuthal components, B_φ, from circuit 1 and 2, respectively (measured anticlockwise from the x-axis).

It holds:

$$\begin{cases} \theta_1 = \arctan(y_1 / x_1) \\ \theta_2 = \arctan(y_2 / x_2) \end{cases} \tag{3.3}$$

and
$$\begin{cases} \varphi_1 = \theta_1 + \pi/2 \\ \varphi_2 = \theta_2 + \pi/2 \end{cases} \tag{3.4}$$

where (x_1,y_1) are the coordinates of cable 1 and (x_2,y_2) are the coordinates of cable 2 in the plane z=0, where $\varphi=\Phi$.

The above theoretical approach has been converted into a calculation tool for the magnetic field from double-circuit twisted three-phase cable lines by implementing relationships (3.1) - (3.4), plus exact formulae (2.6) for B_{r1}, B_{r2}, $B_{\varphi 1}$, $B_{\varphi 2}$ and B_{z1}, B_{z2}, respectively, in a script in Matlab$^{\text{TM}}$ environment.

A proper approach to some practical problems involved by the vector sum can be accomplished by focusing more into the “reference arrangement” sketched in Fig. 3.1. So, for this ***first case study***, the two twisted cable circuits displayed in Fig. 3.1 are ARG7H1RX [63] cables with cross-section 3x120 mm^2, rated voltage 12(phase-to-ground)/20(phase-to-phase) kV, ampacity I=280 A, pitch$p$=1.37 m, radius α=0.020 m and the distance between them has been chosen to be d=1.0 m. Further, five equally-spaced field points on a straight horizontal line that spreads from -1.0 m to 1.0 m at both ends of the line axis and whose vertical distance from the conductors is H=0.5 m have been set.

3.1.1.1 Angle Φ

As clearly shown by relationships (2.6) and (2.12), the total field and the relevant components are also functions of the angle Φ which indicates the angular position of the field-point in the twisted configuration (see Fig. 2.2). Therefore, performing the exact vector sum at each x-y plane of interest for the calculation of magnetic field requires knowing the precise geometrical arrangement of the three phases of each twisted cable at that plane, but it can be argued that this geometrical arrangement – in particular the angle Φ of the three phases of each circuit – can be hardly known precisely in practice.

Because of the above-mentioned practical problems, 16 possible phase arrangements have been chosen as "base arrangements", from which 8 are symmetric and 8 are anti-symmetric phase configurations, as shown in Tables 3.1 and 3.2. the angles θ_1 and θ_2, reported in Tables 3.1 and 3.2, are the angles of eq. 3.3.

***Table 3.1:** Geometrical arrangements of the 8 symmetric "base arrangements" with relevant angles Φ_1 and Φ_2.*

SYMMETRIC PHASE ARRANGEMENTS	
1.a) 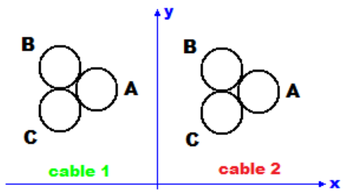 $\Phi_1=\theta_1$ $\Phi_2=\theta_2$	**5.a)** 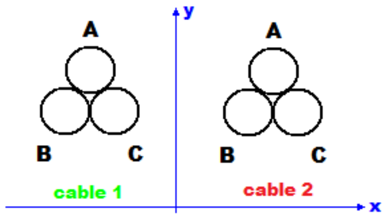 $\Phi_1=\theta_1-\pi/2$ $\Phi_2=\theta_2-\pi/2$
2.a) 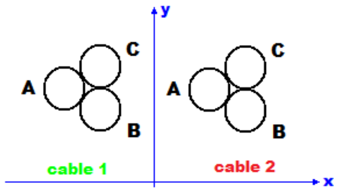 $\Phi_1=\theta_1-\pi$ $\Phi_2=\theta_2-\pi$	**6.a)** 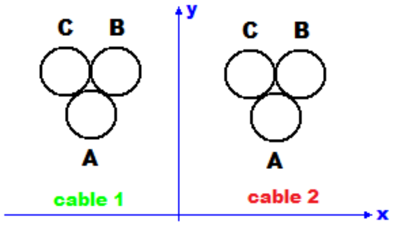 $\Phi_1=\theta_1-3\pi/2$ $\Phi_2=\theta_2-3\pi/2$
3.a) 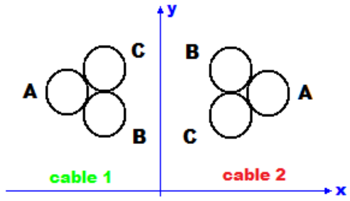 $\Phi_1=\theta_1-\pi$ $\Phi_2=\theta_2$	**7.a)** 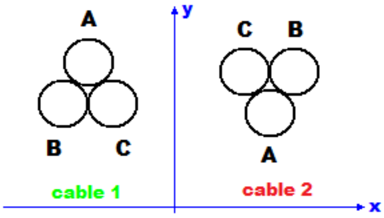 $\Phi_1=\theta_1-\pi/2$ $\Phi_2=\theta_2-3\pi/2$
4.a) 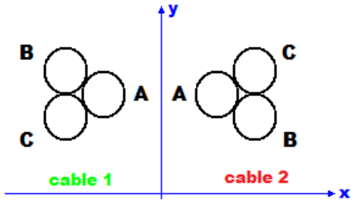 $\Phi_1=\theta_1$ $\Phi_2=\theta_2-\pi$	**8.a)** 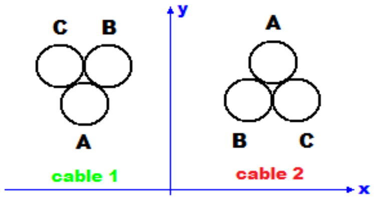 $\Phi_1=\theta_1-3\pi/2$ $\Phi_2=\theta_2-\pi/2$

Table 3.2: *Geometrical arrangements of the 8 anti-symmetric "base arrangements" with relevant angles Φ_1 and Φ_2.*

ANTI-SYMMETRIC PHASE ARRANGEMENTS	
1.b) 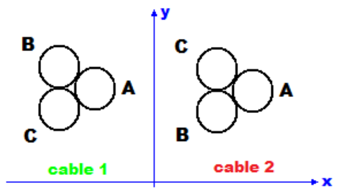 $\Phi_1=\theta_1$ $\Phi_2=2\pi-\theta_2$	**5.b)** 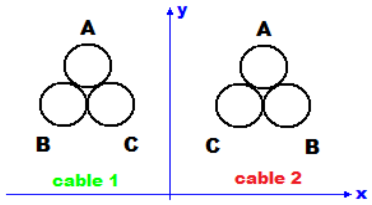 $\Phi_1=\theta_1-\pi/2$ $\Phi_2=\pi/2-\theta_2$
2.b) 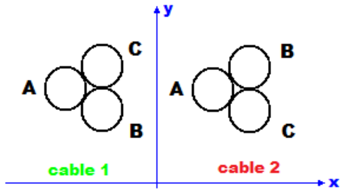 $\Phi_1=\theta_1-\pi$ $\Phi_2=\pi-\theta_2$	**6.b)** 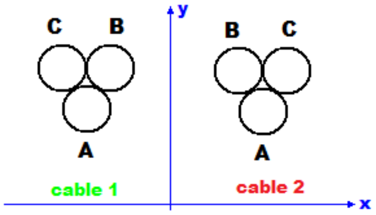 $\Phi_1=\theta_1-3\pi/2$ $\Phi_2=3\pi/2-\theta_2$
3.b) 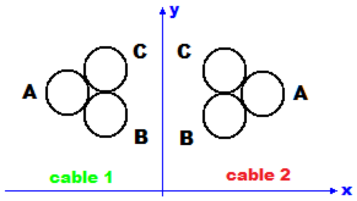 $\Phi_1=\theta_1-\pi$ $\Phi_2=2\pi-\theta_2$	**7.b)** 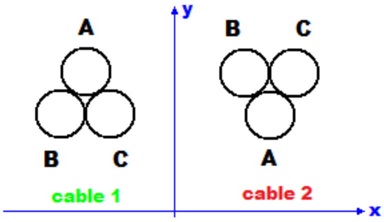 $\Phi_1=\theta_1-\pi/2$ $\Phi_2=3\pi/2-\theta_2$
4.b) 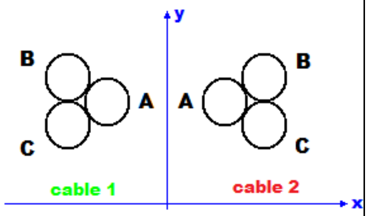 $\Phi_1=\theta_1$ $\Phi_2=\pi-\theta_2$	**8.b)** 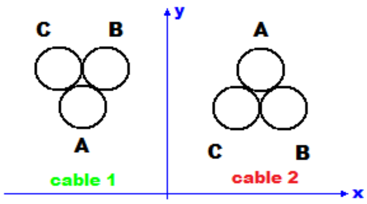 $\Phi_1=\theta_1-3\pi/2$ $\Phi_2=\pi/2-\theta_2$

For each base arrangement, the calculation of the total magnetic field was effectuated in function of the angles Φ_1 and Φ_2, which are not constant along the x-axis. A first remark on the results is that the 8 symmetric and the 8 anti-symmetric base arrangements provide the same value of the magnetic field at the same field-points.

From the comparison between the values of B_{DOUBLE} from Table 3.3, it can be deduced that the 16 base arrangements even if they are geometrically different as to the values of Φ_1, Φ_2 at every field-point, yield practically equivalent magnetic field profiles at the chosen line section. This is confirmed by Fig. 3.2, where the field profiles from -1.0 m to 1.0 m relevant to the first 8 out of 16 base arrangements are plotted: the eight profiles, labelled as $B_{DOUBLE1}$, $B_{DOUBLE2}$,…, $B_{DOUBLE8}$, can hardly – if ever – be distinguished from each other. Moreover, none of the 16 base arrangements resulted as the most unfavourable of all in terms of exposure to magnetic field, since some give rise to highest values at some points, other at other points. Thus, the problem of choosing the most unfavourable geometrical arrangement among all possible arrangements arises.

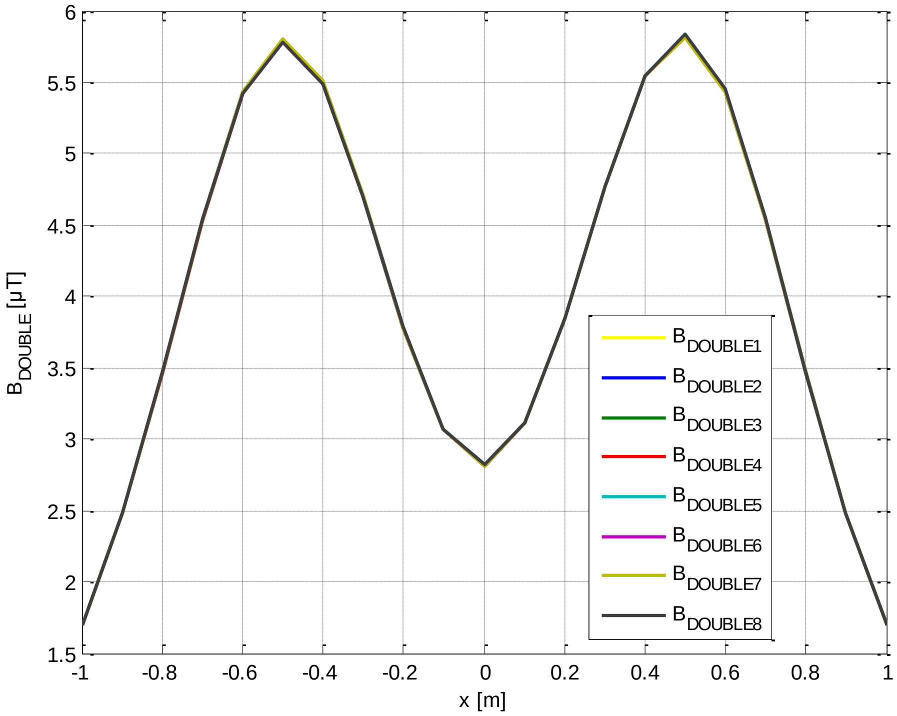

Figure 3.2: *Comparison between the values of the* B_{DOUBLE} *of the first 8 hypothetical symmetric cases for I=280 A.*

A hint at solving this problem in a conservative way comes from the parametrical analysis discussed in Chapter 2. This analysis concluded in setting a constant value for the angle Φ=60° which yields the maximum value of B and corresponds to the most dangerous case in terms of exposure to magnetic field. This choice corresponds to a geometrical arrangement that cannot be found in practice, but it provides at every field point a maximum value of the magnetic field generated by each single circuit. Nevertheless, this is not always true for their vector sum, $B_{DOUBLE,max}$. This is made clear in Tables 3.3 and 3.4, where the values of B_{DOUBLE} of the first 8 symmetric base arrangements are listed (the 8 anti-symmetric cases are omitted since they provide the same value for B_{DOUBLE}), and compared with the values of $B_{DOUBLE,max}$ for Φ=60° through the relevant percent deviations ΔB%.

Table 3.3: *B_{DOUBLE} values of the first 8 symmetric base arrangementsfor I=280 A.*

x [m]	$B_{DOUBLE,1}$ [μT]	$B_{DOUBLE,2}$ [μT]	$B_{DOUBLE,3}$ [μT]	$B_{DOUBLE,4}$ [μT]	$B_{DOUBLE,5}$ [μT]	$B_{DOUBLE,6}$ [μT]	$B_{DOUBLE,7}$ [μT]	$B_{DOUBLE,8}$ [μT]	$B_{DOUBLE,max}$ [μT]
-1.0	1.6986	1.6999	1.6999	1.6986	1.6986	1.6999	1.6986	1.6999	1.7001
-0.9	2.4829	2.4864	2.4864	2.4829	2.4838	2.4855	2.4838	2.4855	2.4866
-0.8	3.4681	3.4757	3.4757	3.4681	3.4717	3.4721	3.4717	3.4721	3.4757
-0.7	4.5350	4.5469	4.5469	4.5350	4.5437	4.5382	4.5436	4.5382	4.5474
-0.6	5.4192	5.4296	5.4295	5.4193	5.4321	5.4167	5.4320	5.4168	5.4336
-0.5	5.7946	5.7946	5.7946	5.7946	5.8050	5.7842	5.8049	5.7843	5.8049
-0.4	5.5038	5.4938	5.4937	5.5038	5.5065	5.4911	5.5061	5.4915	5.5076
-0.3	4.7131	4.7020	4.7021	4.7130	4.7106	4.7046	4.7096	4.7056	4.7131
-0.2	3.7868	3.7803	3.7810	3.7861	3.7846	3.7826	3.7823	3.7849	3.7853
-0.1	3.0730	3.0692	3.0716	3.0706	3.0729	3.0694	3.0687	3.0735	3.0695
-0.0	2.8197	2.8149	2.8200	2.8147	2.8200	2.8147	2.8149	2.8197	2.8136
0.1	3.1168	3.1109	3.1170	3.1106	3.1155	3.1121	3.1126	3.1151	3.1102
0.2	3.8460	3.8437	3.8461	3.8437	3.8451	3.8447	3.8449	3.8449	3.8436
0.3	4.7639	4.7685	4.7639	4.7685	4.7673	4.7652	4.7652	4.7673	4.7687
0.4	5.5409	5.5482	5.5409	5.5482	5.5499	5.5392	5.5391	5.5499	5.5510
0.5	5.8254	5.8254	5.8254	5.8254	5.8341	5.8166	5.8166	5.8342	5.8342
0.6	5.4474	5.4380	5.4474	5.4380	5.4497	5.4358	5.4357	5.4497	5.4511
0.7	4.5564	4.5453	4.5564	4.5453	4.5534	4.5483	4.5483	4.5534	4.5570
0.8	3.4806	3.4732	3.4806	3.4732	3.4767	3.4771	3.4771	3.4767	3.4806
0.9	2.4888	2.4853	2.4888	2.4853	2.4862	2.4879	2.4879	2.4862	2.4889
1.0	1.7010	1.6998	1.7010	1.6998	1.6998	1.7010	1.7010	1.6998	1.7013

Table 3.4: *Relevant percent errors of the values B_{DOUBLE} of first 8 symmetric base arrangements with respect to $B_{DOUBLE,max}$ (I=280 A).*

x [m]	ΔB_1 [%]	ΔB_2 [%]	ΔB_3 [%]	ΔB_4 [%]	ΔB_5 [%]	ΔB_6 [%]	ΔB_7 [%]	ΔB_8 [%]
-1.0	-0.09	-0.02	-0.02	-0.09	-0.09	-0.02	-0.09	-0.02
-0.9	-0.15	-0.01	-0.01	-0.15	-0.11	-0.04	-0.11	-0.04
-0.8	-0.22	-0.00	-0.00	-0.22	-0.12	-0.10	-0.12	-0.10
-0.7	-0.27	-0.01	-0.01	-0.27	-0.08	-0.20	-0.08	-0.20
-0.6	-0.26	-0.07	-0.07	-0.26	-0.03	-0.31	-0.03	-0.31
-0.5	-0.18	-0.18	-0.18	-0.18	-0.01	-0.36	0.00	-0.36
-0.4	-0.07	-0.25	-0.25	-0.07	-0.02	-0.30	-0.03	-0.29
-0.3	0.00	-0.23	-0.23	-0.00	-0.05	-0.18	-0.07	-0.16
-0.2	0.04	-0.13	-0.11	0.02	-0.02	-0.07	-0.08	-0.01
-0.1	0.11	-0.01	0.07	0.04	0.11	-0.00	-0.03	0.13
-0.0	0.22	0.05	0.23	0.04	0.23	0.04	0.05	0.22
0.1	0.21	0.02	0.22	0.02	0.17	0.06	0.08	0.16
0.2	0.06	0.00	0.07	0.00	0.04	0.03	0.04	0.03
0.3	-0.10	-0.00	-0.10	-0.00	-0.03	-0.08	-0.07	-0.03
0.4	-0.18	-0.05	-0.18	-0.05	-0.02	-0.21	-0.21	-0.02
0.5	-0.15	-0.15	-0.15	-0.15	-0.00	-0.30	-0.30	-0.00
0.6	-0.07	-0.24	-0.07	-0.24	-0.03	-0.28	-0.28	-0.03
0.7	-0.01	-0.26	-0.01	-0.26	-0.08	-0.19	-0.19	-0.08
0.8	-0.00	-0.21	-0.00	-0.21	-0.11	-0.10	-0.10	-0.11
0.9	-0.01	-0.14	-0.01	-0.14	-0.11	-0.04	-0.04	-0.11
1.0	-0.02	-0.09	-0.02	-0.09	-0.09	-0.02	-0.02	-0.09

The relevant percent deviations ΔB_1, ΔB_2, …,ΔB_8, from Table 3.4, never exceed 1% meaning that the choice of setting the angle Φ=60°constant for both cables was reasonable.

3.1.1.2 System Symmetry

Considering the twisted double-circuit power line of the *first case-study*, the magnetic field generated by the 8 symmetric phase configurations along with $B_{DOUBLE,max}$ was also calculated on a straight horizontal line that spreads from -1.0 m to 1.0 m at both ends of the line axis and whose vertical distance from the conductors is H=-0.5 mthis time (see Fig. 3.3). This analysis has the purpose of examining the system symmetry in terms of magnetic induction generated and the results are depicted at Table 3.5.

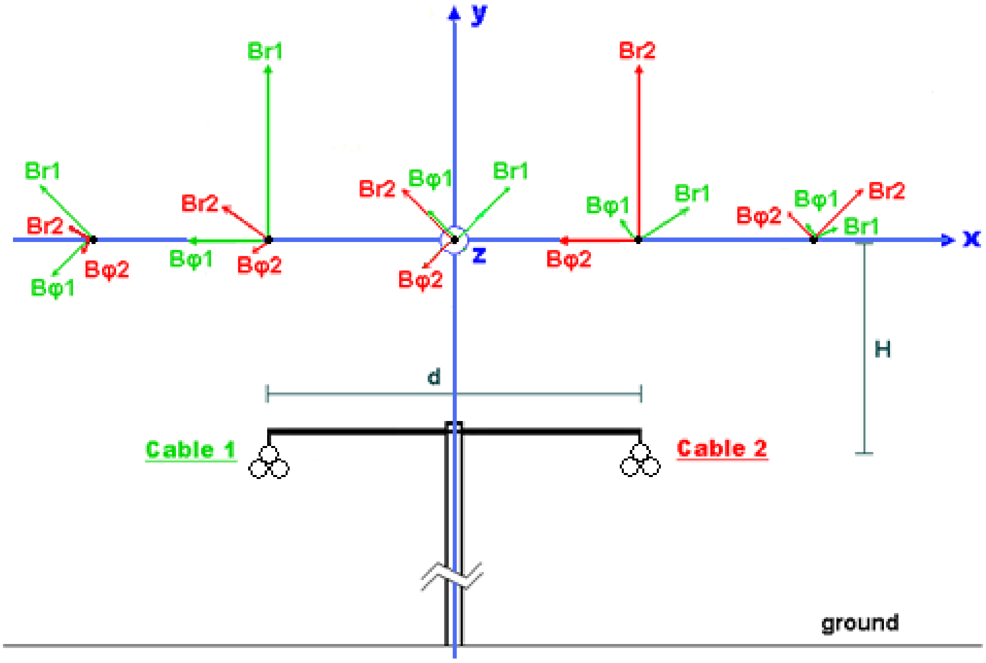

Figure 3.3: *Sketch of the "reference arrangement" of the double-circuit twisted three-phase cable line chosen as first case-study for the vector sum of the Cartesian magnetic field components calculated H=0.5 m above the cables. The relevant radial (B_r) and azimuthal (B_φ) field components generated by circuit 1 (green arrows) and 2 (red arrows) at five equally spaced field-points along the x-axis are shown.*

Table 3.5: *B_{DOUBLE} values of the first 8 symmetric base arrangements for the configuration of Fig. 3.3 for $I_1=I_2=280$ A.*

x [m]	$B_{DOUBLE,1}$ [μT]	$B_{DOUBLE,2}$ [μT]	$B_{DOUBLE,3}$ [μT]	$B_{DOUBLE,4}$ [μT]	$B_{DOUBLE,5}$ [μT]	$B_{DOUBLE,6}$ [μT]	$B_{DOUBLE,7}$ [μT]	$B_{DOUBLE,8}$ [μT]	$B_{DOUBLE,max}$ [μT]
-1.0	1.6998	1.7010	1.7010	1.6998	1.7010	1.6998	1.7010	1.6998	1.7013
-0.9	2.4853	2.4888	2.4888	2.4853	2.4879	2.4862	2.4879	2.4862	2.4889
-0.8	3.4732	3.4806	3.4806	3.4732	3.4771	3.4767	3.4771	3.4767	3.4806
-0.7	4.5453	4.5564	4.5564	4.5453	4.5483	4.5534	4.5483	4.5534	4.5570
-0.6	5.4380	5.4474	5.4474	5.4380	5.4358	5.4497	5.4357	5.4497	5.4511
-0.5	5.8254	5.8254	5.8254	5.8254	5.8166	5.8341	5.8166	5.8342	5.8342
-0.4	5.5482	5.5409	5.5409	5.5482	5.5392	5.5499	5.5391	5.5499	5.5510
-0.3	4.7685	4.7639	4.7639	4.7685	4.7652	4.7673	4.7652	4.7673	4.7687
-0.2	3.8437	3.8460	3.8461	3.8437	3.8447	3.8451	3.8449	3.8449	3.8436
-0.1	3.1109	3.1168	3.1170	3.1106	3.1121	3.1155	3.1126	3.1151	3.1102
-0.0	2.8149	2.8197	2.8200	2.8147	2.8147	2.8200	2.8149	2.8197	2.8136
0.1	3.0692	3.0730	3.0716	3.0706	3.0694	3.0729	3.0687	3.0735	3.0695
0.2	3.7803	3.7868	3.7810	3.7861	3.7826	3.7846	3.7823	3.7849	3.7853
0.3	4.7020	4.7131	4.7021	4.7130	4.7046	4.7106	4.7096	4.7056	4.7131
0.4	5.4938	5.5038	5.4937	5.5038	5.4911	5.5065	5.5061	5.4915	5.5076
0.5	5.7946	5.7946	5.7946	5.7946	5.7842	5.8050	5.8049	5.7843	5.8049
0.6	5.4296	5.4192	5.4295	5.4193	5.4167	5.4321	5.4320	5.4168	5.4336
0.7	4.5469	4.5350	4.5469	4.5350	4.5382	4.5437	4.5436	4.5382	4.5474
0.8	3.4757	3.4681	3.4757	3.4681	3.4721	3.4717	3.4717	3.4721	3.4757
0.9	2.4864	2.4829	2.4864	2.4829	2.4855	2.4838	2.4838	2.4855	2.4866
1.0	1.6999	1.6986	1.6999	1.6986	1.6999	1.6986	1.6986	1.6999	1.7001

Finally, the $B_{DOUBLE,max}$ isolines of 3μT, 10 μT and 100 μT were plotted in Fig. 3.4 for the twisted double-circuit power lines under exam.

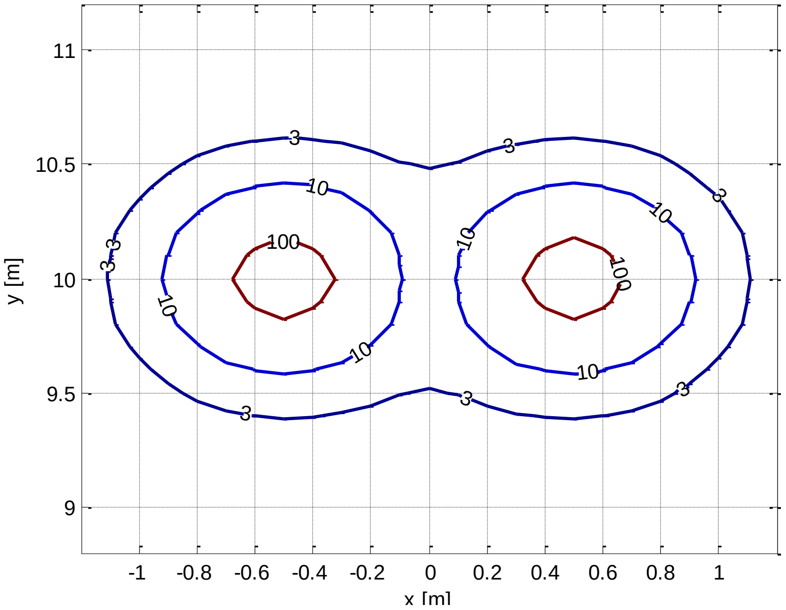

Figure 3.4: *3μT, 10 μT and 100μT $B_{DOUBLE,max}$ ($\Phi_1=\Phi_2=60^o$) isolines for the 'reference arrangement' of the twisted double-circuit for $I_1=I_2=280$ A.*

3.1.2 “Worst Case” Approach

The simplest approach – but also the most approximated one – is the so-called “worst case” estimate. In this approach the magnetic field generated by the double-circuit is calculated as the algebraic sum of the two rms values of the total field B generated by each twisted cable. By calculating the rms values of the total field B from circuit 1 and 2 according to the exact formula (2.12), $B_{1,exact}$ and $B_{2,exact}$, respectively, one obtains the “worst case” estimate of B generated by the double circuit, $B_{WC,exact}$, i.e.:

$$B_{WC,exact} = B_{1,exact} + B_{2,exact} \tag{3.5}$$

This expression of B is drastically approximated, since it is based on the hypothesis that the two magnetic field vectors have the same direction, but it is also the most conservative one, hence it serves as an upper limit reference for exposure evaluation purposes.

Relationship (3.5) can be further simplified by using, firstly, the approximated formula from the literature (2.17) and, secondly, the simplified innovative formula (2.23), in the 1st and 2nd level of approximation, to express the rms values of field B from circuit 1 and 2, and then by composing them according to the “worst-case” approach, thereby attaining respectively:

$$B_{WC,lit} = B_{1,lit} + B_{2,lit} \tag{3.6}$$

and

$$B_{WC,simp1} = B_{1,simp1} + B_{2,simp1} \tag{3.7.a}$$

$$B_{WC,simp2} = B_{1,simp2} + B_{2,simp2} \tag{3.7.b}$$

3.2 APPLICATIONS – SIMULATION RESULTS

The final results of the ***first case-study*** (see Fig. 3.1) are illustrated in Fig. 3.5, which displays the plots of B_{DOUBLE}, $B_{WC,exact}$, $B_{WC,lit}$, $B_{WC,simp1}$, $B_{WC,simp2}$ vs. horizontal distance x from the pole at distance H=0.5 m from both the conductors for Φ_1=60°, Φ_2=60°, and in Table 3.6, which reports the relevant numerical values and percent errors of $B_{WC,exact}$, $B_{WC,lit}$, $B_{WC,simp1}$, $B_{WC,simp2}$ with respect to B_{DOUBLE}.

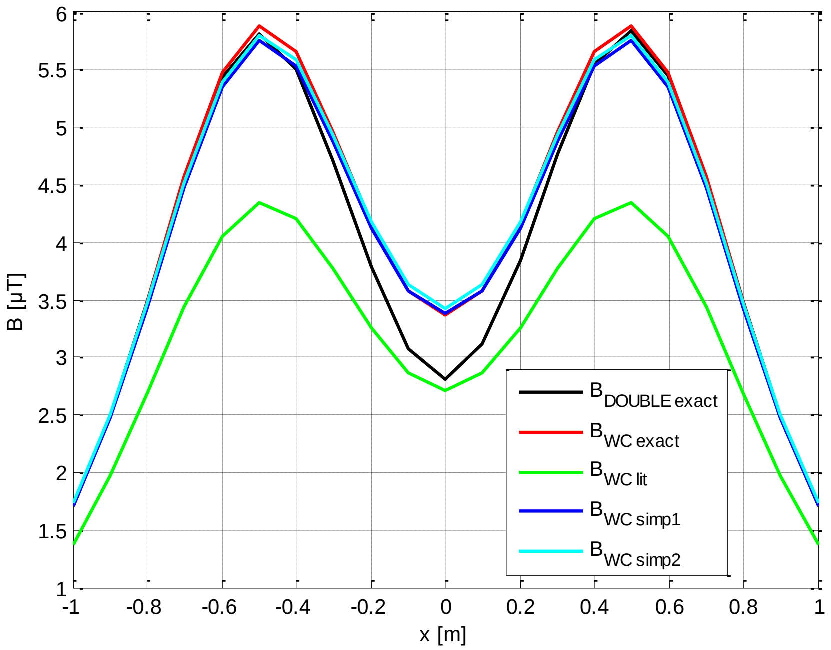

Figure 3.5: *B_{DOUBLE}, $B_{WC,exact}$, $B_{WC,lit}$, $B_{WC,simp1}$, $B_{WC,simp2}$ vs. horizontal distance x for the first case-study (I_1=I_2=280 A).*

Table 3.6: *B_{DOUBLE}, $B_{WC,exact}$, $B_{WC,lit}$, $B_{WC,simp1}$, $B_{WC,simp2}$ vs. distance x and percent errors of $B_{WC,exact}$, $B_{WC,lit}$, $B_{WC,simp1}$ and $B_{WC,simp2}$ with respect to B_{DOUBLE} for the first case study (I_1=I_2=280 A).*

x [m]	**B_{DOUBLE} [μT]**	**$B_{WC,exact}$ [μT]**	**error [%]**	**$B_{WC,lit}$ [μT]**	**error [%]**	**$B_{WC,simp1}$ [μT]**	**error [%]**	**$B_{WC,simp2}$ [μT]**	**error [%]**
-1.0	1.7001	1.7019	0.10	1.3746	-19.15	1.7085	2.04	1.7349	-0.03
-0.9	2.4866	2.4904	0.16	1.9649	-20.98	2.4720	0.75	2.5052	-1.29
-0.8	3.4757	3.4842	0.25	2.6829	-22.81	3.4281	-0.22	3.4680	-2.28
-0.7	4.5474	4.5659	0.41	3.4378	-24.40	4.4694	-0.73	4.5144	-2.83
-0.6	5.4336	5.4724	0.71	4.0553	-25.37	5.3479	-0.69	5.3961	-2.85
-0.5	5.8049	5.8821	1.33	4.3394	-25.25	5.7505	-0.07	5.8009	-2.27
-0.4	5.5076	5.6510	2.60	4.2075	-23.61	5.5338	1.42	5.5859	-0.81
-0.3	4.7131	4.9582	5.20	3.7696	-20.02	4.8755	4.57	4.9285	2.29
-0.2	3.7853	4.1646	10.02	3.2512	-14.11	4.1261	10.40	4.1788	8.01
-0.1	3.0695	3.5788	16.59	2.8594	-6.85	3.5765	18.20	3.6282	15.64
-0.0	2.8136	3.3676	19.69	2.7161	-3.46	3.3789	21.91	3.4301	19.24
0.1	3.1102	3.5788	15.07	2.8594	-8.06	3.5765	16.66	3.6282	14.05
0.2	3.8436	4.1646	8.35	3.2512	-14.41	4.1261	8.72	4.1788	6.29
0.3	4.7687	4.9582	3.97	3.7696	-20.95	4.8755	3.35	4.9285	1.04
0.4	5.5510	5.6510	1.80	4.2075	-24.20	5.5338	0.63	5.5859	-1.62
0.5	5.8342	5.8821	0.82	4.3394	-25.62	5.7505	-0.57	5.8009	-2.78
0.6	5.4511	5.4724	0.39	4.0553	-25.60	5.3479	-1.01	5.3961	-3.17
0.7	4.5570	4.5659	0.20	3.4378	-24.56	4.4694	-0.93	4.5144	-3.04
0.8	3.4806	3.4842	0.11	2.6829	-22.92	3.4281	-0.36	3.4680	-2.42
0.9	2.4889	2.4904	0.06	1.9649	-21.05	2.4720	0.65	2.5052	-1.38
1.0	1.7013	1.7019	0.04	1.3746	-19.20	1.7085	1.97	1.7349	-0.09

It can be noted that the values of the expression $B_{WC,exact}$, result larger than the exact rms value of the total magnetic field, B_{DOUBLE}, in the mid-span area and the relevant percent errors arrive at ~20%. The explanation for this is that the “worst case estimate” results in an addiction of the rms values of the magnetic field of the single-circuits in this area, whereas the exact vector analysis results in a subtraction of the magnetic field vectors of the single-circuits in the same area. Therefore, it is logical to obtain greater values with the “worst case” calculus.Additionally, it can be argued that the profiles brought by the expression $B_{WC,simp1}$ and $B_{WC,simp2}$ are practically overlapped to the ones brought by the expression $B_{WC,exact}$. This is not true for the profiles associated with the expression $B_{WC,lit}$, that in addition yield much lower – thus less conservative - magnetic field estimates. Consequently the expression $B_{WC,simp}$, in both levels of approximation, is more reliable compared to the expression $B_{WC,lit}$.

The analysis has been completed by reporting three more case-studies of interest:

Second case study: Same as the first case with the only difference that the vertical distance between the field points and the conductors is increased by 0.5 m, therefore resulting *H*=1.0 m (see Fig. 3.6). The results of the second case simulations are shown in Fig. 3.7 and Table 3.7.

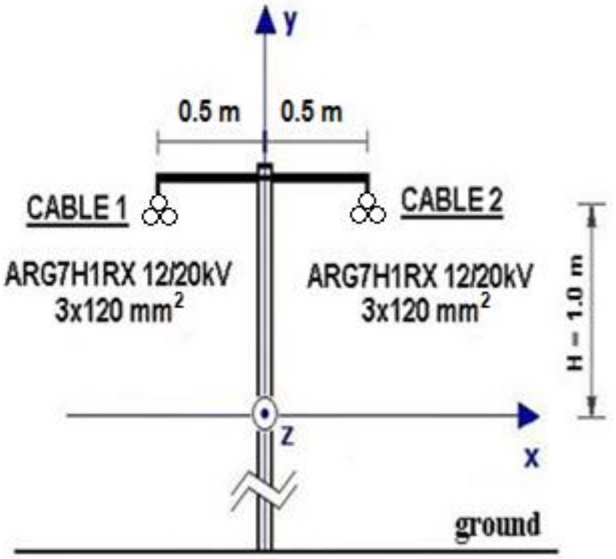

Figure 3.6: *Geometrical and electrical data concerning the second case-study.*

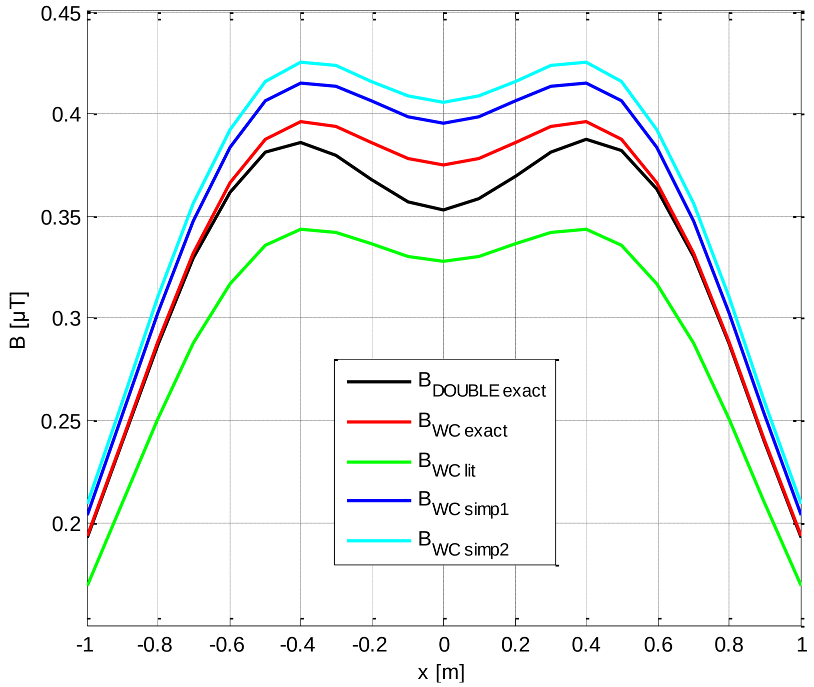

Figure 3.7: *B_{DOUBLE}, $B_{WC,exact}$, $B_{WC,lit}$, $B_{WC,simp1}$, $B_{WC,simp2}$ vs. horizontal distance x for the second case-study (I_1=I_2=280 A).*

Table 3.7: *B_{DOUBLE}, $B_{WC,exact}$, $B_{WC,lit}$, $B_{WC,simp1}$, $B_{WC,simp2}$ vs. distance x and percent errors of $B_{WC,exact}$, $B_{WC,lit}$, $B_{WC,simp1}$ and $B_{WC,simp2}$ with respect to B_{DOUBLE} for the second case study (I_1=I_2=280 A).*

x [m]	**B_{DOUBLE} [μT]**	**$B_{WC,exact}$ [μT]**	**error [%]**	**$B_{WC,lit}$ [μT]**	**error [%]**	**$B_{WC,simp1}$ [μT]**	**error [%]**	**$B_{WC,simp2}$ [μT]**	**error [%]**
-1.0	0.1930	0.1935	0.27	0.1696	-12.10	0.2041	5.75	0.2094	8.50
-0.9	0.2399	0.2408	0.39	0.2101	-12.42	0.2533	5.61	0.2597	8.26
-0.8	0.2869	0.2885	0.56	0.2507	-12.62	0.3029	5.56	0.3103	8.13
-0.7	0.3293	0.3320	0.82	0.2876	-12.65	0.3479	5.65	0.3562	8.18
-0.6	0.3618	0.3662	1.22	0.3168	-12.43	0.3834	5.98	0.3925	8.49
-0.5	0.3809	0.3878	1.81	0.3355	-11.91	0.4061	6.61	0.4157	9.14
-0.4	0.3859	0.3961	2.64	0.3433	-11.04	0.4152	7.60	0.4252	10.19
-0.3	0.3796	0.3937	3.72	0.3422	-9.85	0.4135	8.94	0.4236	11.60
-0.2	0.3677	0.3858	4.91	0.3364	-8.52	0.4061	10.42	0.4162	13.18
-0.1	0.3571	0.3780	5.85	0.3305	-7.45	0.3986	11.61	0.4087	14.44
-0.0	0.3533	0.3749	6.12	0.3281	-7.12	0.3955	11.97	0.4056	14.83
0.1	0.3581	0.3780	5.55	0.3305	-7.71	0.3986	11.30	0.4087	14.12
0.2	0.3694	0.3858	4.42	0.3364	-8.94	0.4061	9.92	0.4162	12.66
0.3	0.3815	0.3937	3.19	0.3422	-10.30	0.4135	8.39	0.4236	11.04
0.4	0.3877	0.3961	2.16	0.3433	-11.45	0.4152	7.10	0.4252	9.67
0.5	0.3824	0.3878	1.41	0.3355	-12.25	0.4061	6.19	0.4157	8.72
0.6	0.3629	0.3662	0.91	0.3168	-12.70	0.3834	5.65	0.3925	8.16
0.7	0.3300	0.3320	0.59	0.2876	-12.85	0.3479	5.41	0.3562	7.93
0.8	0.2874	0.2885	0.38	0.2507	-12.78	0.3029	5.37	0.3103	7.94
0.9	0.2402	0.2408	0.26	0.2101	-12.54	0.2533	5.47	0.2597	8.12
1.0	0.1932	0.1935	0.17	0.1696	-12.18	0.2041	5.64	0.2094	8.39

Third Case-Study: Same as the second case, excepted that cable 2 has a larger cross-section than cable 1, namely 3x185 mm^2, thus larger ampacity I=360 A, pitch p=1.5 m and radius α=0.022 m (see Fig. 3.8). The results of the third case simulations are shown in Fig. 3.9 and Table 3.8.

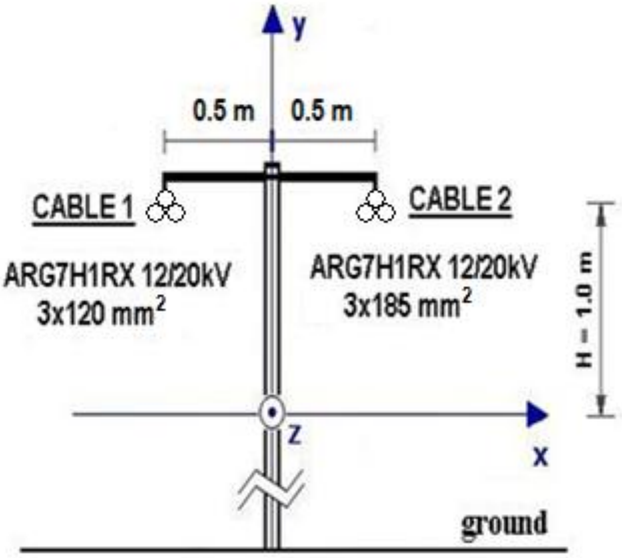

Figure 3.8: *Geometrical and electrical data concerning the third case-study.*

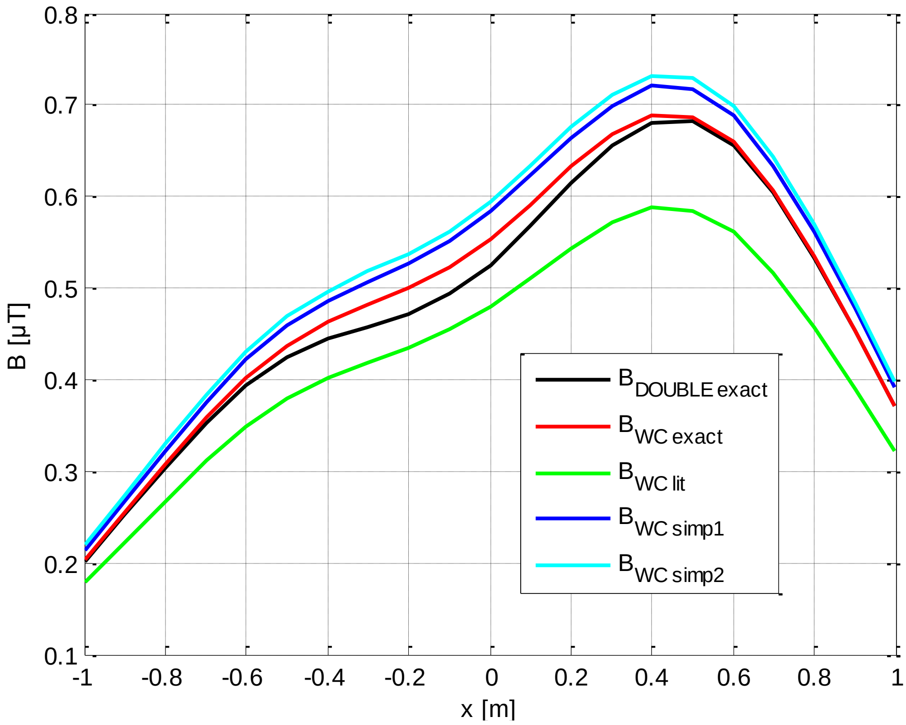

Figure 3.9: *B_{DOUBLE}, $B_{WC,exact}$, $B_{WC,lit}$, $B_{WC,simp1}$, $B_{WC,simp2}$ vs. horizontal distance x for the third case-study (I_1=280A and I_2=360 A).*

Table 3.8: *B_{DOUBLE}, $B_{WC,exact}$, $B_{WC,lit}$, $B_{WC,simp1}$, $B_{WC,simp2}$ vs. distance x and percent errors of $B_{WC,exact}$, $B_{WC,lit}$, $B_{WC,simp1}$ and $B_{WC,simp2}$ with respect to B_{DOUBLE} for the third case study (I_1=280A and I_2=360 A).*

x [m]	**B_{DOUBLE} [μT]**	**$B_{WC,exact}$ [μT]**	**error [%]**	**$B_{WC,lit}$ [μT]**	**error [%]**	**$B_{WC,simp1}$ [μT]**	**error [%]**	**$B_{WC,simp2}$ [μT]**	**error [%]**
-1.0	0.2016	0.2029	0.62	0.1782	-11.64	0.2138	6.03	0.2193	8.73
-0.9	0.2520	0.2541	0.84	0.2221	-11.85	0.2672	6.05	0.2738	8.65
-0.8	0.3038	0.3073	1.16	0.2676	-11.91	0.3226	6.19	0.3303	8.71
-0.7	0.3525	0.3582	1.62	0.3111	-11.75	0.3756	6.54	0.3842	9.00
-0.6	0.3936	0.4025	2.25	0.3491	-11.31	0.4218	7.17	0.4313	9.58
-0.5	0.4241	0.4372	3.10	0.3793	-10.58	0.4585	8.11	0.4687	10.51
-0.4	0.4443	0.4626	4.12	0.4017	-9.59	0.4858	9.34	0.4964	11.73
-0.3	0.4581	0.4817	5.16	0.4189	-8.56	0.5068	10.64	0.5177	13.02
-0.2	0.4720	0.4998	5.89	0.4350	-7.84	0.5267	11.60	0.5378	13.94
-0.1	0.4931	0.5225	5.96	0.4545	-7.83	0.5511	11.77	0.5623	14.04
-0.0	0.5252	0.5531	5.30	0.4799	-8.63	0.5831	11.03	0.5944	13.18
0.1	0.5675	0.5912	4.18	0.5109	-9.98	0.6223	9.65	0.6338	11.68
0.2	0.6139	0.6322	2.99	0.5436	-11.44	0.6639	8.15	0.6755	10.04
0.3	0.6548	0.6679	2.00	0.5717	-12.69	0.6997	6.85	0.7114	8.64
0.4	0.6800	0.6888	1.28	0.5876	-13.60	0.7202	5.90	0.7318	7.62
0.5	0.6815	0.6870	0.81	0.5850	-14.16	0.7177	5.31	0.7290	6.97
0.6	0.6556	0.6589	0.50	0.5611	-14.41	0.6884	5.00	0.6992	6.65
0.7	0.6042	0.6061	0.32	0.5171	-14.42	0.6340	4.93	0.6439	6.58
0.8	0.5339	0.5350	0.20	0.2507	-14.22	0.5607	5.02	0.5696	6.69
0.9	0.4534	0.4540	0.13	0.2101	-13.89	0.4770	5.21	0.4848	6.92
1.0	0.3714	0.3717	0.09	0.1696	-13.45	0.3916	5.46	0.3982	7.22

FourthCase-Study: Same overall arrangement as in the third case with the only difference that cable 2 is 0.5 m farther away from the soil with respect to cable 1. Hence the field points lie on a straight horizontal line whose vertical distance from cable 1 is H_1=1.0 m and from cable 2 is H_2=1.5 m (see Fig 3.10). Figure 3.11 and Table 3.9 show the results of the fourth case simulation developed in MATLAB^{TM} environment.

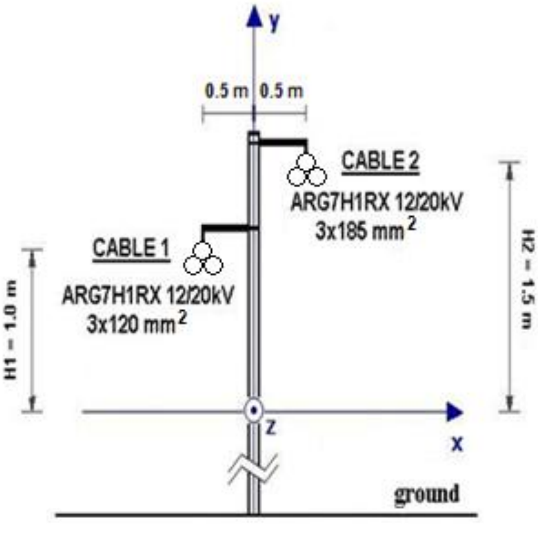

Figure 3.10: *Geometrical and electrical data concerning the fourth case-study.*

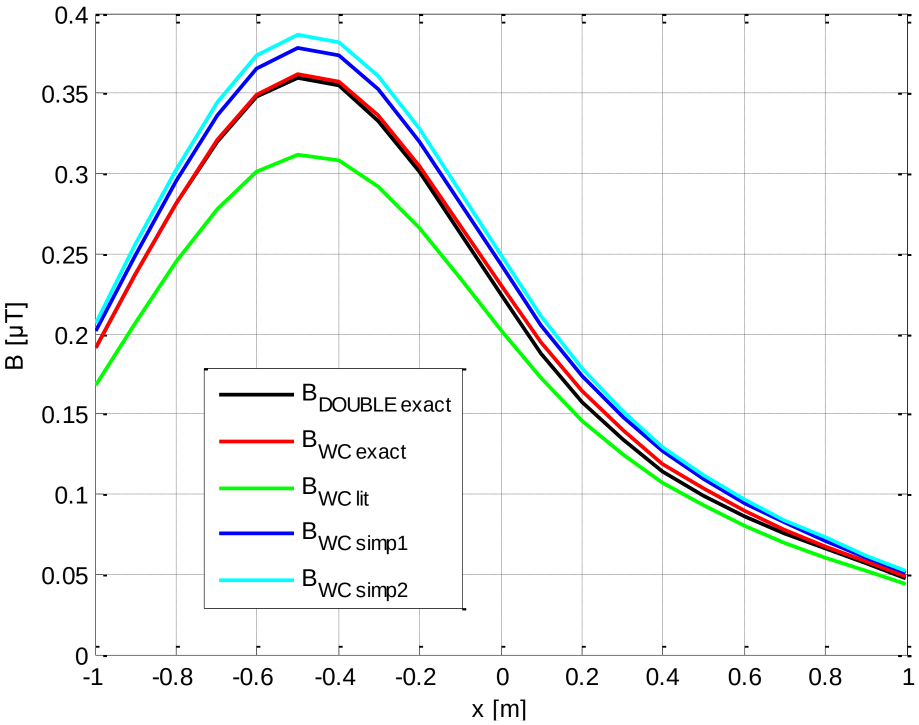

Figure 3.11: *B_{DOUBLE}, $B_{WC,exact}$, $B_{WC,lit}$, $B_{WC,simp1}$, $B_{WC,simp2}$ vs. horizontal distance x for the fourth case-study (I_1=280A and I_2=360 A).*

Table 3.9: *B_{DOUBLE}, $B_{WC,exact}$, $B_{WC,lit}$, $B_{WC,simp1}$, $B_{WC,simp2}$ vs. distance x and percent errors of $B_{WC,exact}$, $B_{WC,lit}$, $B_{WC,simp1}$ and $B_{WC,simp2}$ with respect to B_{DOUBLE} for the fourth case study (I_1=280A and I_2=360 A).*

x [m]	B_{DOUBLE} [μT]	$B_{WC,exact}$ [μT]	error [%]	$B_{WC,lit}$ [μT]	error [%]	$B_{WC,simp1}$ [μT]	error [%]	$B_{WC,simp2}$ [μT]	error [%]
-1.0	0.1910	0.1911	0.08	0.1675	-12.31	0.2015	5.49	0.2066	8.19
-0.9	0.2365	0.2367	0.11	0.2064	-12.73	0.2489	5.25	0.2550	7.84
-0.8	0.2814	0.2818	0.16	0.2446	-13.06	0.2956	5.05	0.3026	7.55
-0.7	0.3204	0.3211	0.22	0.2779	-13.28	0.3362	4.91	0.3440	7.36
-0.6	0.3480	0.3491	0.33	0.3015	-13.36	0.3650	4.89	0.3734	7.30
-0.5	0.3599	0.3616	0.48	0.3122	-13.26	0.3779	5.01	0.3865	7.41
-0.4	0.3544	0.3569	0.70	0.3085	-12.95	0.3732	5.31	0.3818	7.72
-0.3	0.3333	0.3367	1.01	0.2919	-12.43	0.3526	5.80	0.3608	8.25
-0.2	0.3008	0.3052	1.46	0.2657	-11.67	0.3203	6.49	0.3279	9.02
-0.1	0.2625	0.2678	2.04	0.2344	-10.69	0.2818	7.38	0.2887	9.99
-0.0	0.2236	0.2297	2.75	0.2022	-9.56	0.2424	8.40	0.2484	11.11
0.1	0.1880	0.1946	3.50	0.1722	-8.37	0.2057	9.44	0.2110	12.23
0.2	0.1578	0.1643	4.14	0.1462	-7.33	0.1740	10.29	0.1785	13.15
0.3	0.1334	0.1394	4.50	0.1246	-6.61	0.1477	10.75	0.1516	13.64
0.4	0.1142	0.1193	4.46	0.1069	-6.35	0.1264	10.71	0.1297	13.60
0.5	0.0990	0.1030	4.05	0.0925	-6.50	0.1091	10.23	0.1119	13.08
0.6	0.0864	0.0894	3.43	0.0805	-6.91	0.0946	9.47	0.0970	12.27
0.7	0.0756	0.0776	2.74	0.0700	-7.42	0.0821	8.62	0.0841	11.36
0.8	0.0657	0.0670	2.11	0.0605	-7.88	0.0708	7.81	0.0726	10.50
0.9	0.0564	0.0573	1.59	0.0518	-8.23	0.0604	7.09	0.0619	9.75
1.0	0.0478	0.0484	1.18	0.0438	-8.46	0.0509	6.47	0.0522	9.12

A general comment deriving from second, third and fourth case is that the values of the expression $B_{WC,exact}$ result almost equal to the exact rms value of the total magnetic field, B_{DOUBLE}, with a maximum relevant percent error of ~6%. Additionally, the errors brought by simplified formula (2.23), in both levels of approximation, exhibit the same behavior in all cases, being relatively small– $B_{WC,simp1}$ not exceeding 12% and $B_{WC,simp2}$ not exceeding 15%– and positive, providing, thus a fast, simple and conservative evaluation of the magnetic field generated by double-circuit three-phase cable lines. To conclude, the error of the expression $B_{WC,lit}$ (2.17) results larger and always negative, underestimating the total field.

3.3 IN SITU MEASUREMENTS

The proposed theoretical approach was experimentally validated by measurements in situ. That required finding easily accessible double-circuit twisted cable lines with known instant values of rms line currents, fact that was proved to be extremely difficult in practice. The two main reasons for this were, firstly, that the electrical utilities were not prone to make their lines accessible and to provide data about the currents and, secondly, that easily-accessible double circuit twisted lines with fully known geometric parameters are very scarce to be found.The only solution found was performing the measurements inside an inspection well of the underground double-circuit twisted three-phase MV line that connects the wind turbines of the Casoni di Romagna Wind Park – Monterenzio (BO), the largest wind park in Northern Italy – with the nearest substation. Fig. 3.12 is an actual photo of the measurement site and Fig. 3.13 is its schematization reporting all the needed geometric information.

Figure 3.12: *Photo of the twisted double-circuit power line inside the inspection well, along with the magnetic field measuring probe (the black cable is a signal cable and does not affect the measurements).*

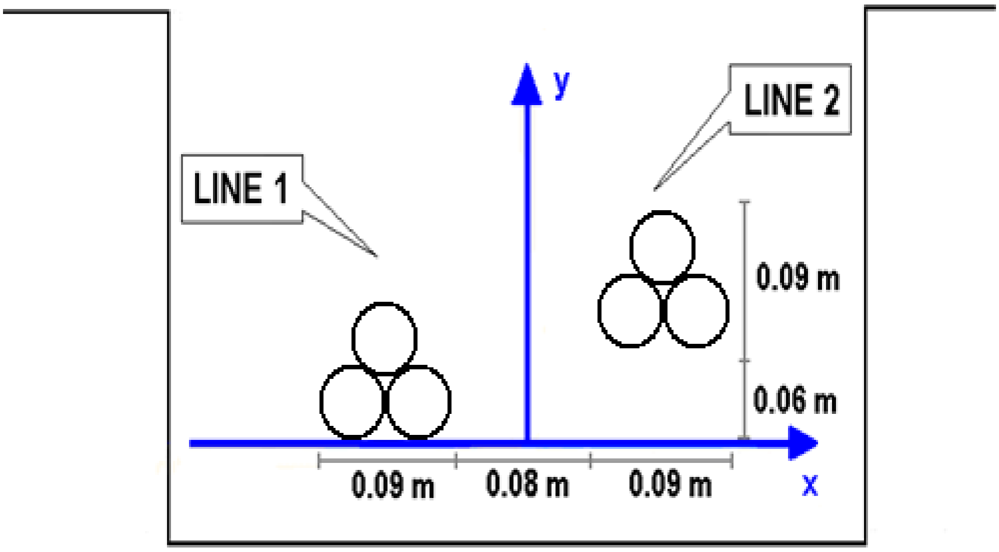

Figure 3.13: *Schematization of the twisted underground double-circuit power lines.*

As Fig.3.12 shows, the twisted double-circuit cables could be hardly accessed. This required the use of an insulating non-magnetic cane for inserting the probe inside the well, thereby limiting the precision concerning all the distances measured. Moreover, the constancy of the pitch of the single helix and the perfect parallelism of the two helixes were not exactly matched. In addition the instant rms values of the line currents provided by the distribution were relevant to one single phase current per circuit and, of course, there is no certainty that the three-phase currents of each circuit are symmetric all the time. Despite all these inconveniences, using the physical data available the magnetic fields were estimated by the software with acceptable errors.

The two underground circuits are placed at different heights above the well's ground; they are parallel to each other, but not to the ground, forming an angle of ~25^o. The two twisted cable circuits are ARE4H5EX [65] cables with cross-section 3x185 mm^2, rated voltage 12(phase-to-ground)/20(phase-to-phase) kV, ampacity I=360 A, pitch p=1.20 m (as actually measured) and radius α=0.022 m.

The rms value of the total magnetic induction field, $B_{DOUBLE,meas}$, has been measured and recorded at subsequent instants of time using a magnetic field measuring device, that consists essentially of a 3D field probe connected with a data-logger system using an optical fiber. The 3D field probe is a cube of side length 0.09 m.

3.3.1 Measurements on December 6th 2011

Two measurements campaigns were effectuated during this PhD course at the same location, one on December 6th 2011 and the other on December 18th 2012. This is due to the low power production on December 6th 2011 that resulted in very small current values (see Fig. 3.14) and therefore in small values of the magnetic field generated by the twisted double-circuit cable line under exam. That constrained the repetition of the measurements on a windier day.

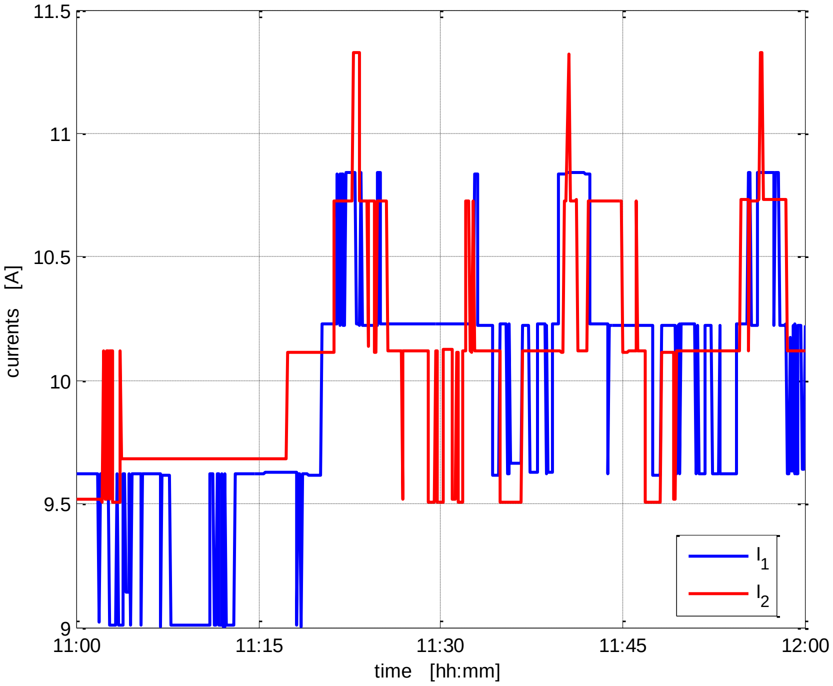

Figure 3.14: *Instant values of the currents I_1 and I_2 for the time interval of the measurements on 06/12/2011*

Nonetheless, all measurement data from December 6th 2011 are illustrated in Table 3.10, and the comparison between the experimental values of $B_{DOUBLE,meas}$ and the theoretical calculated values of B_{DOUBLE}, $B_{WC,exact}$, $B_{WC,lit}$, $B_{WC,simp1}$ and $B_{WC,simp2}$ are presented, highlighting the percent errors of B_{DOUBLE}, $B_{WC,exact}$, $B_{WC,lit}$, $B_{WC,simp1}$ and $B_{WC,simp2}$ with respect to $B_{DOUBLE,meas}$. Measurements took place 0.0 m, 0.2 m, 0.5 m and 1.0 m above each cable and 0.0 m, 0.2 m, 0.5 m, 1.0 m, 1.5 m (at ground level) and 2.5 m (1.0 m from ground level) above the midway point between the two cables.

Table 3.10: *Measurement results (06/12/2011): $B_{DOUBLE,meas}$, $B_{DOUBLE,calc}$, $B_{WC,exact}$, $B_{WC,lit}$, $B_{WC,simp1}$, $B_{WC,simp2}$ at different field-points and percent errors of $B_{DOUBLE,calc}$, $B_{WC,exact}$, $B_{WC,lit}$, $B_{WC,simp1}$ and $B_{WC,simp2}$ with respect to $B_{DOUBLE,meas}$.*

$B_{DOUBLE,meas}$ [μT]	**$B_{DOUBLE,calc}$ [μT]**	**error [%]**	**$B_{WC,exact}$ [μT]**	**error [%]**	**$B_{WC,lit}$ [μT]**	**error [%]**	**$B_{WC,simp1}$ [μT]**	**error [%]**	**$B_{WC,simp2}$ [μT]**	**error [%]**
0.0 m from cable 1										
9.550	11.072	-15.9	12.938	35.5	4.059	-57.5				
9.458	11.067	-17.0	12.932	36.7	4.058	-57.1				
9.404	11.636	-23.7	13.529	43.9	4.220	-55.1				
6.308	11.762	-86.5	13.741	118	4.310	-31.7				

0.0 m from cable 2										
5.413	10.605	-95.9	11.079	-105	3.486	35.6				
0.0 m midway between the two cables										
15.960	13.217	17.2	23.497	-47.2	5.664	64.5				
0.2 m from cable 1										
2.266	2.342	-3.36	2.436	-7.51	1.423	37.2	2.997	-32.3	2.936	-29.6
0.2 m from cable 2										
1.449	1.649	-13.8	1.684	-16.2	1.038	28.4	1.951	34.7	1.919	-32.4
0.2m from the midway point between the two cables										
2.916	3.516	-20.6	3.709	-27.2	1.925	34.0	6.016	-106	5.804	-99.0
0.5m from cable 1										
0.378	0.357	5.50	0.360	4.73	0.277	26.7	0.355	6.09	0.355	6.18
0.5 m from cable 2										
0.381	0.245	35.7	0.246	35.3	0.194	49.2	0.244	36.0	0.244	36.0
0.367	0.245	33.2	0.246	32.9	0.194	47.2	0.244	33.6	0.244	33.5
0.5 m from the midway point between the two cables										
0.435	0.427	1.83	0.431	0.938	0.325	25.4	0.425	2.31	0.424	2.52
1.0 m from cable 1										
0.108	0.0211	80.4	0.021	80.4	0.019	82.9	0.022	79.5	0.022	79.4
1.0 m from cable 2										
0.102	0.0156	84.7	0.016	84.7	0014	86.6	0.016	83.9	0.017	83.8
1.0 m from the midway point between the two cables										
0.108	0.034	68.3	0.034	68.2	0.030	72.7	0.036	67.2	0.036	67.0
0.113	0.038	66.0	0.039	65.9	0.033	70.7	0.040	64.8	0.04	64.6
0.078	0.021	72.8	0.021	72.8	0.019	76.3	0.022	71.5	0.022	71.4
At ground level - 1.5 m from the midway point between the two cables										
0.055	0.003	95.2	0.003	95.2	0.002	95.7	0.003	94.9	0.003	94.9
1.0m from ground level - 2.5 m from the midway point between the two cables										
0.037	0.00	99.95	0.00	99.95	0.00	99.96	0.00	99.95	0.00	99.95

The percent errors of $B_{DOUBLE,calc}$ with respect to $B_{DOUBLE,meas}$ resulted satisfactory concerning the measurements made up to 0.5 m above each cable and above the midway point between the two cables. For distances greater than 1.0 m, the values of $B_{DOUBLE,calc}$ and $B_{DOUBLE,meas}$ begin to diverge significantly.

The expression $B_{WC,exact}$ approximates fairly well the measured values of B, in the range of measurements <1.0 m, as well as its simplifications, $B_{WC,simp1}$ and $B_{WC,simp2}$. In the parametrical analysis that has resulted the innovative simplified expression (Chapter 2), the approximation of ln$B$ vs. r with the equation of a straight line plus a hyperbolic term was effectuated for distances 0.3 m < r < 2.0 m. That is the reason why for the measurements at 0.0 m from each cable and the midway point between the two cables the expressions $B_{WC,simp1}$ and $B_{WC,simp2}$ are omitted from Table 3.10 since they are away from their field of accuracy. The expression $B_{WC,lit}$ has resulted a higher error with respect to $B_{WC,simp1}$ and $B_{WC,simp2}$ in the range of distances >0.2 m.

It must be pointed out, that measurements made at ground level and 1.0 m from it, were affected by the presence of a MV overhead single-circuit power line passing nearby.

3.3.2 Measurements on December 18th 2012

Figure 3.15 illustrates the plots of the currents vs. time for the time interval of the measurements. Measurements took place 0.0 m, 0.3 m, 0.5 m, 0.8 m and 1.0 m above each cable and the midway point between the two cables, and at ground level, i.e. 1.5 m from cable 2. The measurement data are illustrated in Table 3.11, and the comparison between the experimental values of $B_{DOUBLE,meas}$ and the theoretical calculated values of $B_{DOUBLE,calc}$, $B_{WC,exact}$, $B_{WC,lit}$, $B_{WC,simp1}$ and $B_{WC,simp2}$ are presented, highlighting the percent errors of $B_{DOUBLE,calc}$, $B_{WC,exact}$, $B_{WC,lit}$, $B_{WC,simp1}$ and $B_{WC,simp2}$ with respect to $B_{DOUBLE,meas}$.

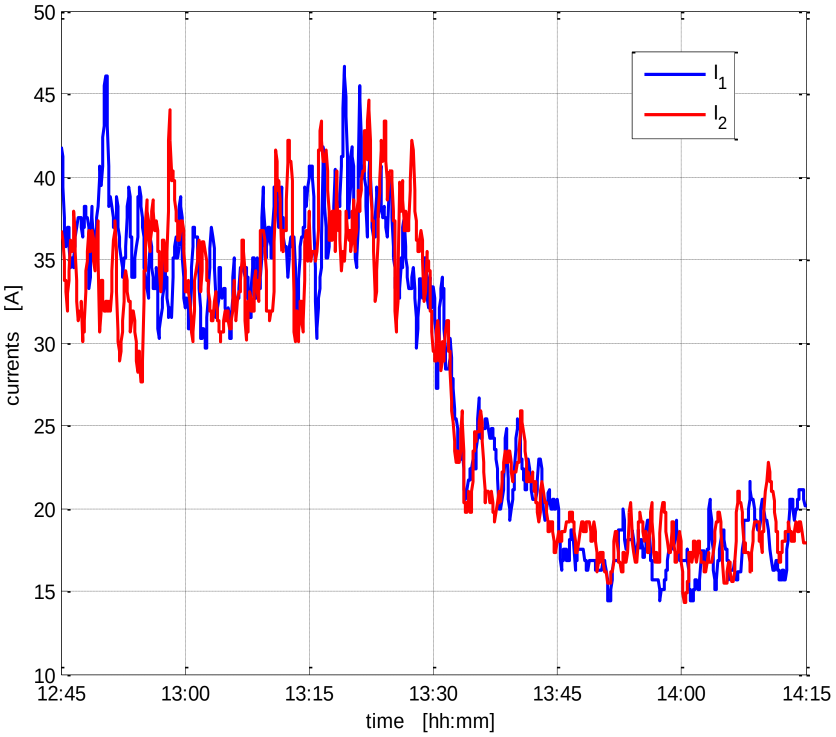

Figure 3.15: *Instant values of the currents I_1 and I_2 for the time interval of the measurements on 18/12/2012*

Table 3.11: *Measurement results (18/12/2012): $B_{DOUBLE,meas}$, $B_{DOUBLE,calc}$, $B_{WC,exact}$, $B_{WC,lit}$, $B_{WC,simp1}$, $B_{WC,simp2}$ at different field-points and percent errors of $B_{DOUBLE,calc}$, $B_{WC,exact}$, $B_{WC,lit}$, $B_{WC,simp1}$ and $B_{WC,simp2}$ with respect to $B_{DOUBLE,meas}$.*

$B_{DOUBLE,meas}$ [μT]	**$B_{DOUBLE,calc}$ [μT]**	**error [%]**	**$B_{WC,exact}$ [μT]**	**error [%]**	**$B_{WC,lit}$ [μT]**	**error [%]**	**$B_{WC,simp1}$ [μT]**	**error [%]**	**$B_{WC,simp2}$ [μT]**	**error [%]**
0.0 m from cable 1										
37.25	44.041	-18.2	46.851	-25.8	13.593	63.5				
40.64	46.933	-15.5	49.814	-22.6	14.362	64.7				
41.91	49.824	-18.9	52.775	-25.9	15.129	63.9				
41.71	49.143	-17.8	52.087	-24.9	14.959	64.1				
0.0 m from cable 2										
31.35	53.346	-0.162	55.8	-78.0	14.680	53.2				
31.65	53.077	-67.7	55.431	-75.4	14.490	54.2				
31.34	52.116	-66.3	54.432	-73.7	14.235	54.6				

0.0 m from the midway point between the two cables										
95.97	36.684	61.8	96.169	-0.207	21.963	77.1				
91.16	33.499	63.3	89.255	2.09	20.437	77.6				
87.25	32.182	63.1	85.945	1.50	19.687	77.4				
88.24	33.919	61.6	87.561	0.769	19.954	77.4				
91.05	36.124	60.3	95.840	-5.26	21.929	75.9				
92.13	35.315	61.7	88.922	3.48	20.202	78.1				
115.7	40.998	64.5	98.810	14.6	22.341	80.7				
119.7	43.724	63.5	99.821	16.6	22.45	81.2				
49.36	38.765	21.5	89.583	-81.5	20.171	59.1				
62.86	39.298	37.5	91.886	-46.2	20.713	67.0				
63.6	49.5	22.1	103.101	-62.1	22.993	63.8				
0.3 m from cable 1										
3.903	3.521	9.79	3.595	7.90	2.401	38.5	3.740	4.18	3.705	5.08
3.754	3.521	6.21	3.595	4.25	2.401	36.0	3.740	0.372	3.705	1.31
3.731	3.612	3.19	3.688	1.17	2.464	34.0	3.836	-2.82	3.800	-1.86
0.3 m from cable 2										
4.561	3.229	29.2	3.266	28.4	2.234	51.0	3.362	26.3	3.335	26.9
4.184	3.099	25.9	3.136	25.1	2.146	48.7	3.226	22.9	3.200	23.5
3.666	2.875	21.6	2.911	20.6	1.997	45.5	2.991	18.4	2.967	19.1
0.3 m from the midway point between the two cables										
9.467	9.255	2.24	9.613	-1.54	5.445	42.5	12.749	-34.7	12.434	-31.3
7.723	9.163	-18.7	9.519	-23.3	5.394	30.2	12.613	-63.3	12.302	-59.3
7.338	8.704	-18.6	9.042	-23.2	5.124	30.2	11.980	-63.3	11.685	-59.2
7.374	8.425	-14.3	8.761	18.8	4.981	32.5	11.544	-56.6	11.264	-52.7
6.944	8.479	-22.1	8.818	-27.0	5.016	27.8	11.609	-67.2	11.327	-63.1
7.678	8.479	-10.4	8.818	-14.9	5.016	34.7	11.609	-51.2	11.327	-47.5
0.5 m from cable 1										
1.165	1.115	4.29	1.125	3.48	0.861	26.1	1.108	4.89	1.107	5.00
1.163	1.096	5.77	1.105	4.98	0.846	27.3	1.089	6.37	1.087	6.48
1.141	1.084	4.98	1.093	4.18	0.837	26.6	1.077	5.58	1.076	5.69
1.288	1.173	8.95	1.183	8.17	0.906	29.7	1.166	9.51	1.164	9.62
1.252	1.194	4.62	1.204	3.80	0.923	26.3	1.187	5.21	1.185	5.32
1.282	1.204	6.10	1.214	5.30	0.930	27.4	1.196	6.68	1.195	6.79
1.341	1.169	12.2	1.179	12.1	0.903	32.6	1.162	13.4	1.160	13.5
1.371	1.190	13.2	1.200	12.5	0.920	32.9	1.183	13.7	1.181	13.8
0.5 m from cable 2										
1.302	0.957	26.5	0.962	26.1	0.758	41.8	0.953	26.8	0.953	26.8
1.257	0.931	25.9	0.936	25.5	0.737	41.4	0.927	26.3	0.927	26.3
1.224	0.897	26.8	0.901	26.4	0.709	42.1	0.892	27.1	0.892	27.1
1.226	0.878	28.4	0.883	28.0	0.695	43.4	0.874	28.7	0.874	28.7
1.257	0.854	32.0	0.859	31.7	0.677	46.2	0.851	32.3	0.851	32.3
0.5 m from the midway point between the two cables										
2.604	2.587	0.654	2.620	-0.618	1.891	27.4	2.609	-0.177	2.597	0.277
2.398	2.571	-7.22	2.604	-8.59	1.879	21.7	2.593	-8.12	2.581	-7.63
2.425	2.606	-7.48	2.640	-8.85	1.903	21.5	2.629	-8.41	2.617	-7.91
0.8 m from cable 1										
0.450	0.240	46.6	0.241	46.4	0.203	54.8	0.246	45.3	0.247	45.1
0.465	0.249	46.5	0.249	46.4	0.210	54.8	0.255	45.2	0.256	45.1
0.462	0.249	46.2	0.249	46.0	0.210	54.5	0.255	44.9	0.256	44.7
0.8 m from cable 2										
0.363	0.179	50.8	0.179	50.6	0.153	57.9	0.184	49.2	0.185	49.0
0.354	0.174	50.9	0.174	50.8	0.149	58.0	0.179	49.4	0.180	49.1
0.351	0.166	52.8	0.166	52.7	0.142	59.6	0.171	51.3	0.172	51.1
0.347	0.163	53.0	0.164	52.9	0.139	59.9	0.168	51.6	0.169	51.3
0.8 m from the midway point between the two cables										
0.534	0.389	27.1	0.391	26.8	0.322	39.7	0.394	26.3	0.395	26.1
0.527	0.384	27.1	0.386	26.8	0.318	39.6	0.389	26.2	0.390	26.0

0.550	0.376	31.6	0.378	31.4	0.312	43.4	0.381	30.8	0.382	30.6
0.539	0.381	29.4	0.382	29.1	0.316	41.5	0.385	28.5	0.386	28.3
0.521	0.368	29.3	0.370	29.1	0.305	41.5	0.373	28.5	0.374	28.3
1.0 m from cable 1										
0.228	0.075	67.3	0.075	67.2	0.065	71.4	0.078	65.8	0.079	65.6
0.240	0.062	74.0	0.063	73.9	0.055	77.3	0.065	72.8	0.066	72.6
0.225	0.061	73.1	0.061	73.0	0.053	76.5	0.063	71.8	0.064	71.7
0.211	0.056	73.7	0.056	73.6	0.049	77.0	0.058	72.5	0.059	72.3
1.0 m from cable 2										
0.165	0.038	77.2	0.038	77.1	0.033	79.9	0.040	76.0	0.040	75.9
0.163	0.035	78.4	0.035	78.3	0.031	81.0	0.037	77.3	0.037	77.1
0.138	0.031	77.3	0.031	77.2	0.028	80.0	0.033	76.1	0.033	76.0
0.137	0.031	77.5	0.031	77.5	0.027	80.2	0.032	76.4	0.033	76.2
0.139	0.032	77.2	0.032	77.1	0.028	79.9	0.033	76.0	0.034	75.9
1.0 m from the midway point between the two cables										
0.203	0.081	60.3	0.081	60.2	0.069	65.8	0.084	58.9	0.084	58.7
0.218	0.084	61.7	0.084	61.6	0.072	67.0	0.087	60.3	0.087	60.1
0.220	0.084	61.7	0.085	61.6	0.073	67.0	0.088	60.2	0.088	60.0
0.218	0.086	60.5	0.086	60.4	0.074	66.0	0.893	59.1	0.090	58.8
0.217	0.088	59.5	0.088	59.4	0.076	65.1	0.091	58.0	0.092	57.8
0.226	0.088	61.1	0.088	61.0	0.076	66.5	0.091	59.7	0.092	59.5
0.224	0.087	61.4	0.087	61.3	0.075	66.7	0.090	60.0	0.090	59.8
At ground level - 1.5 m from cable 2										
0.112	0.003	97.6	0.003	97.6	0.003	97.8	0.003	97.4	0.003	97.4
0.110	0.003	97.6	0.003	97.6	0.002	97.8	0.003	97.5	0.003	97.5
0.104	0.003	97.5	0.003	97.5	0.002	97.7	0.003	97.3	0.003	97.3
0.104	0.003	97.5	0.003	97.5	0.002	97.7	0.003	97.3	0.003	97.3
0.102	0.003	97.5	0.003	97.5	0.002	97.7	0.003	97.3	0.003	97.3

The percent errors of $B_{DOUBLE,calc}$ with respect to $B_{DOUBLE,meas}$ resulted satisfactory concerning the measurements made at 0.3 m and 0.5 m above each cable and above the midway point between the two cables. The expression $B_{WC,exact}$ approximates fairly well the measured values of B, in this range of measurements, as well as its simplifications, $B_{WC,simp1}$ and $B_{WC,simp2}$. Also here, for measurements at 0.0 m from each cable and from the midway point between the two cables, $B_{WC,simp1}$ and $B_{WC,simp2}$ are omitted from Table 3.11 since the innovative simplified formula, in both levels of approximation, is out of its application limits. The expression $B_{WC,lit}$ has resulted a higher error with respect to $B_{WC,simp1}$ and $B_{WC,simp2}$.

For distances 0.8 m and 1.0 m above each cable and above the midway point between the two cables and 1.5 m above cable 2, the relative percent errors of $B_{DOUBLE,calc}$ with respect to $B_{DOUBLE,meas}$ seem to increase. The exact, approximated and simplified ‘worst case’ expressions present the same behaviour as $B_{DOUBLE,calc}$.

Another supplementary set of measurements was also effectuated at 0.0 m, 0.3 m, 0.5 m, 0.8 m and 1.0 m, placing the cane that holds the probe at the other end of the well opening i.e. 0.57 m left from cable 2, as shown in Fig. 3.16. The results of the second set of measurements effectuated are illustrated in Table 3.12.

Figure 3.16: *Photo of the probe at 0.57 m left from cable 2 having positioned the cane at the other end of the well opening.*

Table 3.12: *Supplementary measurement results (18/12/2012):* $B_{DOUBLE,meas}$, $B_{DOUBLE,calc}$, $B_{WC,exact}$, $B_{WC,lit}$, $B_{WC,simp1}$, $B_{WC,simp2}$ *at different field-points (see Fig. 3.16) and percent errors of* $B_{DOUBLE,calc}$, $B_{WC,exact}$, $B_{WC,lit}$, $B_{WC,simp1}$ *and* $B_{WC,simp2}$ *with respect to* $B_{DOUBLE,meas}$.

$B_{DOUBLE,meas}$ [μT]	**$B_{DOUBLE,calc}$ [μT]**	**error [%]**	**$B_{WC,exact}$ [μT]**	**error [%]**	**$B_{WC,lit}$ [μT]**	**error [%]**	**$B_{WC,simp1}$ [μT]**	**error [%]**	**$B_{WC,simp2}$ [μT]**	**error [%]**
0.0 m										
0.340	1.053	-207	1.054	-207	0.757	-121	1.056	-208	1.051	-206
0.356	1.053	-196	1.054	-196	0.757	-113	1.056	-197	1.051	-195
0.359	1.098	-206	1.100	-206	0.791	-120	1.102	-207	1.097	-205
0.354	1.037	-193	1.039	-193	0.747	-111	1.040	-194	1.035	-192
0.3 m										
0.281	0.410	-45.9	0.412	-46.4	0.325	-15.8	0.408	-45.2	0.408	-45.2
0.276	0.410	-48.6	0.412	-49.1	0.325	-17.9	0.408	-47.8	0.408	-47.8
0.269	0.390	-45.0	0.391	-45.5	0.310	-15.1	0.388	-44.2	0.388	-44.3
0.267	0.385	-44.2	0.386	-44.7	0.306	-14.4	0.383	-43.4	0.383	-43.5
0.5m										
0.209	0.152	27.5	0.152	27.3	0.126	39.7	0.154	26.5	0.154	26.3
0.183	0.148	19.0	0.149	18.8	0.123	32.3	0.150	17.9	0.151	17.7
0.184	0.147	19.9	0.148	19.7	0.123	33.4	0.149	18.8	0.150	18.6
0.8 m										
0.152	0.041	73.4	0.041	73.3	0.035	76.8	0.042	72.2	0.043	72.0
0.152	0.041	73.3	0.041	73.2	0.035	76.7	0.042	72.1	0.043	71.9
0.142	0.040	71.9	0.04	71.8	0.035	75.5	0.042	70.6	0.042	70.5
1.0 m										
0.138	0.016	88.4	0.016	88.4	0.014	89.7	0.017	87.8	0.017	87.7
0.131	0.016	87.8	0.016	87.8	0.014	89.2	0.017	87.1	0.017	87.0
0.122	0.016	86.9	0.016	86.9	0.014	88.3	0.017	86.1	0.017	86.0

Measurements at 0.3 m and 0.5 m had a positive outcome, unlike measurements at distances higher than 0.8m that have manifested significant errors.

Thus, the experiment results can be retained as satisfactory since the agreement between the code and the measurements is good where the field is higher. Discrepancies are found only where the field is either close to or even below the sensitivity of the measuring instruments. The reasons for these discrepancies are:

- the twisted double-circuit cables could be hardly accessed. The use of an insulating non-magnetic cane for inserting the probe inside the well was required, limiting the precision concerning all the distances measured.
- the constancy of the pitch of the single helix and the perfect parallelism of the two helixes were not exactly matched.
- the instant rms values of the line currents provided by the distribution utility were relevant to one single phase current per circuit and, of course, there is no certainty that the three-phase currents of each circuit are symmetric all the time.
- magnetic field values below 0.1 μT are difficult to be tracked because they are below the sensitivity of the measuring device. Additionally, 0.1 μT is the minimum average magnetic field value found everywhere due to the use of electricity.

For distances higher than 0.5 m, the measured and calculatedmagnetic field values diverge significantly. This issue has been treated in literature, where similar divergent results have been obtained between measured and calculated magnetic fields in the vicinity of twisted cables: Pettersson et al. in [14], [15] concluded that this is due to deviations of the windings from perfect helices. In particular, Karady et al. in [22] returned to using three straight, parallel conductors to model the twisted cables because this method provides conservative results at distances greater than 1 m.

It seems that predictions for twisted cables based on models using ideal helices underestimate the measured magnetic fields and it is also possible that these non-conservative results are due to the well-known first term of B_φ from (1.b), equal to $\mu_0 I / 2\pi r$, implying that at large distances the helical line current acts as a straight line current, in particular when the helix is not perfect. In the exact twisted theory [14] this term is not considered for the composition of the total magnetic field generated by a three wire helix.

3.4 CONCLUSIONS

The magnetic field generated by an overhead or underground (the theoretical approach is the same) double-circuit twisted three-phase power cable line was treated following two different approaches both respecting the superposition principle; the exact approach which effectuates a complex vector sum of the two vectors of the magnetic field from each twisted three-phase single-circuit and the ‘worst case’ approach which implies the algebraic sum of the two individual values of the magnetic field from each twisted three-phase single-circuit.

The exact vector sum has resulted a rather complex procedure since computational hypotheses were obligated to be set, such as the constancy of the pitch of the single helix and also the constancy of the perfect parallelism of the two helixes, and conventions that would facilitate the analysis since it is impossible to obtain exact information about the geometrical arrangement of the power line in practice were introduced. On the other hand, the 'worst case' assumption for the calculation of the magnetic field is a simple approximated calculus that yields a good interpretation of the reality. Additionally, the 'worst case' approach permits further approximation by using both the approximated formula from the literature and the simplified innovative one, in both levels of approximation. The simulation results have proven the efficiency of such an approach, since the expressions $B_{WC,simp}$ provide a small and positive relative percent error with respect to the exact vector calculus.

Comparing the calculations with results from measurements relevant to a three-phase double-circuit twisted power cable line carried out in situ, it can be deducted that the theoretical approach of the double-circuit twisted cable line is correct and provides - especially when considering the difficult circumstances under which the experiment took place - magnetic field values near to the real ones, particularly for field points where the magnetic induction is large enough for being detected by measurement instruments.

Concluding, expression $B_{WC,exact}$ exhibits similar behavior to the expression $B_{DOUBLE,calc}$ and it is a simpler alternative to the exact calculus. Moreover, as expected, $B_{WC,simp}$ results more accurate than $B_{WC,lit}$. So, $B_{WC,simp}$ is a "quick-and-easy" calculation tool that provides magnetic field results close to the actual ones where the magnetic field is large enough for being detected by measurement instruments. In this way, the calculation of the magnetic field generated by any multiple-circuit twisted three-phase power cable lines – standard lines for transporting renewable energy – becomes possible.

CHAPTER 4

MULTIPLE-CIRCUIT TWISTED THREE - PHASE CABLE LINES

4.1 THEORY

In Chapter 3, the exact and approximated formulae from the literature along with the simplified innovative formulations were extended and applied to double-circuit twisted cable lines, under the following assumptions:

- the current terns carried by both cable lines are in-phase;
- since the medium is linear, at every field-point the magnetic field can be calculated composing linearly the two magnetic fields generated by each circuit separately (superposition principle);
- the exact treatment of the magnetic field from the double-circuit, B_{DOUBLE}, was obtained as the vector sum of the Cartesian components of the magnetic field from circuit 1 and 2 after formulae (3.1), (3.2), (3.3) and (3.4).
- for being conservative, a "worst case" estimate of the magnetic field from the double-circuit, $B_{WC,exact}$ (eq. 3.5) was obtained as the sum of the two rms values of total field B from circuit 1 and 2 after the exact formula (eq. 2.12), $B_{1,exact}$ and $B_{2,exact}$, respectively.
- relationship (3.5) was further simplified by using the approximate formula of the literature (eq. 2.17) and the simplified innovative formula (eq. 2.23), in both levels of approximation, to express the rms values of B from circuit 1 and 2, therefore obtaining the expressions $B_{WC,lit}$ (eq. 3.6), $B_{WC,simp1}$ (eq. 3.7.a) and $B_{WC,simp2}$ (eq. 3.7.b).

Analogously to what done in Chapter 3 for double-circuit lines, the exact and the "worst case" approach is extended here to multiple-circuit twisted cable lines. The need for such an extension comes from the fact that not only single and double circuit three-phase cables are used for the connection of renewable sources to the grid, but also multiple-circuit twisted cable lines in underground configuration, especially when the generators (photovoltaic panels or wind generators) are numerous and/or dispersed over a vast surface, and nevertheless have all to be connected to one single substation.

4.1.1 Exact Vector Analysis

The magnetic field from amultiple-circuit, $B_{MULTIPLE}$, is given by the following formula:

$$B_{MULTIPLE} = \sqrt{B_x^2 + B_y^2 + B_z^2} \tag{4.1}$$

being

$$\begin{cases} B_x = B_{r1}\cos\theta_1 + B_{r2}\cos\theta_2 + \ldots + B_{rn}\cos\theta_\mathrm{n} + B_{\phi 1}\cos\varphi_1 + B_{\phi 2}\cos\varphi_2 + \ldots + B_{\phi n}\cos\varphi_\mathrm{n} \\ B_y = B_{r1}\sin\theta_1 + B_{r2}\sin\theta_2 + \ldots + B_{rn}\sin\theta_\mathrm{n} + B_{\phi 1}\sin\varphi_1 + B_{\phi 2}\sin\varphi_2 + \ldots + B_{\phi n}\sin\varphi_\mathrm{n} \\ B_z = B_{z1} + B_{z2} + \ldots + B_{zn} \end{cases} \tag{4.2}$$

where B_{r1}, B_{r2}, ..., B_{rn}, $B_{\varphi 1}$, $B_{\varphi 2}$, ..., $B_{\varphi n}$ and B_{z1}, B_{z2}, ..., B_{zn} are the exact values of the radial, azimuthal and axial components of the magnetic field from *n* circuits.

Angles θ_1, θ_2, ..., θ_n and φ_1, φ_2, ..., φ_n are the angles formed by the *x*-axis and the radial, B_r, and azimuthal components, B_φ, from the *n* circuits, respectively (measured anticlockwise from the *x*-axis):

$$\begin{cases} \theta_1 = \arctan(y_1 / x_1) \\ \theta_2 = \arctan(y_2 / x_2) \\ \ldots \\ \theta_\mathrm{n} = \arctan(y_n / x_n) \end{cases} \tag{4.3}$$

and

$$\begin{cases} \varphi_1 = \theta_1 + \pi/2 \\ \varphi_2 = \theta_2 + \pi/2 \\ \ldots \\ \varphi_\mathrm{n} = \theta_\mathrm{n} + \pi/2 \end{cases} \tag{4.4}$$

where (x_1, y_1), (x_2, y_2), …, (x_n, y_n) are the coordinates of the *n* cables in the plane $z=0$, where $\varphi=\Phi$.

The above exact vector approach has been converted into a calculation tool for the magnetic field from multiple-circuit twisted three-phase cable lines by implementing relationships (4.1) - (4.4), plus exact formulae (2.6) for B_{r1}, B_{r2}, ..., B_{rn}, $B_{\varphi 1}$, $B_{\varphi 2}$, ..., $B_{\varphi n}$ and B_{z1}, B_{z2}, ..., B_{zn}, respectively, in a script in Matlab^{TM} environment. The value $\Phi_1=\Phi_2=\ldots=\Phi_n=60°$ has been set and kept constant also in the twisted multiple-circuit case considering the results of the angle Φanalysis made in the previous Chapters.

4.1.2 “Worst Case” Approach

For being conservative, the “worst case” estimate of the magnetic field from the multiple-circuit is obtained as the sum of all rms values of total field *B* from *n* circuits after the exact formula (2.12). Also in the multiple-circuit case, $B_{WC,exact}$ has the following expression:

$$B_{WC,exact} = B_{1,exact} + B_{2,exact} + \ldots + B_{n,exact} \tag{4.5}$$

Relationship (4.5) can be further simplified by using the approximate formula of the literature (eq. 2.17) and the simplified innovative formula (eq. 2.23), in both levels of approximation, to express the rms values of field *B* from *n* circuits and by composing them according to the "worst-case" approach. Also in the multiple-circuit case $B_{WC,lit}$, $B_{WC,simp1}$ and $B_{WC,simp2}$ have the following expressions:

$$B_{WC,lit} = B_{1,lit} + B_{2,lit} + \ldots + B_{n,lit} \tag{4.6}$$

and

$$B_{WC,simp1} = B_{1,simp1} + B_{2,simp1} + \ldots + B_{n,simp1} \tag{4.7.a}$$

$$B_{WC,simp2} = B_{1,simp2} + B_{2,simp2} + \ldots + B_{n,simp2} \tag{4.7.b}$$

4.2 APPLICATIONS – SIMULATION RESULTS

By implementing this theoretical approach in Matlab™ environment, for a ***triple-circuit twisted three-phase power line*** a script is obtained which – given the coordinates of the first, (x_1,y_1), second, (x_2,y_2), and third, (x_3,y_3), twisted cable in a 2-dimensional Cartesian reference system orthogonal to line axis, where line axis is located at $x = 0$ and ground level is located at $y = 0$ – calculates the value of the magnetic field generated by the triple-circuit twisted three-phase cable line along a horizontal line parallel to the to the ground and placed at a certain vertical distance *H* from the cables. This script uses eqs. (4.1) - (4.4) for the exact calculus, B_{TRIPLE}, eqs. (4.5) - (4.7) for the "worst-case" calculus, $B_{WC,exact}$, $B_{WC,lit}$, $B_{WC,simp1}$ and $B_{WC,simp2}$, plus the exact formula (2.12), the approximate formula of the literature (2.17) and the simplified formula (2.23) for B_{1exact}, B_{2exact}, B_{3exact}, B_{1lit}, B_{2lit}, B_{3lit}, B_{1simp1}, B_{2simp1}, B_{3simp1} and B_{1simp2}, B_{2simp2}, B_{3simp2}, respectively, and has been applied to some case-studies taking into account different cross-sections of different cable types and different geometric configurations. Also in these applicative case-studies the percent errors of $B_{WC,lit}$, $B_{WC,simp1}$ and $B_{WC,simp2}$ with respect to B_{TRIPLE} have been computed at the various field points.

4.2.1 Underground MV Triple-Circuit Three-Phase Twisted Cable Line

First Case: the three twisted cable circuits are ARE4H1RX cables [64], each with cross-section 3×240 mm^2, rated voltage 12(phase-to-ground)/ 20(phase-to-phase) kV, ampacity I = 423 A, pitch p = 1.52 m, radius α= 0.022 m. The coordinates of the three twisted cables are (-0.5,-1.0), (0,-1.0), (0.5, -1.0), i.e. the triple-circuit twisted cable line is laid underground at a burying depth H=1.0 m below the soil, with the single circuits horizontally spaced of 0.5 m from each other. The field points lie on the soil along a straight horizontal coordinate axis x whose vertical distance from the laying plane of the triple-circuit twisted cable line is H=1.0 m and are spread from -1.5 m to 1.5 m at both ends of the central circuit – having coordinates (0, -1.0) – that is taken as the line axis.The geometry of the line section is depicted in Fig. 4.1 and the results of the first case-study are plotted in Fig. 4.2, which displays the curves of B_{TRIPLE}, $B_{WC,exact}$, $B_{WC,lit}$, $B_{WC,simp1}$ and $B_{WC,simp2}$ vs. abscissa x, and in Table 4.1, which reports the relevant numerical values and percent errors of $B_{WC,exact}$, $B_{WC,lit}$, $B_{WC,simp1}$ and $B_{WC,simp2}$ with respect to B_{TRIPLE}.

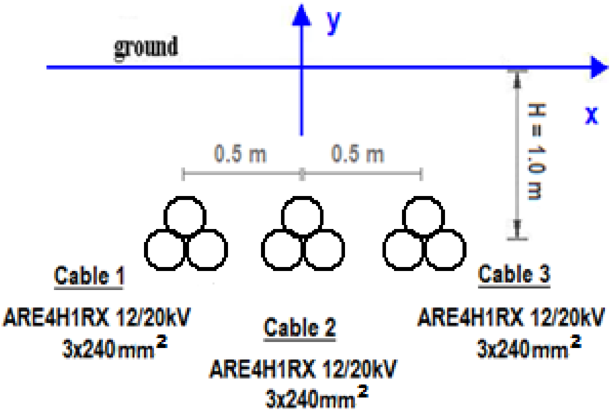

Figure 4.1: *Geometrical and electrical data concerning the first case-study.*

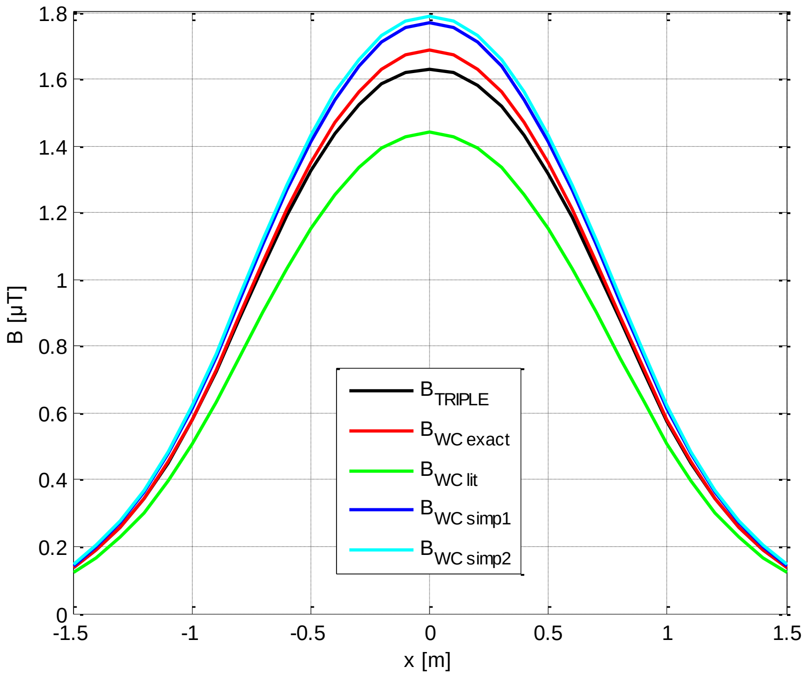

Figure 4.2: B_{TRIPLE}, $B_{WC,exact}$, $B_{WC,lit}$, $B_{WC,simp1}$, $B_{WC,simp2}$ *vs. distance x for the first case-study* (I_1=I_2=I_3=423 A).

Table 4.1: *Numerical values of B_{TRIPLE}, $B_{WC,exact}$, $B_{WC,lit}$, $B_{WC,simp1}$, $B_{WC,simp2}$ vs. distance x and percent errors of $B_{WC,exact}$, $B_{WC,lit}$, $B_{WC,simp1}$ and $B_{WC,simp2}$ with respect to B_{TRIPLE} for the first case-study ($I_1=I_2=I_3=423$ A).*

x [m]	**B_{TRIPLE} [μT]**	**$B_{WC,exact}$ [μT]**	**error [%]**	**$B_{WC,lit}$ [μT]**	**error [%]**	**$B_{WC,simp1}$ [μT]**	**error [%]**	**$B_{WC,simp2}$ [μT]**	**error [%]**
-1.5	0.1360	0.1362	0.13	0.1218	-10.47	0.1438	5.70	0.1463	7.54
-1.4	0.1882	0.1885	0.17	0.1676	-10.93	0.1993	5.90	0.2027	7.68
-1.3	0.2566	0.2571	0.22	0.2273	-11.39	0.2720	6.01	0.2764	7.72
-1.2	0.3437	0.3447	0.28	0.3030	-11.84	0.3645	6.04	0.3701	7.68
-1.1	0.4514	0.4531	0.38	0.3960	-12.27	0.4785	6.02	0.4857	7.60
-1.0	0.5792	0.5821	0.50	0.5060	-12.64	0.6138	5.98	0.6227	7.51
-0.9	0.7243	0.7291	0.67	0.6307	-12.92	0.7675	5.97	0.7783	7.46
-0.8	0.8805	0.8884	0.89	0.7652	-13.10	0.9336	6.03	0.9464	7.48
-0.7	1.039	1.051	1.18	0.9025	-13.14	1.103	6.19	1.118	7.61
-0.6	1.190	1.208	1.52	1.035	-13.04	1.267	6.46	1.284	7.87
-0.5	1.324	1.350	1.91	1.154	-12.83	1.415	6.82	1.433	8.23
-0.4	1.436	1.469	2.31	1.256	-12.54	1.540	7.24	1.5601	8.64
-0.3	1.523	1.563	2.68	1.336	-12.24	1.639	7.65	1.6604	9.05
-0.2	1.584	1.631	2.97	1.394	-11.98	1.710	7.98	1.7323	9.38
-0.1	1.620	1.671	3.17	1.429	-11.81	1.753	8.20	1.7756	9.61
-0.0	1.631	1.685	3.27	1.440	-11.72	1.767	8.32	1.7900	9.73
0.1	1.618	1.671	3.29	1.429	-11.71	1.753	8.32	1.7756	9.73
0.2	1.580	1.631	3.20	1.394	-11.79	1.710	8.22	1.7323	9.63
0.3	1.518	1.563	3.01	1.336	-11.95	1.639	8.00	1.6604	9.40
0.4	1.430	1.469	2.73	1.256	-12.18	1.540	7.68	1.5601	9.08
0.5	1.318	1.350	2.37	1.154	-12.44	1.415	7.30	1.4332	8.71
0.6	1.185	1.208	1.98	1.035	-12.65	1.267	6.94	1.2836	8.36
0.7	1.035	1.051	1.61	0.9025	-12.76	1.103	6.65	1.1182	8.08
0.8	0.8771	0.8884	1.29	0.7652	-12.76	0.9336	6.44	0.9464	7.90
0.9	0.7218	0.7291	1.01	0.6307	-12.63	0.7675	6.33	0.7783	7.82
1.0	0.5775	0.5821	0.79	0.5060	-12.38	0.6138	6.29	0.6227	7.82
1.1	0.4503	0.4531	0.62	0.3960	-12.06	0.4785	6.27	0.4857	7.86
1.2	0.3431	0.3447	0.48	0.3030	-11.67	0.3645	6.25	0.3701	7.90
1.3	0.2561	0.2571	0.38	0.2273	-11.25	0.2720	6.19	0.2764	7.89
1.4	0.1880	0.1885	0.30	0.1676	-10.81	0.1993	6.05	0.2027	7.83
1.5	0.1359	0.1362	0.24	0.1218	-10.37	0.1438	5.82	0.1463	7.67

The error computed according to the “worst case” approach, $B_{WC,exact}$ (eq. 4.5), is below 3.5% and always positive. The errors computed by the application of the simplified formula in the “worst case” estimate calculation (eqs. 4.7), $B_{WC,simp1}$ and $B_{WC\ simp2}$, are fairly small (maximum ~8% for the 1st approximation level and maximum ~10% for the 2nd approximation level) and always positive. The errors computed by the approximate formula of the literature in the “worst case” estimate calculation, $B_{WC,lit}$ (eq. 4.6), arrive at ~-13% being always negative.

***Second Case*:** same as the first case, apart that the central cable has a larger cross-section than the other two cables, namely 3x300 mm^2, thus larger ampacity I=478 A, pitch p=1.66 m and radius α=0.024 m (see Fig. 4.3). The results of the second case simulations are shown in Fig. 4.4 and Table 4.2.

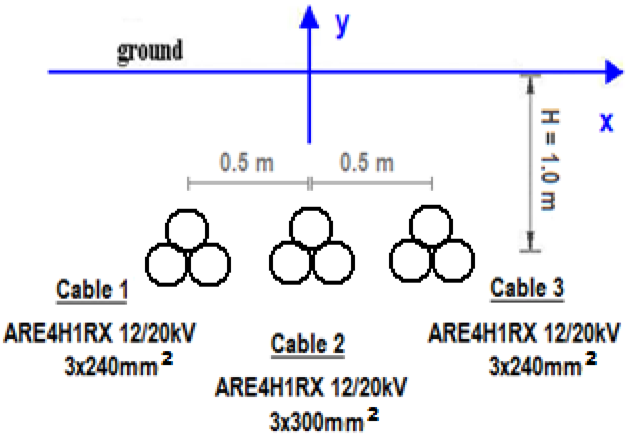

Figure 4.3: *Geometrical and electrical data concerning the second case-study.*

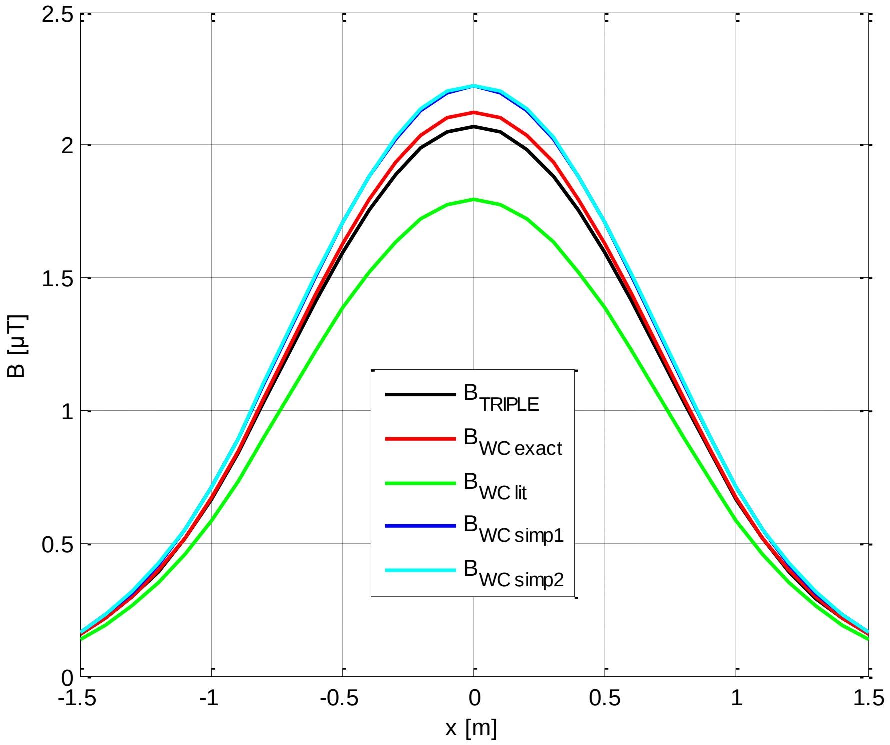

Figure 4.4: B_{TRIPLE}, $B_{WC,exact}$, $B_{WC,lit}$, $B_{WC,simp1}$, $B_{WC,simp2}$ *vs. distance x for the second case-study* (I_1=I_3=423 A and I_2=478 A).

Table 4.2: *Numerical values of B_{TRIPLE}, $B_{WC,exact}$, $B_{WC,lit}$, $B_{WC,simp1}$, $B_{WC,simp2}$ vs. distance x and percent errors of $B_{WC,exact}$, $B_{WC,lit}$, $B_{WC,simp1}$ and $B_{WC,simp2}$ with respect to B_{TRIPLE} for the second case-study (I_1=I_3=423 A and I_2=478 A).*

x [m]	**B_{TRIPLE} [μT]**	**$B_{WC,exact}$ [μT]**	**error [%]**	**$B_{WC,lit}$ [μT]**	**error [%]**	**$B_{WC,simp1}$ [μT]**	**error [%]**	**$B_{WC,simp2}$ [μT]**	**error [%]**
-1.5	0.1564	0.1567	0.19	0.1402	-10.36	0.1650	5.51	0.1664	6.40
-1.4	0.2160	0.2165	0.24	0.1927	-10.82	0.2286	5.81	0.2304	6.65
-1.3	0.2942	0.2951	0.30	0.2610	-11.28	0.3119	6.00	0.3142	6.79
-1.2	0.3943	0.3958	0.38	0.3480	-11.73	0.4184	6.11	0.4213	6.85
-1.1	0.5185	0.5211	0.49	0.4555	-12.16	0.5505	6.16	0.5540	6.84
-1.0	0.6674	0.6716	0.63	0.5837	-12.54	0.7087	6.19	0.7129	6.81
-0.9	0.8387	0.8455	0.81	0.7308	-12.86	0.8908	6.22	0.8956	6.79
-0.8	1.027	1.037	1.03	0.8922	-13.10	1.091	6.30	1.096	6.80
-0.7	1.223	1.238	1.30	1.061	-13.24	1.301	6.43	1.307	6.87
-0.6	1.416	1.439	1.60	1.228	-13.29	1.510	6.62	1.515	7.00
-0.5	1.597	1.627	1.90	1.385	-13.27	1.706	6.85	1.711	7.16
-0.4	1.756	1.794	2.17	1.523	-13.24	1.880	7.06	1.884	7.32
-0.3	1.887	1.932	2.39	1.638	-13.22	2.024	7.23	2.027	7.44
-0.2	1.986	2.036	2.52	1.723	-13.23	2.131	7.32	2.135	7.49
-0.1	2.047	2.100	2.59	1.776	-13.25	2.198	7.36	2.201	7.50
-0.0	2.068	2.122	2.61	1.794	-13.26	2.221	7.38	2.223	7.51
0.1	2.047	2.100	2.62	1.776	-13.23	2.198	7.39	2.201	7.53
0.2	1.984	2.036	2.59	1.723	-13.17	2.131	7.40	2.135	7.57
0.3	1.885	1.932	2.52	1.638	-13.11	2.024	7.37	2.027	7.58
0.4	1.752	1.794	2.37	1.523	-13.07	1.880	7.27	1.884	7.53
0.5	1.593	1.627	2.16	1.385	-13.05	1.706	7.12	1.711	7.44
0.6	1.412	1.439	1.89	1.228	-13.03	1.510	6.93	1.515	7.31
0.7	1.219	1.238	1.61	1.061	-12.97	1.301	6.75	1.307	7.20
0.8	1.024	1.037	1.33	0.8922	-12.84	1.091	6.61	1.096	7.12
0.9	0.8364	0.8455	1.09	0.7308	-12.62	0.8908	6.51	0.8956	7.08
1.0	0.6658	0.6716	0.87	0.5837	-12.33	0.7087	6.45	0.7129	7.07
1.1	0.5174	0.5211	0.70	0.4555	-11.97	0.5505	6.38	0.5540	7.07
1.2	0.3936	0.3958	0.56	0.3480	-11.57	0.4184	6.30	0.4213	7.04
1.3	0.2938	0.2951	0.45	0.2610	-11.14	0.3119	6.16	0.3142	6.95
1.4	0.2158	0.2165	0.36	0.1927	-10.71	0.2286	5.94	0.2304	6.79
1.5	0.1563	0.1567	0.30	0.1402	-10.27	0.1650	5.62	0.1664	6.52

The error computed according to the “worst case” approach, $B_{WC,exact}$ (eq. 4.5), is below 3% and always positive. The errors computed by the application of the simplified formula in the “worst case” estimate calculation (eqs. 4.7), $B_{WC,simp1}$ and $B_{WC\ simp2}$, are fairly small (maximum ~7.5% for both approximation levels) and always positive. The errors computed by the approximate formula of the literature in the “worst case” estimate calculation, $B_{WC,lit}$ (eq. 4.6), arrive at ~-13% being always negative.

Third Case: same overall arrangement as in the second case, apart that the central cable, with the larger cross-section, is at a burying depth H_2=1.5 m, thus the field points lie on a straight horizontal line whose vertical distance from the central cable is 1.5 m, while their vertical distance from the other two cables is still 1.0 m (see Fig. 4.5). Figure 4.6 and Table 4.3 show the results of the third case simulation.

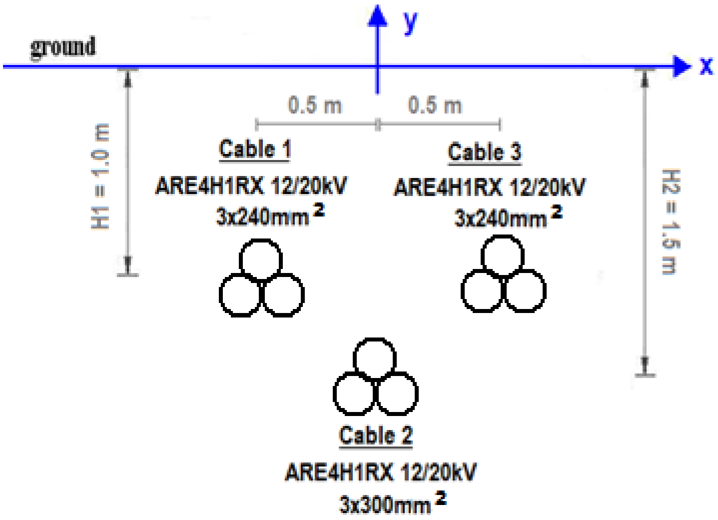

Figure 4.5: *Geometrical and electrical data concerning the third case-study.*

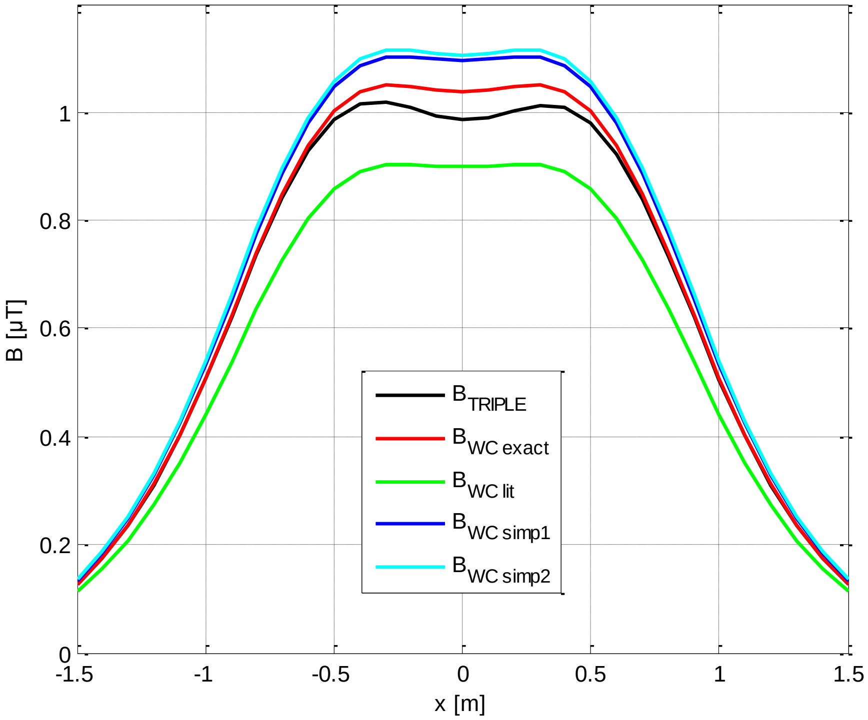

Figure 4.6: *B_{TRIPLE}, $B_{WC,exact}$, $B_{WC,lit}$, $B_{WC,simp1}$, $B_{WC,simp2}$ vs. distance x for the third case-study (I_1=I_3=423 A and I_2=478 A).*

Table 4.3: *Numerical values of B_{TRIPLE}, $B_{WC,exact}$, $B_{WC,lit}$, $B_{WC,simp1}$, $B_{WC,simp2}$ vs. distance x and percent errors of $B_{WC,exact}$, $B_{WC,lit}$, $B_{WC,simp1}$ and $B_{WC,simp2}$ with respect to B_{TRIPLE} for the third case-study (I_1=I_3=423 A and I_2=478 A).*

x [m]	**B_{TRIPLE} [μT]**	**$B_{WC,exact}$ [μT]**	**error [%]**	**$B_{WC,lit}$ [μT]**	**error [%]**	**$B_{WC,simp1}$ [μT]**	**error [%]**	**$B_{WC,simp2}$ [μT]**	**error [%]**
-1.5	0.1274	0.1274	0.05	0.1139	-10.61	0.1343	5.41	0.1361	6.88
-1.4	0.1745	0.1746	0.06	0.1551	-11.12	0.1842	5.59	0.1867	7.00
-1.3	0.2352	0.2354	0.08	0.2078	-11.63	0.2485	5.66	0.2517	7.02
-1.2	0.3111	0.3114	0.11	0.2733	-12.14	0.3286	5.62	0.3327	6.94
-1.1	0.4025	0.4031	0.15	0.3517	-12.62	0.4248	5.53	0.4298	6.79
-1.0	0.5076	0.5087	0.22	0.4413	-13.06	0.5350	5.40	0.5412	6.62
-0.9	0.6215	0.6235	0.32	0.5381	-13.42	0.6544	5.30	0.6617	6.47
-0.8	0.7363	0.7398	0.47	0.6359	-13.64	0.7751	5.27	0.7835	6.40
-0.7	0.8419	0.8478	0.70	0.7266	-13.69	0.8872	5.37	0.8965	6.48
-0.6	0.9278	0.9375	1.05	0.8024	-13.52	0.9805	5.68	0.9906	6.77
-0.5	0.9863	1.002	1.55	0.8574	-13.06	1.048	6.26	1.059	7.33
-0.4	1.015	1.038	2.24	0.8902	-12.32	1.088	7.12	1.098	8.19
-0.3	1.019	1.051	3.11	0.9037	-11.32	1.103	8.24	1.114	9.32
-0.2	1.008	1.049	4.07	0.9048	-10.22	1.103	9.48	1.114	10.56
-0.1	0.9936	1.042	4.90	0.9013	-9.29	1.098	10.53	1.109	11.62
-0.0	0.9864	1.039	5.34	0.8993	-8.83	1.096	11.06	1.106	12.16
0.1	0.9905	1.042	5.22	0.9013	-9.01	1.098	10.87	1.109	11.97
0.2	1.003	1.049	4.62	0.9048	-9.75	1.103	10.05	1.114	11.14
0.3	1.013	1.051	3.76	0.9037	-10.77	1.103	8.92	1.114	10.01
0.4	1.009	1.038	2.88	0.8902	-11.77	1.088	7.79	1.098	8.87
0.5	0.9808	1.002	2.12	0.8574	-12.57	1.048	6.85	1.059	7.94
0.6	0.9234	0.9375	1.53	0.8024	-13.11	0.9805	6.18	0.9906	7.28
0.7	0.8387	0.8478	1.09	0.7266	-13.36	0.8872	5.78	0.8965	6.89
0.8	0.7341	0.7398	0.77	0.6359	-13.38	0.7751	5.58	0.7835	6.73
0.9	0.6200	0.6235	0.55	0.5381	-13.21	0.6544	5.54	0.6617	6.72
1.0	0.5067	0.5087	0.40	0.4413	-12.91	0.5350	5.59	0.5412	6.81
1.1	0.4020	0.4031	0.29	0.3517	-12.51	0.4248	5.67	0.4298	6.93
1.2	0.3108	0.3114	0.21	0.2733	-12.05	0.3286	5.73	0.3327	7.04
1.3	0.2350	0.2354	0.15	0.2078	-11.56	0.2485	5.73	0.2517	7.10
1.4	0.1744	0.1746	0.11	0.1551	-11.07	0.1842	5.65	0.1867	7.06
1.5	0.1273	0.1274	0.09	0.1139	-10.58	0.1343	5.45	0.1361	6.92

The error computed according to the “worst case” approach, $B_{WC,exact}$ (eq. 4.5), is below 5% and always positive. The errors computed by the application of the simplified formula in the “worst case” estimate calculation (eqs. 4.7), $B_{WC,simp1}$ and $B_{WC\ simp2}$, are fairly small (maximum ~11% for the 1st level of approximation and maximum ~12% for the 2nd level of approximation) and always positive. The errors computed by the approximate formula of the literature in the “worst case” estimate calculation, $B_{WC,lit}$ (eq. 4.6), arrive at ~-13.5% being always negative.

4.2.2 Overhead MV Triple-Circuit Three-Phase Twisted Cable Line

First Case: the three twisted cable circuits are ARG7H1RX cables [63], each with cross-section 3×120 mm^2, rated voltage 12(phase-to-ground)/ 20(phase-to-phase) kV, ampacity I = 280 A, pitch p = 1.37 m, radius α = 0.020 m. The coordinates of the three twisted cables are (-0.4,10), (0,10), (0.4, 10), i.e. the triple-circuit twisted cable line is situated at a height of 10 m above the ground, with the single circuits horizontally spaced of 0.4 m from each other. The field points lie on a straight horizontal line whose vertical distance from the laying plane of the triple-circuit twisted cable line is H=0.5 m and are spread from -1.5 m to 1.5 m at both ends of the central circuit – having coordinates (0, 10) – that is taken as the line axis. The geometry of the line section is depicted in Fig. 4.7 and the results of the first case-study are plotted in Fig. 4.8, which displays the curves of B_{TRIPLE}, $B_{WC,exact}$, $B_{WC,lit}$, $B_{WC,simp1}$ and $B_{WC,simp2}$ vs. abscissa x, and in Table 4.4, which reports the relevant numerical values and percent errors of $B_{WC,exact}$, $B_{WC,lit}$, $B_{WC,simp1}$ and $B_{WC,simp2}$ with respect to B_{TRIPLE}.

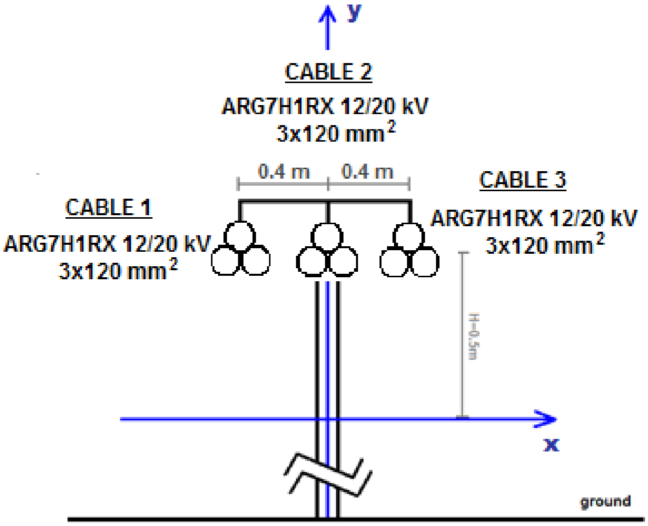

Figure 4.7: *Geometrical and electrical data concerning the first case-study.*

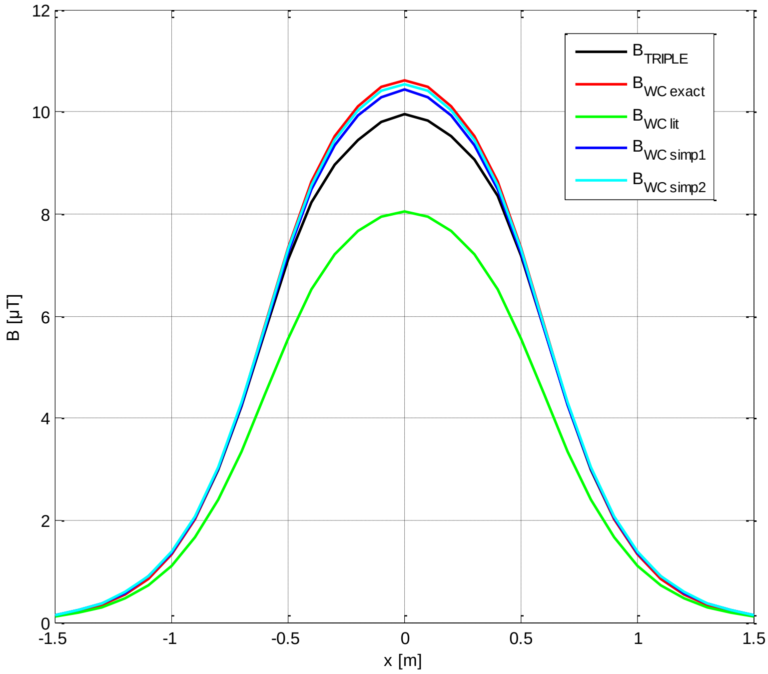

Figure 4.8: *B_{TRIPLE}, $B_{WC,exact}$, $B_{WC,lit}$, $B_{WC,simp1}$, $B_{WC,simp2}$ vs. distance x for the first case-study (I_1=I_2=I_3=280 A).*

Table 4.4: *Numerical values of B_{TRIPLE}, $B_{WC,exact}$, $B_{WC,lit}$, $B_{WC,simp1}$, $B_{WC,simp2}$ vs. distance x and percent errors of $B_{WC,exact}$, $B_{WC,lit}$, $B_{WC,simp1}$ and $B_{WC,simp2}$ with respect to B_{TRIPLE} for the first case-study ($I_1=I_2=I_3=280$ A).*

x [m]	**B_{TRIPLE} [μT]**	**$B_{WC,exact}$ [μT]**	**error [%]**	**$B_{WC,lit}$ [μT]**	**error [%]**	**$B_{WC,simp1}$ [μT]**	**error [%]**	**$B_{WC,simp2}$ [μT]**	**error [%]**
-1.5	0.1387	0.1388	0.08	0.1233	-11.08	0.1469	5.90	0.1512	8.99
-1.4	0.2206	0.2208	0.11	0.1944	-11.89	0.2330	5.63	0.2393	8.49
-1.3	0.3495	0.3500	0.15	0.3047	-12.82	0.3674	5.15	0.3766	7.76
-1.2	0.5506	0.5517	0.20	0.4742	-13.87	0.5751	4.46	0.5882	6.84
-1.1	0.8604	0.8628	0.28	0.7308	-15.05	0.8913	3.60	0.9099	5.76
-1.0	1.328	1.334	0.40	1.111	-16.37	1.364	2.65	1.389	4.58
-0.9	2.015	2.027	0.59	1.656	-17.80	2.050	1.72	2.084	3.43
-0.8	2.976	3.002	0.88	2.403	-19.26	3.005	0.97	3.049	2.48
-0.7	4.226	4.283	1.34	3.356	-20.60	4.251	0.60	4.307	1.93
-0.6	5.679	5.797	2.08	4.457	-21.52	5.724	0.79	5.791	1.98
-0.5	7.108	7.335	3.20	5.566	-21.69	7.223	1.63	7.301	2.72
-0.4	8.236	8.622	4.69	6.512	-20.94	8.479	2.94	8.567	4.01
-0.3	8.965	9.519	6.18	7.202	-19.66	9.349	4.29	9.447	5.37
-0.2	9.442	10.10	6.98	7.664	-18.83	9.917	5.03	10.02	6.14
-0.1	9.797	10.48	6.93	7.950	-18.85	10.29	5.04	10.40	6.15
-0.0	9.950	10.62	6.71	8.053	-19.07	10.44	4.88	10.55	5.98
0.1	9.822	10.48	6.66	7.950	-19.05	10.29	4.78	10.40	5.89
0.2	9.510	10.10	6.22	7.664	-19.41	9.917	4.28	10.02	5.38
0.3	9.071	9.519	4.93	7.202	-20.60	9.349	3.06	9.447	4.14
0.4	8.347	8.622	3.30	6.512	-21.99	8.479	1.58	8.567	2.63
0.5	7.193	7.335	1.97	5.566	-22.62	7.223	0.42	7.301	1.50
0.6	5.732	5.797	1.12	4.457	-22.26	5.724	-0.15	5.791	1.03
0.7	4.255	4.283	0.64	3.356	-21.14	4.251	-0.10	4.307	1.22
0.8	2.991	3.002	0.37	2.403	-19.67	3.005	0.46	3.049	1.96
0.9	2.022	2.027	0.23	1.656	-18.10	2.050	1.35	2.084	3.06
1.0	1.332	1.334	0.14	1.111	-16.59	1.364	2.39	1.389	4.31
1.1	0.8620	0.8628	0.09	0.7308	-15.21	0.8913	3.41	0.9099	5.56
1.2	0.5513	0.5517	0.06	0.4742	-13.99	0.5751	4.31	0.5882	6.69
1.3	0.3498	0.3500	0.04	0.3047	-12.91	0.3674	5.03	0.3766	7.65
1.4	0.2208	0.2208	0.03	0.1944	-11.96	0.2330	5.55	0.2393	8.40
1.5	0.1388	0.1388	0.02	0.1233	-11.13	0.1469	5.84	0.1512	8.92

The error computed according to the “worst case” approach, $B_{WC,exact}$ (eq. 4.5), is below 7% and always positive. The errors computed by the application of the simplified formula in the “worst case” estimate calculation (eqs. 4.7), $B_{WC,simp1}$ and $B_{WC\ simp2}$, are fairly small (maximum ~5% for the 1st level of approximation and maximum ~6% for the 2nd level of approximation) and always positive. The errors computed by the approximate formula of the literature in the “worst case” estimate calculation, $B_{WC,lit}$ (eq. 4.6), arrive at ~-23% being always negative.

Second Case: same as the first case, apart thatthe field points lie on a straight horizontal line whose vertical distance from the laying plane of the triple-circuit twisted cable line is, now, *H*=1.0 m (see Fig. 4.9).The results of the second case simulations are shown in Fig. 4.10 and Table 4.5.

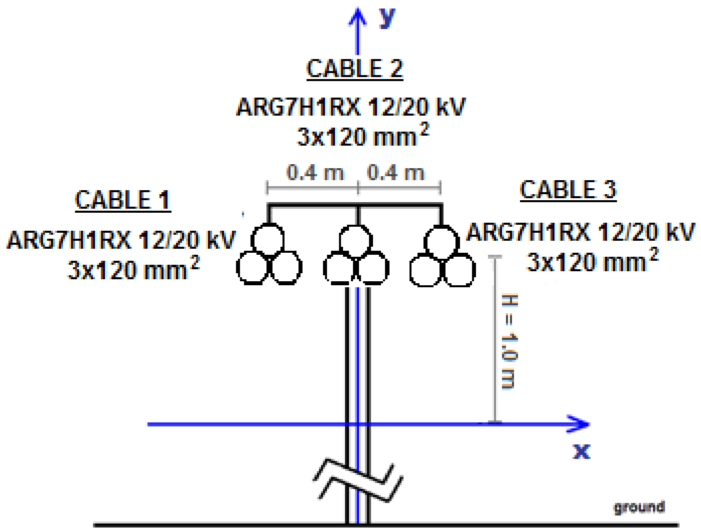

Figure 4.9: *Geometrical and electrical data concerning the second case-study.*

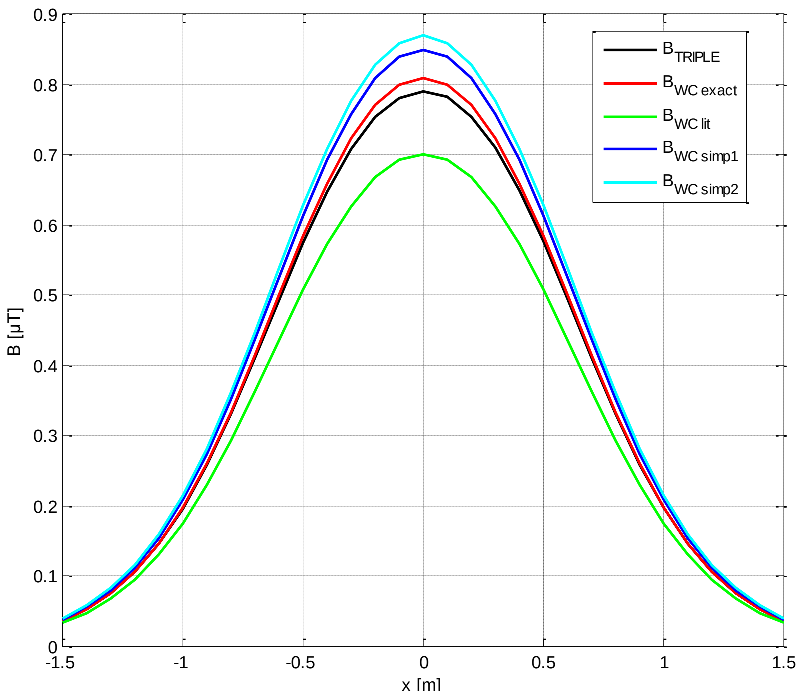

Figure 4.10: B_{TRIPLE}, $B_{WC,exact}$, $B_{WC,lit}$, $B_{WC,simp1}$, $B_{WC,simp2}$ *vs. distance x for the second case-study* (I_1=I_2=I_3=*280 A*).

Table 4.5: *Numerical values of B_{TRIPLE}, $B_{WC,exact}$, $B_{WC,lit}$, $B_{WC,simp1}$, $B_{WC,simp2}$ vs. distance x and percent errors of $B_{WC,exact}$, $B_{WC,lit}$, $B_{WC,simp1}$ and $B_{WC,simp2}$ with respect to B_{TRIPLE} for the second case-study ($I_1=I_2=I_3=280$ A).*

x [m]	**B_{TRIPLE} [μT]**	**$B_{WC,exact}$ [μT]**	**error [%]**	**$B_{WC,lit}$ [μT]**	**error [%]**	**$B_{WC,simp1}$ [μT]**	**error [%]**	**$B_{WC,simp2}$ [μT]**	**error [%]**
-1.5	0.0361	0.0362	0.17	0.0329	-8.98	0.0381	5.53	0.0395	9.31
-1.4	0.0524	0.0525	0.21	0.0475	-9.37	0.0554	5.88	0.0573	9.49
-1.3	0.0748	0.0750	0.26	0.0675	-9.77	0.0794	6.11	0.0820	9.57
-1.2	0.1052	0.1056	0.33	0.0945	-10.17	0.1118	6.26	0.1153	9.56
-1.1	0.1452	0.1458	0.41	0.1299	-10.56	0.1544	6.32	0.1590	9.49
-1.0	0.1960	0.1971	0.53	0.1746	-10.92	0.2085	6.35	0.2144	9.37
-0.9	0.2581	0.2598	0.67	0.2291	-11.23	0.2745	6.35	0.2820	9.26
-0.8	0.3305	0.3333	0.85	0.2925	-11.48	0.3515	6.36	0.3608	9.17
-0.7	0.4104	0.4148	1.06	0.3627	-11.64	0.4368	6.42	0.4480	9.15
-0.6	0.4936	0.5000	1.31	0.4358	-11.70	0.5258	6.54	0.5390	9.20
-0.5	0.5744	0.5835	1.58	0.5073	-11.68	0.6130	6.71	0.6280	9.33
-0.4	0.6475	0.6595	1.85	0.5725	-11.59	0.6924	6.93	0.7091	9.51
-0.3	0.7082	0.7230	2.08	0.6270	-11.47	0.7588	7.14	0.7770	9.71
-0.2	0.7534	0.7705	2.26	0.6678	-11.36	0.8085	7.31	0.8278	9.87
-0.1	0.7813	0.7997	2.35	0.6930	-11.31	0.8391	7.40	0.8591	9.95
-0.0	0.7910	0.8095	2.34	0.7015	-11.32	0.8495	7.40	0.8697	9.95
0.1	0.7821	0.7997	2.25	0.6930	-11.39	0.8391	7.29	0.8591	9.85
0.2	0.7549	0.7705	2.07	0.6678	-11.53	0.8085	7.11	0.8278	9.66
0.3	0.7101	0.7230	1.82	0.6270	-11.70	0.7588	6.86	0.7770	9.42
0.4	0.6495	0.6595	1.54	0.5725	-11.86	0.6924	6.60	0.7091	9.18
0.5	0.5763	0.5835	1.25	0.5073	-11.96	0.6130	6.37	0.6280	8.98
0.6	0.4951	0.5000	0.99	0.4358	-11.98	0.5258	6.20	0.5390	8.85
0.7	0.4116	0.4148	0.77	0.3627	-11.90	0.4368	6.11	0.4480	8.83
0.8	0.3313	0.3333	0.58	0.2925	-11.71	0.3515	6.09	0.3608	8.89
0.9	0.2587	0.2598	0.44	0.2291	-11.43	0.2745	6.11	0.2820	9.01
1.0	0.1964	0.1971	0.34	0.1746	-11.09	0.2085	6.14	0.2144	9.17
1.1	0.1454	0.1458	0.25	0.1299	-10.70	0.1544	6.16	0.1590	9.31
1.2	0.1054	0.1056	0.19	0.0945	-10.29	0.1118	6.12	0.1153	9.42
1.3	0.0749	0.0750	0.15	0.0675	-9.87	0.0794	6.00	0.0820	9.45
1.4	0.0524	0.0525	0.12	0.0475	-9.45	0.0554	5.78	0.0573	9.39
1.5	0.0362	0.0362	0.09	0.0329	-9.05	0.0381	5.45	0.0395	9.23

The error computed according to the “worst case” approach, $B_{WC,exact}$ (eq. 4.5), is below 2.5% and always positive. The errors computed by the application of the simplified formula in the “worst case” estimate calculation (eqs. 4.7), $B_{WC,simp1}$ and $B_{WC\ simp2}$, are fairly small (maximum ~7.5% for the 1st level of approximation and maximum ~10% for the 2nd level of approximation) and always positive. The errors computed by the approximate formula of the literature in the “worst case” estimate calculation, $B_{WC,lit}$ (eq. 4.6), arrive at ~-11% being always negative.

Third Case: same overall arrangement as in the second case, apart that the central cable has a larger cross-section than the other two cables, namely 3x185 mm^2, thus larger ampacity I=360 A, pitch p=1.5 m and radius α=0.022 m (see Fig. 4.11). Figure 4.12 and Table 4.6 show the results of the third case simulation.

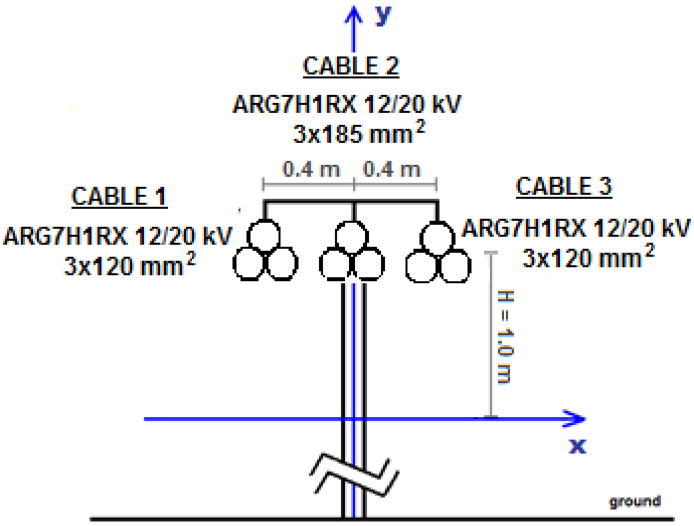

Figure 4.11: *Geometrical and electrical data concerning the third case-study.*

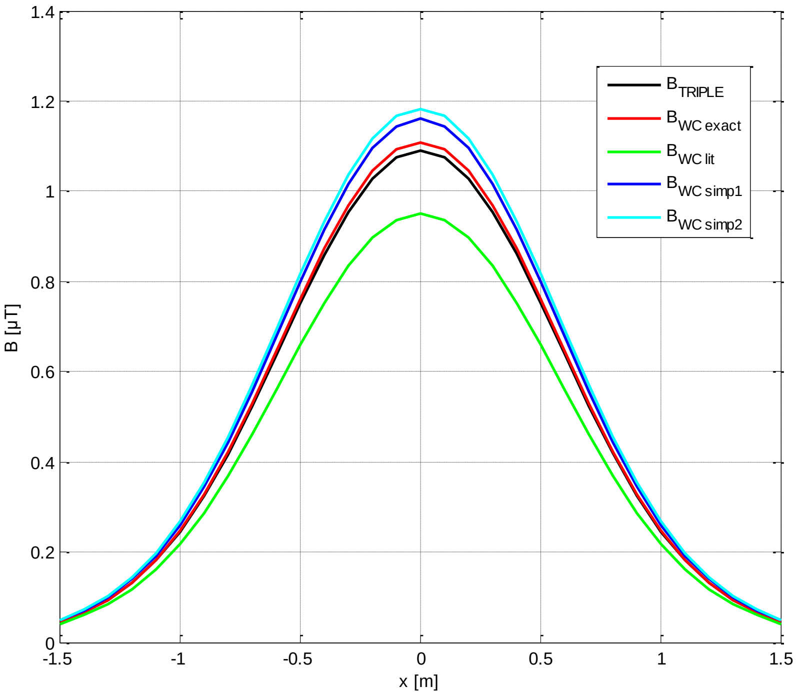

Figure 4.12: *B_{TRIPLE}, $B_{WC,exact}$, $B_{WC,lit}$, $B_{WC,simp1}$, $B_{WC,simp2}$ vs. distance x for the third case-study (I_1=I_3=280 A and I_2=360 A).*

***Table 4.6:** Numerical values of B_{TRIPLE}, $B_{WC,exact}$, $B_{WC,lit}$, $B_{WC,simp1}$, $B_{WC,simp2}$ vs. distance x and percent errors of $B_{WC,exact}$, $B_{WC,lit}$, $B_{WC,simp1}$ and $B_{WC,simp2}$ with respect to B_{TRIPLE} for the third case-study (I_1=I_3=280 A and I_2=360 A).*

x [m]	B_{TRIPLE} [μT]	$B_{WC,exact}$ [μT]	error [%]	$B_{WC,lit}$ [μT]	error [%]	$B_{WC,simp1}$ [μT]	error [%]	$B_{WC,simp2}$ [μT]	error [%]
-1.5	0.0455	0.0456	0.19	0.0414	-8.94	0.0479	5.22	0.0494	8.54
-1.4	0.0657	0.0658	0.24	0.0595	-9.33	0.0694	5.66	0.0715	8.84
-1.3	0.0936	0.0938	0.29	0.0844	-9.74	0.0992	5.99	0.1020	9.02
-1.2	0.1314	0.1318	0.36	0.1180	-10.15	0.1395	6.21	0.1433	9.11
-1.1	0.1813	0.1821	0.45	0.1621	-10.55	0.1928	6.35	0.1978	9.11
-1.0	0.2452	0.2465	0.55	0.2183	-10.94	0.2609	6.42	0.2674	9.06
-0.9	0.3241	0.3263	0.68	0.2875	-11.31	0.3451	6.45	0.3532	8.97
-0.8	0.4178	0.4212	0.83	0.3692	-11.63	0.4447	6.46	0.4548	8.87
-0.7	0.5236	0.5288	1.00	0.4612	-11.91	0.5575	6.47	0.5696	8.79
-0.6	0.6370	0.6445	1.17	0.5597	-12.13	0.6783	6.49	0.6926	8.72
-0.5	0.7516	0.7617	1.35	0.6591	-12.30	0.8006	6.52	0.8168	8.68
-0.4	0.8598	0.8727	1.50	0.7528	-12.44	0.9161	6.54	0.9342	8.65
-0.3	0.9540	0.9694	1.61	0.8342	-12.56	1.017	6.56	1.036	8.62
-0.2	1.027	1.045	1.69	0.8973	-12.65	1.095	6.55	1.116	8.59
-0.1	1.074	1.092	1.72	0.9372	-12.72	1.144	6.54	1.166	8.55
-0.0	1.090	1.109	1.72	0.9509	-12.76	1.161	6.52	1.183	8.53
0.1	1.074	1.092	1.69	0.9372	-12.75	1.144	6.51	1.166	8.52
0.2	1.028	1.045	1.62	0.8973	-12.71	1.095	6.49	1.116	8.52
0.3	0.9550	0.9694	1.51	0.8342	-12.65	1.017	6.45	1.036	8.51
0.4	0.8610	0.8727	1.36	0.7528	-12.56	0.9161	6.40	0.9342	8.50
0.5	0.7528	0.7617	1.18	0.6591	-12.45	0.8006	6.34	0.8168	8.50
0.6	0.6382	0.6445	0.99	0.5597	-12.29	0.6783	6.30	0.6926	8.52
0.7	0.5245	0.5288	0.81	0.4612	-12.07	0.5575	6.27	0.5696	8.58
0.8	0.4185	0.4212	0.65	0.3692	-11.79	0.4447	6.27	0.4548	8.68
0.9	0.3247	0.3263	0.52	0.2875	-11.45	0.3451	6.28	0.3532	8.79
1.0	0.2455	0.2465	0.41	0.2183	-11.07	0.2609	6.27	0.2674	8.90
1.1	0.1815	0.1821	0.32	0.1621	-10.66	0.1928	6.22	0.1978	8.98
1.2	0.1315	0.1318	0.26	0.1180	-10.24	0.1395	6.10	0.1433	9.00
1.3	0.0936	0.0938	0.20	0.0844	-9.82	0.0992	5.90	0.1020	8.93
1.4	0.0657	0.0658	0.16	0.0595	-9.40	0.0694	5.58	0.0715	8.76
1.5	0.0455	0.0456	0.13	0.0414	-9.00	0.0479	5.16	0.0494	8.48

The error computed according to the "worst case" approach, $B_{WC,exact}$ (eq. 4.5), is below 2% and always positive. The errors computed by the application of the simplified formula in the "worst case" estimate calculation (eqs. 4.7), $B_{WC,simp1}$ and $B_{WC\ simp2}$, are fairly small (maximum ~6.5% for the 1st level of approximation and maximum ~9% for the 2nd level of approximation) and always positive. The errors computed by the approximate formula of the literature in the "worst case" estimate calculation, $B_{WC,lit}$ (eq. 4.6), arrive at ~-13% being always negative.

<u>Fourth Case</u>: same overall arrangement as in the third case, apart that the central cable, with the larger cross-section, is situated 0.5 m higher than the other two (H_2=1.5 m), thus the field points lie on a straight horizontal line whose vertical distance from the central cable is 1.5 m, while their vertical distance from the other two cables is still 1.0 m (see Fig. 4.13). Figure 4.14 and Table 4.7 show the results of the fourth case simulation.

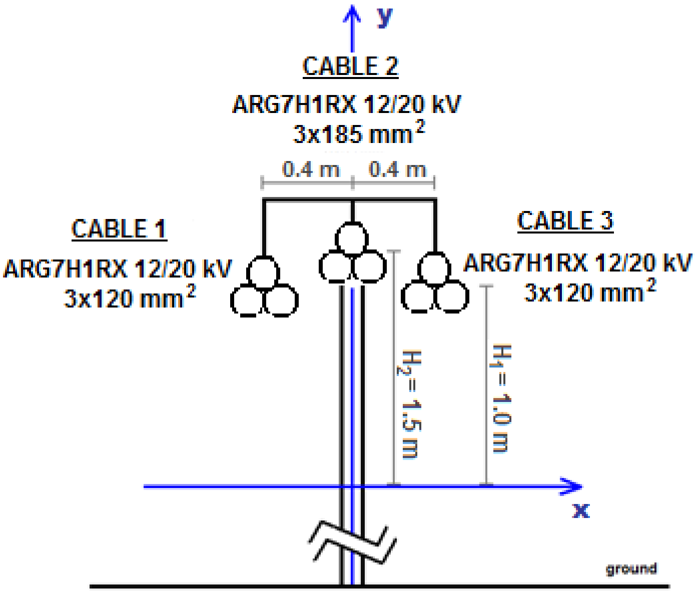

Figure 4.13: *Geometrical and electrical data concerning the fourth case-study.*

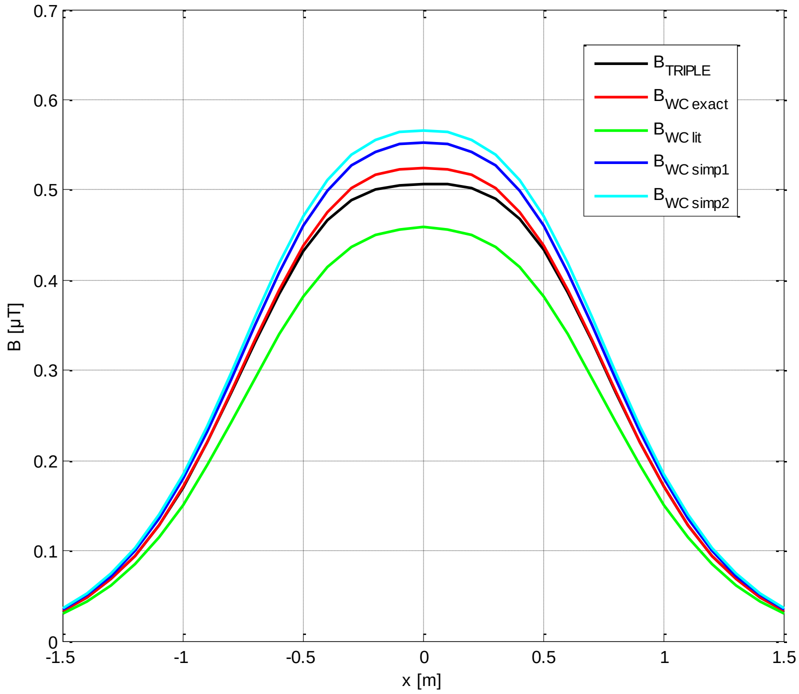

Figure 4.14: *B_{TRIPLE}, $B_{WC,exact}$, $B_{WC,lit}$, $B_{WC,simp1}$, $B_{WC,simp2}$ vs. distance x for the fourth case-study (I_1=I_3=280 A and I_2=360 A).*

Table 4.7: *Numerical values of B_{TRIPLE}, $B_{WC,exact}$, $B_{WC,lit}$, $B_{WC,simp1}$, $B_{WC,simp2}$ vs. distance x and percent errors of $B_{WC,exact}$, $B_{WC,lit}$, $B_{WC,simp1}$ and $B_{WC,simp2}$ with respect to B_{TRIPLE} for the fourth case-study ($I_1=I_3=280$ A and $I_2=360$ A).*

x [m]	**B_{TRIPLE} [μT]**	**$B_{WC,exact}$ [μT]**	**error [%]**	**$B_{WC,lit}$ [μT]**	**error [%]**	**$B_{WC,simp1}$ [μT]**	**error [%]**	**$B_{WC,simp2}$ [μT]**	**error [%]**
-1.5	0.0338	0.0338	0.08	0.0307	-9.09	0.0355	5.13	0.0367	8.73
-1.4	0.0484	0.0484	0.10	0.0438	-9.51	0.0510	5.48	0.0527	8.92
-1.3	0.0682	0.0683	0.12	0.0615	-9.95	0.0721	5.71	0.0744	8.99
-1.2	0.0946	0.0948	0.16	0.0848	-10.39	0.1001	5.83	0.1031	8.97
-1.1	0.1285	0.1288	0.22	0.1146	-10.82	0.1360	5.86	0.1399	8.87
-1.0	0.1704	0.1709	0.30	0.1513	-11.22	0.1803	5.84	0.1852	8.72
-0.9	0.2197	0.2206	0.41	0.1943	-11.56	0.2325	5.81	0.2386	8.58
-0.8	0.2746	0.2762	0.57	0.2422	-11.81	0.2906	5.80	0.2979	8.48
-0.7	0.3315	0.3342	0.80	0.2919	-11.94	0.3510	5.88	0.3597	8.49
-0.6	0.3856	0.3899	1.10	0.3397	-11.90	0.4091	6.09	0.4190	8.65
-0.5	0.4318	0.4384	1.52	0.3815	-11.66	0.4598	6.48	0.4708	9.02
-0.4	0.4666	0.4760	2.03	0.4142	-11.22	0.4995	7.06	0.5114	9.60
-0.3	0.4887	0.5015	2.62	0.4368	-10.63	0.5267	7.77	0.5393	10.34
-0.2	0.5002	0.5161	3.18	0.4501	-10.01	0.5427	8.49	0.5557	11.10
-0.1	0.5049	0.5229	3.56	0.4566	-9.56	0.5504	9.00	0.5636	11.63
-0.0	0.5063	0.5247	3.63	0.4585	-9.45	0.5525	9.12	0.5659	11.76
0.1	0.5059	0.5229	3.34	0.4566	-9.75	0.5504	8.78	0.5636	11.40
0.2	0.5020	0.5161	2.80	0.4501	-10.34	0.5427	8.10	0.5557	10.69
0.3	0.4908	0.5015	2.17	0.4368	-11.01	0.5267	7.31	0.5393	9.87
0.4	0.4686	0.4760	1.59	0.4142	-11.60	0.4995	6.60	0.5114	9.13
0.5	0.4335	0.4384	1.12	0.3815	-12.01	0.4598	6.07	0.4708	8.60
0.6	0.3869	0.3899	0.77	0.3397	-12.19	0.4091	5.74	0.4190	8.30
0.7	0.3324	0.3342	0.53	0.2919	-12.18	0.3510	5.60	0.3597	8.20
0.8	0.2752	0.2762	0.36	0.2422	-12.00	0.2906	5.58	0.2979	8.26
0.9	0.2201	0.2206	0.25	0.1943	-11.70	0.2325	5.64	0.2386	8.41
1.0	0.1706	0.1709	0.18	0.1513	-11.32	0.1803	5.72	0.1852	8.60
1.1	0.1286	0.1288	0.13	0.1146	-10.89	0.1360	5.77	0.1399	8.77
1.2	0.0947	0.0948	0.10	0.0848	-10.44	0.1001	5.76	0.1031	8.90
1.3	0.0683	0.0683	0.08	0.0615	-9.99	0.0721	5.66	0.0744	8.95
1.4	0.0484	0.0484	0.07	0.0438	-9.54	0.0510	5.45	0.0527	8.89
1.5	0.0338	0.0338	0.06	0.0307	-9.11	0.0355	5.12	0.0367	8.71

The error computed according to the “worst case” approach, $B_{WC,exact}$ (eq. 4.5), is below 3.5% and always positive. The errors computed by the application of the simplified formula in the “worst case” estimate calculation (eqs. 4.7), $B_{WC,simp1}$ and $B_{WC\ simp2}$, are fairly small (maximum ~9% for the 1st level of approximation and maximum ~12% for the 2nd level of approximation) and always positive. The errors computed by the approximate formula of the literature in the “worst case” estimate calculation, $B_{WC,lit}$ (eq. 4.6), arrive at ~-12% being always negative.

4.3 CONCLUSIONS

Theexact calculation of the magnetic field generated by multiple-circuit twisted three-phase power cable lines that are the standard lines for transporting renewable energy has been calculated as a generalization of the vector theory brought about in Chapter 3 concerning a double-circuit twisted three-phase power cable lines. In the framework of the‘worst-case’ approach, the analysis has also extended to multiple-circuit twisted three-phase cables both the exact and approximated formula derived from the literature about single-circuits and the simple innovative formula developed in both levels of approximation.

As shown by the simulations regarding a triple-circuit twisted three-phase cable lines, underground and overhead, the error computed by the ‘worst case’ estimate is fairly small making the relevant expression (eq. 4.5) an efficient alternative way of calculating the magnetic field. The use of the innovative simplified formula (eqs. 4.7) in the ‘worst case’ approach further simplifies the field calculation with an inevitable positive error of maximum ~9% for the first and ~12% for the second level of approximation. On the other hand, the error computed by the use of the approximated formula of the literature in the ‘worst case’ approach, (eq. 4.6), is always higher in absolute terms and negative, underestimating the field. It is thus confirmed once more that the innovative formula results definitely much simpler than the exact one and provides a much smaller relative error compared to the approximated one from the literature and it can be used for the calculus of the magnetic field from multiple twisted field sources without problems of accuracy.

Concluding, expressions (4.7) result an efficient alternative way of calculating the magnetic field of a multiple-circuit twisted three-phase cable lines. This is due to its advantages which lie on its simplicity – an algebraic sum of the rms values of the total field B generated by each twisted cable, calculated without using sophisticated mathematics – and on its reliability – the maximum error presented is below 12% for both levels of approximation and positive providing a conservative estimation of the magnetic field. Unfortunately, experimental validation by measurements in situ of the above used formulas for multiple-circuit twisted three-phase cable lines was not effectuated due to the extreme difficulty of finding easily accessible multiple-circuit twisted cable lines with known instant values of rms line currents.

CHAPTER 5

DEVELOPMENT OF NUMERICAL CODES FOR THE CALCULATION OF THE MAGNETIC FIELD GENERATED BY OVERHEAD LINES

5.1 MAGNETIC FIELD CALCULUS

The magnetic field generated by an electrical current is given by the Biot–Savart law that relates the magnetic field to the magnitude, direction, length, and proximity of the electric current. The Biot–Savart law is used to compute the resultant magnetic field *B* at position *r* generated by a current *i(t)* (see Fig. 5.1).

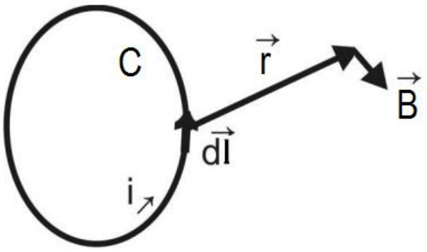

Figure 5.1: *Representation of a filamentary conductor in close path C carrying current i(t).*

The law is a physical example of a line integrale valuated over the path *C* where the electric currents flow:

$$\vec{B}(t) = \frac{\mu_0}{4\pi} i(t) \int_c \frac{d\vec{l} \times \vec{r}}{|\vec{r}|^2} \tag{5.1}$$

In case of a straight current-carrying wire of finite length AB (see Fig. 5.2) the Biot-Savart law (eq. 5.1) becomes:

$$\Delta\vec{B}(t) = \frac{\mu_0}{2\pi R} i(t) \frac{\cos\alpha + \cos\beta}{2} \vec{u}_n \tag{5.2}$$

where R is the distance between the field-point P and the finite length segment AB, α and β are the angles indicated in Fig. 5.2, and $\vec{u}_n$ is a vector orthogonal to the plane determined by points A, B and P with the direction of the vector product $d\vec{l} \times \vec{r}$.

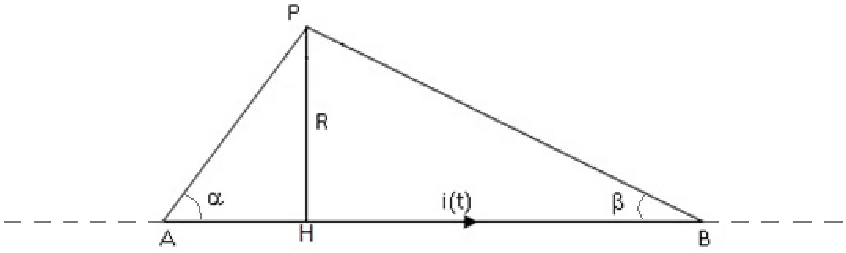

Figure 5.2: *Representation of a filamentary conductor segment AB carrying current i(t).*

One can notice that by increasing the length of the segment AB the term $\frac{\cos\alpha+\cos\beta}{2}$ tends to 1, and so the classic formula of Biot-Savart for filamentary, straight, infinitely long wires derives:

$$\vec{\mathrm{B}}(t)_\infty = \frac{\mu_0}{2\pi r}\cdot i(t)\cdot \vec{u}_n \tag{5.3}$$

5.2 2D MAGNETIC FIELD CALCULATION CODE

5.2.1 Theory

As far as an overhead or underground power line with *n* conductors is concerned, making the following assumptions and simplifications:

- the algorithm considers all conductors constituting the line to be straight, horizontal, of infinite length and parallel to each other;
- the currents on each conductor are considered to be in-phase;
- the soil is considered flat and free of irregularities -perfectly transparent from the magnetic point of view;
- the presence of towers, utility poles, buildings, vegetation and any other object is in the area concerned is neglected.

the calculation of the magnetic field is reduced into a simple plane problem, easily implemented into a software tool, since the situation is exactly the same on every section of the line, meaning the vertical plane orthogonal to the longitudinal axis of the line (i.e. the direction of the conductors that constitute it) that passes through the field-point of interest. In this case, the magnetic field components are given by the following formulas, as also defined by the Italian law [48]:

$$B_x(t) = \frac{\mu_0}{2\pi}\sum_n i_n(t)\left[\frac{(y_n - y_p)}{(x_p - x_n)^2 + (y_p - y_n)^2}\right] \tag{5.4.a}$$

$$B_y(t) = \frac{\mu_0}{2\pi}\sum_n i_n(t)\left[\frac{(x_p - x_n)}{(x_p - x_n)^2 + (y_p - y_n)^2}\right] \tag{5.4.b}$$

In order to fully characterize the given power line from both a geometric and an electric point of view, a set of input data is required that includes the number of conductors that constitute the power line, n, the position of the conductors given in Cartesian coordinates (x_1, y_1), (x_2, y_2), (x_3, y_3), …, (x_n, y_n), the coordinates of the field-points of interest, (x_p, y_p), the rms currents that flow in these conductors, I_1, I_2, I_3, …, I_n, and the electrical phase of the currents,φ_1, φ_2, φ_3, ..., φ_n. The field-points lay on the x-axis that is situated at a distance H from the ground (see Fig. 5.3).

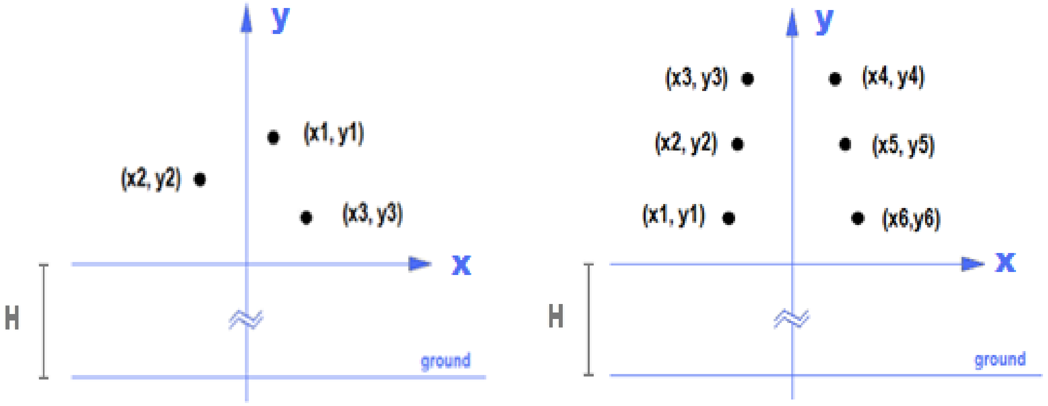

(a) **(b)**

Figure 5.3:_Vertical section (x, y plane) of a **(a)** single- and a**(b)** double-circuit three-phase overhead line._

One can notice that expressions (5.4) use the instantaneous values of the currents $i(t)$. In the case of currents that vary sinusoidally with time it is possible, and preferable, to use the phasors (complex numbers) of the currents, providing thus the phasors of the magnetic induction components. Programming in MatLab™ environment consents the direct treatment of complex numbers and eqs. (5.4) were implemented using the currents phasors. So, after having calculated the magnetic field components phasors, the program provides their rms values to be subsequently used for the composistion of the total bi-dimensional magnetic field from the equation:

$$B = \sqrt{B_x^2 + B_y^2} \tag{5.5}$$

5.2.2 Applications – Simulation Results

5.2.2.1 132 kV Single-Circuit Three-Phase Overhead Line

Figures 5.4 show the geometrical characteristics of the 132 kV single-circuit three-phase overhead line used for the simulations, along with the vertical section under exam, corresponding at the mid-span between two adjacent poles.

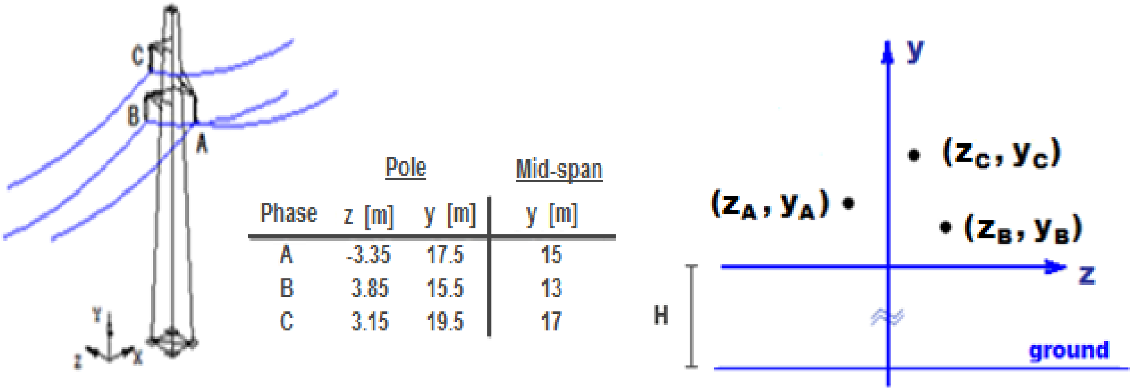

	Pole		Mid-span
Phase	z [m]	y [m]	y [m]
A	-3.35	17.5	15
B	3.85	15.5	13
C	3.15	19.5	17

(a) **(b)**

Figure 5.4: *132 kV single-circuit three-phase overhead line:*
(a) *geometrical characteristics and* ***(b)*** *vertical mid-span section (z-y plane).*

The profiles of the field components B_z and B_y along with the total magnetic field B were calculated for I = 385 A and $z \in$[-50 m; 50 m] at different heights H from the ground and the results are depicted in Figs. 5.5 - 5.8.

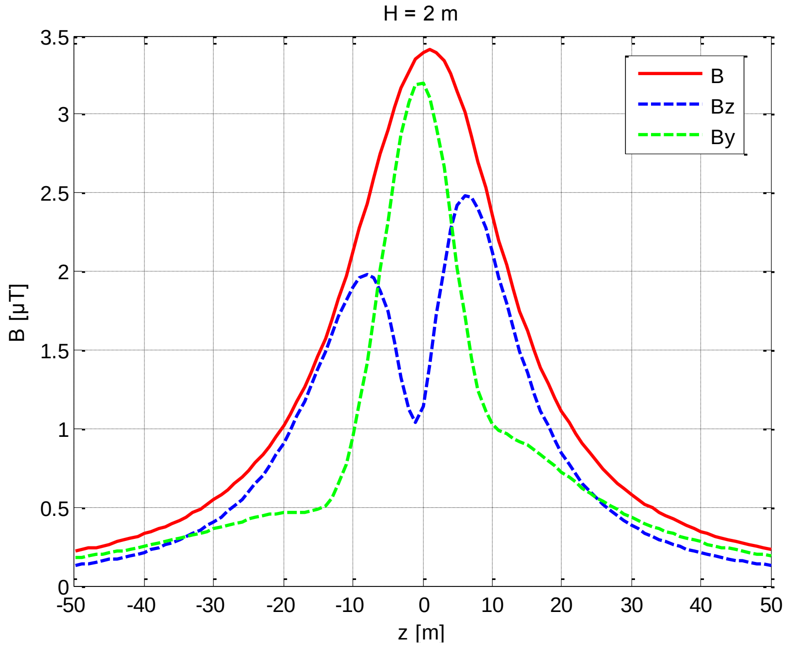

Figure 5.5: *B_z, B_y, B vs. z at 2 m from the ground calculated at the mid-span section of the 132 kV single-circuit overhead line with I = 385 A.*

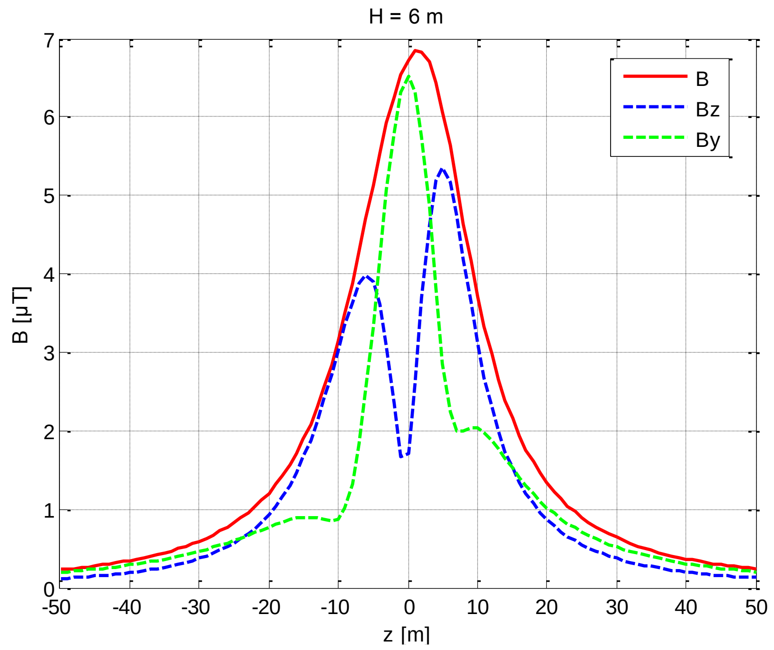

Figure 5.6: *B_z, B_y, B vs. z at 6 m from the ground calculated at the mid-span section of the 132 kV single-circuit overhead line with I = 385 A.*

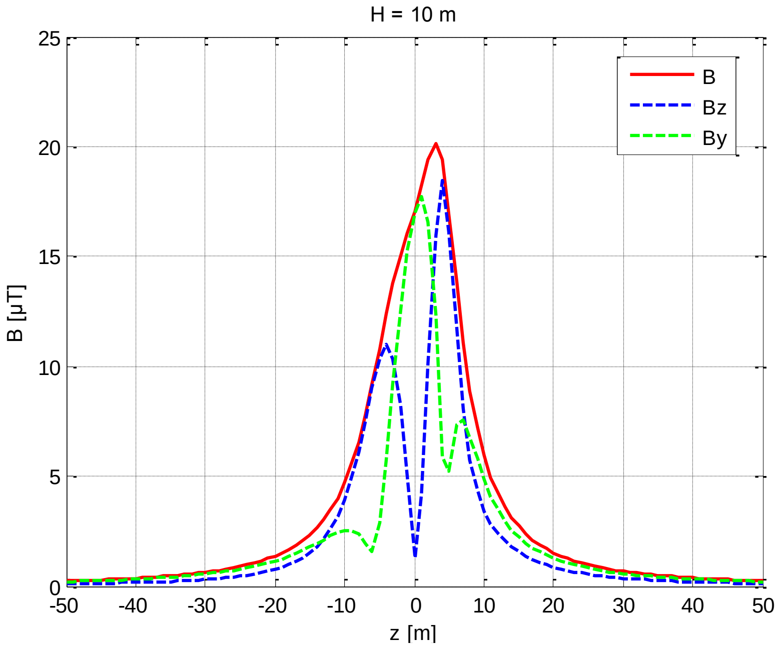

Figure 5.7: *B_z, B_y, B vs. z at 10 m from the ground calculated at the mid-span section of the 132 kV single-circuit overhead line with I = 385 A.*

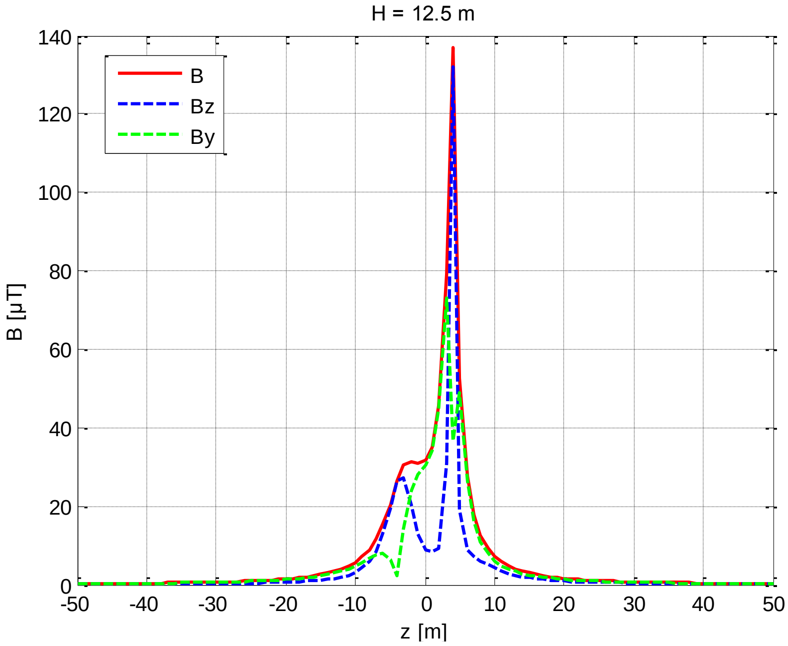

Figure 5.8: *B_z, B_y, B vs. z at 12.5 m from the ground calculated at the mid-span section of the 132 kV single-circuit overhead line with I = 385 A.*

5.2.2.2 380 kV Double-Circuit Three-Phase Overhead Line

Figures 5.9 show the geometrical characteristics of a typical Italian 380 kV double-circuit three-phase overhead line used for the simulations, along with the vertical section under exam, corresponding at the mid-span between two adjacent poles. The simulation has been made considering the reverse arrangement of the conductors phases with $I_1 = I_2$ = 2040 A, i.e. the winter season ampacity for Italy, zone B, according to [49].

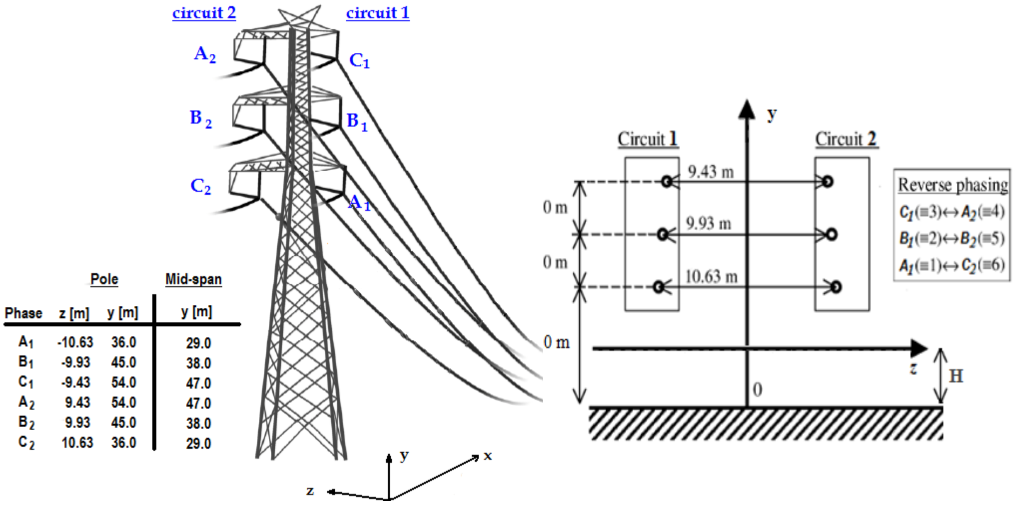

	Pole		Mid-span
Phase	z [m]	y [m]	y [m]
A_1	-10.63	36.0	29.0
B_1	-9.93	45.0	38.0
C_1	-9.43	54.0	47.0
A_2	9.43	54.0	47.0
B_2	9.93	45.0	38.0
C_2	10.63	36.0	29.0

(a)

(b)

Figure 5.9: *380 kV double-circuit three-phase overhead line:*
(a) *geometrical characteristics and* ***(b)*** *vertical mid-span section (not in scale).*

The profiles of the field components B_z and B_y along with the total magnetic field B were calculated for I_1=I_2=2040 A and $z\in$[-100 m; 100 m] at different heights H from the ground and the results are depicted in Figs. 5.10 - 5.13.

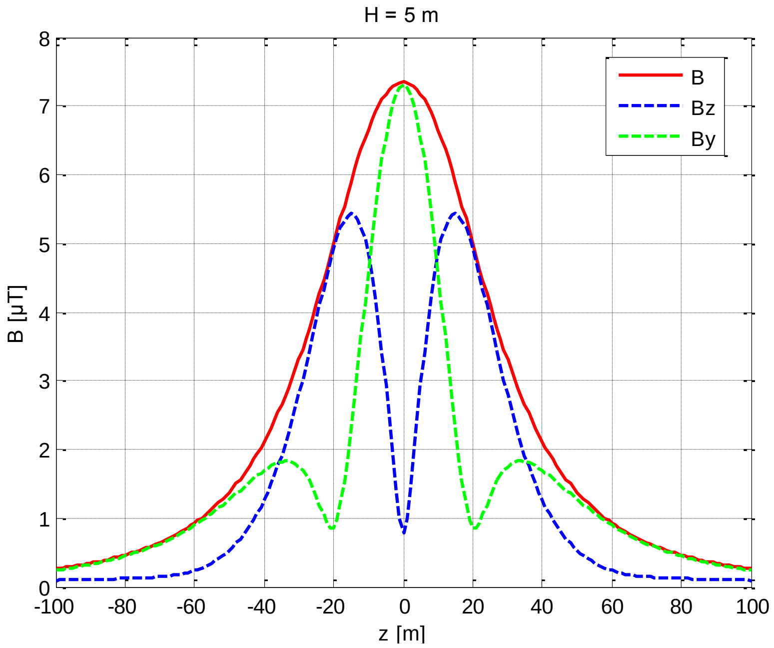

Figure 5.10: *B_z, B_y, B vs. z at 5 m from the ground calculated at the mid-span section of the 380 kV double-circuit overhead line with I_1= I_2= 2040 A.*

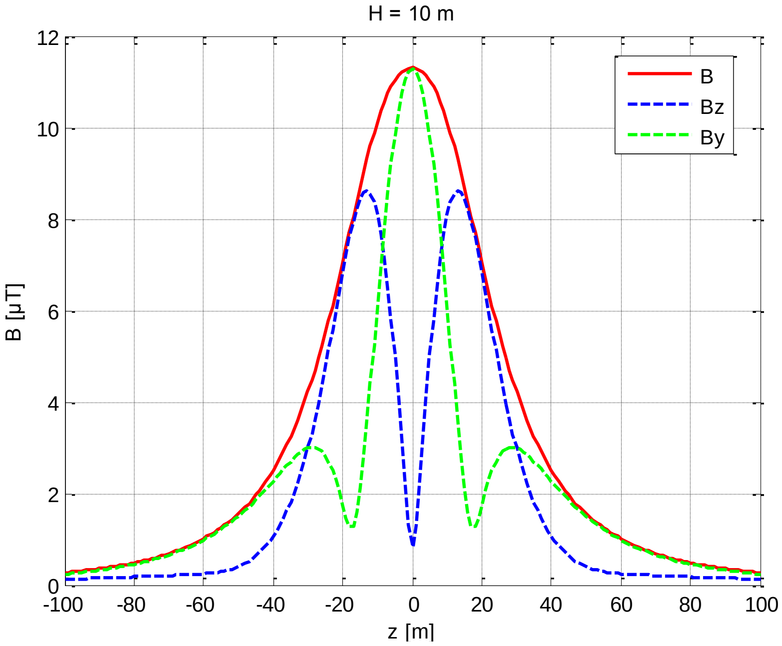

Figure 5.11: *B_z, B_y, B vs. z at 10 m from the ground calculated at the mid-span section of the 380 kV double-circuit overhead line with I_1= I_2= 2040 A.*

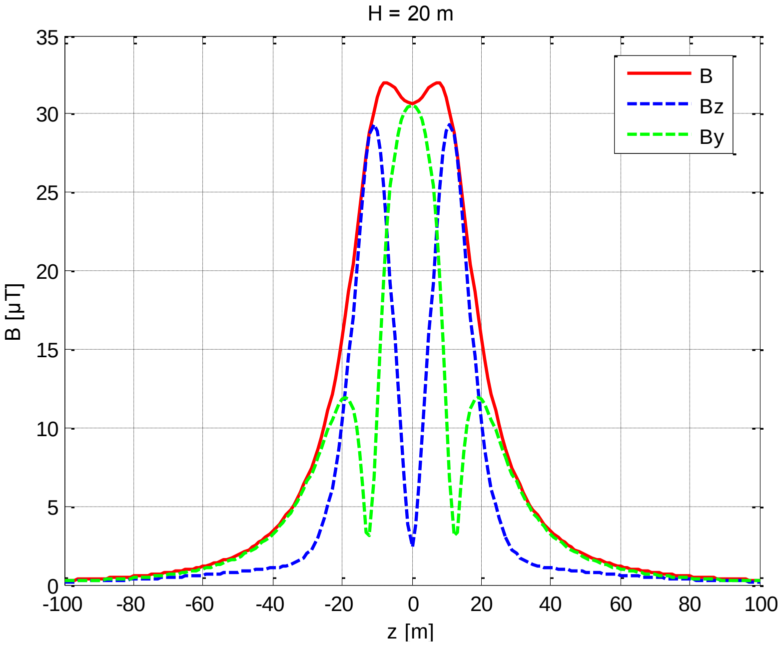

Figure 5.12: *B_z, B_y, B vs. z at 20 m from the ground calculated at the mid-span section of the 380 kV double-circuit overhead power with $I_1 = I_2 = 2040$ A.*

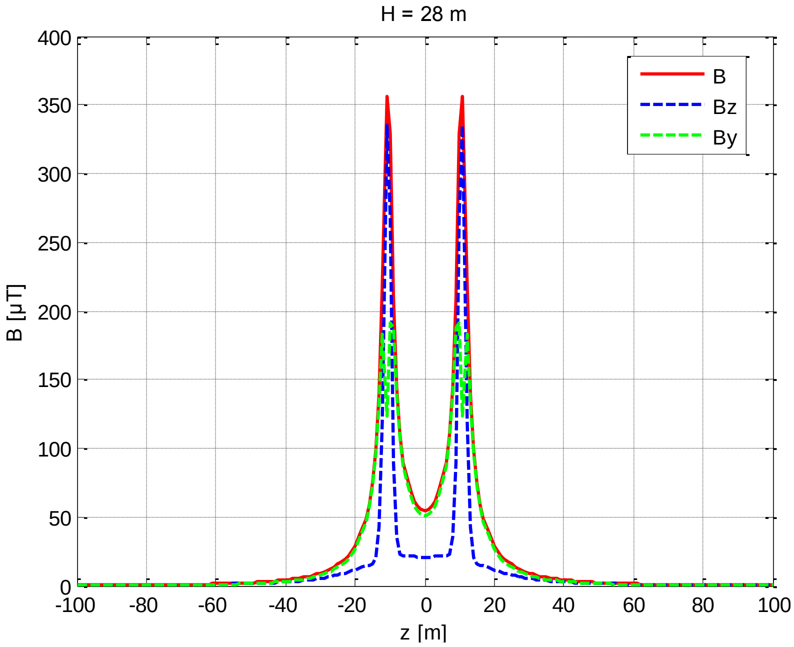

Figure 5.13: *B_z, B_y, B vs. z at 28 m from the ground calculated at the mid-span section of the 380 kV double-circuit overhead line with $I_1 = I_2 = 2040$ A.*

5.3 3D MAGNETIC FIELD CALCULATION CODE

5.3.1 Theory

The exact calculation of the magnetic field generated by real catenary-form overhead lines has been treated in [34] - [50] and, in particular, the Italian law [48] defines two methods of calculating the total tridimensional magnetic field generated by *n* conductors, considering that the each conductor is divided in infinite straight segments carrying current *i(t)*. Doing so, it is possible to reconstruct the catenary form of the conductor line by simulating it with a sequence of a large number of straight segments. Calculating the contribution of each segment and performing the summation over the entire conductor line and repeating this procedure for every conductor present in the power line, the three magnetic field components, B_x, B_y, B_z, at the given field point will be also calculated.

<u>Method 1</u>

- Determination of the direction parameters (a, b, c) of the line that passes from points A (x_A, y_A, z_A) and B (x_B, y_B, z_B) (see Fig. 5.2):

$$a = x_B - x_A \tag{5.6.a}$$

$$b = y_B - y_A \tag{5.6.b}$$

$$c = z_B - z_A \tag{5.6.c}$$

- Determination of the coefficients (a_1, b_1, c_1, d_1) of the plane equation that passes from point P (x_P, y_P, z_P) and is orthogonal to the line (see Fig. 5.2):

$$a_1 = a \tag{5.7.a}$$

$$b_1 = b \tag{5.7.b}$$

$$c_1 = c \tag{5.7.c}$$

$$d_1 = -\left(a \cdot x_P + b \cdot y_P + c \cdot z_P\right) \tag{5.8}$$

- Determination of the intersection point H (x_H, y_H, z_H) of the orthogonal plane with the line (see Fig. 5.2):

$$x_H = x_A + a \cdot t \tag{5.9.a}$$

$$y_H = y_A + b \cdot t \tag{5.9.b}$$

$$z_H = z_A + c \cdot t \tag{5.9.c}$$

with
$$t=-\frac{a_1\cdot x_A+b_1\cdot y_A+c_1\cdot z_A+d_1}{a\cdot a_1+b\cdot b_1+c\cdot c_1} \tag{5.10}$$

- Determination of the segment PH length L_{PH} (distance R between the line and point P) (see Fig. 5.2):

$$R=L_{PH}=\sqrt{(x_P-x_H)^2+(y_P-y_H)^2+(y_P-y_H)^2} \tag{5.11}$$

Method 2

- Determination of the segment PH length L_{PH} (distance R between the line and point P) from the rectangle PHA (see Fig. 5.2):

$$R=L_{PH}=\sqrt{{L_{PA}}^2-{L_{AH}}^2} \tag{5.12}$$

with
$$L_{PA}=\sqrt{(x_P-x_A)^2+(y_P-y_A)^2+(y_P-y_A)^2} \tag{5.13}$$

Once calculated the distance R, the magnetic field magnitude can be then valuated from the following formula:

$$\Delta B(t)=\frac{i(t)}{4\cdot\pi\cdot R}\left(\frac{(L_{AB}-L_{AH})}{L_{PB}}+\frac{L_{AH}}{L_{PA}}\right) \tag{5.14}$$

with
$$L_{PB}=\sqrt{(x_P-x_B)^2+(y_P-y_B)^2+(y_P-y_B)^2} \tag{5.15}$$

In order to calculate the total magnetic field generated by all the segments of all conductors constituting the line, it is necessary determine the three spatial components of the magnetic field by means of the following expressions:

$$\Delta B_x(t)=\Delta B(t)\cdot\frac{\cos\alpha}{\sqrt{\cos\alpha^2+\cos\beta^2+\cos\gamma^2}} \tag{5.16.a}$$

$$\Delta B_y(t)=\Delta B(t)\cdot\frac{\cos\beta}{\sqrt{\cos\alpha^2+\cos\beta^2+\cos\gamma^2}} \tag{5.16.b}$$

$$\Delta B_z(t)=\Delta B(t)\cdot\frac{\cos\gamma}{\sqrt{\cos\alpha^2+\cos\beta^2+\cos\gamma^2}} \tag{5.16.c}$$

where the direction cosines are functions of the spatial coordinates of the points A, B and P, as follows:

$$\cos\alpha = y_A \cdot z_B + z_A \cdot y_P + y_B \cdot z_P - z_B \cdot y_P - z_A \cdot y_B - y_A \cdot z_P \qquad (5.17.a)$$

$$\cos\beta = z_B \cdot x_P + z_P \cdot x_A + z_A \cdot x_B - x_A \cdot z_B - z_A \cdot x_P - x_B \cdot z_P \qquad (5.17.b)$$

$$\cos\gamma = x_A \cdot y_B + x_P \cdot y_A + x_B \cdot y_P - x_P \cdot y_B - x_B \cdot y_A - x_A \cdot y_P \qquad (5.17.c)$$

Finally, the data needed for the definition of power lines also include the parameters of the catenary formula in Cartesian coordinates:

$$y = \alpha \cdot \cosh\left(\frac{x - (L/2 - X_1)}{\alpha}\right) + (F - a) \qquad (5.18)$$

where X1 and X2 are the catenary suspension points positioned at height F and having length L (see Fig. 5.14) and a is the catenary parameter given by the following expression as a function of the sag *f*:

$$a = \frac{(L^2)}{8f} \qquad (5.19)$$

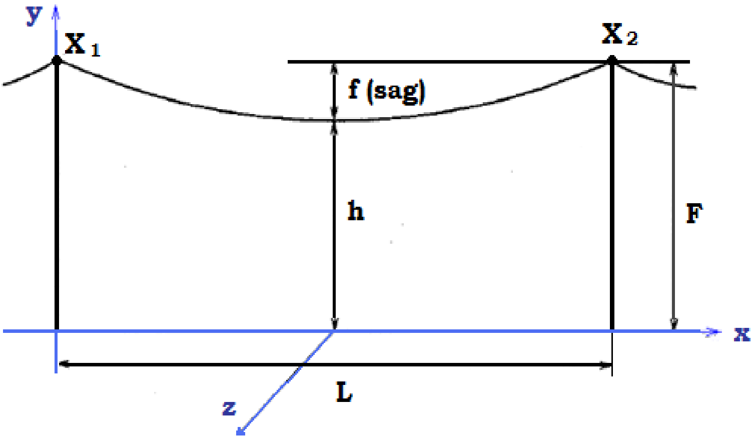

Figure 5.14: *Schematization of the catenary parameters.*

5.3.2 Applications – Simulation Results

5.3.2.1 132 kV Single-Circuit Three-Phase Overhead Line

Considering the same 132 kV single-circuit three-phase overhead line of Fig. 5.4 suspended at six poles, thus, forming five catenaries, each with length of 200 m for a total of 1000 m, the following Figs. 5.15- 5.26 were plotted as the results of the 3D simulations of the magnetic field generated by such a line carrying balanced three-phase current I = 385 A.

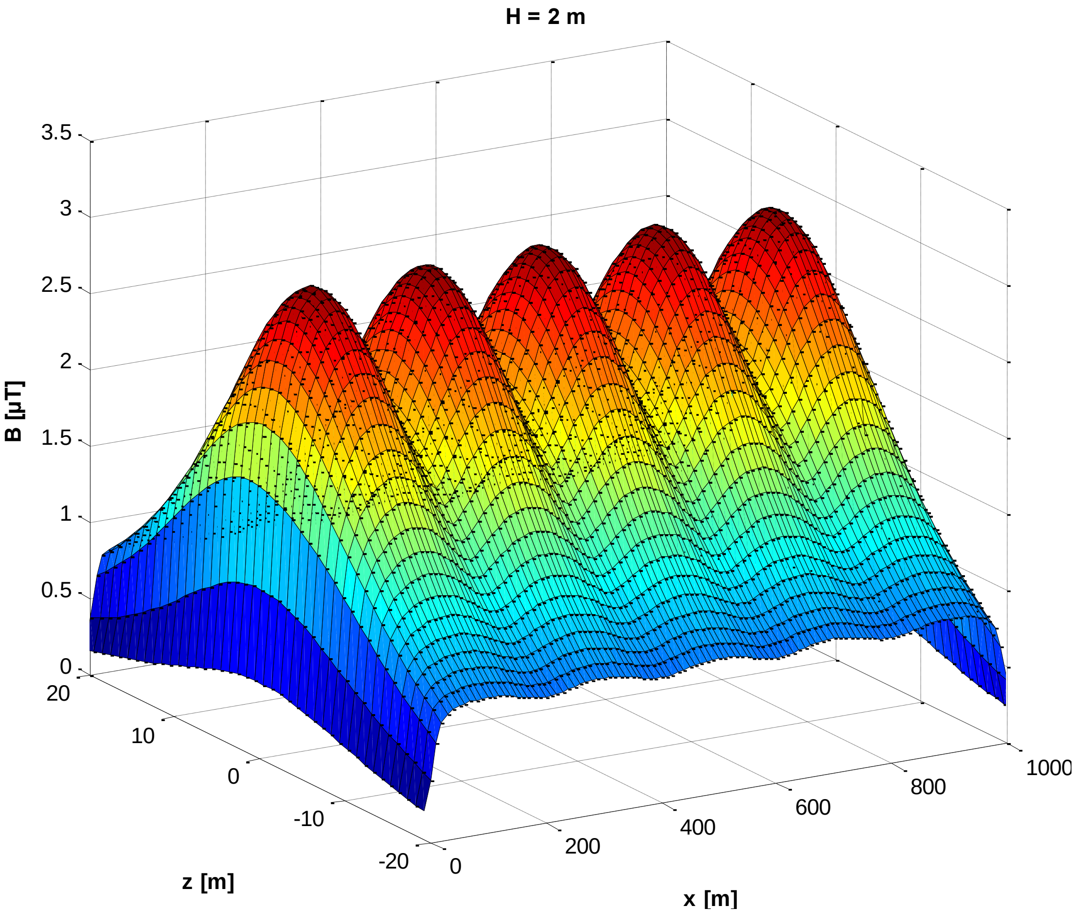

Figure 5.15: *3D plot of B vs. z and x at 2 m from the ground for the 132 kV single-circuit overhead line with I=385 A.*

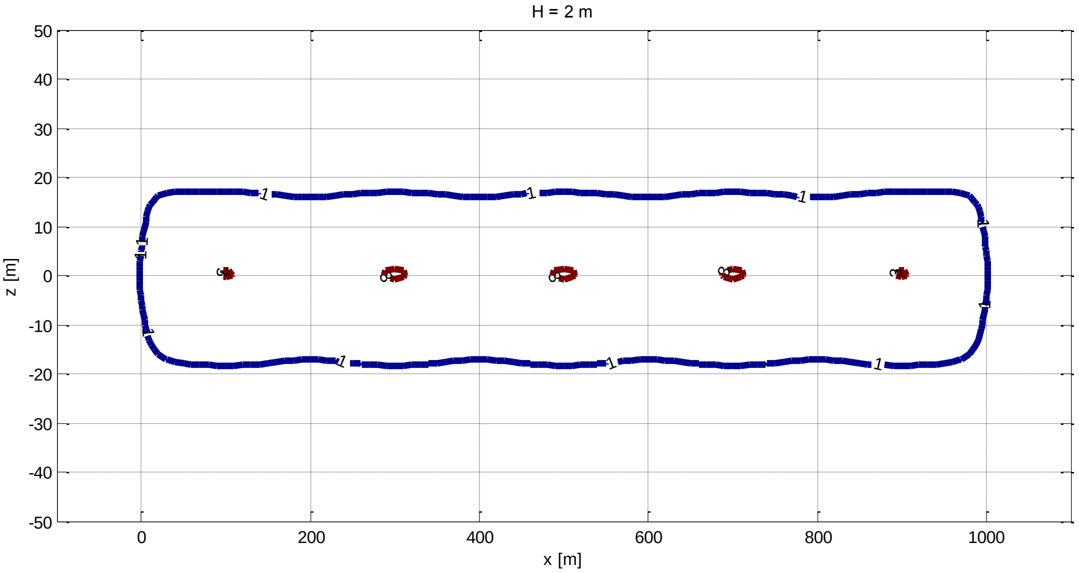

Figure 5.16: *B isolines (1 μT and 3 μT) at 2 m from the ground for the 132 kV single-circuit overhead line with I = 385 A.*

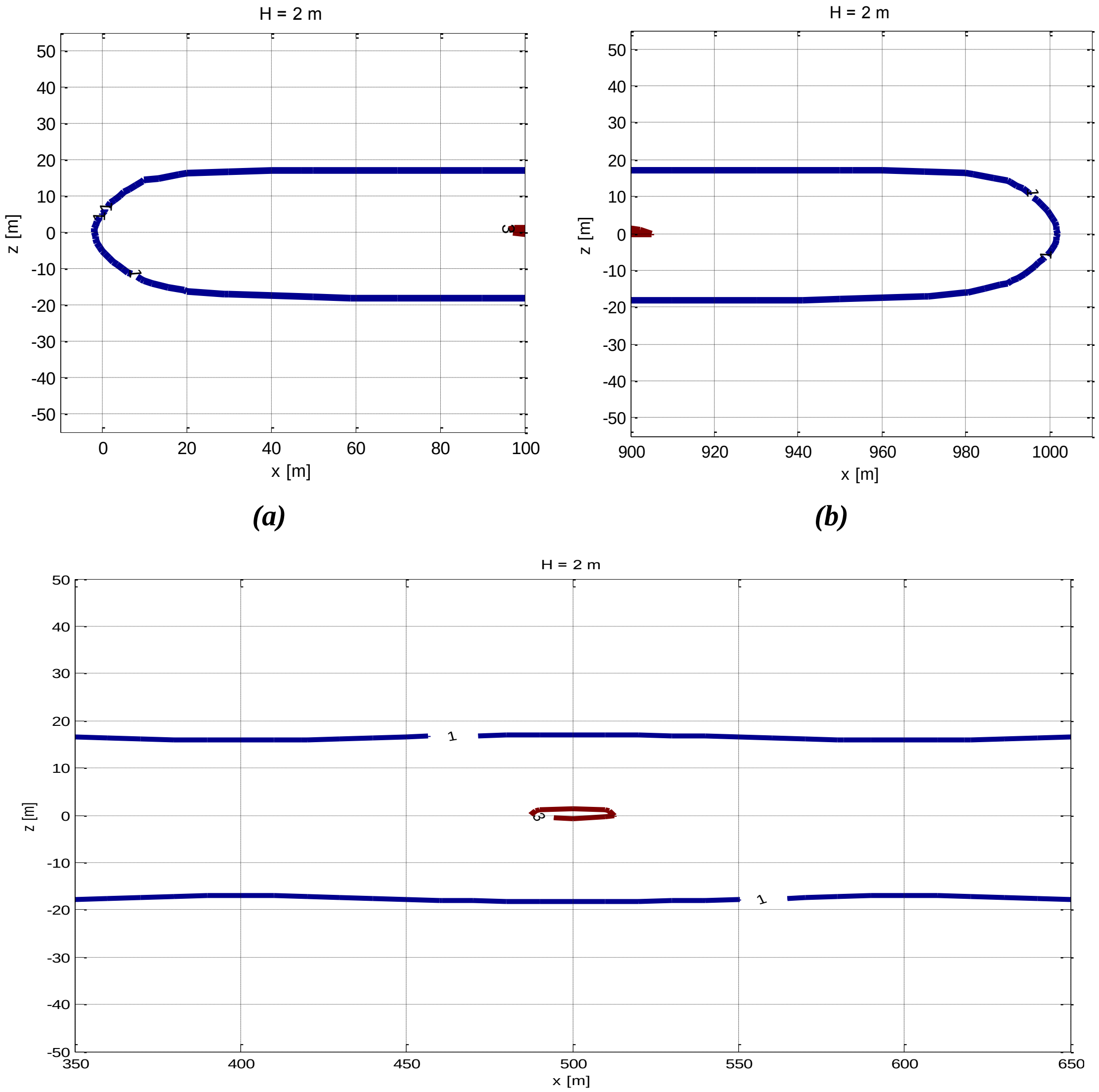

(a) *(b)*

(c)

Figure 5.17: *Details of Fig. 5.16 concerning* ***(a)*** *the beginning (in equal-scaled axes),* ***(b)*** *the end (in equal-scaled axes) and* ***(c)*** *the middle of the 132 kV single-circuit overhead lines (I = 385 A).*

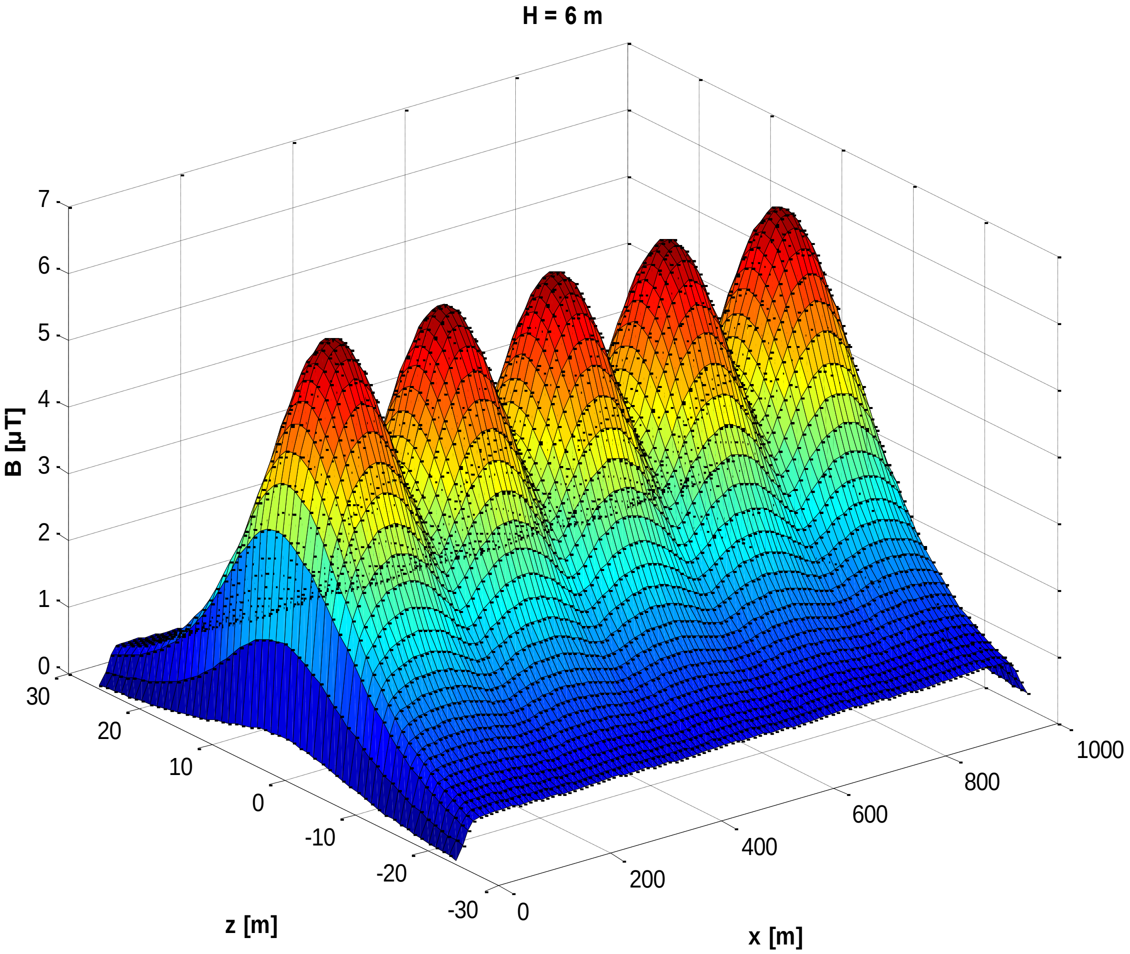

Figure 5.18: *3D plot of B vs. z and x at 6 m from the ground for the 132 kV single-circuit overhead line with I=385 A..*

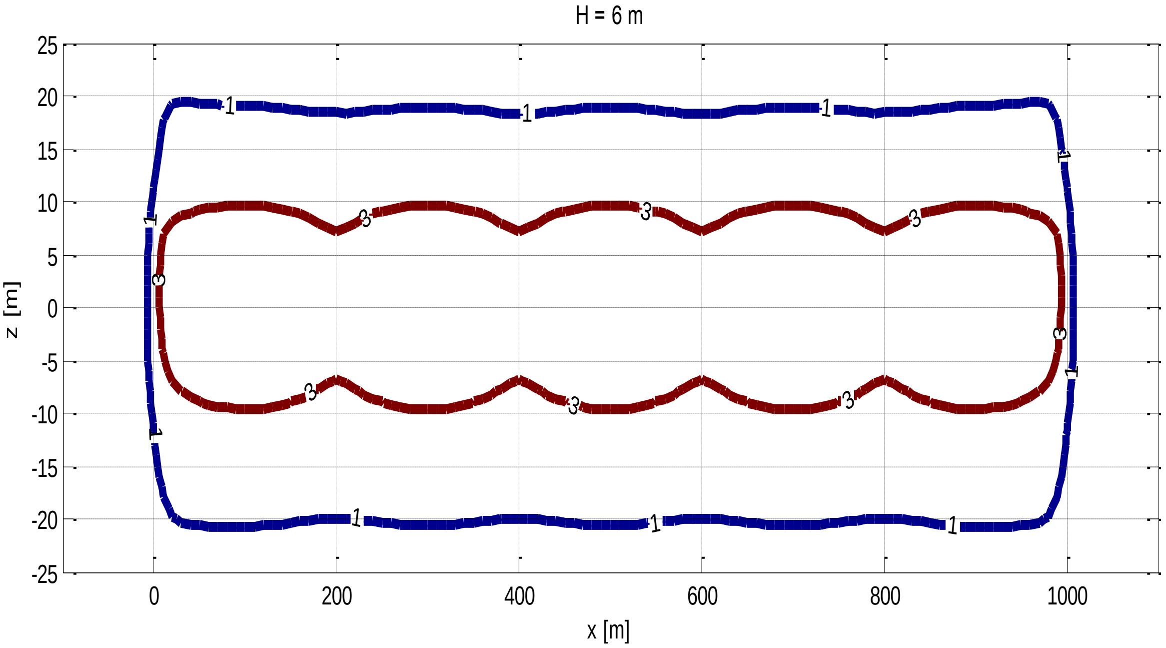

Figure 5.19: *B isolines (1 μT and 3 μT) at 6 m from the ground for the 132 kV single-circuit overhead line with I = 385 A.*

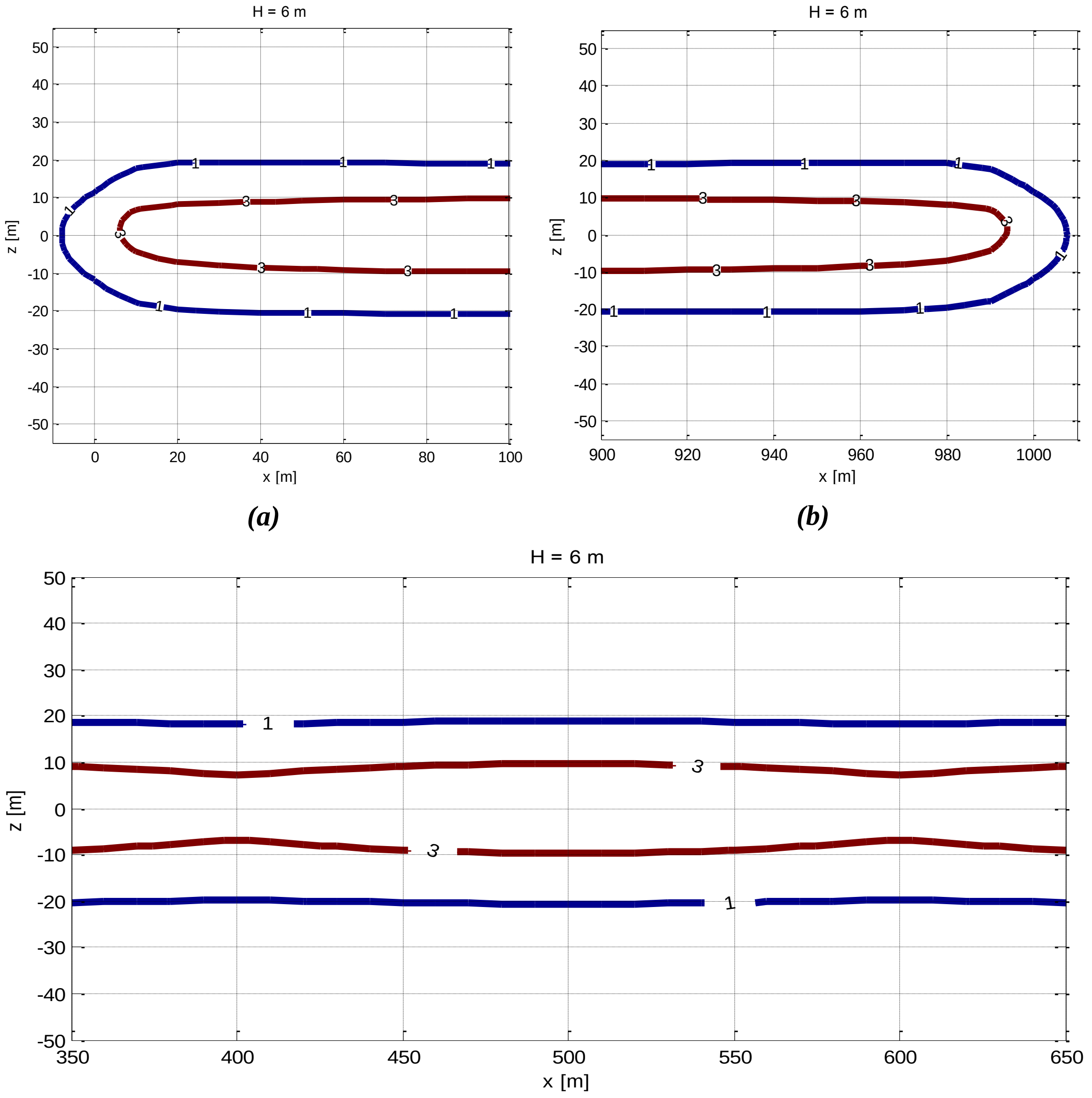

(a) *(b)* *(c)*

Figure 5.20: *Details of Fig. 5.19 concerning* ***(a)*** *the beginning (in equal-scaled axes),* ***(b)*** *the end (in equal-scaled axes) and* ***(c)*** *the middle of the 132 kV single-circuit overhead line (I = 385 A).*

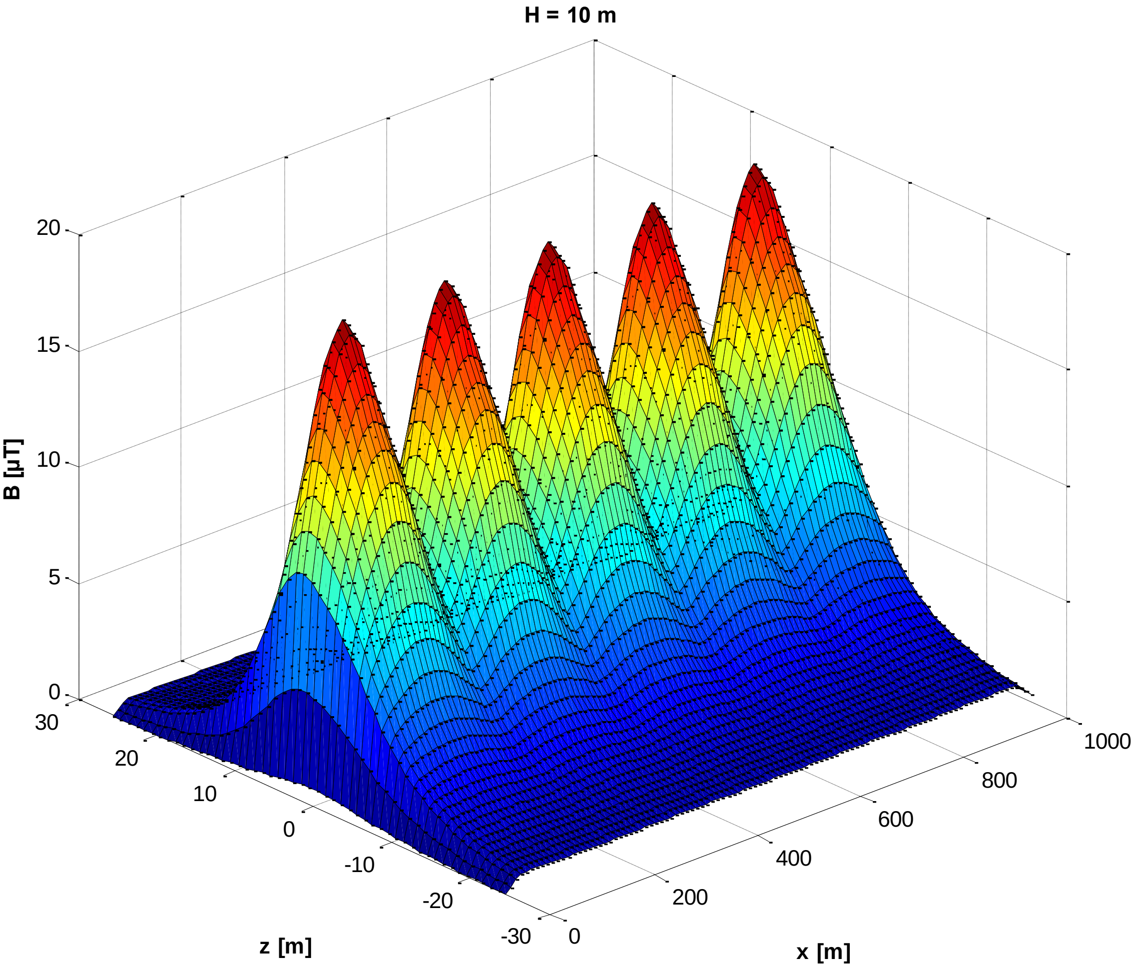

Figure 5.21: *3D plot of B vs. z and x at 10 m from the ground for the 132 kV single-circuit overhead line with I=385 A.*

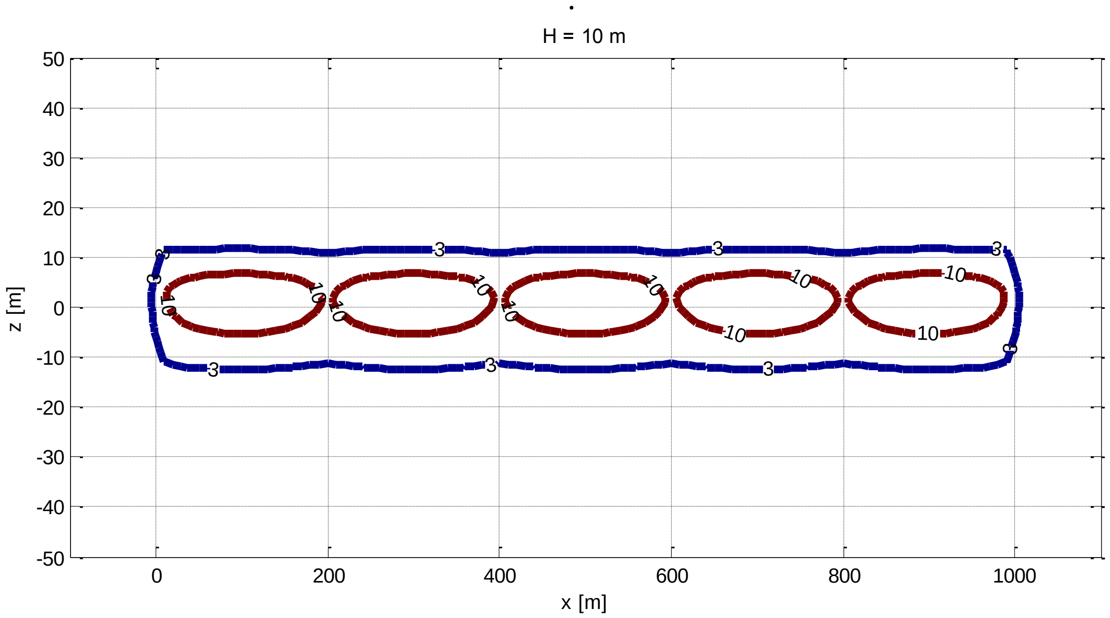

Figure 5.22: *B isolines (3µT and 10µT) at 10m from the ground for the 132 kV single-circuit overhead line with I = 385 A.*

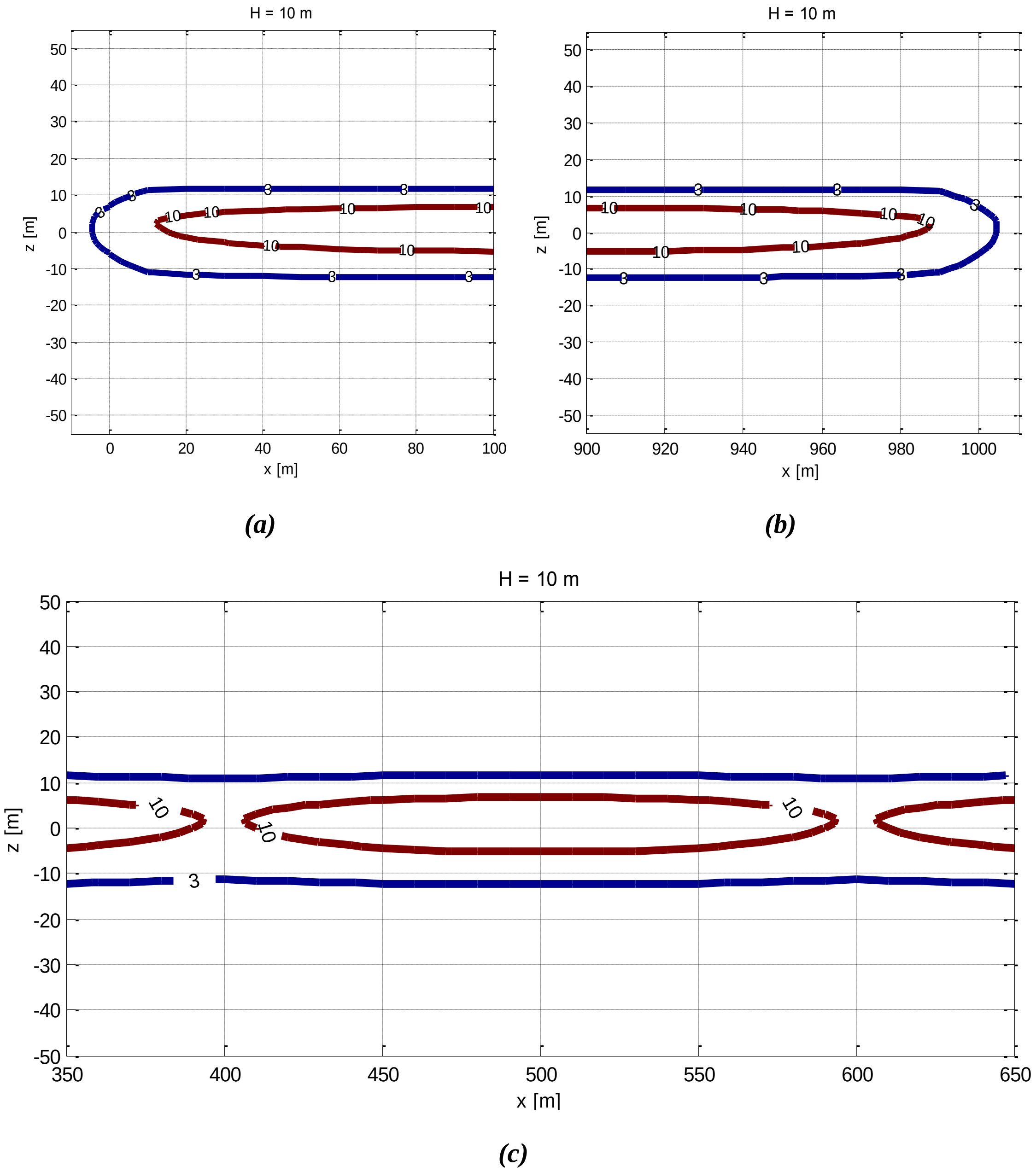

(a)

(b)

(c)

Figure 5.23: *Details of Fig. 5.22 concerning* ***(a)*** *the beginning (in equal-scaled axes),* ***(b)*** *the end (in equal-scaled axes) and* ***(b)*** *the middle of the 132 kV single-circuit overhead line (I = 385 A).*

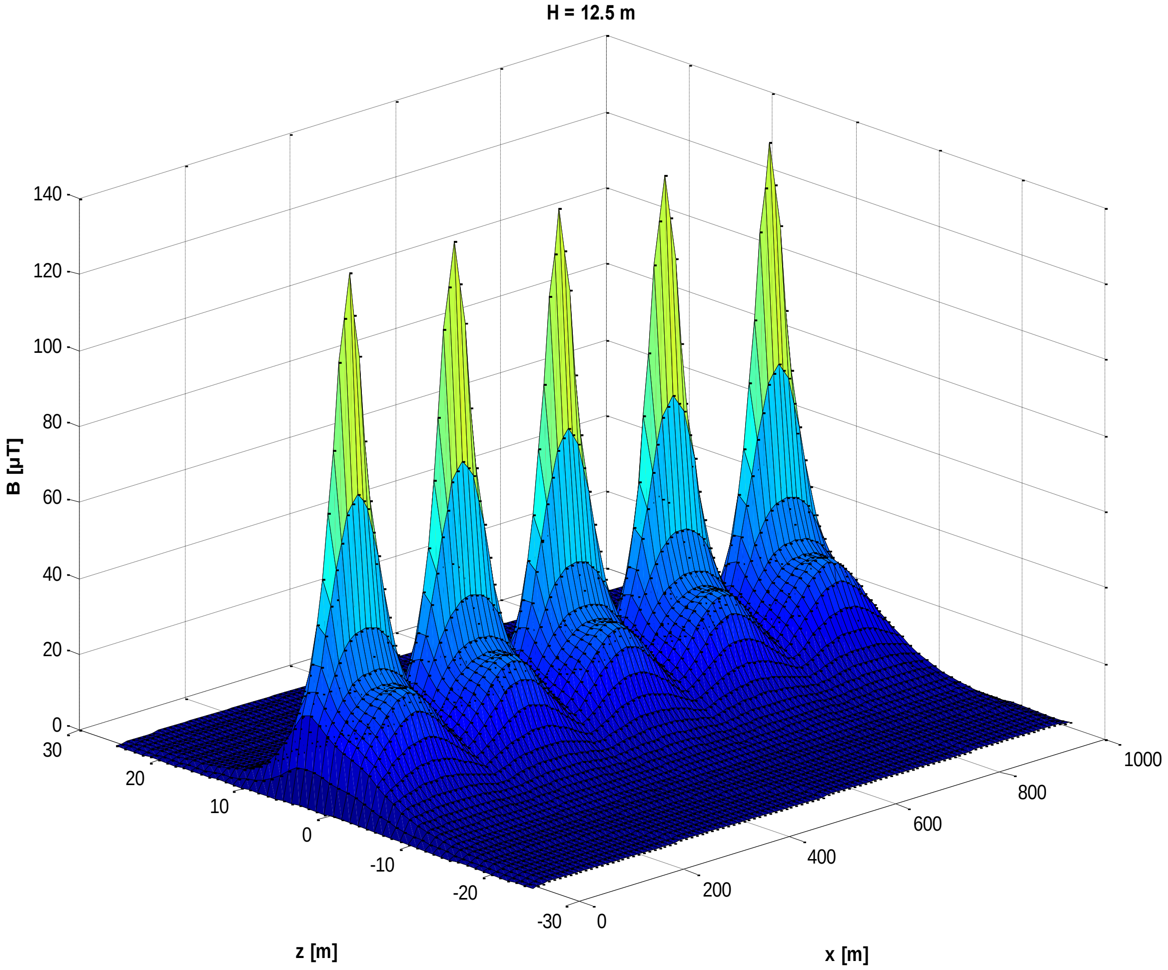

Figure 5.24: *3D plot of B vs. z and x at 12.5 m from the ground for the 132 kV single-circuit overhead line with I=385 A.*

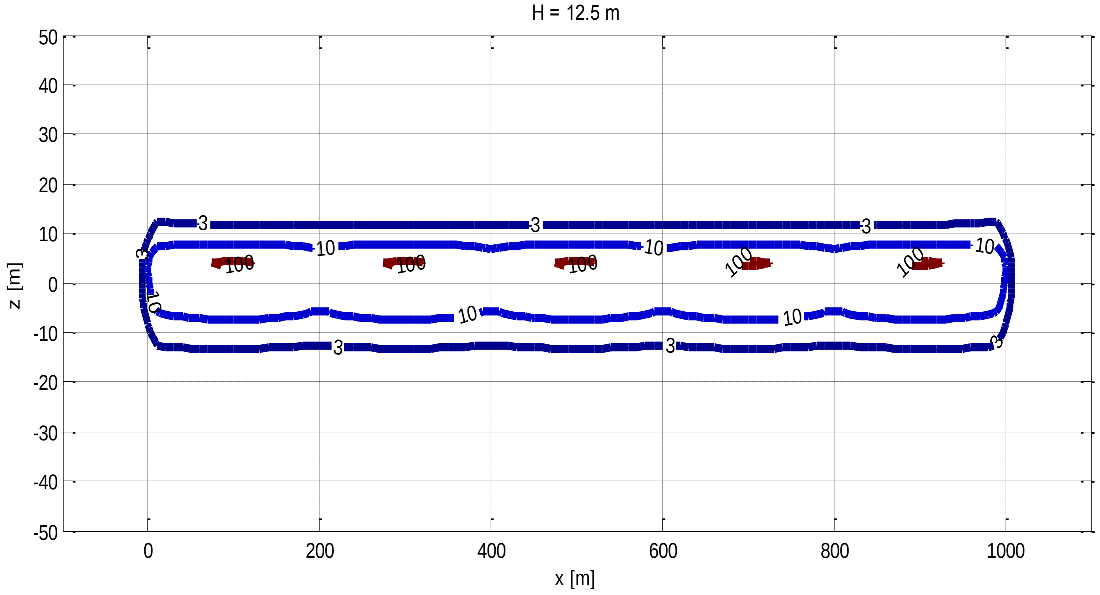

Figure 5.25: *B isolines (3μT, 10 μT and 100μT) at 12.5m from the ground for the 132 kV single-circuit overhead line with I = 385 A.*

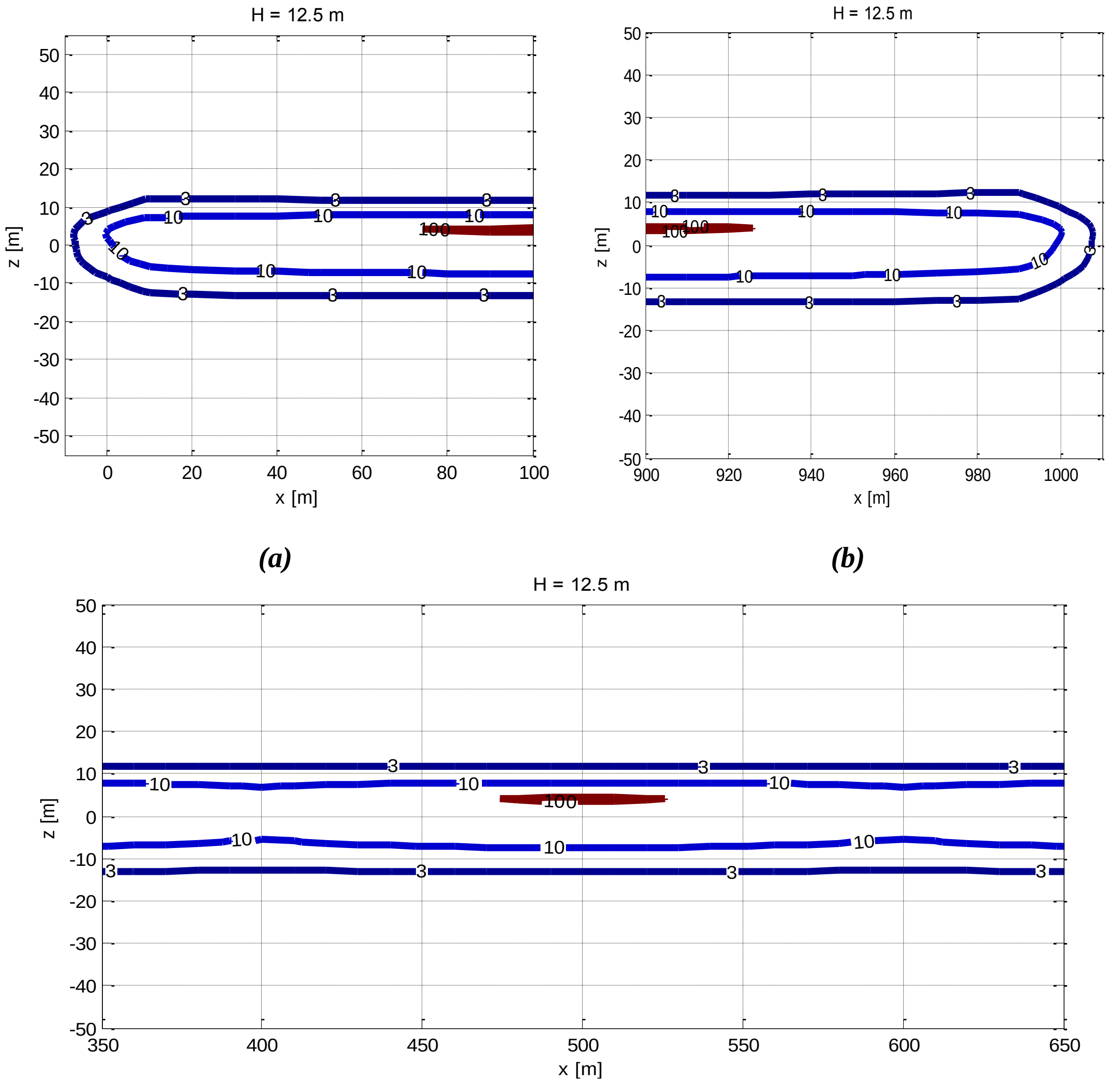

(a)

(b)

(c)

Figure 5.26: *Details of Fig. 5.25 concerning* ***(a)*** *the beginning (in equal-scaled axes),* ***(b)*** *the end (in equal-scaled axes) and* ***(c)*** *the middle of the 132 kV single-circuit overhead line (I =385 A).*

5.3.2.2 380 kV Double-Circuit Three-Phase Overhead Line

Considering the 380 kV single-circuit three-phase overhead line of Fig. 5.9 carrying balanced three-phase currents $I_1 = I_2 = 2040$ A, suspended at six poles, thus, forming five catenaries, each with length of 400 m for a total of 2000 m with sag $f = 7$ m, Figs. 5.27- 5.38 were plotted as the results of the 3D simulations of the magnetic field generated by such a line.

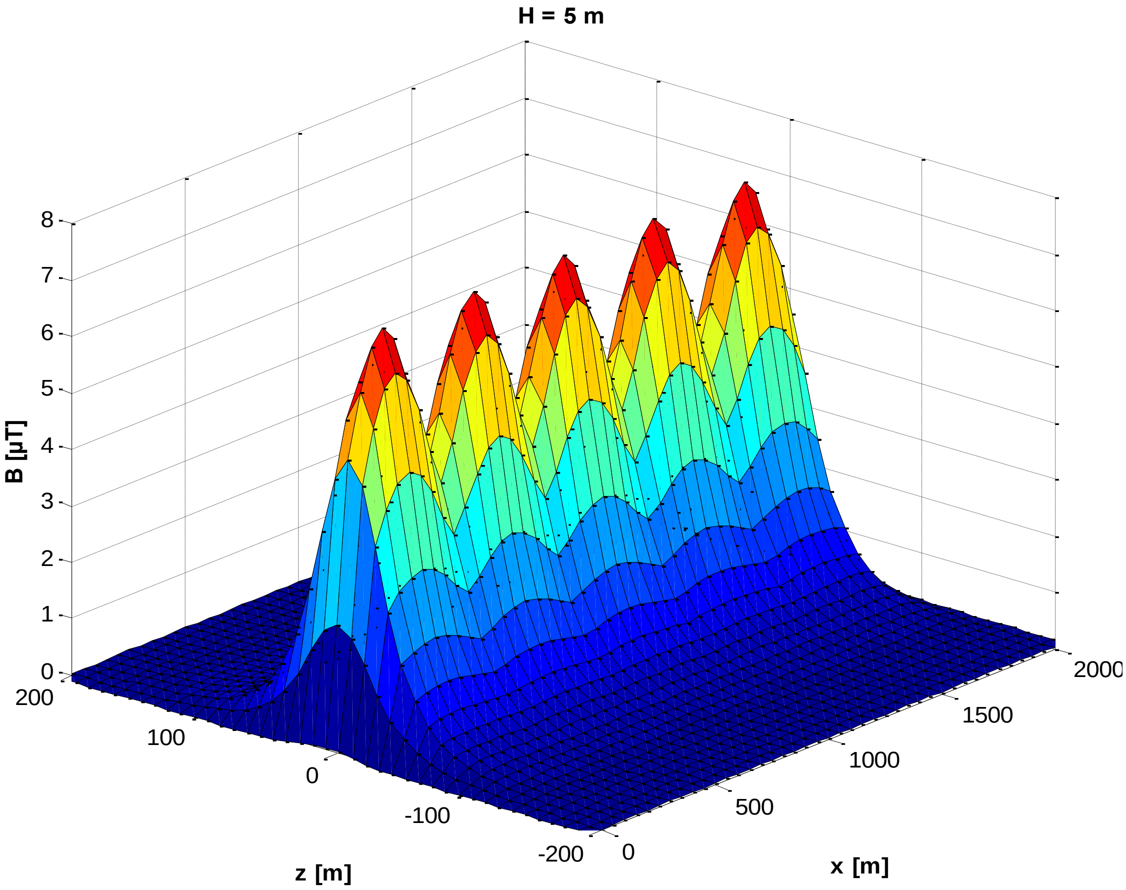

Figure 5.27: *3D plot of B vs. z and x at 5 m from the ground for the 380 kV double-circuit overhead line with* $I_1 = I_2 = 2040$ *A.*

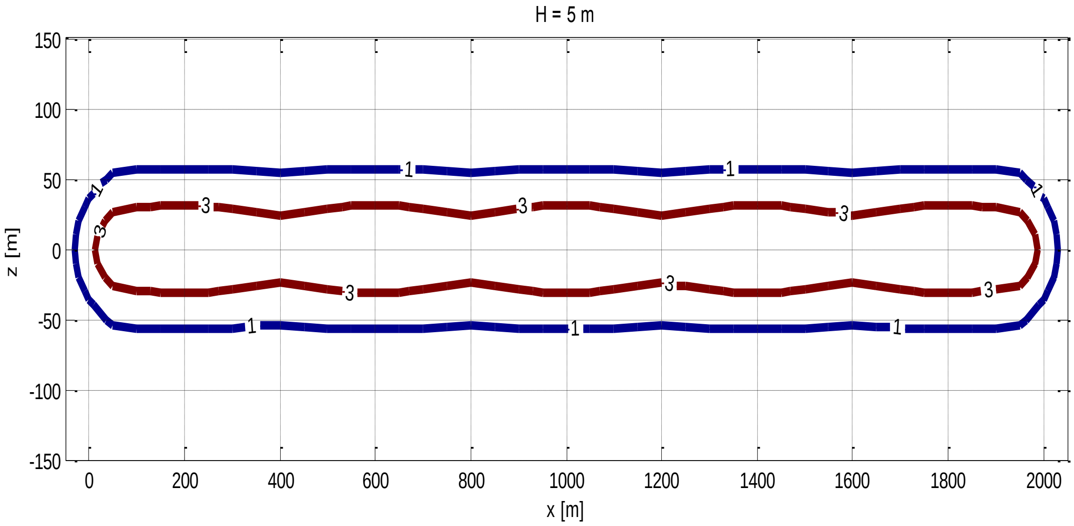

Figure 5.28: *B isolines (1µT and 3µT) at 5m from the ground for the 380 kV double-circuit overhead line with* $I_1 = I_2 = 2040$ *A.*

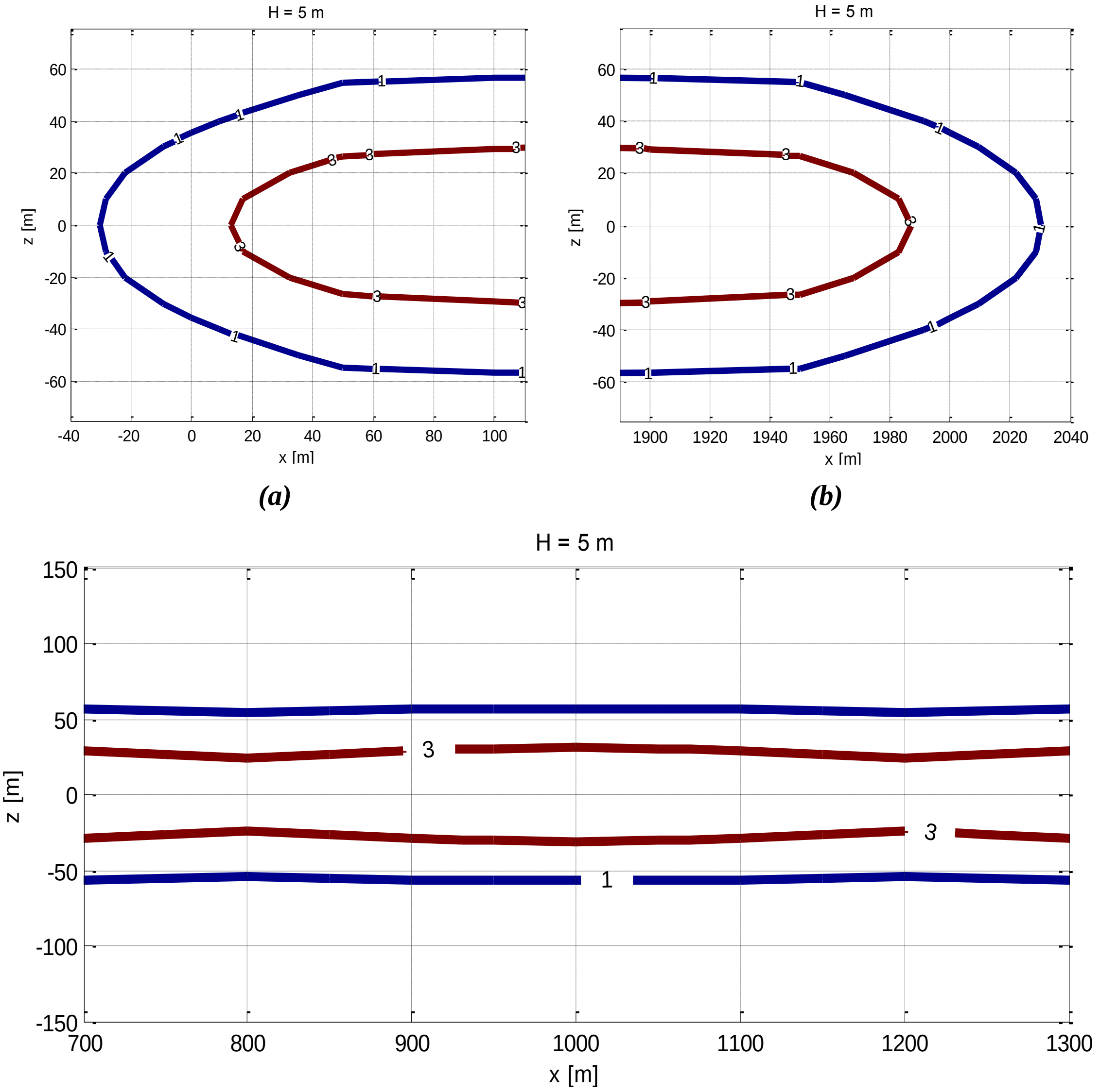

(a)

(b)

(c)

Figure 5.29: *Details of Fig. 5.28 concerning **(a)** the beginning (in equal-scaled axes), **(b)** the end (in equal-scaled axes) and **(c)** the middle of the 380 kV double-circuit overhead line* (I_1= I_2= *2040 A).*

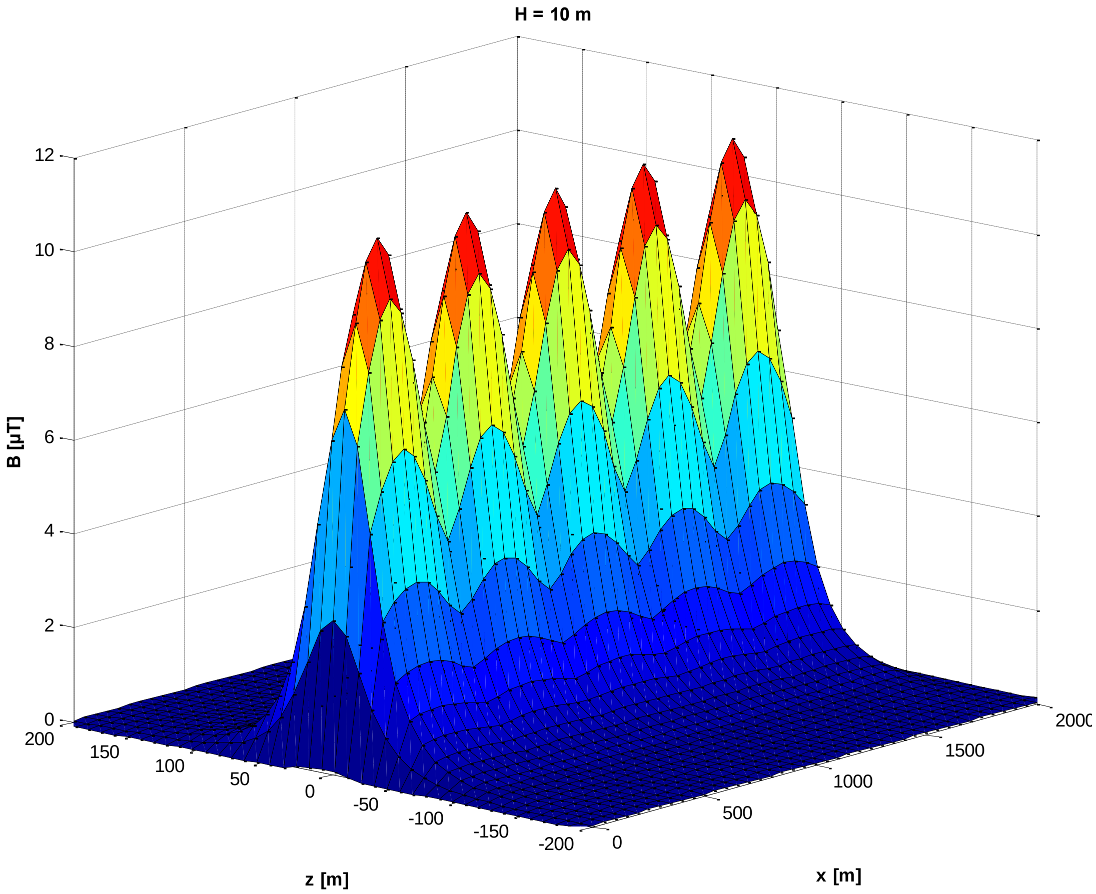

Figure 5.30: *3D plot of B vs. z and x at 10 m from the ground for the 380 kV double-circuit overhead line with $I_1 = I_2 = 2040$ A.*

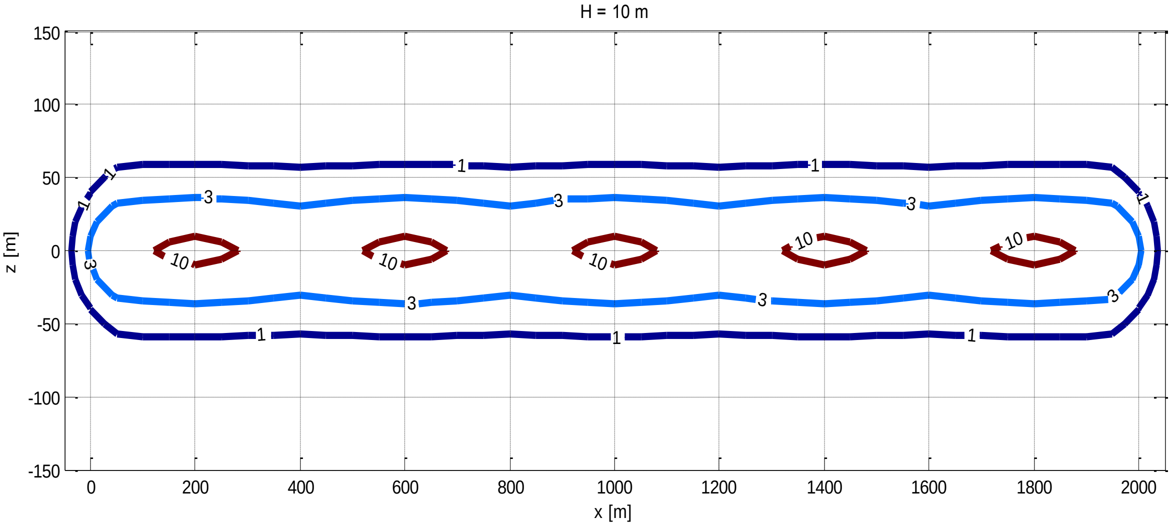

Figure 5.31: *B isolines (1µT, 3µT and 10 µT) at 10m from the ground for the 380 kV double-circuit overhead line with $I_1 = I_2 = 2040$ A.*

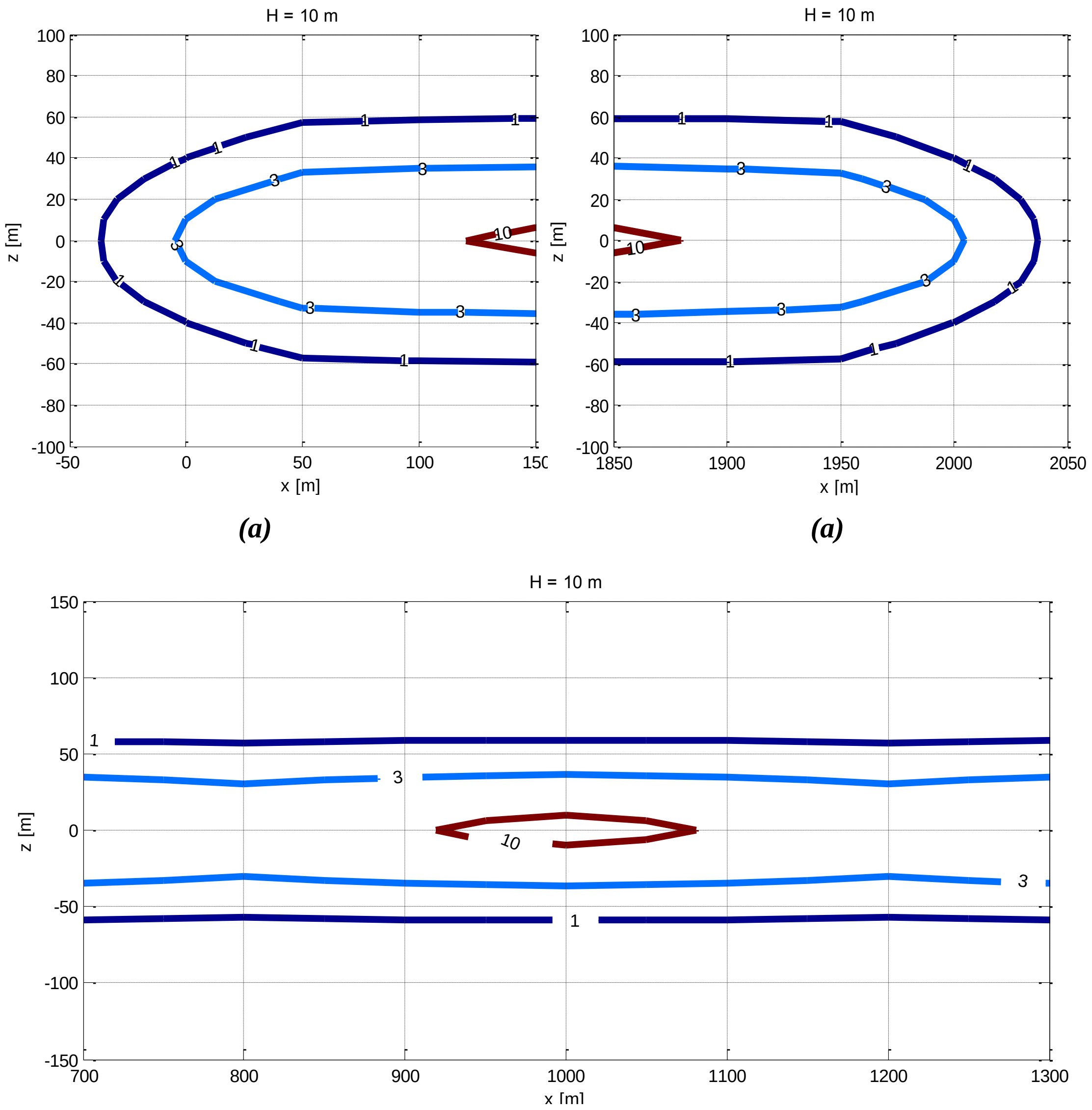

(a) *(a)*

(c)

Figure 5.32: *Details of Fig. 5.31 concerning* ***(a)*** *the beginning (in equal-scaled axes),* ***(b)*** *the end (in equal-scaled axes) and* ***(c)*** *the middle of the 380 kV double-circuit overhead line (*$I_1 = I_2 = 2040$ *A).*

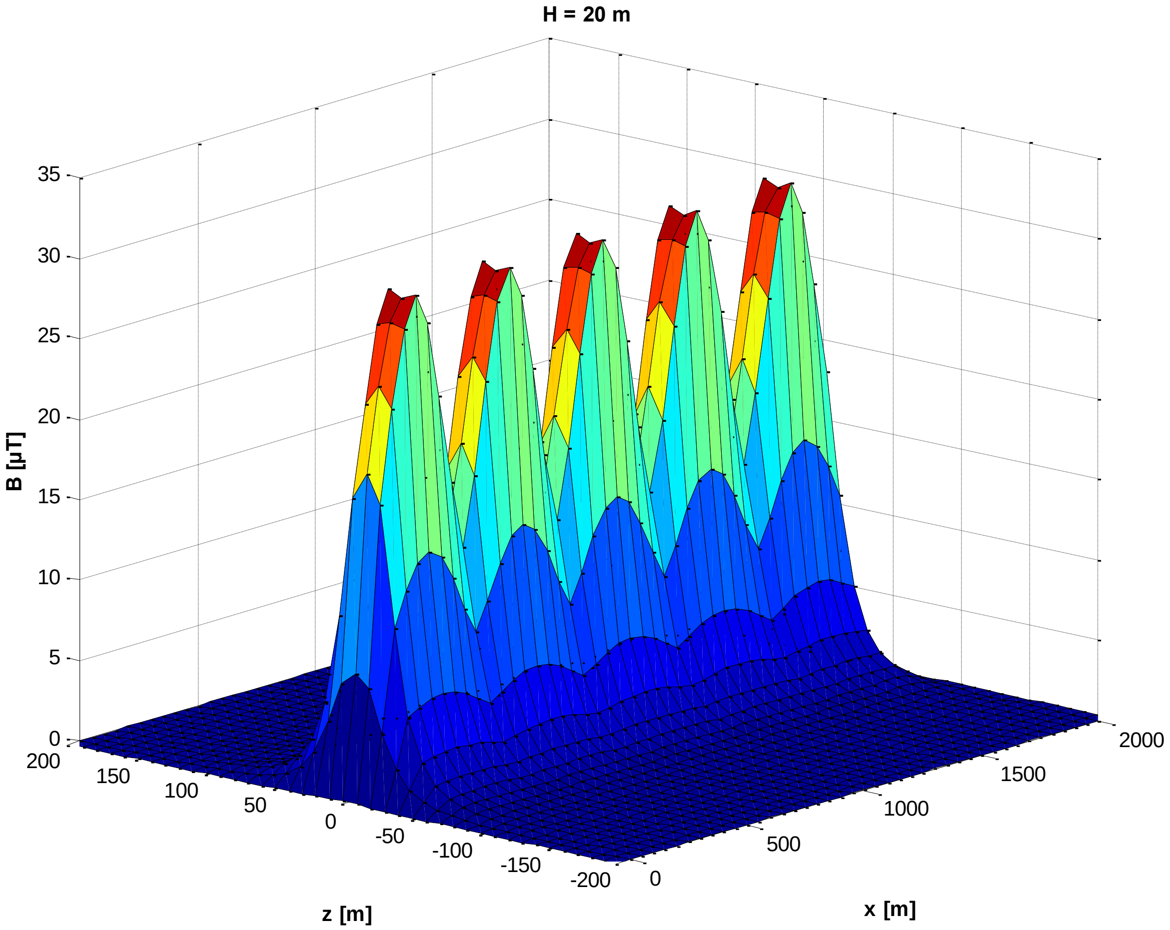

Figure 5.33: *3D plot of B vs. z and x at 20 m from the ground for the 380 kV double-circuit overhead line with* $I_1 = I_2 = 2040$ *A.*

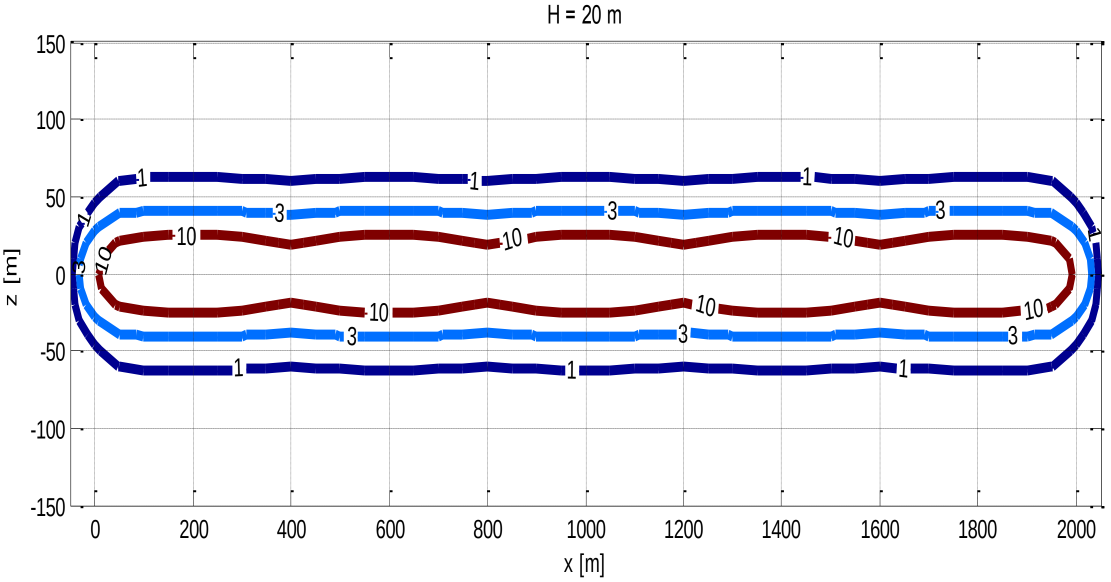

Figure 5.34: *B isolines (1* μT*, 3*μT *and 10* μT*) at 20m from the ground for the 380 kV double-circuit overhead line with* $I_1 = I_2 = 2040$ *A.*

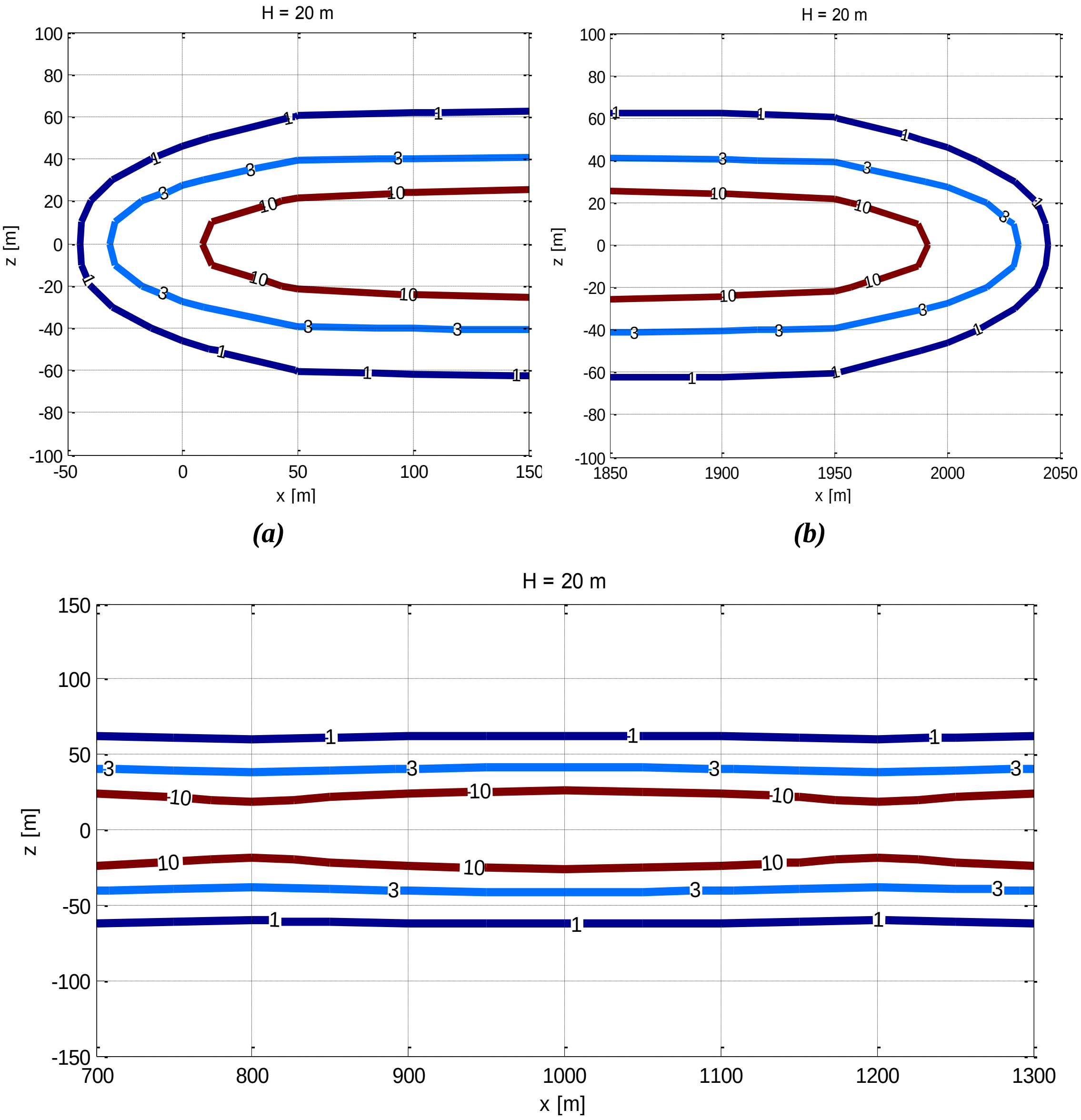

(a) ***(b)***

(c)

Figure 5.35: *Details of Fig. 5.34 concerning* ***(a)*** *the beginning (in equal-scaled axes),* ***(b)*** *the end (in equal-scaled axes) and* ***(c)*** *the middle of the 380 kV double-circuit overhead line (I_1= I_2= 2040 A).*

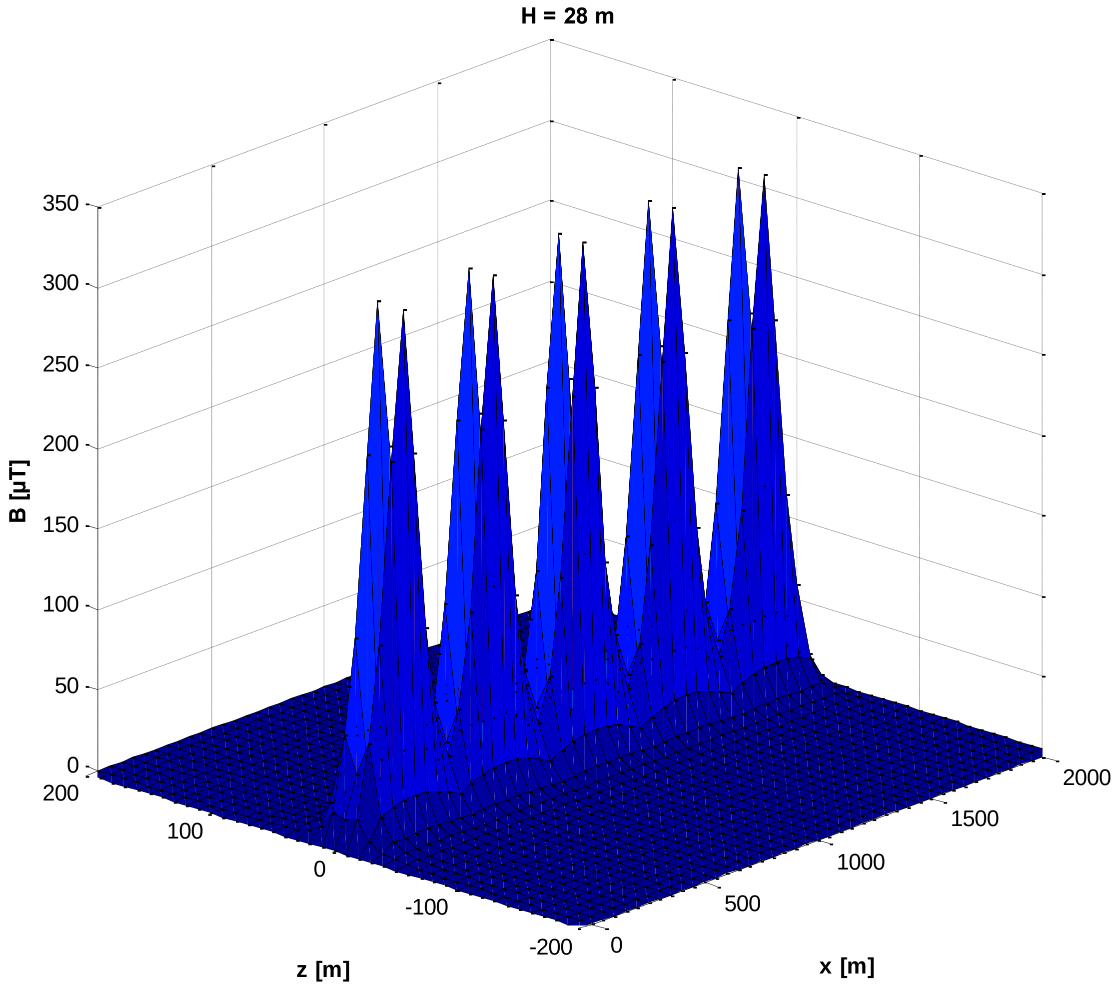

Figure 5.36: *3D plot of B vs. z and x at 28 m from the ground for the 380 kV double-circuit overhead line with $I_1 = I_2 = 2040$ A.*

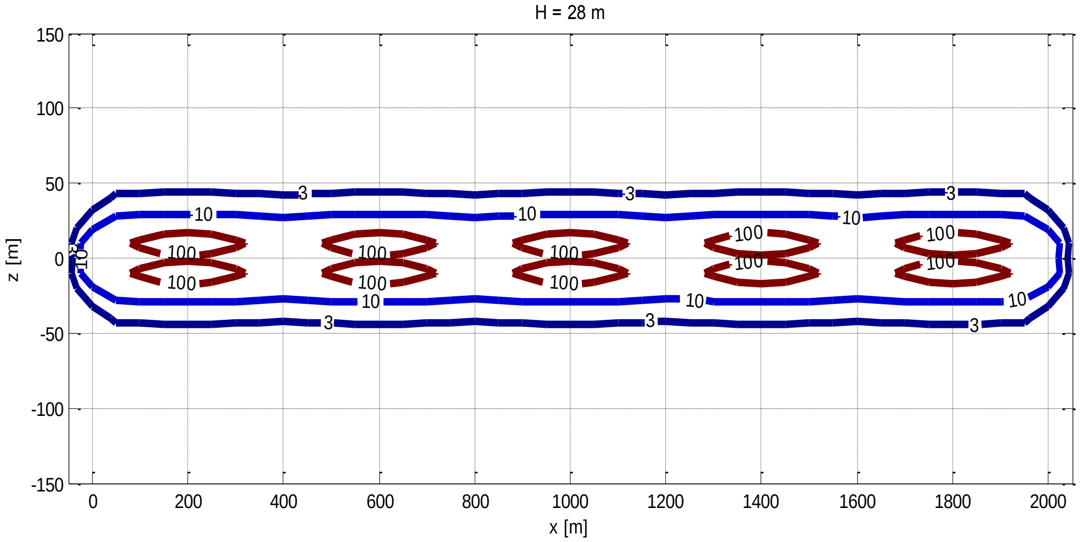

Figure 5.37: *B isolines (3μT, 10 μT and 100 μT) at 28m from the ground for the 380 kV double-circuit overhead line with $I_1 = I_2 = 2040$ A.*

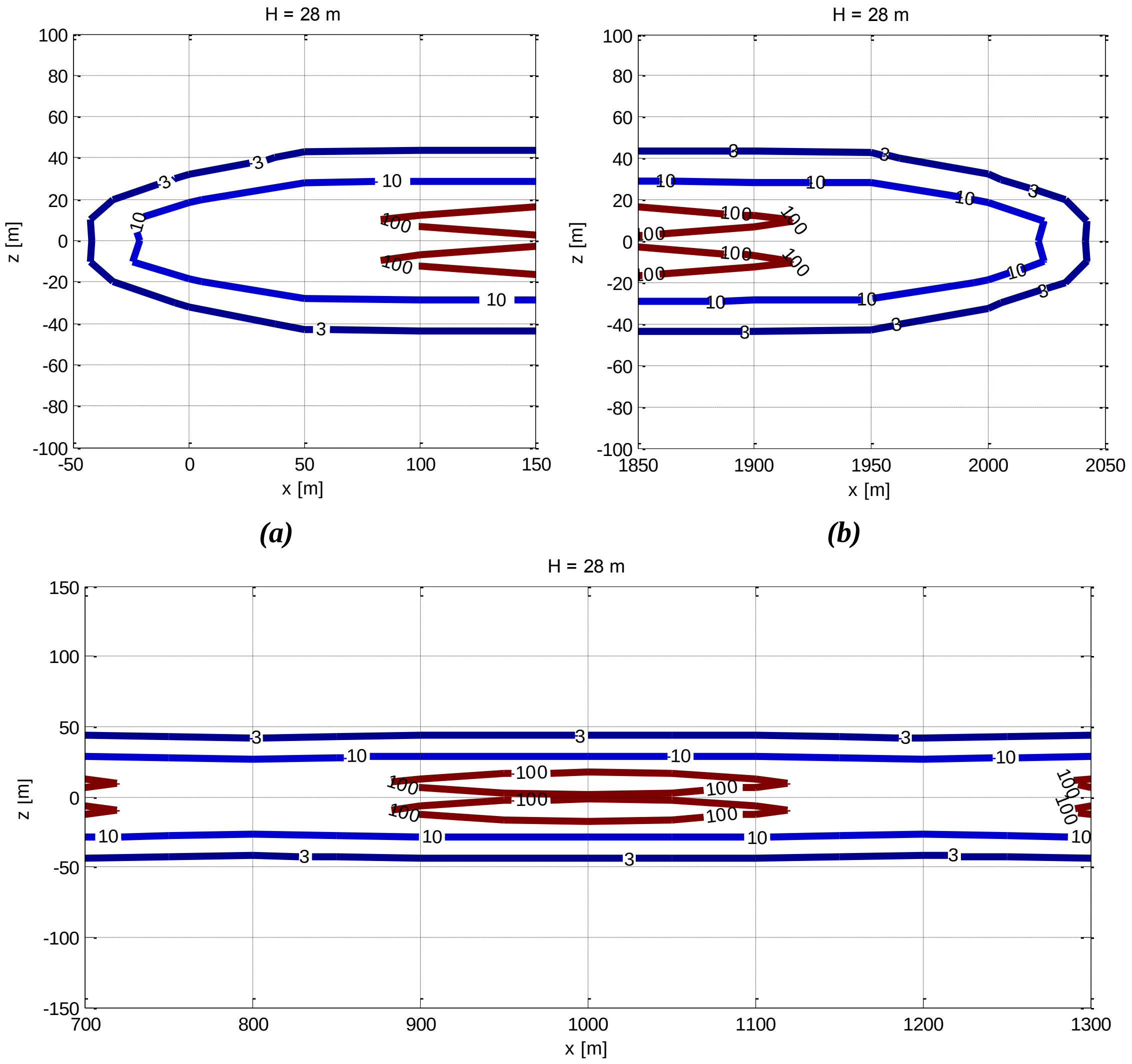

(a) *(b)*

(c)

Figure 5.38: *Details of Fig. 5.37 concerning* ***(a)*** *the beginning (in equal-scaled axes),* ***(b)*** *the end (in equal-scaled axes) and* ***(c)*** *the middle of the 380 kV double-circuit overhead line (I_1= I_2= 2040 A).*

5.4 CONCLUSIONS

The results of all 2D simulations made were compared with magnetic field calculation programs commercially available. In particular, the software used, that calculates the electric and magnetic field generated by overhead and underground power lines, is "CAMPI" [51], in C++ language, developed and distributed by the "NelloCarrara" Institute of Applied Physics (IFAC), part of the National Research Council (CNR), which is the main public organization pursuing research and innovation in Italy.

The results of all 3D simulations made were compared with magnetic field calculation programs not commercially available and classified. Nevertheless, some critical observations concerning the correctness of the script were made and are depicted in Figs. 5.39 - 5.70.

Three sections of the 132 kV single-circuit overhead line relative to the middle catenary (for *x* values from 400 m to 600 m) were further examined, for the purpose of comparing the values of the magnetic field calculated according to the bi-dimensional approach, B_{2D}, with that calculated according to the tri-dimensional approach, B_{3D}, and the relative percent error of B_{2D} with respect to B_{3D} has been estimated, at different heights from the ground. More precisely, the first section considered is at $x = 400$ m (under the pole), the second is at $x = 450$ m (¼ of the catenary) and the third section is at $x = 500$ m (at the mid-span) and the simulation results are depicted in Figs. 5.39 - 5.46.

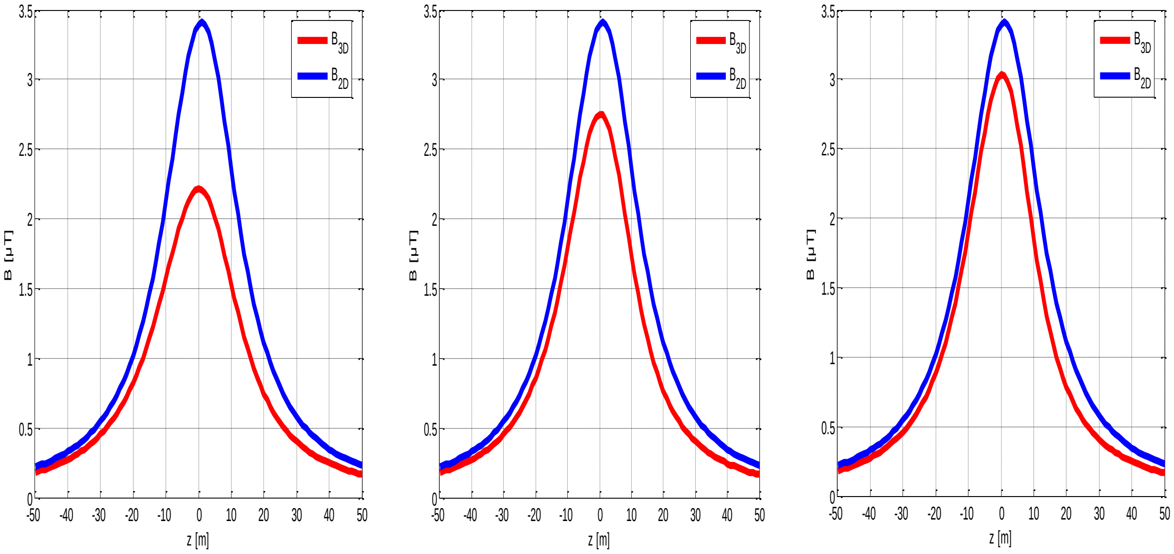

Figure 5.39: *Comparison between B_{2D} and B_{3D} at the three vertical sections of x=400 m, x=450 m and x=500 m for the 132 kV single-circuit overhead line at 2 m from the ground with I=385 A.*

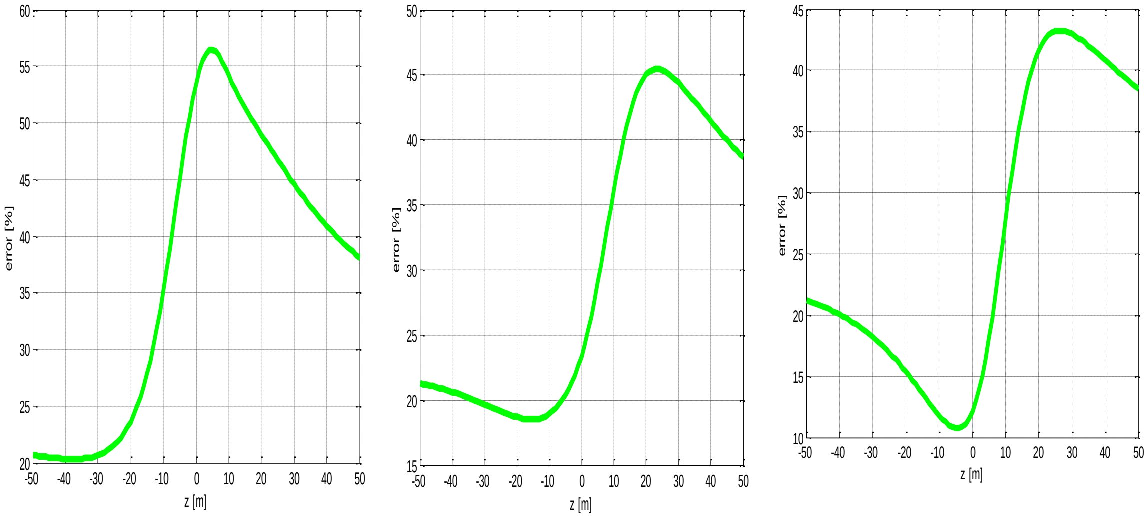

Figure 5.40: *Relative percent error of B_{2D} with respect to B_{3D} for the sections considered at Fig. 5.39.*

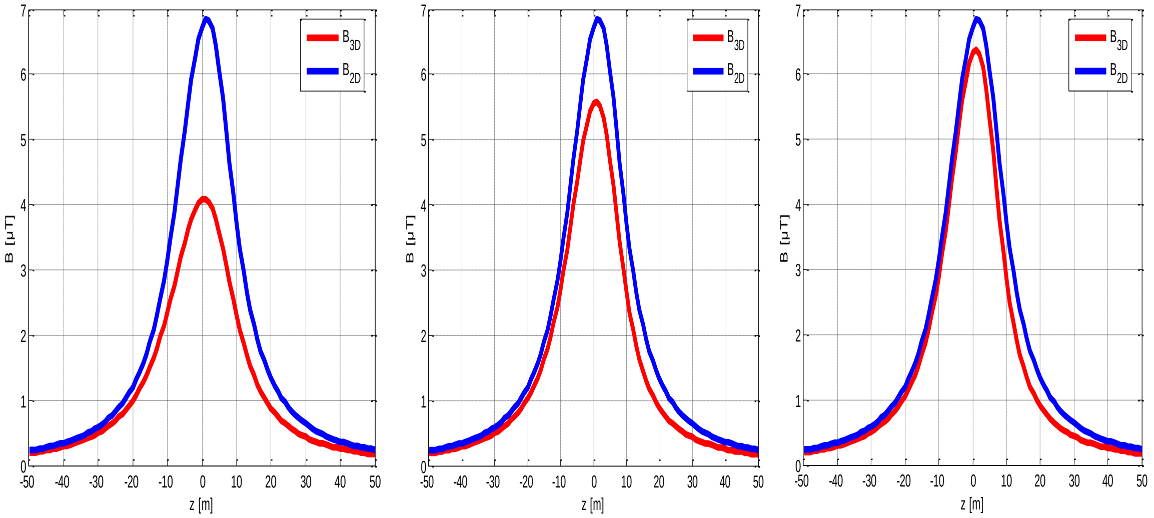

Figure 5.41: *Comparison between B_{2D} and B_{3D} at the three vertical sections of x=400 m, x=450 m and x=500 m for the 132 kV single-circuit overhead line at 6 m from the ground with I=385 A.*

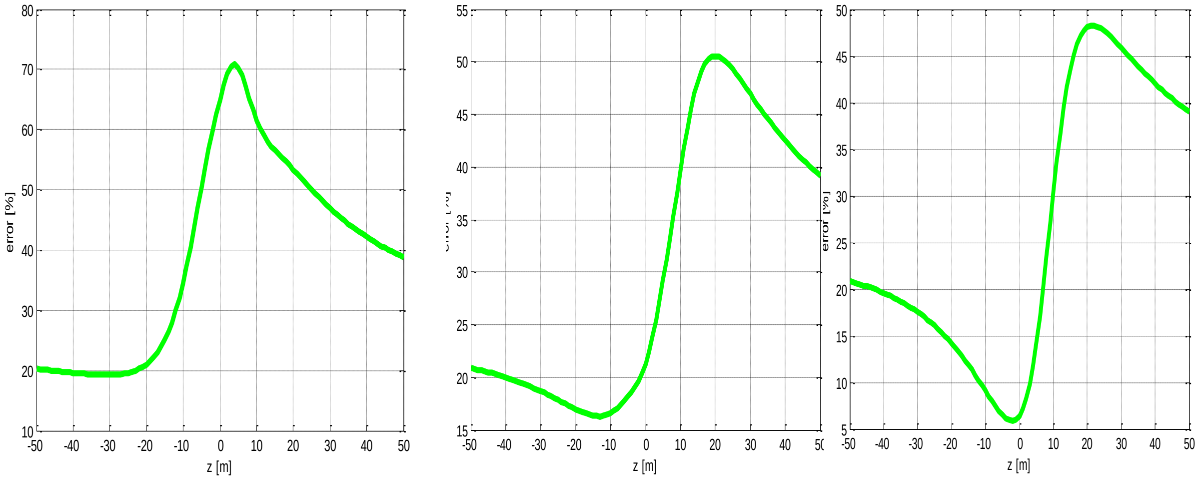

Figure 5.42: *Relative percent error of B_{2D} with respect to B_{3D} for the sections considered at Fig. 5.41.*

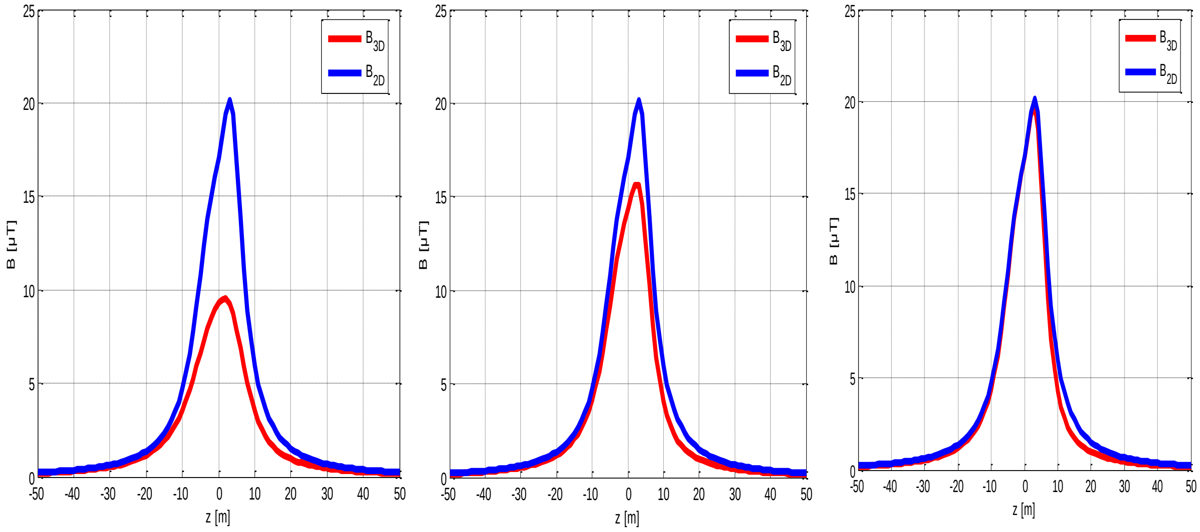

Figure 5.43: *Comparison between B_{2D} and B_{3D} at the three vertical sections of x=400 m, x=450 m and x=500 m for the 132 kV single-circuit overhead line at 10 m from the ground with I = 385 A.*

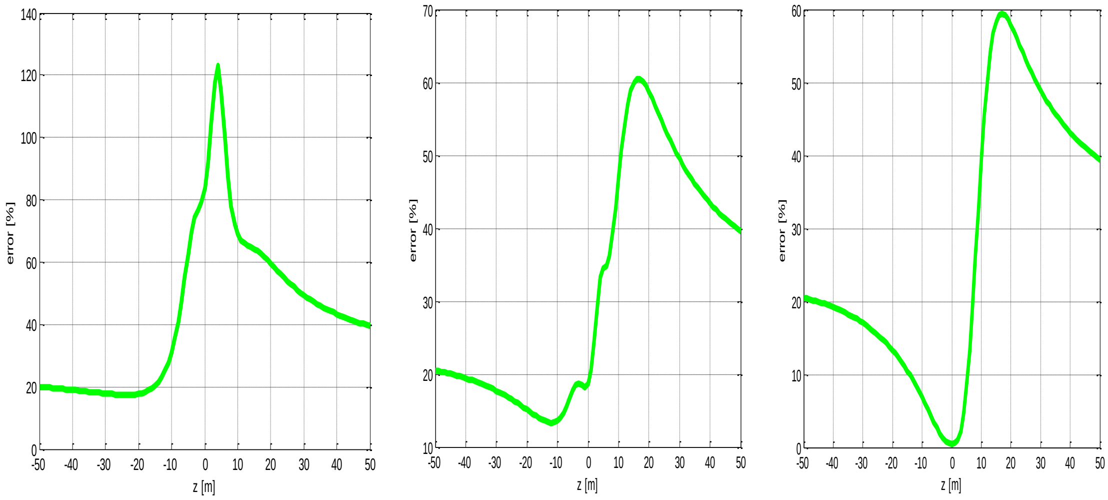

Figure 5.44: *Relative percent error of B_{2D} with respect to B_{3D} for the sections considered at Fig. 5.43.*

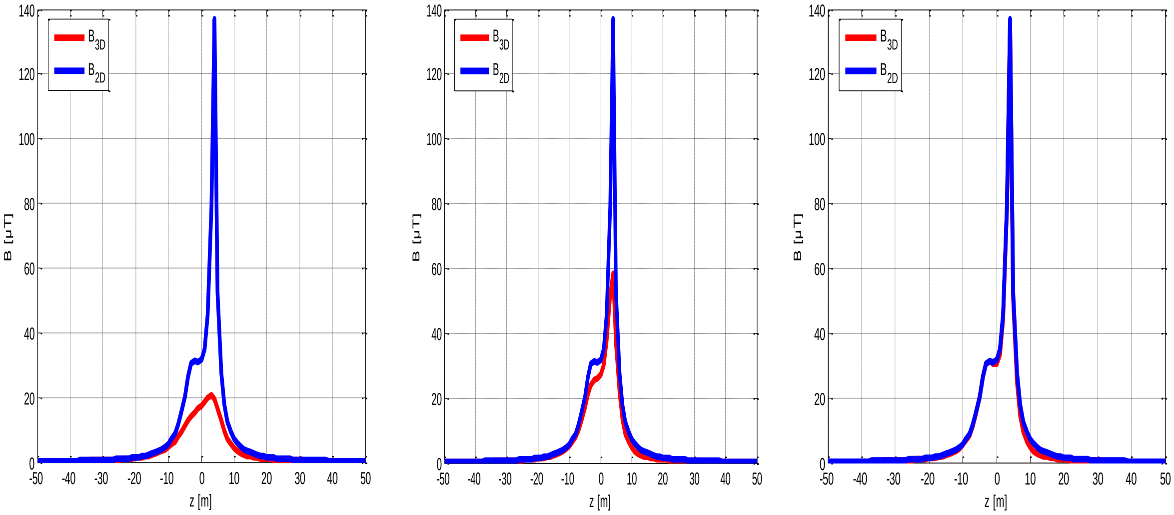

Figure 5.39: *Comparison between B_{2D} and B_{3D} at the three vertical sections of x=400 m, x=450 m and x=500 m for the 132 kV single-circuit overhead line at 12.5 m from the ground with I=385 A.*

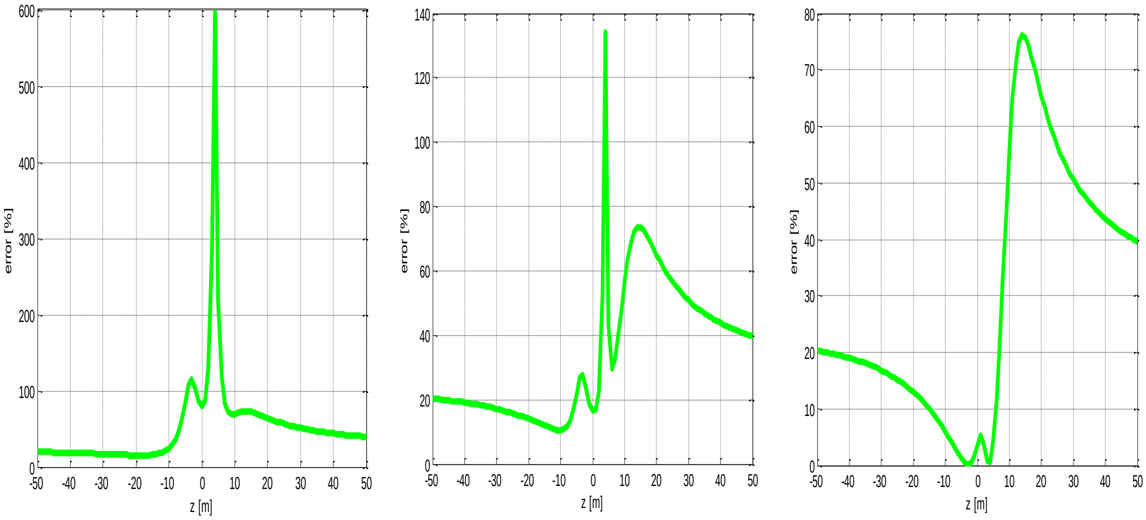

Figure 5.46: *Relative percent error of B_{2D} with respect to B_{3D} for the sections considered at Fig. 5.45.*

The same considerations were made also for the 380 kV power line case where also three vertical sections relative to the middle catenary (for *x* values from 800 m to 1200 m) were further examined, at different heights from the ground, for the purpose of comparing the values of B_{2D} with that of B_{3D} and estimating the relative percent error of B_{2D} with respect to B_{3D}. The first section considered is at x = 800 m (under the pole), the second is at x = 900 m (¼ of the catenary) and the third section is at x = 1000 m (at the mid-span) and the results are depicted in Figs. 5.47 - 5.54.

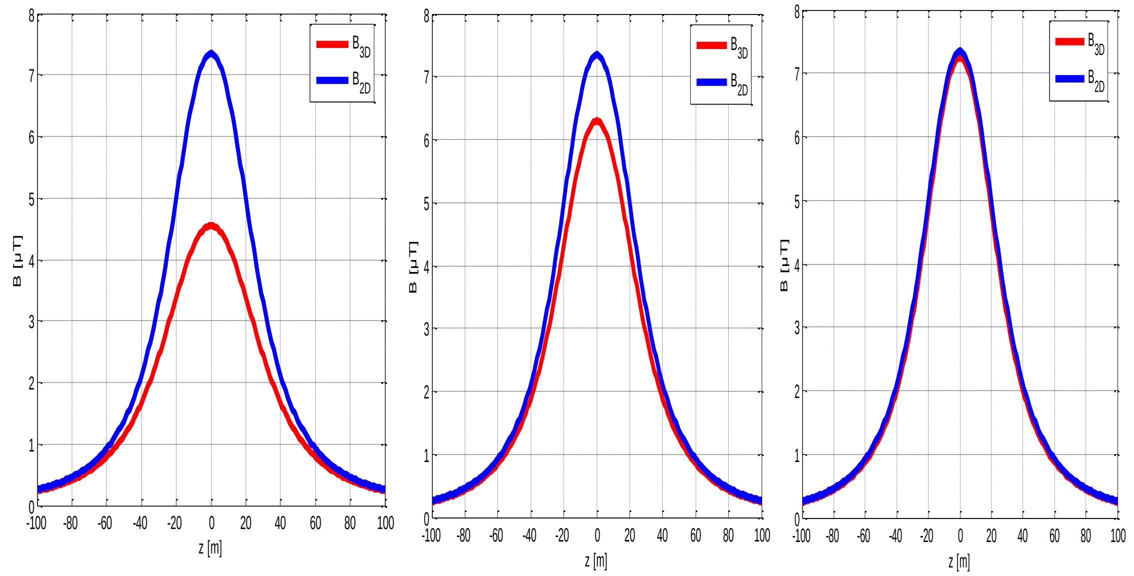

Figure 5.47: *Comparison between B_{2D} and B_{3D} at the three vertical sections of x=800 m, x=900 m and x=1000 m for the 380 kV double-circuit overhead line at 5 m from the ground with I_1=I_2=2040 A.*

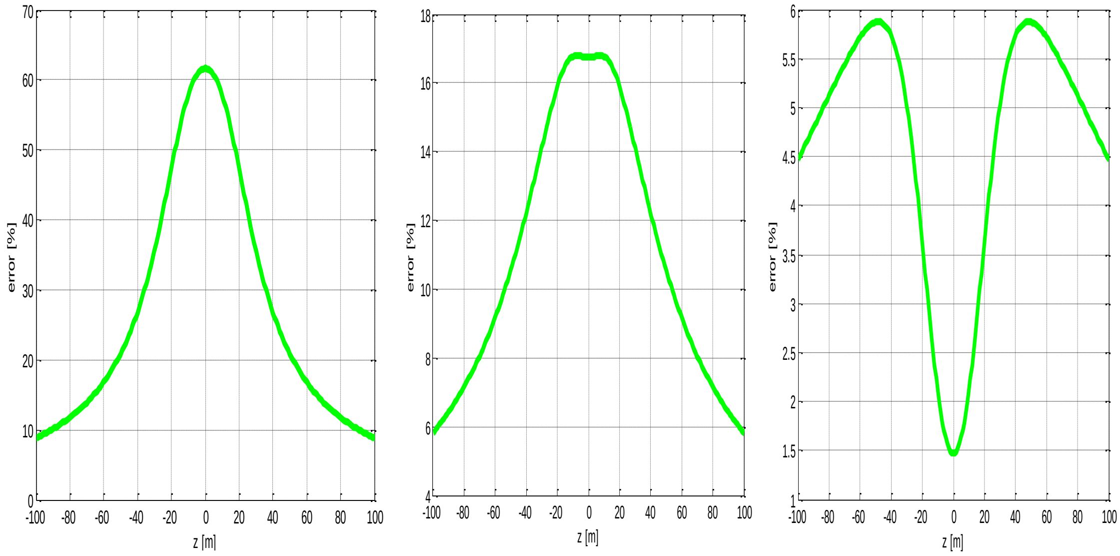

Figure 5.48: *Relative percent error of B_{2D} with respect to B_{3D} for the sections considered at Fig. 5.47.*

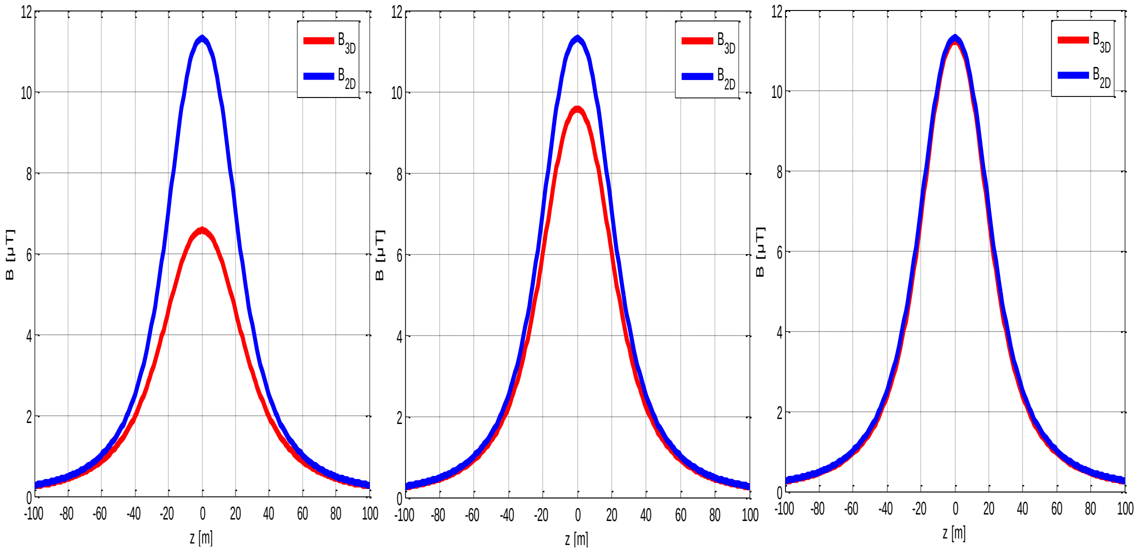

Figure 5.49: *Comparison between B_{2D} and B_{3D} at the three vertical sections of x=800 m, x=900 m and x=1000 m for the 380 kV double-circuit overhead line at 10 m from the ground with $I_1= I_2=2040$ A.*

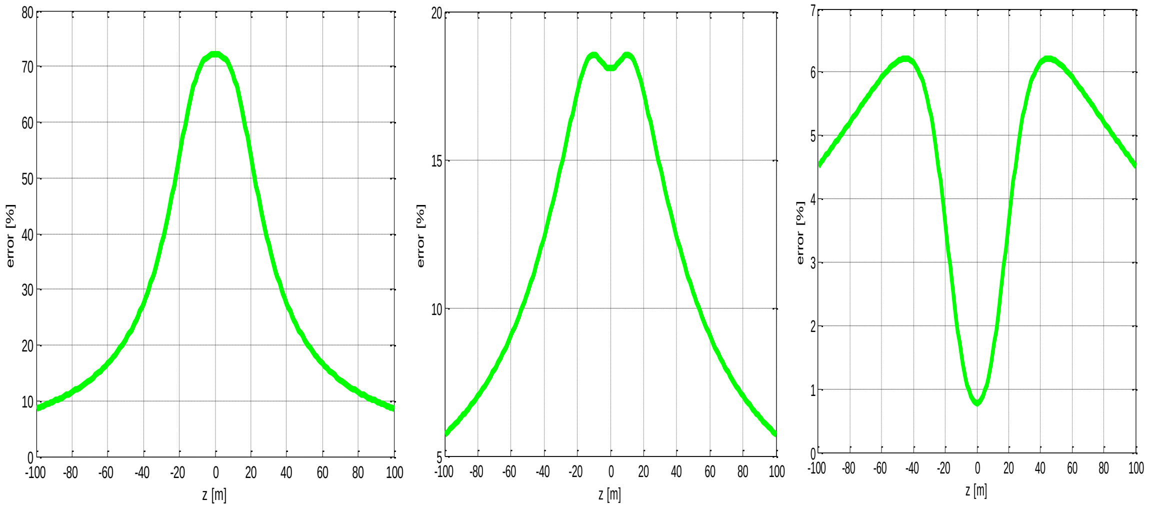

Figure 5.50: *Relative percent error of B_{2D} with respect to B_{3D} for the sections considered at Fig. 5.49.*

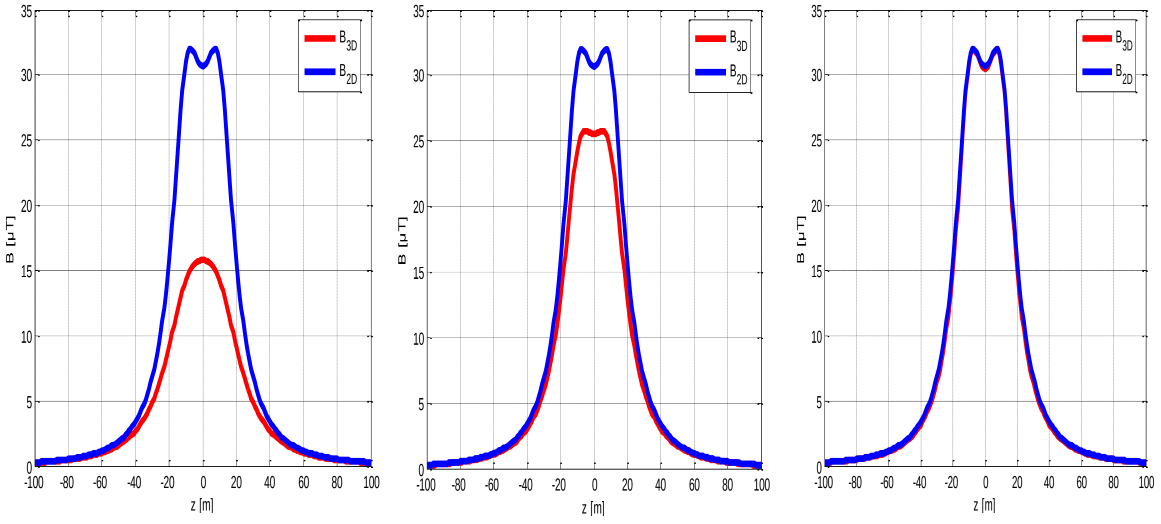

Figure 5.51: *Comparison between B_{2D} and B_{3D} at the three vertical sections of x=800 m, x=900 m and x=1000 m for the 380 kV double-circuit overhead line at 20 m from the ground with $I_1=I_2=2040$ A.*

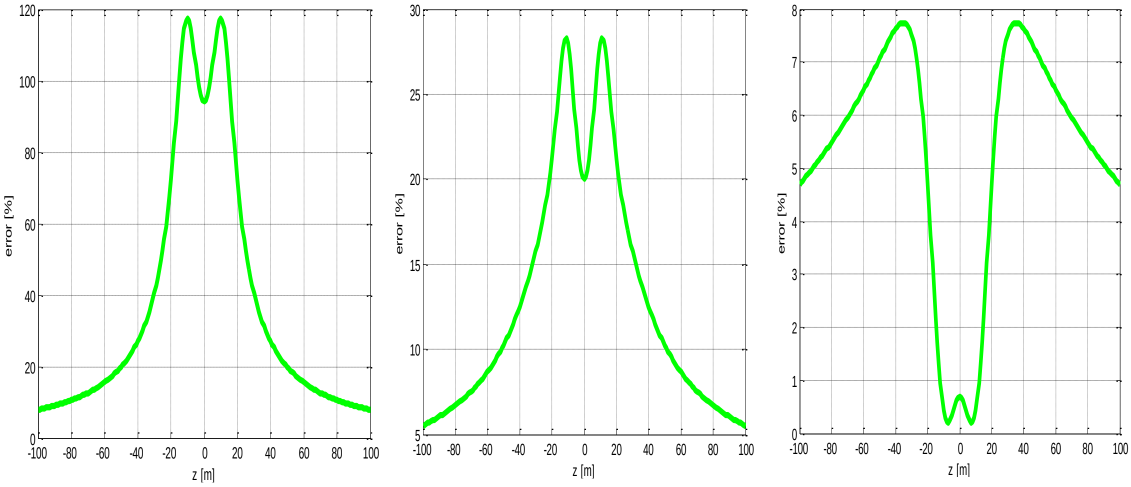

Figure 5.52: *Relative percent error of B_{2D} with respect to B_{3D} for the sections considered at Fig. 5.51.*

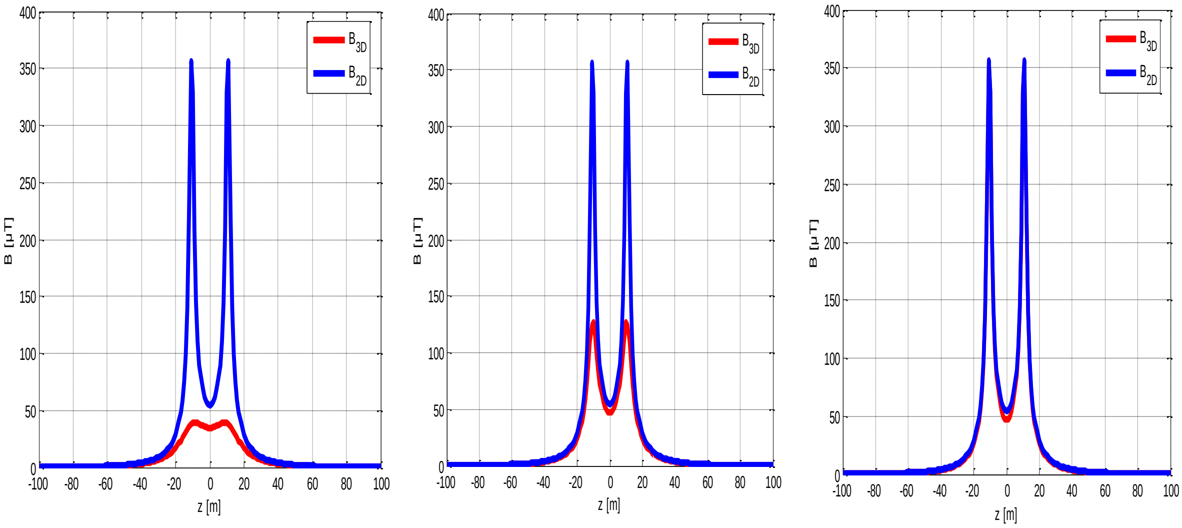

Figure 5.53: *Comparison between B_{2D} and B_{3D} at the three vertical sections of $x=800$ m, $x=900$ m and $x=1000$ m for the 380 kV double-circuit overhead line at 28 m from the ground with $I_1=I_2=2040$ A.*

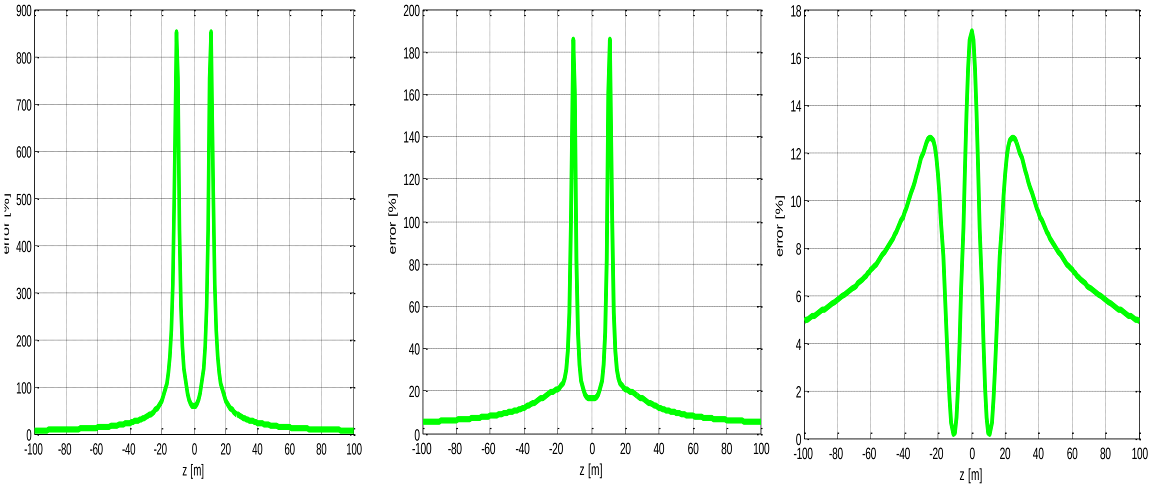

Figure 5.54: *Relative percent error of B_{2D} with respect to B_{3D} for the sections considered at Fig. 5.53.*

One can notice the growing discrepancy between the results obtained at the mid-span between the poles (third section) and those under the pole (first section). For reasons of providing conservative results, the bi-dimensional approach calculates the field in correspondence to the mid-span between two poles where the conductors are closer to the ground and the field results higher. That explains why the field curves of obtained at the third section are almost coincident unlike the field curves obtained at the second and, particularly, the first section, where the maximum divergence between B_{2D} and B_{3D} is presented. Another reason for this deviation of the results, is the fact that in the area under the pole, the line segments are not horizontal and parallel to each other as hypothesized by the bi-dimensional calculus.

Additionally, it must be pointed out, that for the 132 kV single-circuit overhead line, the curves of B_{3D} become closer to those of B_{2D} as the distance H from the ground rises. This is logical and expected since the effect of the catenary-form of the line is compensated by the small distance from the field sources. This is not true, though, for the 380 kV double-circuit overhead line case due, firstly, to the greater value of the currents and, secondly, to the geometry of the line that is more similar to the considered geometry of the line in the bi-dimensional case (i.e. a straight horizontal line parallel to the ground), due to the greater length L of every catenary and the greater value of a in eq. (5.18).

Another interesting point to be examined is the overall behavior of the B_{3D} field along the whole overhead line (from $x = 0$ m up to $x = 1000$ m for the 132 kV single-circuit overhead line and from $x = 0$ m up to $x = 2000$ m for the 380 kV double-circuit overhead line) under every pole and under every mid-span area. For this reason, Figs. 5.55-5.62 are plotted that depict the magnetic field B_{3D} as a function of the coordinate z calculated at the vertical sections of $x = 0$ m (first pole), $x = 100$ m (first mid-span), $x = 200$ m (second pole), $x = 300$ m (second mid-span), $x = 400$ m (third pole), $x = 500$ m (third mid-span), $x = 600$ m (fourth pole), $x = 700$ m (fourth mid-span), $x = 800$ m (fifth pole), $x = 900$ m (fifth mid-span) and $x = 1000$ m (sixth and last pole) for the 132 kV single-circuit overhead line and at the vertical sections of $x = 0$ m (first pole), $x = 200$ m (first mid-span), $x = 400$ m (second pole), $x = 600$ m (second mid-span), $x = 800$ m (third pole), $x = 1000$ m (third mid-span), $x = 1200$ m (fourth pole), $x = 1400$ m (fourth mid-span), $x = 1600$ m (fifth pole), $x = 1800$ m (fifth mid-span) and $x = 2000$ m (sixth and last pole) for the 380 kV double-circuit overhead line.

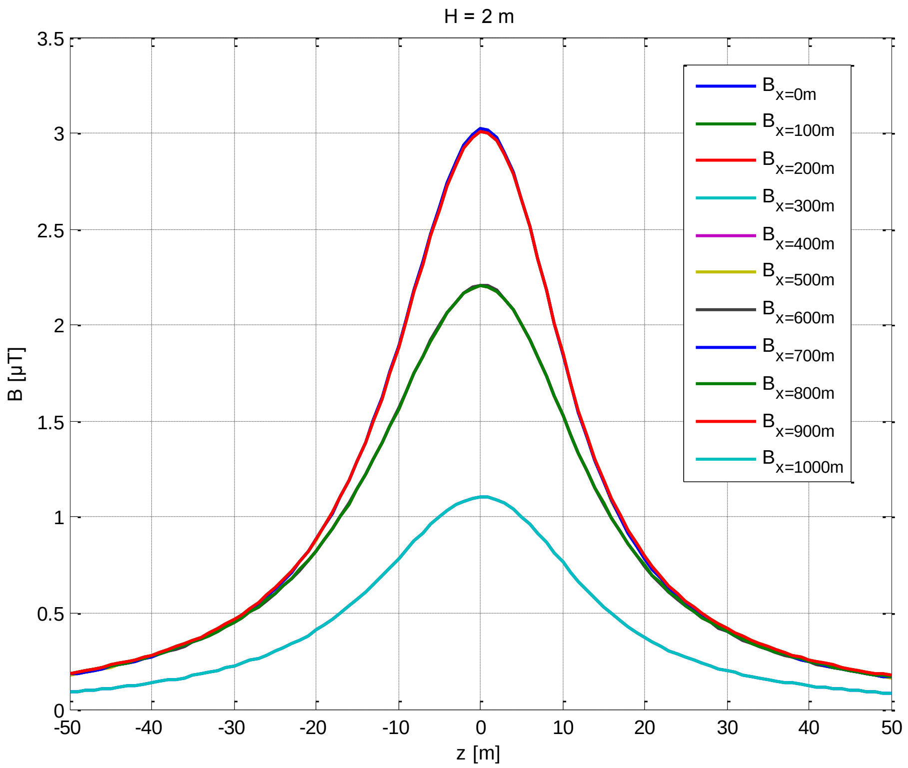

Figure 5.55: *Comparison between the magnetic field profiles at the vertical sections of interest, i.e. under the poles and the mid-spans, for the 132 kV single-circuit overhead line, at 2 m from the ground with I = 385 A.*

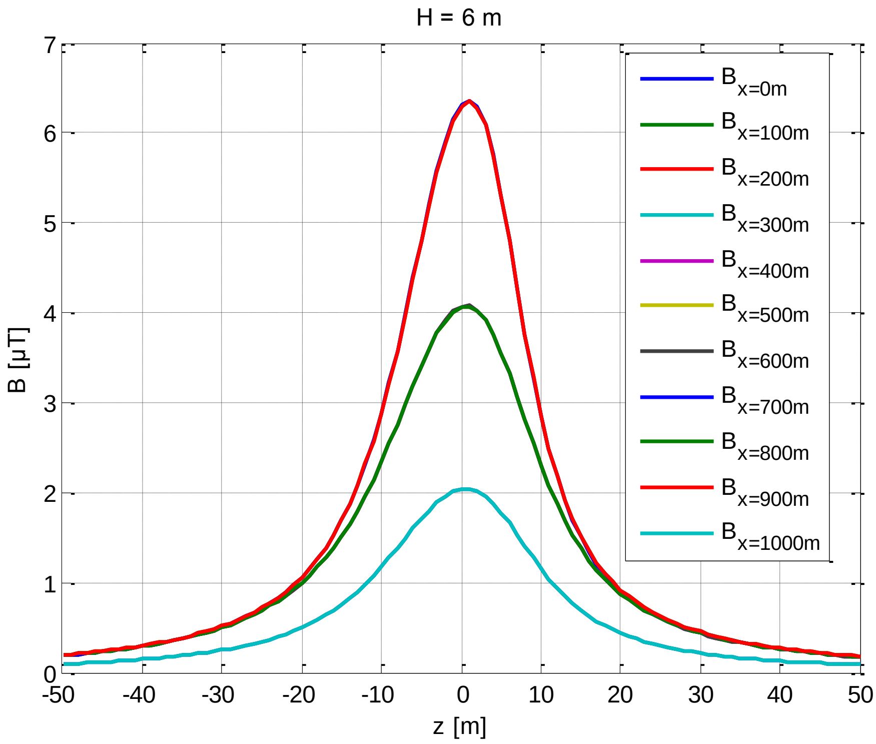

Figure 5.56: *Comparison between the magnetic field profiles at the vertical sections of interest, i.e. under the poles and the mid-spans, for the 132 kV single-circuit overhead line, at 6 m from the ground with I = 385 A.*

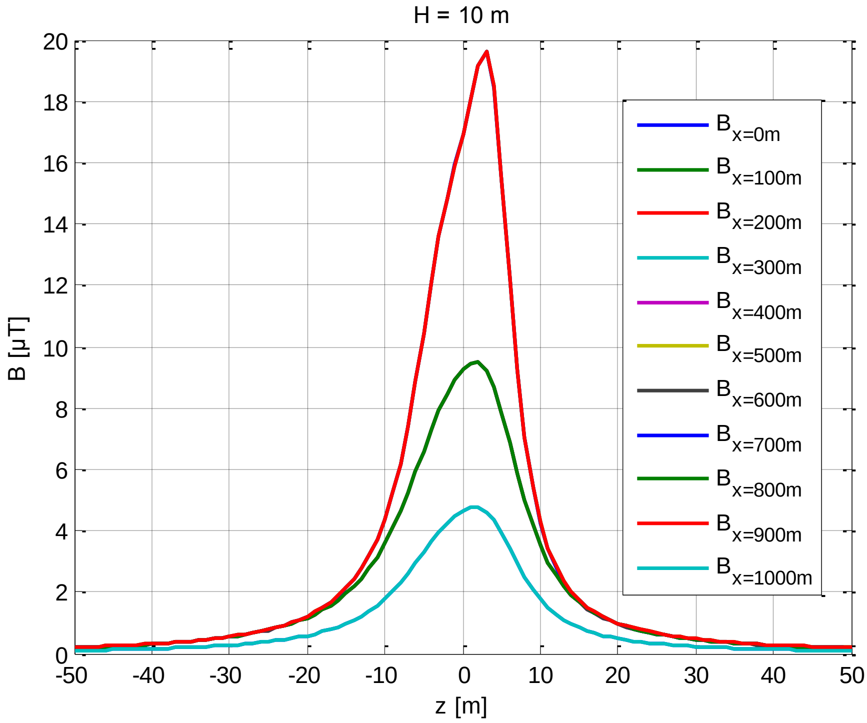

***Figure 5.57:** Comparison between the magnetic field profiles at the vertical sections of interest, i.e. under the poles and the mid-spans, for the 132 kV single-circuit overhead line, at 10 m from the ground with I = 385 A.*

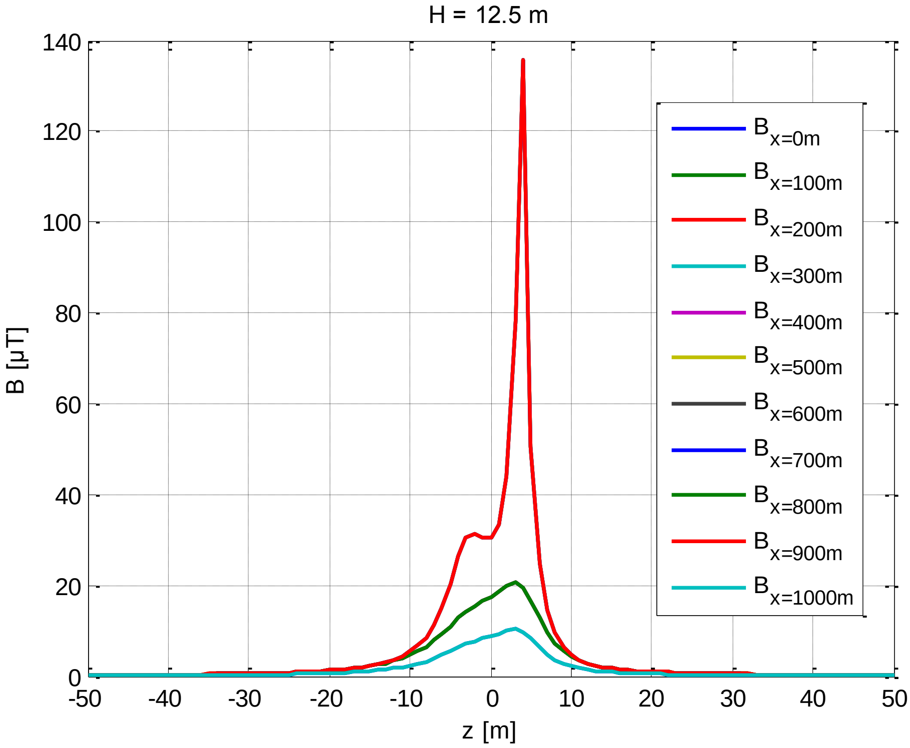

***Figure 5.58:** Comparison between the magnetic field profiles at the vertical sections of interest, i.e. under the poles and the mid-spans, for the 132 kV single-circuit overhead line, at 12.5 m from the ground with I = 385 A.*

In Figs. 5.55-5.58 the magnetic field profiles are categorized in three groups since their curves are practically coincident. There is the first group of $B_{x=100m}$, $B_{x=300m}$, $B_{x=500m}$, $B_{x=700m}$ and $B_{x=900m}$ (under the mid-span areas), the second group of the $B_{x=400m}$, $B_{x=600m}$ and $B_{x=800m}$ (under the second, third and fourth pole) and the third group of $B_{x=100m}$ and $B_{x=1000m}$ (under the first and fifth pole). The results, at all heights from the ground considered, have had a positive outcome since the first group of the B_{3D} profiles provide the highest values of the field and the second group provides two times the values of the third group. These considerations were expected: the first group provides the magnetic field values under the mid-span areas where the field is maximum; the third group calculates the field under the poles situated at the two ends of the line, meaning that the magnetic field contribute of half the line is missing, resulting unavoidably at being ~50% of the field calculated under the intermediate poles of the line, i.e. second, third and fourth pole (second group).

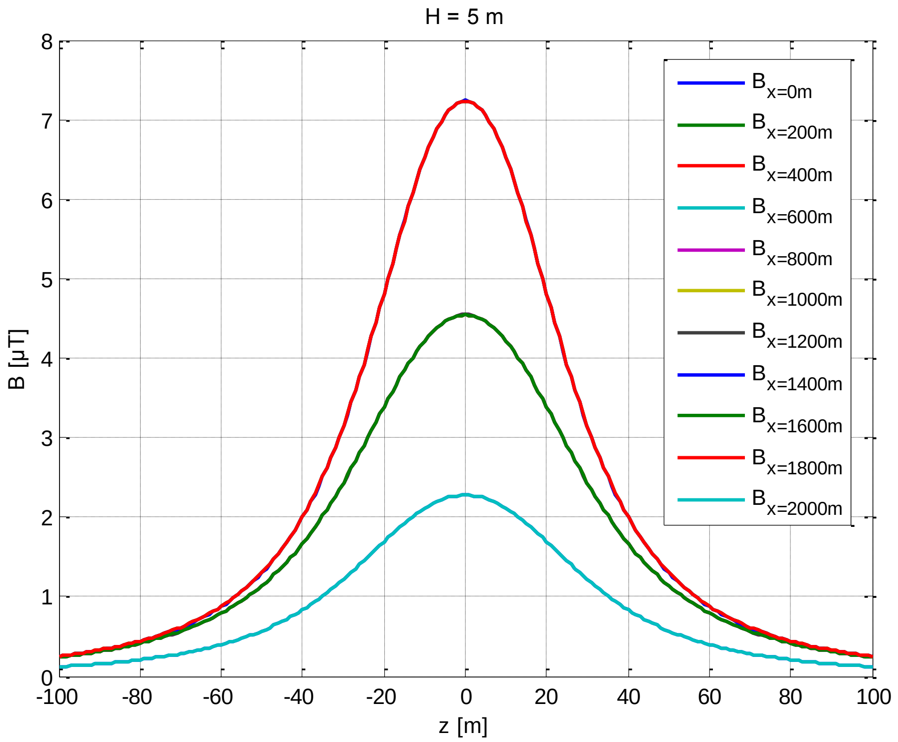

Figure 5.59: *Comparison between the magnetic field profiles at the vertical sections of interest, i.e. under the poles and the mid-spans, for the 380 kV double-circuit overhead line, at 5 m from the ground with* $I_1 = I_2 = 2040$ *A.*

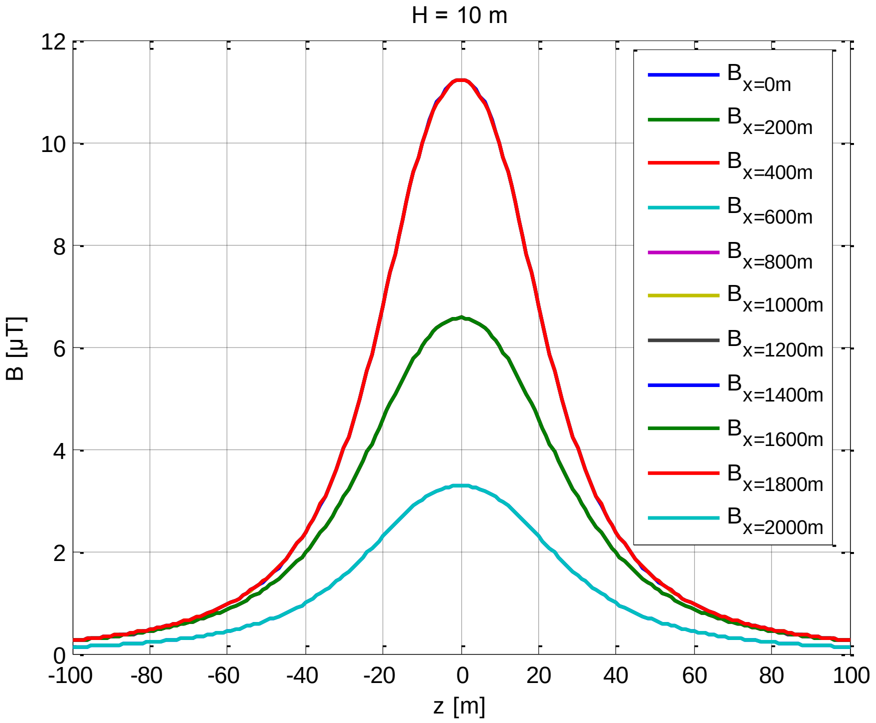

Figure 5.60: *Comparison between the magnetic field profiles at the vertical sections of interest, i.e. under the poles and the mid-spans, for the 380 kV double-circuit overhead line, at 10 m from the ground with* $I_1 = I_2 = 2040$ *A.*

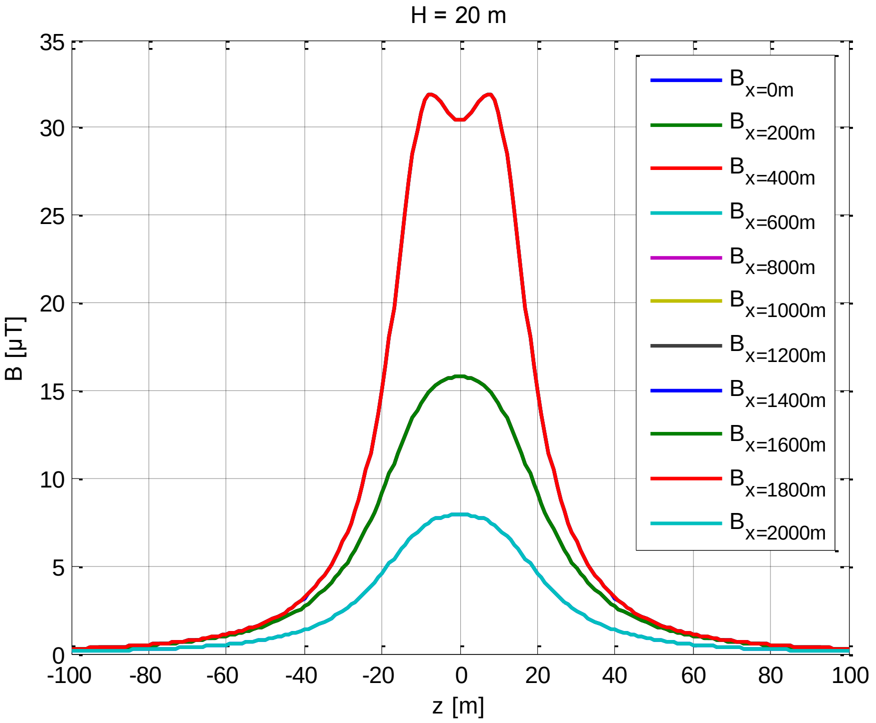

Figure 5.61: *Comparison between the magnetic field profiles at the vertical sections of interest. i.e. under the poles and the mid-spans, for the 380 kV double-circuit overhead line, at 20 m from the ground with* $I_1 = I_2 = 2040$ *A.*

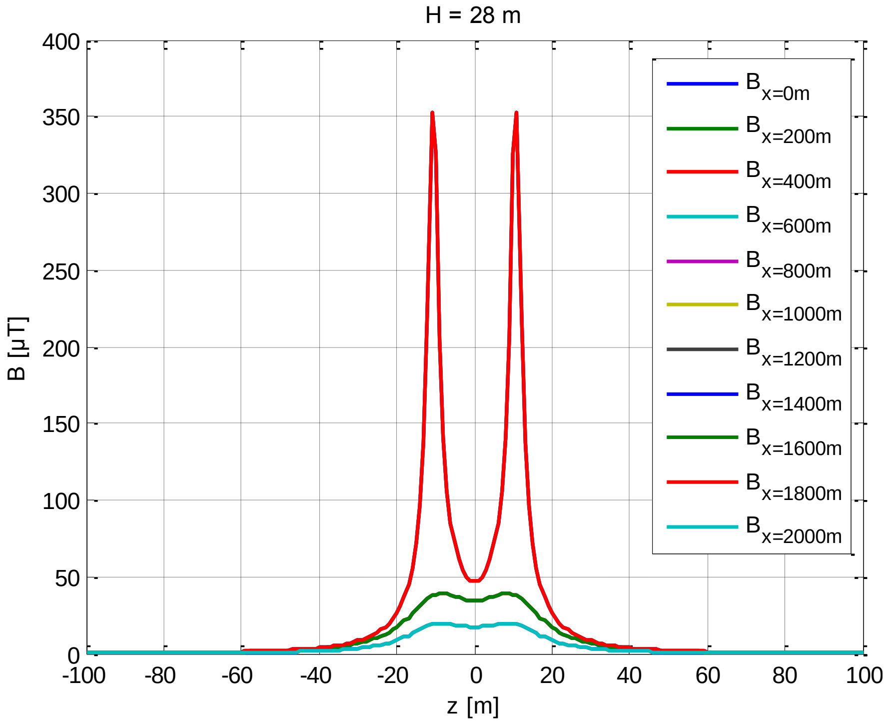

Figure 5.62: *Comparison between the magnetic field profiles at the vertical sections of interest, i.e. under the poles and the mid-spans, for the 380 kV double-circuit overhead line, at 28 m from the ground with* $I_1 = I_2 = 2040$ *A.*

Same considerations hold for the results depicted in Figs. 5.59-5.62 about the 380 kV double-circuit overhead line. There are three groups of coincident magnetic field profiles: the first group of $B_{x=200m}$, $B_{x=600m}$, $B_{x=1000m}$, $B_{x=1400m}$ and $B_{x=1800m}$ (under the mid-span areas), the second group of $B_{x=800m}$, $B_{x=1200m}$ and $B_{x=1600m}$ (under the second, third and fourth pole) and the third group of $B_{x=200m}$ and $B_{x=2000m}$ (under the first and fifth pole). The results, at all heights from the ground considered, have also proven that the first group of the B_{3D} profiles provide the highest values of the field and the second group provides two times the values of the third group. The same considerations as in the single-circuit case hold: the first group of field profiles is the highest since it effectuates the calculation under the mid-span areas and the second group of field profiles results two times the third group since it calculates the field under the intermediate poles of the line.

Finally, the case where B_{3D} tends at B_{2D} is examined, in the sense that the tri-dimensional calculation is made without considering the catenary effect of the line. This is achieved by increasing the parameter a of the catenary in eq. 5.18 and Figs. 5.63 - 5.70 are the results of the simulations made for the sake of comparison between B_{2D} and B_{3D} at the same vertical sections considered previously, i.e. at x = 0 m, x = 100 m, x = 200 m, x = 300 m, x = 400 m, x = 500 m, x = 600 m, x = 700 m, x = 800 m, x = 900 m and x = 1000 m for the 132 kV single-circuit overhead line and at x = 0 m, x = 200 m, x = 400 m, x = 600 m, x = 800 m, x = 1000 m, x = 1200 m, x = 1400 m, x = 1600 m, x =

1800 m and *x* = 2000 m for the 380 kV double-circuit overhead line. The simulations according to the tri-dimensional approach have been also made in correspondence to the mid-span area, similar to the bi-dimensional approach, in order to have comparable results.

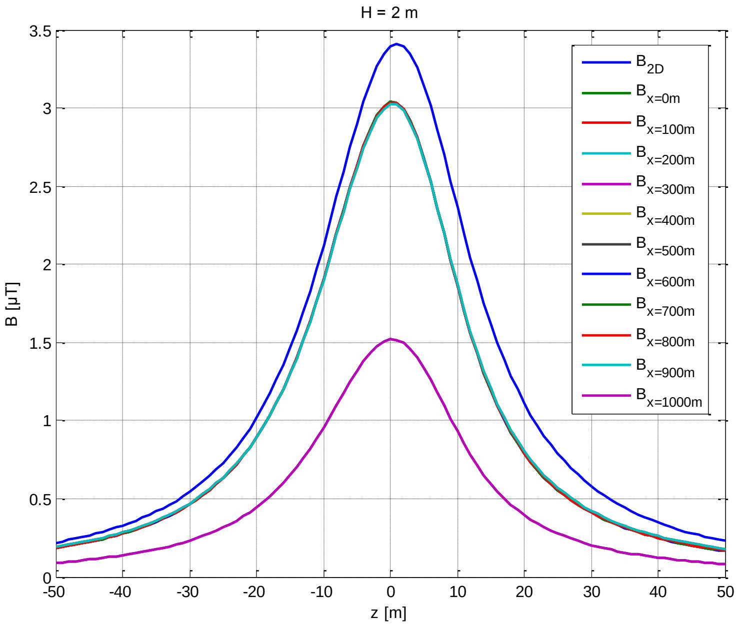

Figure 5.63: *Comparison between the magnetic field profiles of B_{2D} and B_{3D} calculated without considering the catenary form of the 132 kV single-circuit overhead line, at the vertical sections of interest, i.e. under the poles and the mid-spans, at 2 m from the ground with I = 385 A.*

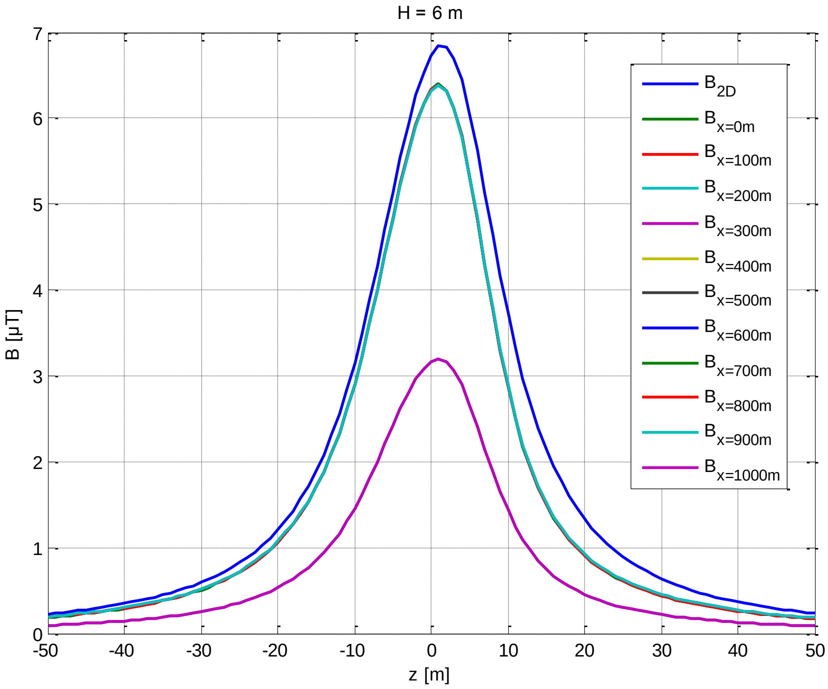

Figure 5.64: *Comparison between the magnetic field profiles of B_{2D} and B_{3D} calculated without considering the catenary form of the 132 kV single-circuit overhead line, at the vertical sections of interest, i.e. under the poles and the mid-spans, at 6 m from the ground with I = 385 A.*

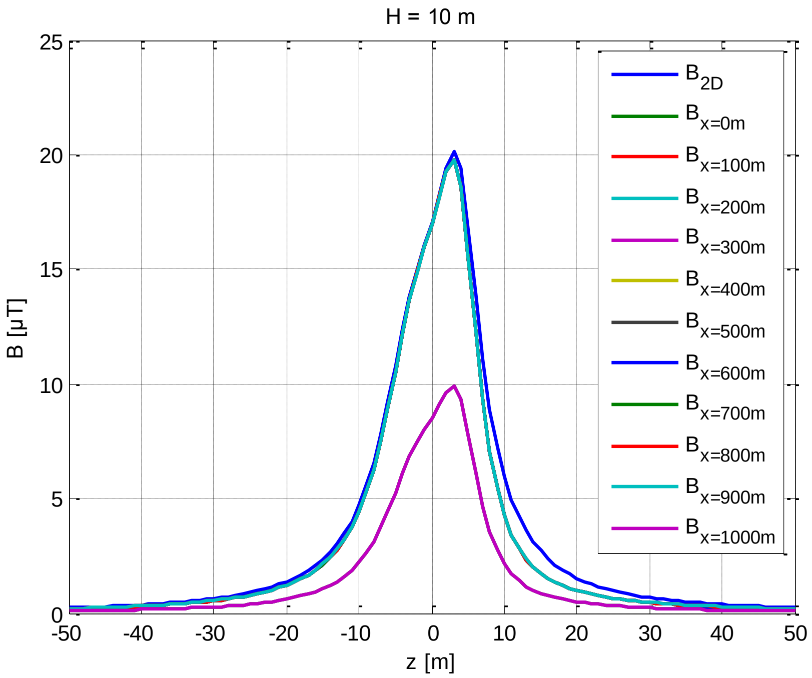

Figure 5.65: *Comparison between the magnetic field profiles of B_{2D} and B_{3D} calculated without considering the catenary form of the 132 kV single-circuit overhead line, at the vertical sections of interest, i.e. under the poles and the mid-spans, at 10 m from the ground with I = 385 A.*

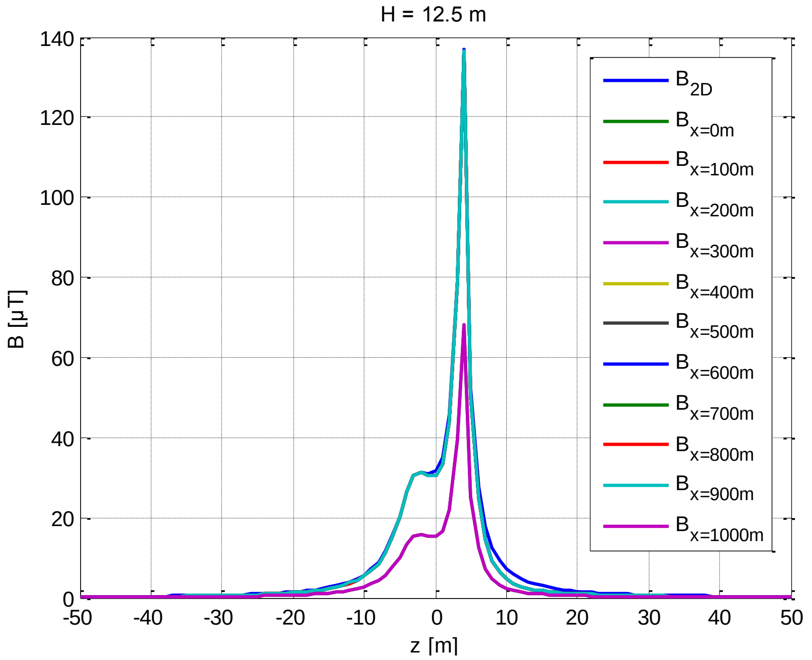

Figure 5.66: *Comparison between the magnetic field profiles of B_{2D} and B_{3D} calculated without considering the catenary form of the 132 kV single-circuit overhead line, at the vertical sections of interest, i.e. under the poles and the mid-spans, at 12.5 m from the ground with I = 385 A.*

From Figs. 5.63-5.66, dealing the 132 kV single-circuit overhead line, is verified, as expected, that the magnetic field profiles ($B_{x=100m}$, $B_{x=200m}$, $B_{x=300m}$, $B_{x=400m}$, $B_{x=500m}$, $B_{x=600m}$, $B_{x=700m}$, $B_{x=800m}$ and $B_{x=900m}$) along the straight, finite, parallel to the ground line, calculated at different heights from the ground are the same, except for the two extreme cases of $B_{x=0m}$ and $B_{x=1000m}$ that result half times smaller, as explained previously. Another consequence of the fact that the line conductors have not infinite length is that in the cases of the field calculation at 2 m and 6 m from the ground, the field B_{2D}, derived by the bi-dimensional calculation code, still results higher than the field B_{3D} derived by the tri-dimensional calculation code. Nevertheless, the influence of the finite length of the line is compensated by the smaller distance of the conductors from the field-points in the cases where the conductors distant 10 m and 12.5 m from the ground resulting at coincident curves of the B_{2D} and B_{3D} profiles.

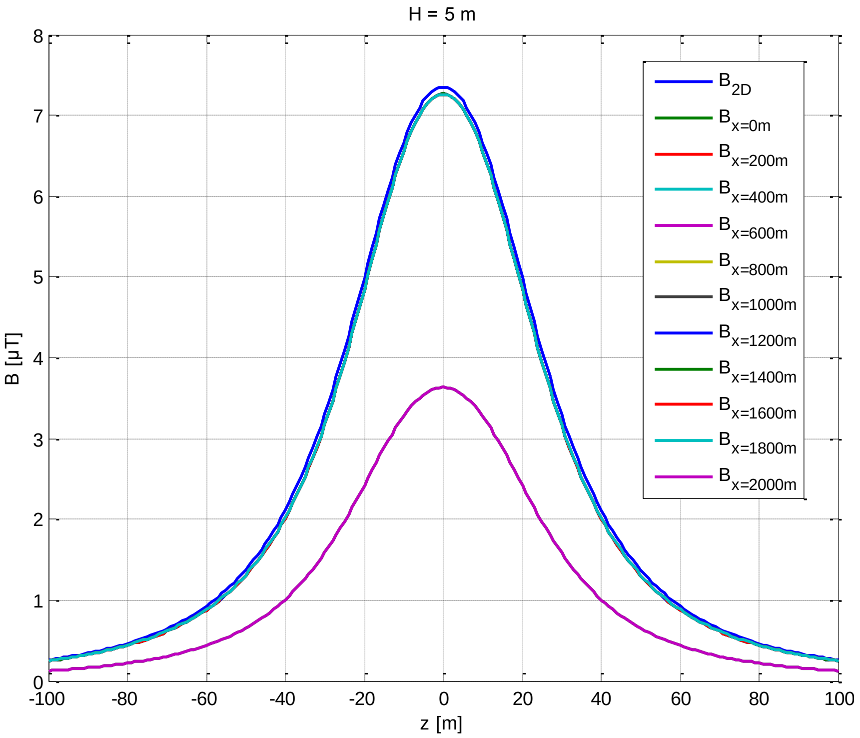

Figure 5.67: *Comparison between the magnetic field profiles of* B_{2D} *and* B_{3D} *calculated without considering the catenary form of the 380 kV double-circuit overhead line, at the vertical sections of interest, i.e. under the poles and the mid-spans, at 5 m from the ground with* $I_1 = I_2 = 2040$ *A.*

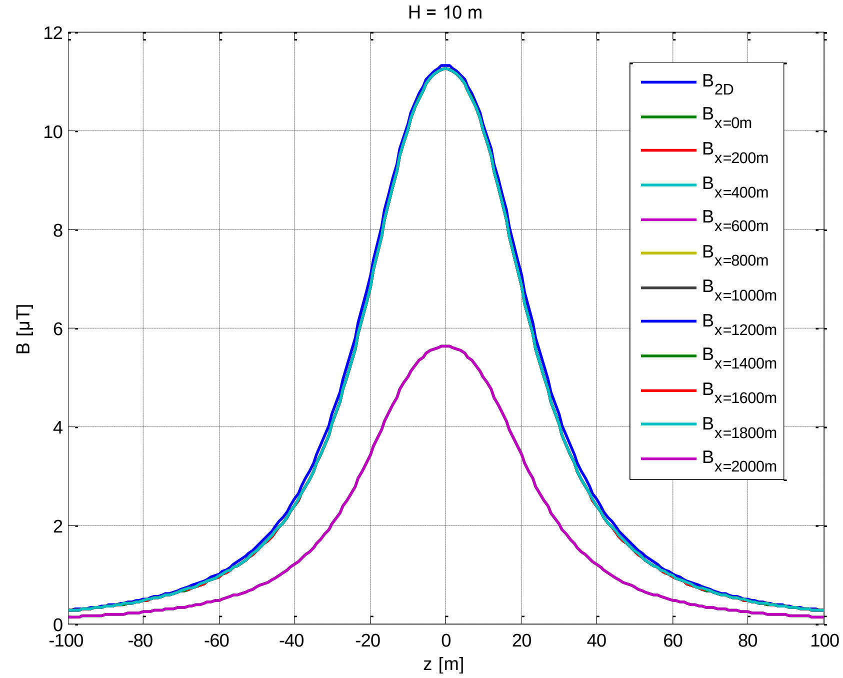

Figure 5.68: *Comparison between the magnetic field profiles of* B_{2D} *and* B_{3D} *calculated without considering the catenary form of the 380 kV double-circuit overhead line, at the vertical sections of interest, i.e. under the poles and the mid-spans, at 10 m from the ground with* $I_1 = I_2 = 2040$ *A.*

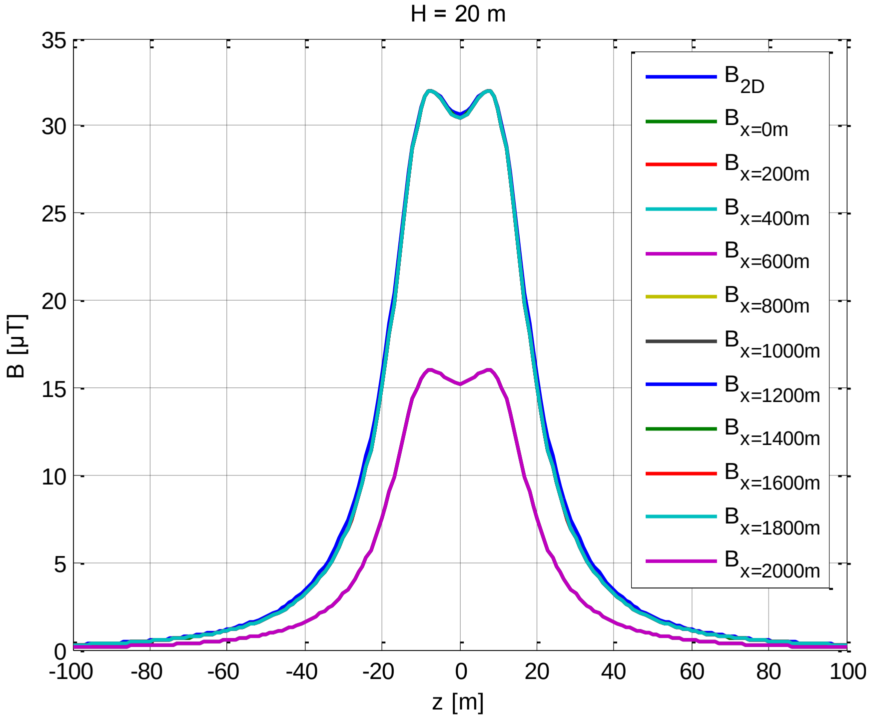

Figure 5.69: *Comparison between the magnetic field profiles of* B_{2D} *and* B_{3D} *calculated without considering the catenary form of the 380 kV double-circuit overhead line, at the vertical sections of interest, i.e. under the poles and the mid-spans, at 20 m from the ground with* $I_1 = I_2 = 2040$ *A.*

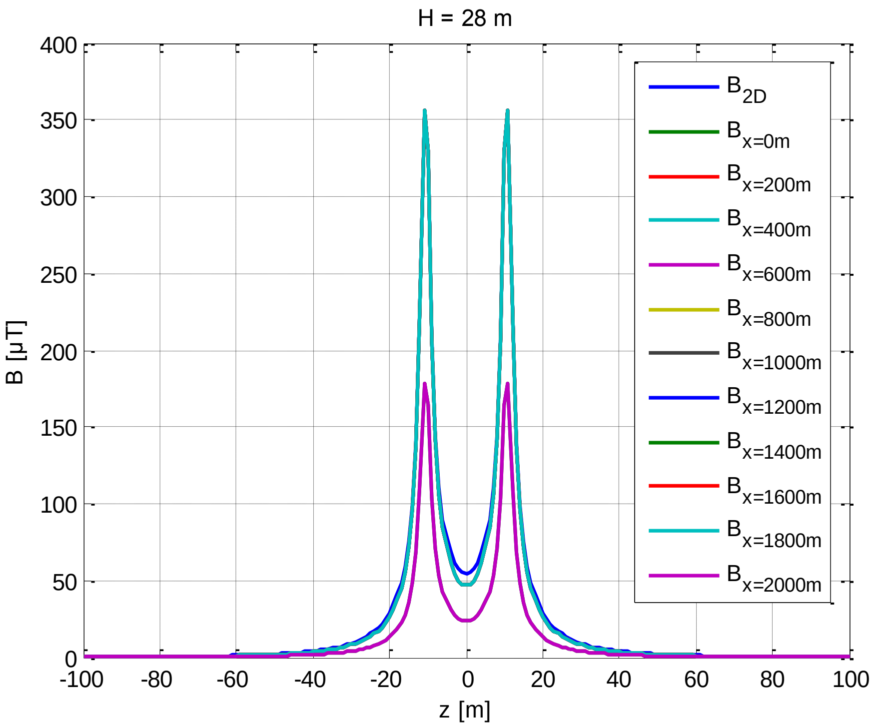

Figure 5.70: *Comparison between the magnetic field profiles of B_{2D} and B_{3D} calculated without considering the catenary form of the 380 kV double-circuit overhead line, at the vertical sections of interest, i.e. under the poles and the mid-spans, at 28 m from the ground with $I_1 = I_2 = 2040$ A.*

Same considerations hold for the 380 kV double-circuit overhead line as proven by Figs. 5.67-5.70. The magnetic field profiles ($B_{x=200m}$, $B_{x=400m}$, $B_{x=600m}$, $B_{x=800m}$, $B_{x=1000m}$, $B_{x=1200m}$, $B_{x=1400m}$, $B_{x=1600m}$ and $B_{x=1800m}$) along the straight, finite, parallel to the ground line, calculated at different heights from the ground are the same, except for the two extreme cases of $B_{x=0m}$ and $B_{x=2000m}$ that result half times smaller, because they are calculated at the two extreme points of the line. In these cases, the influence of the finite length of the line is drastically compensated by the great value of the currents, resulting thus, at coincident curves of the B_{2D} and B_{3D} profiles for all calculated heights of the ground.

Concluding, all the above mentioned observations regarding the tri-dimensional numerical code for the calculation of the magnetic field generated by overhead power lines, can serve as proves for the proper implementation of the magnetic field theory and for the correct functioning of the software created.

CHAPTER 6

“SMART” MEASUREMENT AND EVALUATION SYSTEM OF THE MAGNETIC FIELD

6.1 GENERAL IDEA

The growing concern among the population for the impact of electromagnetic fields from power systems, unavoidably leads to the construction of sophisticated measurement and evaluation systems of the magnetic field that can provide reliable and accurate indications even in complex 3D arrangements of the field sources. Such arrangements occur more and more frequently in the vicinity of residential and industrial areas, where overhead and underground lines of different voltage rating and geometry, as well as more or less wide substations, often lie close to each other. In this framework, an innovative measurement and evaluation system capable of matching this need has been constructed, calibrated and tested by actual measurements in situ.

The innovation of this measurement and evaluation system is twofold:

1) the “smart” measurement device - that consists essentially of a 3D field probe plus proper signal conditioning circuits plus a data-logger system - not only measures the components of the magnetic induction field in a Cartesian coordinate system, B_x, B_y and B_z [53] - [56], but also records and stores the rms value of the three field components as a function of time, for subsequent analytical processing. Usually magnetic field measuring devices record and store only the rms value of total magnetic induction field, B;

2) a 3D post-processing of the three field components stored over the monitoring period is performed, where the values of the field components are correlated to the corresponding rms values of source currents – that vary randomly with time as the load changes - via a multi-linear regression technique. This enables the extrapolation of the rms value of the magnetic field to any combination of source currents of interest. Indeed, when the number and the geometrical complexity of the sources is increased, a linear relationship between the rms value of total magnetic induction and source currents can be hardly found, whereas one can be pretty confident that such a linear relationship exists between the rms values of magnetic induction components and source currents. Moreover, it must be pointed out that in cases of multiple and complex 3D field sources, in practice the exact geometry of the sources is often unknown or not accessible: in such cases, even powerful 3D codes might fail in forecasting accurately the field value at a given point of interest. For this reason, where a 3D code fails an empirically-derived multi-linear relationship can succeed.

The investigation is divided in three stages:

1) the first stage is carried out in the laboratory and has the purpose of creating an appropriate three-dimensional measurement device of the magnetic field, that is based on an isotropic 3D coil employed as a magnetic field probe (see Fig. 6.1);

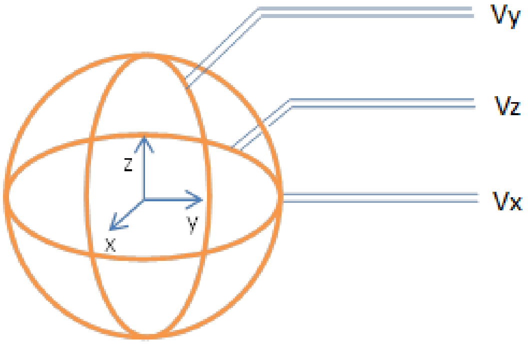

Figure 6.1: *An isotropic 3D coil employed as a magnetic field probe.*

2) the second stage is a theoretical study, where analytical multilinear regression algorithms are developed in Matlab® environment for correlating measurement results of B_x, B_y and B_z at a given field point to the relevant values of time-varying currents of a certain batch of sources. An increasing number of sources can be considered, thereby increasing the complexity and the effectiveness of the algorithm at the same time. The theoretical basis for this development is contained in [57] - [59]. Of course, this stage can be performed at the same time or even before the first stage;

3) the third part consists in an experimental campaign in the field in the presence of multiple current sources. The field components monitored and recorded are processed later on via the algorithm developed at stage 2), in order to derive the numerical values of the coefficients of the multilinear relationship between field components and source currents, thereby validating the evaluation algorithm.

6.2 CONSTRUCTION, CALIBRATION AND CHARACTERIZATION OF THE MEASUREMENT DEVICE

The block diagram of a single channel of the 3D measurement device – i.e. the field probe (in this case an one-dimensional induction coil), plus the relevant signal conditioning circuit, plus a data-logger system – is displayed in Fig. 6.2; a picture of the electronic signal conditioning circuit of a single channel is shown in Fig. 6.3.

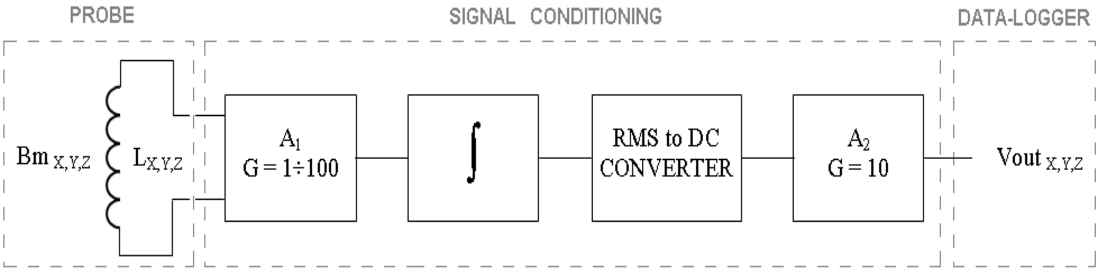

Figure 6.2: *Block diagram of a single channel of the measurement device of the magnetic induction field (X, Y, Z denotes that this channel is repeated over all the three Cartesian components of the field) isotropic 3D coil employed as a magnetic field probe.*

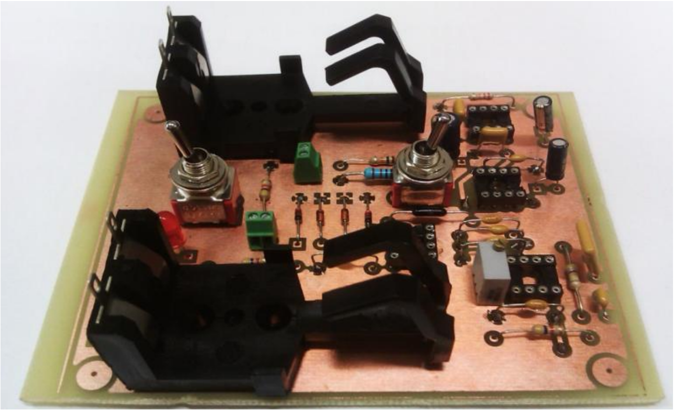

Figure 6.3: *Picture of the electronic signal conditioning circuit of a single channel of the 3D measurement device*

The rms magnetic induction B under exam is converted into a voltage signal by the induction coil *L*. According to the European legislation, that imposes constraints on the coil surface limits, a rectangular coil with 100 turns and an area of ~0.01 m^2 has been selected.

The transfer function $V = f(B)$ results from the fundamental Faraday's law of induction:

$$v(t) = -N \cdot \frac{\mathrm{d}\Phi(t)}{\mathrm{d}t} = -N \cdot \frac{\mathrm{d}}{\mathrm{d}t}\left[\int_A \vec{B}(t) \cdot \vec{n} \cdot \mathrm{d}A\right] = -N \cdot \frac{\mathrm{d}}{\mathrm{d}t}\left[B(t) \cdot A\right] \tag{6.1}$$

$$V_{RMS} = N \cdot \frac{2\pi}{\sqrt{2}} \cdot f \cdot \hat{B} \cdot A = N \cdot 2\pi \cdot f \cdot B \cdot A \tag{6.2}$$

where Φ is the magnetic flux passing through the coil with an area *A* and a number of turns *N*, *B* is the rms value of magnetic induction and *f* is the current frequency.

By substituting $A = 0.01$ m^2, $N = 100$, $f = 50$ Hz and by assuming the minimum measured value of magnetic induction $B = 0.1$ μT, equation (6.1) gives a voltage of *V*

= 31 μV: therefore, the integrated electronic circuit must be able to accept a minimum input voltage of 31 μV.

This signal is amplified by the first stage A1 of Fig. 6.2, which has two possible gain settings – 1 and 100 – and also includes a simple circuit for overvoltage protection.

In order to restore the waveform of the magnetic field and eliminate the dependence of equation (6.2) on frequency, the inverse of the mathematical operation carried out in (6.2) should be performed, namely integration, by introducing an integrator with variable gain (to permit calibration of the system). The integrator circuit ensures that the signal frequency response is flat in the frequency range concerned (from a few Hz to 400 Hz for low frequency magnetic field measurements according to [50]). A True RMS to DC Converter follows, that generates a dc output equal to the rms value of the input signal and finally, since the maximum expected amplitude of the output signal is approximately 200 mV, a second amplifier stage A2 has been added with gain 10.

Each channel - shown in Fig. 6.2 - of the 3D measurement device of the magnetic induction field here developed has to be tested and calibrated in order to estimate the device proportionality coefficient between applied current and generated magnetic field, by checking for linearity and comparing the reading of the instrument with other commercial instrumentation available. After all these tests have given a positive outcome, the whole instrument is finally assembled (see Fig. 6.4), achieving in this way a three-axial probe that performs 3D field measurements and stores the three field components values.

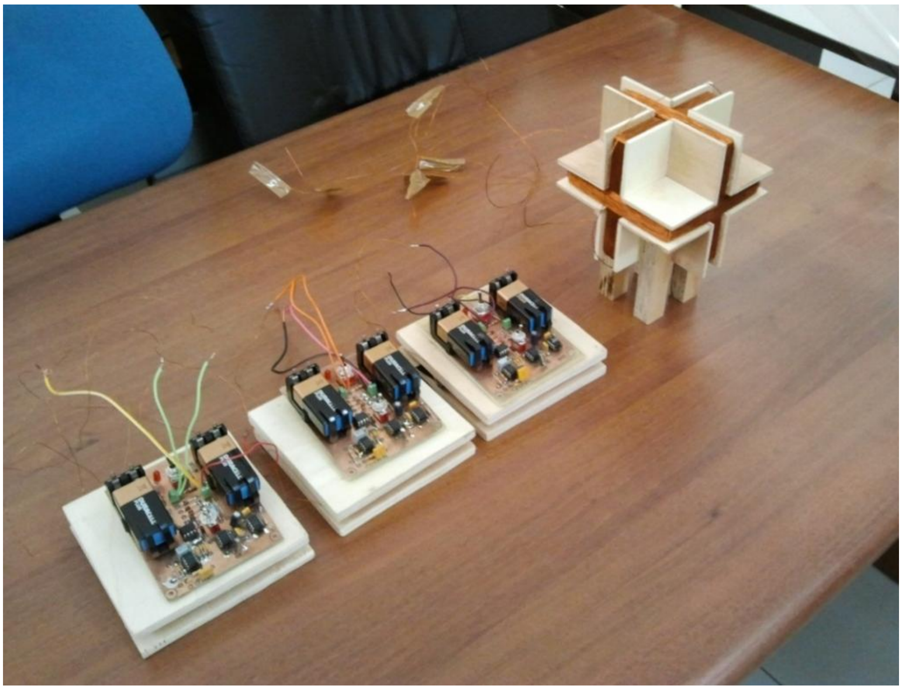

Figure 6.4: *3D 'smart' measurement system.*

The circuit for testing the performance of the proposed measurement device consists of a Keithley AC current source plus a "Helmholtz" system, made of a square coil with a side length of 1 m that ensures an internal region of nearly uniform magnetic field; the field points of interest are located in the coil center. The value and the direction of the magnetic induction field in the center of the Helmholtz coil are known, since the value of the current applied is known, and are used for the calibration of the measuring instrument. Thus, by adjusting the current value through the circuit shown in Fig. 6.5, it is possible to adjust the value and direction of magnetic induction at the center of the Helmholtz coil.

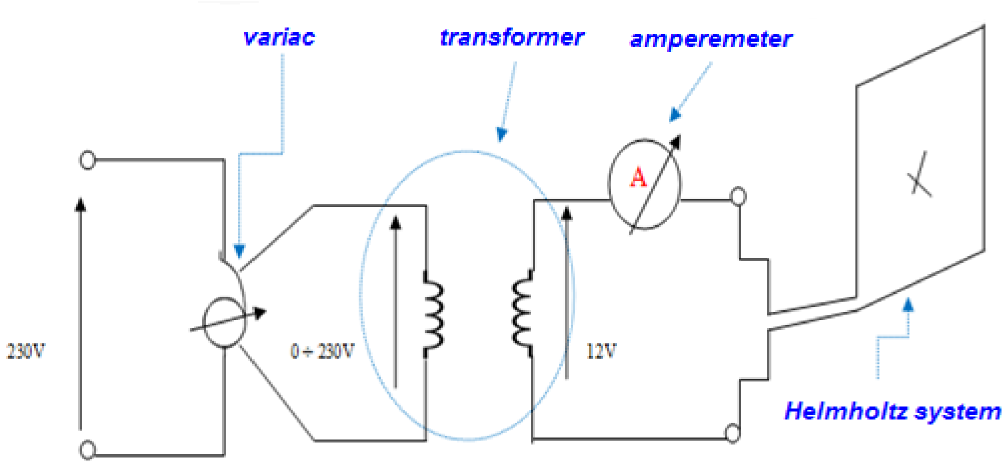

Figure 6.5: *Testing performance circuit of the measurement device.*

Applying the Biot-Savart law to the magnetic circuit represented by the "Helmholtz" system, the relationship between the current flowing in the system and the value of the magnetic induction generated was obtained. Taking into account the uncertainty due to the mechanical design, we have:

$$B_{ref} = 1.14\mu T \cdot A \pm 0.4\% \tag{6.3}$$

This result was verified with measurements made using as a reference instrument the Wandel & Goltermann mod. EFA 3.

In order to calibrate each channel of the 3D measurement device proposed, different measurements were carried out by setting different rms values of 50 Hz current in the "Helmholtz" system, ranging from 0.175 A to 3.51 A in steps of 0.175 A, thereby yielding rms values of magnetic field ranging from 0.2 μT to 4.0 μT (the so-called reference magnetic field values, B_{ref}). The quantities to be measured (coil current and output voltage of the signal conditioning system applied to the coil that act as probe) were acquired using a National Instruments board (model NI 9239, with 4 simultaneous input channels of 24 bit, 50 kS/s) managed by an appropriate software for automatic processing of the acquired data, thereby achieving the measured magnetic field values, B_{meas}. The results were then verified by a further series of measures carried out by varying the magnetic field from 0.1 μT to 2.0 μT in steps of 0.1 μT. The results obtained are depicted in Figs. 6.6 and 6.7 and have shown that the measurement uncertainty (with coverage factor k = 2) is 0.5% maximum for all three systems.

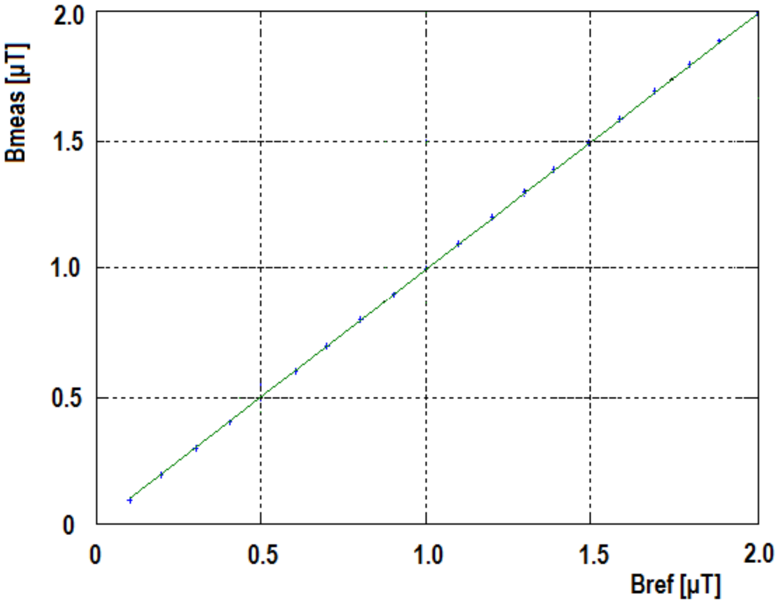

Figure 6.6: *Comparison between reference (solid line) and measured (crosses) values of the magnetic field.*

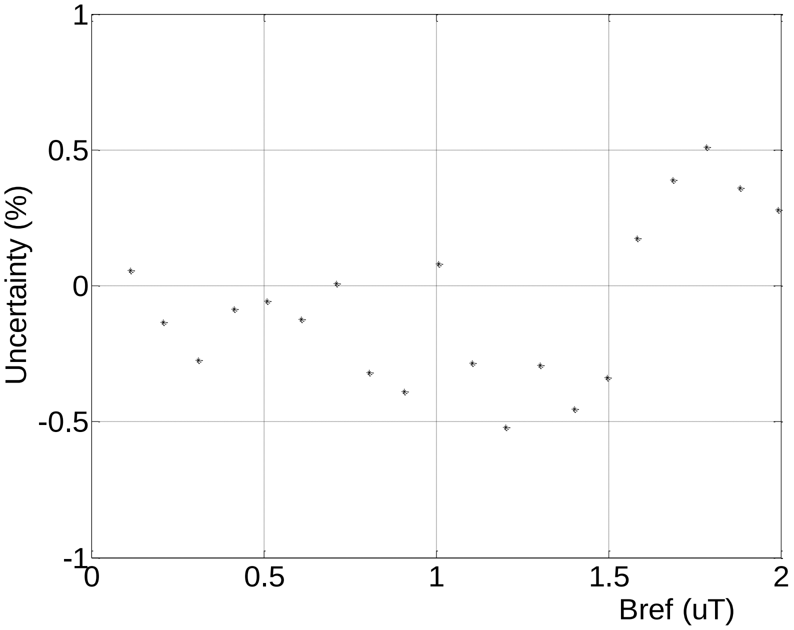

Figure 6.7: *Measurement uncertainty from the comparison between reference and measured values of the magnetic field.*

To improve the characterization of the measurement system, an estimate S of the standard deviation of the measurements performed using the proposed measurement device has also been attained as follows:

1) several field measurements have been carried out in sequence with the same value of pre-set current in the "Helmholtz" system and the relevant standard deviation has been estimated (see standard deviation of measured values of the magnetic field, red dots in Fig. 6.8);

2) these field measurements have been compared with the field values calculated simultaneously from synchronous current measurements, and the relevant standard deviation has been estimated (see standard deviation of reference values of the magnetic field, blue dots in Fig. 6.8);

3) points 1) and 2) have been repeated by varying the pre-set magnetic induction values in the range from 0.25 μT to 4 μT.

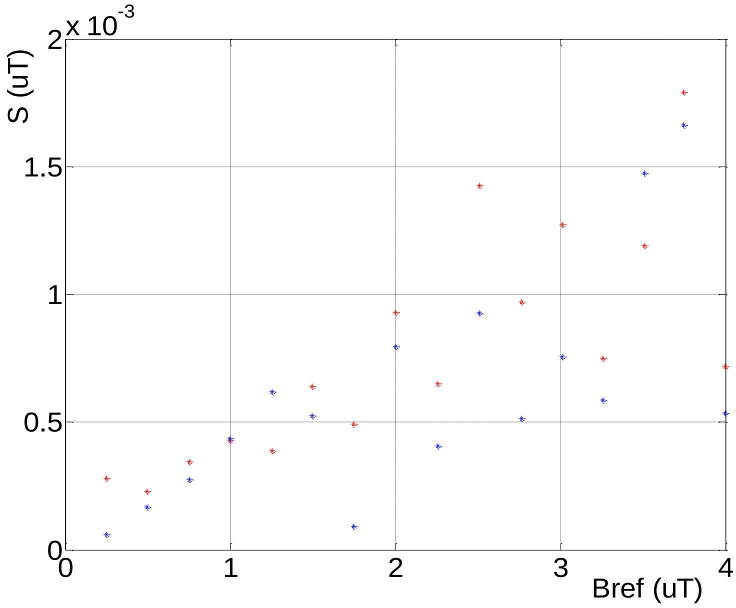

__Figure 6.8:__ Standard deviation of reference (blue points) and measured (red points) values of the magnetic field.

As it can be argued from Fig. 6.8, very similar amplitude values of estimated standard deviation have been obtained for reference and measured field values. This means that the variation in the measurement results does not depend on the measuring system itself, but on the power supply of the "Helmholtz" system. Indeed, since the power supply depends directly on the instant value of the grid voltage, that in turn varies randomly with the load demand, it is unable to keep the current strictly constant over time in the "Helmholtz" system, that acts as reference magnetic field source.

6.3 FIRST TESTING OF THE MEASUREMENT DEVICE

6.3.1 Measurements in Situ

The performance of the proposed measurement device has been tested in situ. Figure 6.9 is an actual photo of the area of interest and Fig. 6.10 is its schematization.

Figure 6.9: *Photo of the double-circuit power line close to the measurement point.*

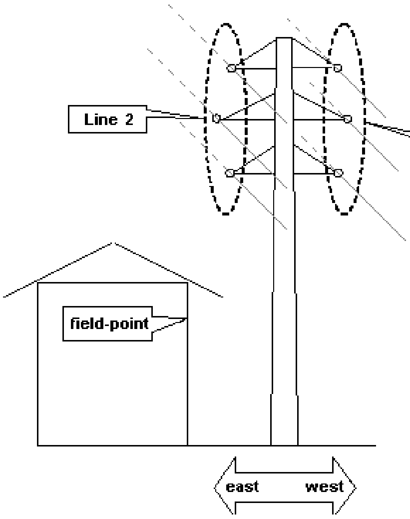

Figure 6.10: *Schematization of the double-circuit power line tower and of the measurement point nearby.*

The measurements were performed in the proximity of a double-circuit overhead MV power line of known geometry, in correspondence of the half span between one pole and the adjacent transformation cabin. This fact is depicted in the map of the area of interest in Fig. 6.11, and is the main reason why this particular point was chosen since it can guarantee the presence of a significant contribute of the magnetic field on the z-axis. The two circuits consist of bare conductors with ampacity I_1=285 A and I_2=230 A, attached on opposite sides of the poles and placed at the same height from the ground (~9 m). Measurements took place at 6 m from the ground and at 5 m distance from the pole.

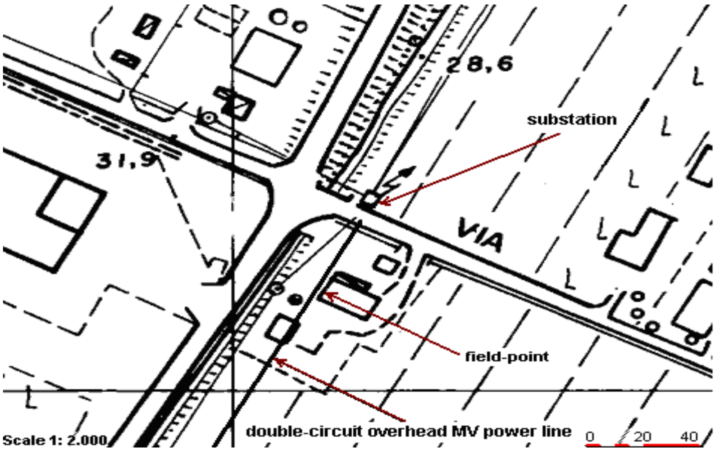

Figure 6.11: *Map of the area of interest.*

The magnetic field components have been monitored and recorded every 5 min for a period of 24 h. The instant values of the line currents have been provided by the distribution utility. The measurement data are illustrated in Fig. 6.12, which displays the plots of the currents vs. time, and in Fig. 6.13, which displays the plots of the magnetic field components vs. time. In Fig. 6.13 the value of B_{tot} is calculated by the composition of the three components, B_x, B_y and B_z using the relationship:

$$B = \sqrt{B_x^2 + B_y^2 + B_z^2} \tag{6. 4}$$

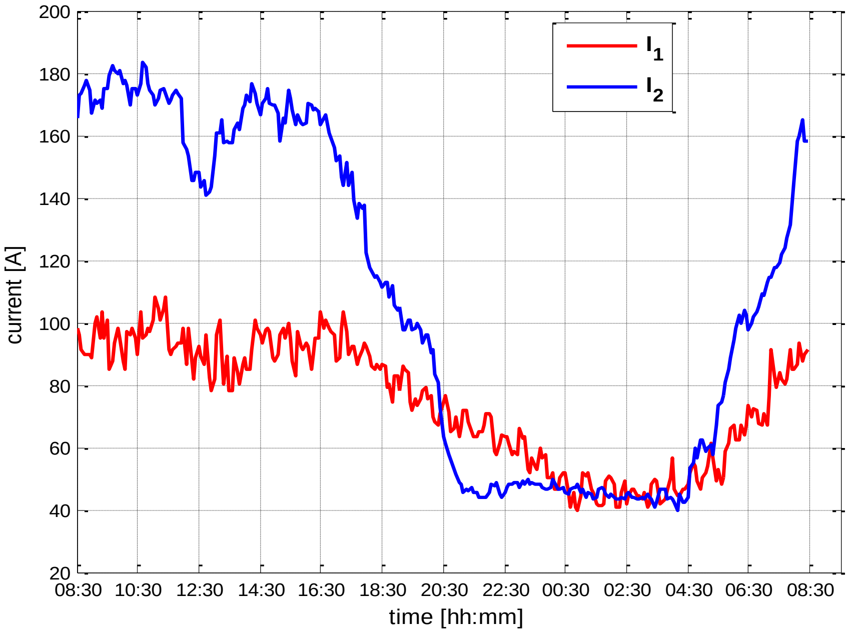

Figure 6.12: *24 h monitored instant values of the currents I_1 and I_2.*

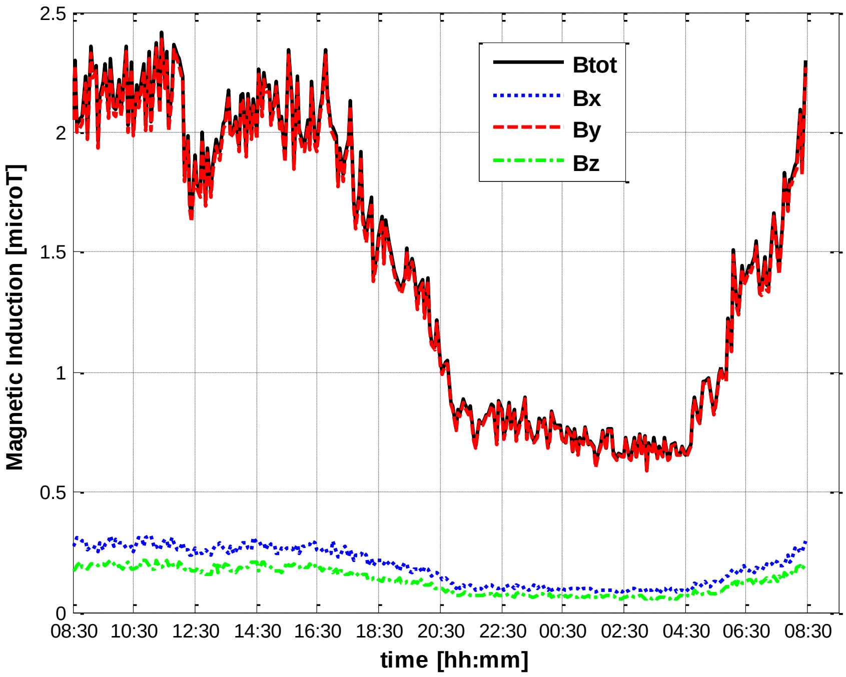

Figure 6.13: *24 h measurements of the magnetic field components.*
B_{tot} *calculated via the three components according to eq. (6.4) is also displayed.*

6.3.2 Data Processing

The handling and storage of measurement results are managed by a PLC in order to be subsequently used for extrapolating the functional relationship between the applied current and the generated magnetic field components.

Coming to this stage of the investigation, as previously argued, in the presence of multiple (say, *M*) source currents the vector composition of the total magnetic field makes the linear dependence of the total magnetic field *B* on the currents unlikely to happen in general, whereas a linear functional relationships can be expected to hold between source currents and the components of the magnetic field. Following this procedure, expressions like the following can be derived:

$$B_x = \sum_{i=1}^{M} k_{x,i}\, I_i \tag{6. 5.a}$$

$$B_y = \sum_{i=1}^{M} k_{y,i}\, I_i \tag{6. 5.b}$$

$$B_z = \sum_{i=1}^{M} k_{z,i}\, I_i \tag{6. 5.c}$$

Equations (6.5) have been validated experimentally using the measured data of *B*-field components (see Fig. 6.13) in Matlab® environment and the numerical values of coefficients $k_{x,1}$, $k_{x,2}$, $k_{y,1}$, $k_{y,2}$, $k_{z,1}$ and $k_{z,2}$, (since $i = 1, 2$ in our case), have been derived by the procedure of multiple linear regression. Doing so, the following expressions have been established:

$$B_x = k_{x,1} I_1 + k_{x,2} I_2 \Rightarrow B_x = 0.0008 \cdot I_1 + 0.0012 \cdot I_2 \tag{6. 6.a}$$

$$B_y = k_{y,1} I_1 + k_{y,2} I_2 \Rightarrow B_y = 0.0059 \cdot I_1 + 0.0091 \cdot I_2 \tag{6. 6.b}$$

$$B_Z = k_{Z,1} I_1 + k_{Z,2} I_2 \Rightarrow B_Z = 0.0005 \cdot I_1 + 0.0008 \cdot I_2 \tag{6. 6.c}$$

Figs. 6.14 are the results of the correlation analysis and show the trends of the components $B_{x,measured}$, $B_{y,measured}$ and $B_{z,measured}$ vs. B_x, B_y and B_z calculated.

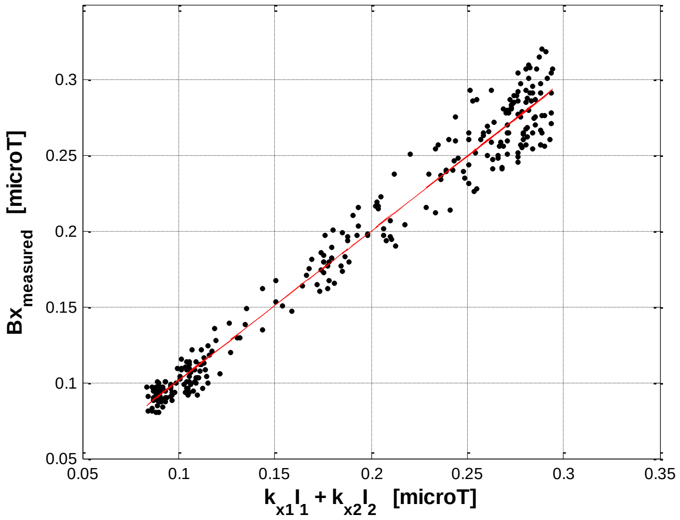

Figure 6.14.a: *Correlation analysis of B_x measured vs. B_x calculated.*

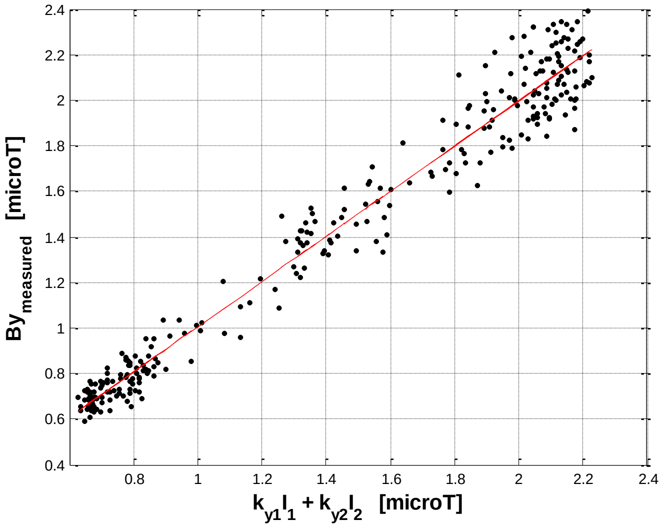

Figure 6.14.b: *Correlation analysis of B_y measured vs. B_y calculated.*

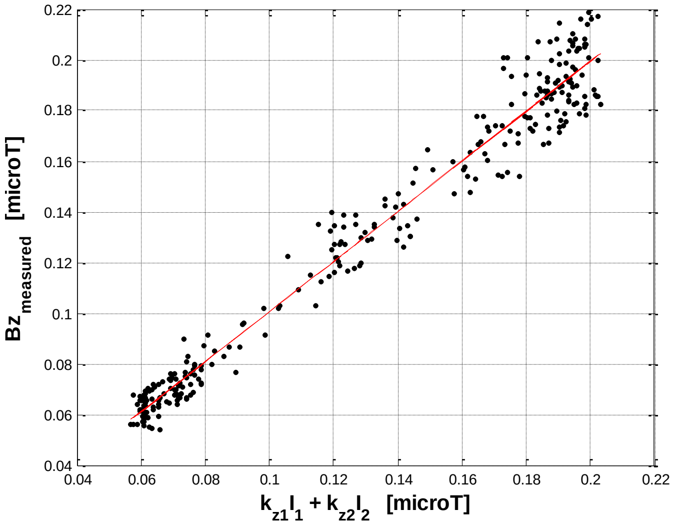

Figure 6.14.c: *Correlation analysis of B_z measured vs. B_z calculated.*

The knowledge of these coefficients enables the estimation of the magnetic field under load conditions different from those encountered during the measurement, in particular allows the estimation of the three components of the magnetic field vector at the point of maximum exposure and also allows the comparison of that value with the legal limits. The method of estimating the magnetic field described above is called "indirect method" and the Italian legislation has set boundaries in its use: the maximum value of the current should be the ampacity of conductors, and the correlation index between current and magnetic field should not less than 0.9. In the case of multiple linear regression, the Italian law has not yet been updated since this is an innovative approach. However, the correlation coefficients of the multiple linear regression applied to the field components in this paper, result greater than 96% for all three components, fact that indicates that the regression lines approximate satisfactorily the real data points.

The relations used are listed below:

$$B_{x,\max} = k_{x,1}\, I_{1,\max} + k_{x,2}\, I_{2,\max} \Rightarrow B_{x,\max} = 0.504\,\mu T \qquad (6.\ 7.a)$$

$$B_{y,\max} = k_{y,1}\, I_{1,\max} + k_{y,2}\, I_{2,\max} \Rightarrow B_{y,\max} = 3.775\,\mu T \qquad (6.\ 7.b)$$

$$B_{z,\max} = k_{z,1}\, I_{1,\max} + k_{z,2}\, I_{2,\max} \Rightarrow B_{z,\max} = 0.327\,\mu T \qquad (6.\ 7.c)$$

$$B_{\max} = \sqrt{B^2_{x,\max} + B^2_{y,\max} + B^2_{z,\max}} \Rightarrow B_{\max} = 3.823 \mu T \qquad (6.\ 8)$$

with $I_{1,max}$=285 A, $I_{2,max}$=230 A, $k_{x,1}$= 0.0008, $k_{x,2}$= 0.0012, $k_{y,1}$= 0.0059, $k_{y,2}$= 0.0091, $k_{z,1}$= 0.0005, $k_{z,2}$= 0.0008.

6.4 SECOND TESTING OF THE MEASUREMENT DEVICE

The novelty here is that the measurement device and the multilinear regression algorithm are applied to a three-phase single-circuit power line where the time-dependent rms values of each phase are known. In practice, power systems rarely have perfectly balanced loads, currents, voltages and impedances in all three phases, so the particular interest of this case is to examine if the three-phase currents are equilibrated and in case that they are not, which are the consequences in terms of the magnetic field.

6.4.1 Measurements in Situ

A second campaign of measurements in situ has been effectuated for testing the proposed measurement device performance. Fig. 6.15 is an actual photo of the area of interest and Fig. 6.16 is its schematization.

Figure 6.15: *Photo of the single-circuit power line close to the measurement point.*

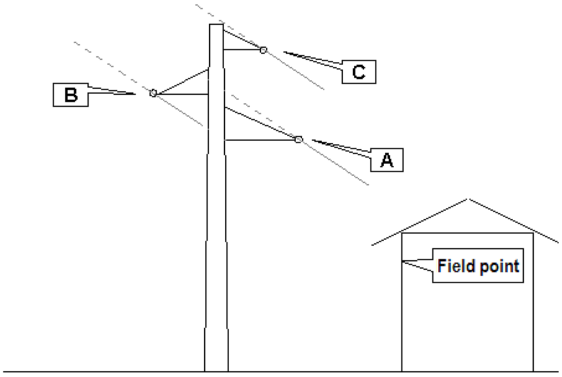

Figure 6.16: *Schematization of the single-circuit power line tower and of the measurement point nearby.*

The measurements were performed in the proximity of a single-circuit overhead HV power line of known geometry, near the half span between two adjacent towers (see Fig. 6.17). The single-circuit consists of 3 bare conductors (phases A, B, C) with ampacity I=385 A and attached on opposite sides of the pole (see Fig. 6.16). Phase A is placed at 10 m height from the ground and at 4.45 m distance from the pole, phase B is placed at 12.25 m height from the ground and at 3.60 m distance from the pole and phase C is placed at 14.5 m height from the ground and at 3.45 m distance from the pole. Measurements took place at 6 m from the ground and at 8.5 m distance from the line.

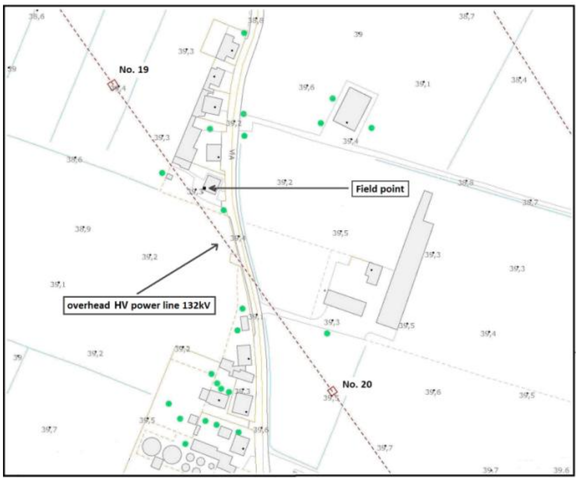

Figure 6.17: *Map of the area of interest.*

The time-dependent rms values of the line currents have been provided by the distribution utility (see Fig. 6.18). The magnetic field components have been monitored and recorded every 1 min for a period of 24 h and in Fig. 6.19 their plots vs. time are displayed along with the plot of B_{tot} vs. time, calculated by the composition of the three components, B_x, B_y and B_z using the relationship (6.4).

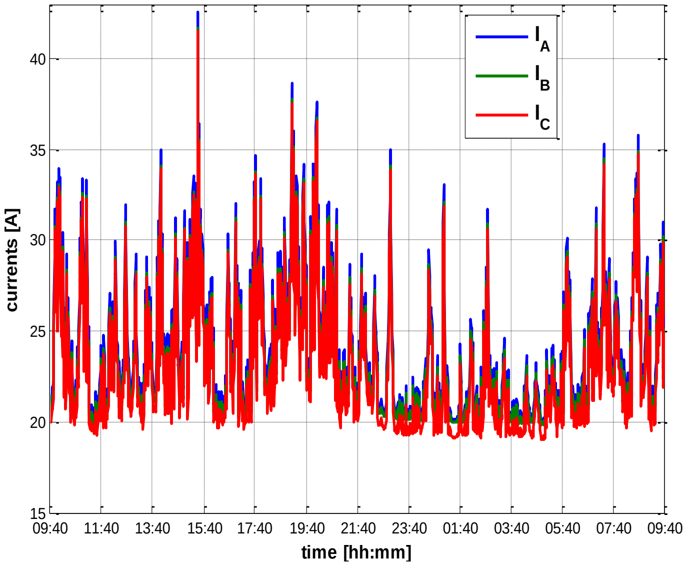

Figure 6.18: *24 h monitored instant values of the currents I_A, I_B and I_C.*

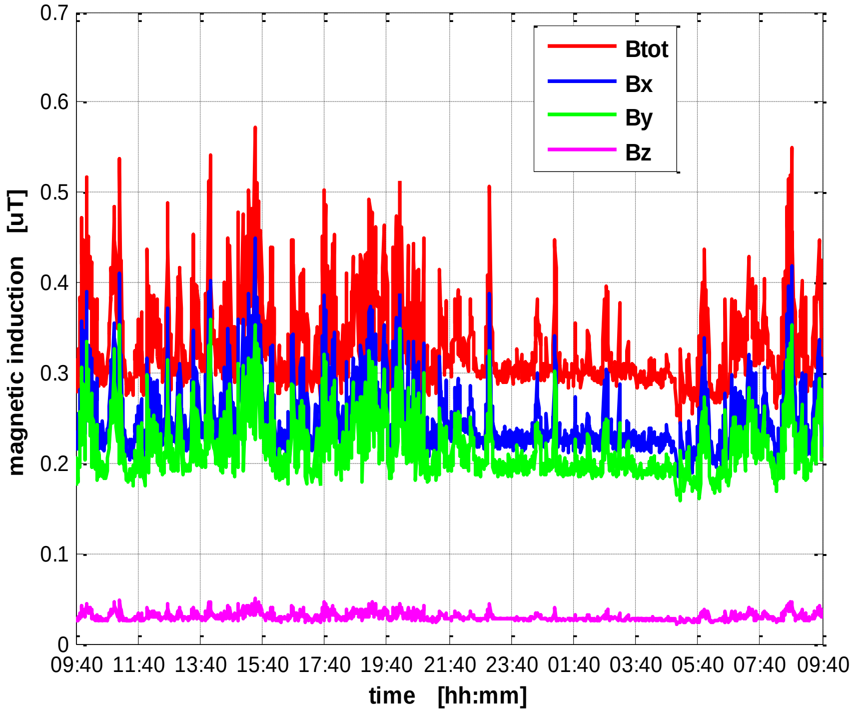

Figure 6.19: *24 h measurements of the magnetic field components.*
B_{tot} *calculated via the three components according to eq. (6.4) is also displayed.*

Elaborating the currents data in Matlab^{TM} environment it was seen that the three-phase currents are not equilibrated since the vector sum of the line currents does not result zero. The estimated values of that non-zero current are shown in Fig. 6.20 and its median value results $I_{\mathrm{N,median}} = 0.919$ A.

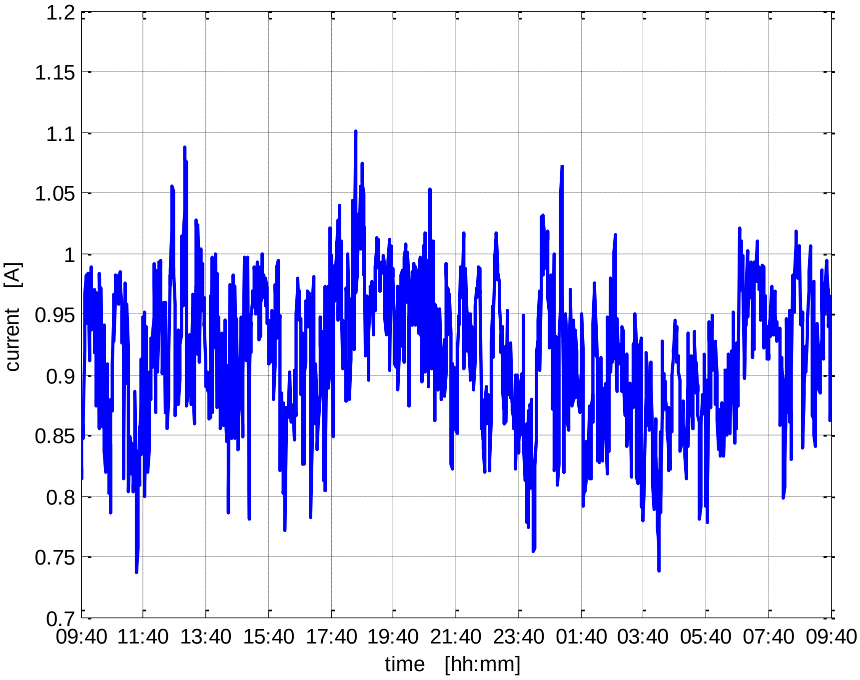

Figure 6.20: *24 h calculated neutral current.*

6.4.2 Data Processing

The handling and storage of measurement results are managed by a Laptop with a data acquisition card NI USB 9239 (4 simultaneous channels of 24 bits, 50kS/s per channel). Subsequently, the functional relationships between the applied currents and the generated magnetic field components, eqs. (6.5), have been validated experimentally using the measured data of *B*-field components (see Fig. 6.19) in Matlab® environment. The numerical values of coefficients $k_{x,1}$, $k_{x,2}$, $k_{x,3}$, $k_{y,1}$, $k_{y,2}$, $k_{y,3}$, $k_{z,1}$, $k_{z,2}$, and $k_{z,3}$, (since $i = 1, 2, 3$ in our case), have been derived by the procedure of multiple linear regression and the following expressions have been established:

$$B_x = k_{x,1} I_A + k_{x,2} I_B + k_{x,3} I_C \Rightarrow B_x = 0.0014 \cdot I_A + 0.0206 \cdot I_B - 0.0115 \cdot I_C \tag{6. 9.a}$$

$$B_y = k_{y,1} I_A + k_{y,2} I_B + k_{y,3} I_C \Rightarrow B_y = 0.0080 \cdot I_A + 0.0162 \cdot I_B - 0.0154 \cdot I_C \tag{6. 9.b}$$

$$B_z = k_{z,1} I_A + k_{z,2} I_B + k_{z,2} I_C \Rightarrow B_z = 0.0009 \cdot I_A + 0.0024 \cdot I_B - 0.0021 \cdot I_C \tag{6. 9.c}$$

Figs. 6.21 are the results of the correlation analysis and show the trends of the components $B_{x,measured}$, $B_{y,measured}$ and $B_{z,measured}$ vs. B_x, B_y and B_z calculated.

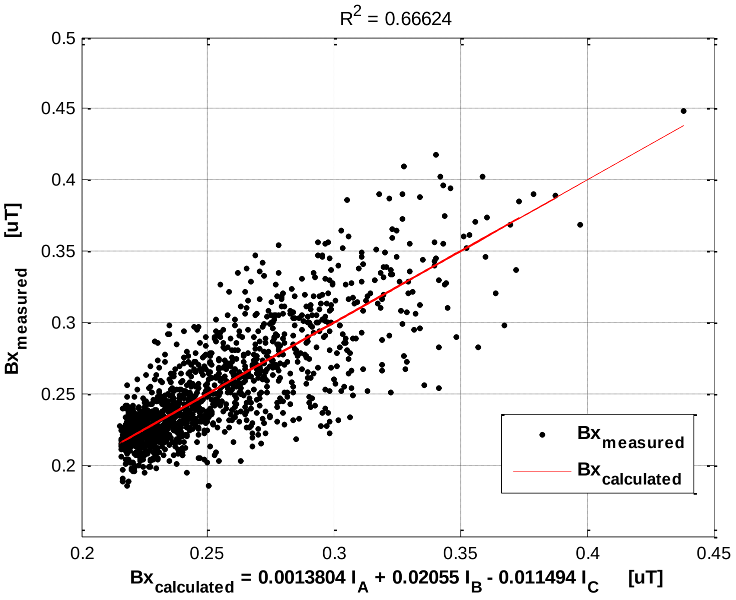

Figure 6.21.a: *Correlation analysis of B_x measured vs. B_x calculated.*

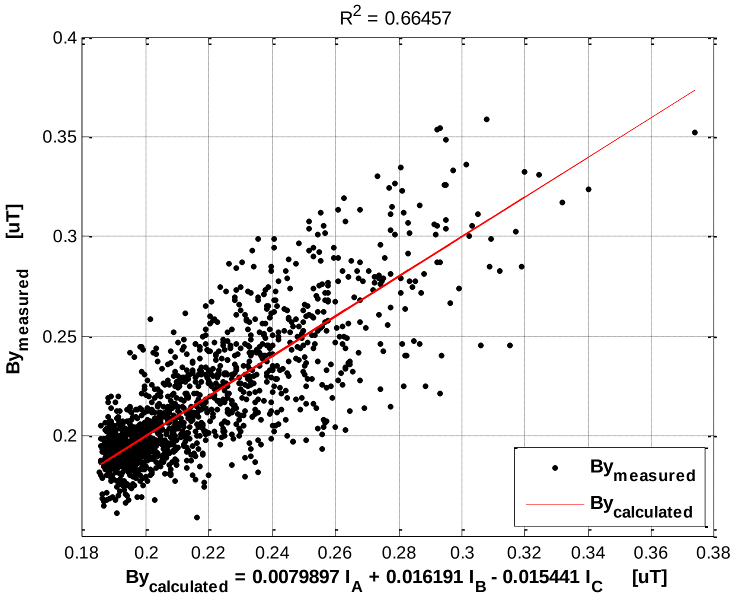

Figure 6.21.b: *Correlation analysis of B_y measured vs. B_y calculated.*

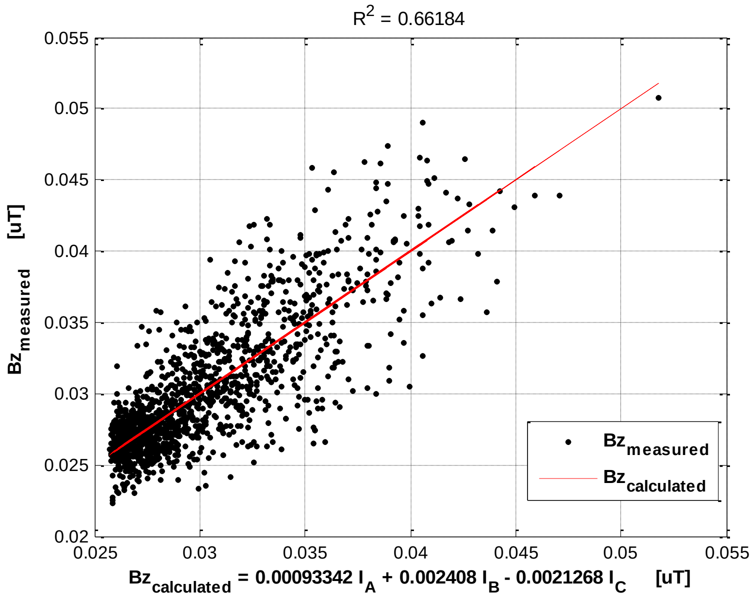

Figure 6.21.c: *Correlation analysis of B_z measured vs. B_z calculated.*

Using the "indirect method", described previously, the estimation of the three components of the magnetic field vector at the point of maximum exposure for the comparison of that value with the legal limits, has been achieved. The results are depicted in the following relationships:

$$B_{x,\max} = k_{x,1}\, I_{A,\max} + k_{x,2}\, I_{B,\max} + k_{x,3}\, I_{C,\max} \Rightarrow B_{x,\max} = 4.04\,\mu T \qquad (6.\ 10.a)$$

$$B_{y,\max} = k_{y,1}\, I_{A,\max} + k_{y,2}\, I_{B,\max} + k_{y,3}\, I_{C,\max} \Rightarrow B_{y,\max} = 3.39\,\mu T \qquad (6.\ 10.b)$$

$$B_{z,\max} = k_{z,1}\, I_{A,\max} + k_{z,2}\, I_{B,\max} + k_{z,3}\, I_{C,\max} \Rightarrow B_{z,\max} = 0.46\mu T \qquad (6.\ 10.c)$$

$$B_{\max} = \sqrt{B^2_{x,\max} + B^2_{y,\max} + B^2_{z,\max}} \Rightarrow B_{\max} = 5.29\mu T \qquad (6.\ 11)$$

with $I_{\mathrm{A,max}}$ = 385 A, $I_{\mathrm{B,max}}$ = 385 A, $I_{\mathrm{C,max}}$ = 385 A, $k_{x,1}$ = 0.0014, $k_{x,2}$ = 0.0206, $k_{x,3}$ = -0.0115, $k_{y,1}$ = 0.0080, $k_{y,2}$ = 0.0162, $k_{y,3}$ = -0.0154, $k_{z,1}$ = 0.0009, $k_{z,2}$ = 0.0024 and $k_{z,3}$ = -0.0021.

6.4 CONCLUSIONS

The construction, calibration and characterization of the innovative 3D measurement and evaluation system of the magnetic field has enabled the measuring, recording and storing of the rms values of the magnetic field components in a Cartesian reference system, B_x, B_y and B_z, and its performance has been successfully tested in laboratory and in situ.

Through 24 h continuous measurements and acquiring the load curves of the double-circuit three-phase line under exam, the coefficients that describe the proportionality relationship between magnetic induction components and intensity of the currents flowing in the two lines were estimated. The same procedure was followed also for the case of a single-circuit three-phase line, where the coefficients that describe the proportionality relationship between magnetic induction components and intensity of the each phase current flowing in the line were estimated.

The correlation coefficients of the multiple linear regression applied to the field components in the case of the double-circuit three-phase line, result greater than 96% for all three components, fact that indicates that the regression lines approximate satisfactorily the real data points. On the other hand, the correlation coefficients of the multiple linear regression applied to each field component in the case of the single-circuit three-phase line, result approximately 66%, fact that indicates that the regression lines approximate satisfactorily enough the real data points but not as well as in the first case. Such a result was expected since the three-phase line was not balanced and a non-zero current flowing in the neutral was present.

The knowledge of these coefficients enable us to estimate the magnetic field under load conditions different from those encountered during the measurement, in particular allows the estimation of the three components of the magnetic field vector at the point of maximum exposure and also allows the comparison of that value with the legal limits. In the case of the double-circuit three-phase line, the magnetic field can arrive up to maximum 3.82 μT and in the case of the single-circuit three-phase line, the magnetic field can arrive up to maximum 5.29 μT. In both cases, the maximum magnetic field value is within the legal limits (in particular below the attention value of 10 μT) as set by the Italian law for existing lines.

The method of estimating the magnetic field described above is called "indirect method" and the Italian legislation has set boundaries in its use: the maximum value of the current should be the ampacity of conductors, and the correlation index between current and magnetic field should not less than 0.9. In the case of multiple linear regression, the Italian law has not yet been updated since this is an innovative approach. However, the correlation coefficients of the multiple linear regression applied to the field components in the case of the double-circuit three-phase line, result greater than 96% for all three components. This is not true though for the single-circuit three-phase line, where the correlation coefficients of the multiple linear regression applied to the field components result approximately 66% for all three components. Even if this value is less than 90%, as defined by the Italian law, still remains an acceptable value as far as the results multiple linear regression are concerned.

Finally, it can be argued, that the "indirect method" of estimating the magnetic field has proven to be more accurate and reliable for multiple and complex 3D field sources, where the exact geometry of the sources is unknown or not accessible and even powerful 3D codes might not work: where a 3D code fails an empirically-derived multi-linear relationship can succeed.

CHAPTER 7

CONCLUSIONS

The calculation of the human exposure to magnetic field generated by complex configurations of the field sources was the subject of this PhD Thesis. The need of precise evaluation of the magnetic field arises from the public concern about its impact near sensitive receptors and also for the determination of the safety distances corresponding to a maximum limit value of the rms magnetic induction, as defined by the national and international legislation.

More precisely, the main object of the scientific research made included the calculation of the magnetic field generated by twisted configurations of the conductors, since this is the main trend in the electric power distribution networks. This helical configuration provides a drastic reduction of the magnetic field generated and – both for this and for other practical reasons – twisted three-phase cables are more and more often the preferred solution for LV and MV power lines. This holds not only close to residential areas, but also in rural and wilderness areas, where twisted three-phase cables are often chosen as a replacement of existing traditional bare conductors overhead lines, since their external insulation protects them against external faults. Additionally, it must be pointed out that twisted three-phase cables are the environmental friendly solution used for connecting “green energy” production systems, such as photovoltaic systems and wind-generators, to the grid.

The exact and approximate theory for the calculation of the magnetic field generated by a twisted three-phase cable configuration was presented. The literature approximation provides acceptable results for large distances from the helix axis only, whereas for distances close to the twisted cable it exhibits large errors compared to the exact rigorous expression of the magnetic field. For this reason, a parametric heuristic analysis was performed that results in an innovative simplified expression of the rms magnetic induction as a function of the distance from the helix axis. This innovative expression approximates the logarithm of B with the equation of a straight line plus a hyperbolic term for simulating the deviation from linearity close to the helix axis. The coefficients of the straight line equation plus the hyperbolic term depend on the pitch and radius of the helix, and can be expressed as pure numbers – 1st level of approximation – or as analytical functions of the pitch and radius – 2nd level of approximation. The great advantage of the 2nd level of approximation is the total explanation of the dependence of B on pitch and radius, without the need to know the exact values of those coefficients, but its disadvantage is that the higher level of approximation has inevitably brought a higher error. The effectiveness of the innovative expression is evaluated by some numerical simulations relevant to typical MV cable designs and the comparison between the results provided by the exact and the approximate formulae from the literature with those obtained via the innovative simplified formula has shown that the error involved by the innovative simplified formula in 1st level of approximation is always smaller than that brought about by the approximate formula from the literature, both for small and for large distances from the helix axis and always positive, providing a conservative estimation of the magnetic field. It can be said that the innovative formula in the 1st level of approximation results definitely much simpler than the exact one and provides a much smaller relative error compared to the approximated one from the literature, especially for small distances from the helix axis. As to the 2nd level of approximation, similar considerations hold, apart some field point ranges where the absolute error of the simplified innovative formula in the 2nd level of approximation is practically the same in absolute terms as the error of the approximate formula from the literature: this is the price paid to the further level of approximation. However, in these ranges (and mostly elsewhere) the 2nd level of approximation overestimates *B*, contrarily to the approximated one from the literature; hence – as the 1st level of approximation – also the 2nd level provides a conservative estimate with respect to the literature approximation.

Subsequently, the magnetic field generated by an overhead or underground double-circuit twisted three-phase power cable line was treated following two different approaches; the exact calculus which effectuates a complex vector sum of the two vectors of the magnetic field from each twisted three-phase single-circuit and the ‘worst case’ calculus which implies the algebraic sum of the two individual values of the magnetic field from each twisted three-phase single-circuit. The exact vector sum has resulted a rather complex procedure since computational hypotheses were set – such as the constancy of the pitch of the single helix, as well as the constancy of the perfect parallelism of the two helixes. Moreover, conventions that would facilitate the analysis were introduced, since it is impossible to obtain exact information about the geometrical arrangement of the power line in practice. On the other hand, the ‘worst case’ assumption for the calculation of the magnetic field is a simple approximated calculus that yields a good interpretation of the reality. Additionally, the ‘worst case’ approach permits further approximation by using both the approximated formula from the literature and the simplified innovative one, in both levels of approximation. The simulations made using a typical MV cable have concluded that the relative percent error of the innovative simplified formula with respect to the approximated one from the literature is always smaller and positive, confirming the better performances of the innovative simplified formula in the ‘worst case’ calculus.

Comparing the calculations with results from actual measurements relevant to a three-phase double-circuit twisted power cable line carried out in situ, it can be deducted that the theoretical approach of the double-circuit twisted cable line is correct and provides - especially when considering the difficult circumstances under which the experiment took place - magnetic field values near to the real ones, particularly for field points where the magnetic induction is large enough for being detected by measurement instruments. Moreover, at these same field points the expression $B_{WC,simp}$, calculated using the innovative simplified formula, can provide a "quick-and-easy" way of calculating the generated magnetic field. The simplicity of this innovative expression lies on the fact that it is the algebraic sum of the two rms values of the total field B generated by each twisted cable that are calculated without using sophisticated mathematics. In this way, the calculation of the magnetic field generated by any multiple-circuit twisted three-phase power cable line becomes possible in the framework of a worst-case approach.

By generalizing the vector theory concerning a double-circuit twisted three-phase power cable line to a multiple-circuit twisted three-phase power cable line – the standard lines for transporting renewable energy – the exact calculation of the magnetic field generated by any number of circuits has been calculated. Also, in the framework of the 'worst-case' approach, the analysis has been extended to multiple-circuit twisted three-phase cables using both the exact and approximated formula derived from the literature about single-circuits and the simple innovative formula developed in both levels of approximation. The simulation results have proven, once more, that the smaller and positive relative error of the simplified innovative formula compared to the approximated one from the literature, make expressions $B_{WC,simp}$ an efficient alternative way of calculating the magnetic field of a multiple-circuit twisted three-phase cable line. This is due to its advantages which lie on its simplicity – an algebraic sum of the rms values of the total field B generated by each twisted cable, calculated without using sophisticated mathematics – and on its reliability – the maximum error presented is small for both levels of approximation and positive, providing a conservative estimation of the magnetic field.

Dealing now with complex configurations of overhead power lines, an appropriate software was created for the exact three-dimensional calculation of the generated magnetic field, following the guidelines of the Italian law, taking into consideration the real geometrical configuration of the lines. This has permitted the exact calculation of the magnetic field at field points of interest near the overhead power lines without overestimating the field as existing two-dimensional magnetic field calculating programs do. For the sake of comparison a two-dimensional calculating program has also been created, following the guidelines of the Italian law, and the results of all the simulations made were satisfactorily compared with 2D magnetic field calculation programs commercially available. The results of all 3D simulations made concerning single- and double-circuit overhead power lines by the three-dimensional code created were compared with a powerful 3D magnetic field calculation program (unfortunately not commercially available and classified).

Nevertheless, critical observations concerning the correctness of the script were made, by comparing the two-dimensional results with the three-dimensional ones.

Finally, for complex three-dimensional configurations of the field sources, where their exact geometry is unknown or not accessible and even powerful 3D codes might not work, the magnetic field has been successfully estimated via the so-called "indirect method" and via the use of an innovative ‘smart’ measurement instrument. The construction, calibration and characterization of the innovative 3D measurement and evaluation system of the magnetic field has enabled measuring and recording the rms values of the magnetic field components in a Cartesian reference system, B_x, B_y and B_z, and its performance has been successfully tested in laboratory and in situ. The post-processing of the measurement results has permitted the calculation of the coefficients that describe the proportionality relationship between magnetic induction components and intensity of the currents via multilinear regression techniques appropriately created. The knowledge of these coefficients enables the estimation of the magnetic field under any load conditions and in particular allows the estimation of the three components of the magnetic field vector at the point of maximum exposure for controlling whether this value lies within the legal limits. This method of estimating the magnetic field described above is called "indirect method" and has proven to be more accurate and reliable for multiple and complex 3D field sources: where a 3D code fails an empirically-derived multi-linear relationship may succeed.

Concluding, the purpose of this PhD Thesis, that was the analysis and calculation of the magnetic field generated by complex configurations of electric power systems, has been successfully achieved by:

- ✓ firstly, presenting a complete exact theory regarding a single-, double- and multiple-circuit twisted three-phase power cable lines along with a simplified approach for the magnetic field calculation generated by these configurations proposing an innovative formula derived from a parametrical analysis;
- ✓ secondly, creating appropriate 3D numerical codes for simulating real existing overhead power lines and calculating the magnetic field in their vicinity;
- ✓ finally proposing an innovative ‘smart’ measurement and evaluation system, which measures and records the rms magnetic field components values for finding the proportionality coefficients between them and the intensity of the currents via multilinear regression techniques for the final extrapolation of the maximum value of the field at the point of interest ("indirect method").

APPENDIX 1

CALCULATION OF COEFFICIENTS a_0, a_1, a_2, a_3

The unknown parameters of the innovative approximate expression (eq. 2.23) discussed in Chapter 2, are a_0, a_1, a_2 and a_3. These parameters are α and p functions, and they have been derived by best-fitting techniques developed in Matlab^{TM}.

The helix radius depends from the geometrical arrangement of the three conductors as shown in Fig. A1.1, where the section of a three-phase twisted cable is depicted along with the quantities D_{out}, R_{out} (cable outer diameter and radius), D_{in}, R_{in} (single conductor diameter and radius) and the helix radius α.

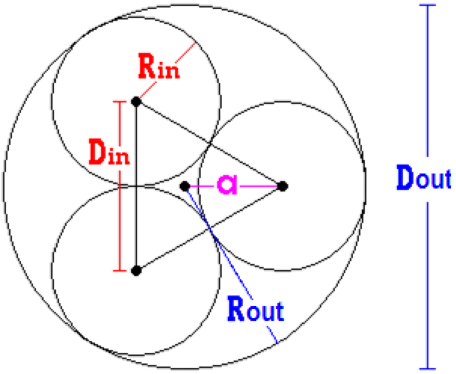

Figure A1.1: *Three-phase twisted cable section.*

The helix radius derives from the relationship:

$$\alpha = D_{in} \cdot \sqrt{3} \qquad \text{(A1.1)}$$

Even though the cable manufacturing companies provide the value of D_{in}, in their datasheets, it is preferable use the value of D_{out} for calculating helix radius α: this is why, D_{in} is usually an approximate value without taking into consideration the conductor insulation thickness and, in cases of missing cable datasheet, it is easier acquiring the D_{out} value simply by measuring it. So, after some elementary mathematical processes, the following expression has resulted that gives the value D_{in} as a function of D_{out}:

$$D_{in} = 0.4641 \cdot D_{out} \qquad \text{(A1.2)}$$

As far as the helix pitch value is concerned, there is a general empirical rule that says:

$$p = 40 \cdot D_{in} \qquad \text{(A1.3)}$$

but is not always applied and it is better if every case is treated using the real, measured value of the helix pitch.

Subsequently, the cases of the cables ARE4H1RX 12/20 kV [64], ARG7H1RX 12/20 kV [63] and RG7H1OR 12/20 kV [66] are treated, providing two Tables, for every existing cross-section of these cables, one with their construction and electrical characteristics, and the other with the values of the coefficients a_0, a_1, a_2, and a_3 with respect to some practical helix pitch values. The calculated helix radius value is also provided.

1) ARE4H1RX 12/20 kV

Table A1.1.a: *Cable ARE4H1RX 12/20 kV 3x35 mm^2: construction and electrical characteristics.*

conductor cross-section	**[mm^2]**	**3x35**
approx conductor diameter	[mm]	7.0
insulation thickness	[mm]	5.5
max outer diameter	[mm]	56.1
approx weight	[kg/km]	1930
min bending radius	[mm]	520
open air installation	[A]	154
underground installation ρ=1^o Cm/W	[A]	147
underground installation ρ=2^o Cm/W	[A]	112

Table A1.1.b: *Cable ARE4H1RX 12/20 kV 3x35 mm^2: coefficients a_0, a_1, a_2, a_3 for different pitch values.*

helix radius α [m]	**helix pitch *p* [m]**	**coefficient a_0**	**coefficient a_1**	**coefficient a_2**	**coefficient a_3**
0.015	**1.0**	-0.6204	-6.6444	0.1	1.69
0.015	**1.2**	-0.5014	-5.6066	0.1	1.75
0.015	**1.4**	-0.3957	-4.8682	0.1	1.80
0.015	**1.6**	-0.2997	-4.3169	0.1	1.85
0.015	**1.8**	-0.2111	-3.8904	0.1	1.89
0.015	**2.0**	-0.1283	-3.5512	0.1	1.93

Table A1.2.a: *Cable ARE4H1RX 12/20 kV 3x50 mm^2: construction and electrical characteristics.*

conductor cross-section	[mm^2]	3x50
approx conductor diameter	[mm]	8.2
insulation thickness	[mm]	5.5
max outer diameter	[mm]	58.8
approx weight	[kg/km]	2140
min bending radius	[mm]	540
open air installation	[A]	185
underground installation ρ=1° Cm/W	[A]	174
underground installation ρ=2° Cm/W	[A]	131

Table A1.2.b: *Cable ARE4H1RX 12/20 kV 3x50 mm^2: coefficients a_0, a_1, a_2, a_3 for different pitch values.*

helix radius α [m]	helix pitch *p* [m]	coefficient a_0	coefficient a_1	coefficient a_2	coefficient a_3
0.016	**1.0**	-0.6199	-6.6444	0.1	1.70
0.016	**1.2**	-0.5011	-5.6066	0.1	1.75
0.016	**1.4**	-0.3955	-4.8682	0.1	1.80
0.016	**1.6**	-0.2995	-4.3169	0.1	1.85
0.016	**1.8**	-0.2109	-3.8904	0.1	1.89
0.016	**2.0**	-0.1282	-3.5512	0.1	1.93

Table A1.3.a: *Cable ARE4H1RX 12/20 kV 3x70 mm^2: construction and electrical characteristics.*

conductor cross-section	[mm^2]	3x70
approx conductor diameter	[mm]	9.7
insulation thickness	[mm]	5.5
max outer diameter	[mm]	62.6
approx weight	[kg/km]	2490
min bending radius	[mm]	580
open air installation	[A]	230
underground installation ρ=1° Cm/W	[A]	212
underground installation ρ=2° Cm/W	[A]	160

Table A1.3.b: *Cable ARE4H1RX 12/20 kV 3x70 mm^2: coefficients a_0, a_1, a_2, a_3 for different pitch values.*

helix radius α [m]	helix pitch *p* [m]	coefficient a_0	coefficient a_1	coefficient a_2	coefficient a_3
0.017	**1.0**	-0.6194	-6.6444	0.1	1.70
0.017	**1.2**	-0.5008	-5.6066	0.1	1.75
0.017	**1.4**	-0.3952	-4.8682	0.1	1.80
0.017	**1.6**	-0.2993	-4.3169	0.1	1.85
0.017	**1.8**	-0.2108	-3.8904	0.1	1.89
0.017	**2.0**	-0.1280	-3.5513	0.1	1.93

Table A1.4.a: *Cable ARE4H1RX 12/20 kV 3x95 mm^2: construction and electrical characteristics.*

conductor cross-section	[mm^2]	3x95
approx conductor diameter	[mm]	11.4
insulation thickness	[mm]	5.5
max outer diameter	[mm]	66.3
approx weight	[kg/km]	2860
min bending radius	[mm]	610
open air installation	[A]	280
underground installation ρ=1° Cm/W	[A]	253
underground installation ρ=2° Cm/W	[A]	190

Table A1.4.b: *Cable ARE4H1RX 12/20 kV 3x95 mm^2: coefficients a_0, a_1, a_2, a_3 for different pitch values.*

helix radius α [m]	helix pitch *p* [m]	coefficient a_0	coefficient a_1	coefficient a_2	coefficient a_3
0.018	**1.0**	-0.6189	-6.6444	0.1	1.70
0.018	**1.2**	-0.5004	-5.6066	0.1	1.75
0.018	**1.4**	-0.3949	-4.8682	0.1	1.81
0.018	**1.6**	-0.2991	-4.3169	0.1	1.85
0.018	**1.8**	-0.2106	-3.8904	0.1	1.89
0.018	**2.0**	-0.1279	-3.5513	0.1	1.93

Table A1.5.a: *Cable ARE4H1RX 12/20 kV 3x120 mm^2: construction and electrical characteristics.*

conductor cross-section	[mm^2]	3x120
approx conductor diameter	[mm]	12.9
insulation thickness	[mm]	5.5
max outer diameter	[mm]	70.2
approx weight	[kg/km]	3260
min bending radius	[mm]	650
open air installation	[A]	323
underground installation ρ=1° Cm/W	[A]	288
underground installation ρ=2° Cm/W	[A]	216

Table A1.5.b: *Cable ARE4H1RX 12/20 kV 3x120 mm^2: coefficients a_0, a_1, a_2, a_3 for different pitch values.*

helix radius α [m]	helix pitch *p* [m]	coefficient a_0	coefficient a_1	coefficient a_2	coefficient a_3
0.019	**1.0**	-0.6184	-6.6444	0.1	1.70
0.019	**1.2**	-0.5000	-5.6066	0.1	1.76
0.019	**1.4**	-0.3947	-4.8682	0.1	1.81
0.019	**1.6**	-0.2989	-4.3169	0.1	1.85
0.019	**1.8**	-0.2104	-3.8904	0.1	1.89
0.019	**2.0**	-0.1277	-3.5513	0.1	1.93

Table A1.6.a: *Cable ARE4H1RX 12/20 kV 3x150 mm^2: construction and electrical characteristics.*

conductor cross-section	**[mm^2]**	**3x150**
approx conductor diameter	[mm]	14.0
insulation thickness	[mm]	5.5
max outer diameter	[mm]	72.7
approx weight	[kg/km]	3560
min bending radius	[mm]	670
open air installation	[A]	365
underground installation ρ=1° Cm/W	[A]	322
underground installation ρ=2° Cm/W	[A]	241

Table A1.6.b: *Cable ARE4H1RX 12/20 kV 3x150 mm^2: coefficients a_0, a_1, a_2, a_3 for different pitch values.*

helix radius α [m]	**helix pitch *p* [m]**	**coefficient a_0**	**coefficient a_1**	**coefficient a_2**	**coefficient a_3**
0.019	**1.0**	-0.6184	-6.6444	0.1	1.70
0.019	**1.2**	-0.5000	-5.6066	0.1	1.76
0.019	**1.4**	-0.3947	-4.8682	0.1	1.81
0.019	**1.6**	-0.2989	-4.3169	0.1	1.85
0.019	**1.8**	-0.2104	-3.8904	0.1	1.89
0.019	**2.0**	-0.1277	-3.5513	0.1	1.93

Table A1.7.a: *Cable ARE4H1RX 12/20 kV 3x185 mm^2: construction and electrical characteristics.*

conductor cross-section	**[mm^2]**	**3x185**
approx conductor diameter	[mm]	15.8
insulation thickness	[mm]	5.5
max outer diameter	[mm]	77.2
approx weight	[kg/km]	4100
min bending radius	[mm]	720
open air installation	[A]	421
underground installation ρ=1° Cm/W	[A]	365
underground installation ρ=2° Cm/W	[A]	272

Table A1.7.b: *Cable ARE4H1RX 12/20 kV 3x185 mm^2: coefficients a_0, a_1, a_2, a_3 for different pitch values.*

helix radius α [m]	**helix pitch *p* [m]**	**coefficient a_0**	**coefficient a_1**	**coefficient a_2**	**coefficient a_3**
0.021	**1.0**	-0.6172	-6.6444	0.1	1.70
0.021	**1.2**	-0.4992	-5.6066	0.1	1.76
0.021	**1.4**	-0.3941	-4.8682	0.1	1.81
0.021	**1.6**	-0.2984	-4.3169	0.1	1.85
0.021	**1.8**	-0.2100	-3.8904	0.1	1.89
0.021	**2.0**	-0.1274	-3.5513	0.1	1.93

Table A1.8.a: *Cable ARE4H1RX 12/20 kV 3x240 mm^2: construction and electrical characteristics.*

conductor cross-section	[mm^2]	3x240
approx conductor diameter	[mm]	18.2
insulation thickness	[mm]	5.5
max outer diameter	[mm]	82.6
approx weight	[kg/km]	4830
min bending radius	[mm]	770
open air installation	[A]	498
underground installation ρ=1° Cm/W	[A]	423
underground installation ρ=2° Cm/W	[A]	314

Table A1.8.b: *Cable ARE4H1RX 12/20 kV 3x240 mm^2: coefficients a_0, a_1, a_2, a_3 for different pitch values.*

helix radius α [m]	helix pitch *p* [m]	coefficient a_0	coefficient a_1	coefficient a_2	coefficient a_3
0.022	**1.0**	-0.6166	-6.6444	0.1	1.70
0.022	**1.2**	-0.4987	-5.6066	0.1	1.76
0.022	**1.4**	-0.3937	-4.8682	0.1	1.81
0.022	**1.6**	-0.2982	-4.3169	0.1	1.85
0.022	**1.8**	-0.2098	-3.8904	0.1	1.89
0.022	**2.0**	-0.1272	-3.5513	0.1	1.93

Table A1.9.a: *Cable ARE4H1RX 12/20 kV 3x300 mm^2: construction and electrical characteristics.*

conductor cross-section	[mm^2]	3x300
approx conductor diameter	[mm]	20.8
insulation thickness	[mm]	5.5
max outer diameter	[mm]	89.8
approx weight	[kg/km]	5720
min bending radius	[mm]	740
open air installation	[A]	576
underground installation ρ=1° Cm/W	[A]	478
underground installation ρ=2° Cm/W	[A]	354

Table A1.9.b: *Cable ARE4H1RX 12/20 kV 3x300 mm^2: coefficients a_0, a_1, a_2, a_3 for different pitch values.*

helix radius α [m]	helix pitch *p* [m]	coefficient a_0	coefficient a_1	coefficient a_2	coefficient a_3
0.024	**1.0**	-0.6152	-6.6444	0.1	1.70
0.024	**1.2**	-0.4978	-5.6066	0.1	1.76
0.024	**1.4**	-0.3930	-4.8682	0.1	1.81
0.024	**1.6**	-0.2976	-4.3169	0.1	1.85
0.024	**1.8**	-0.2094	-3.8904	0.1	1.90
0.024	**2.0**	-0.1268	-3.5513	0.1	1.93

2) ARG7H1RX 12/20 kV

Table A1.10.a: *Cable ARG7H1RX 12/20 kV 3x70 mm^2: construction and electrical characteristics.*

conductor cross-section	**[mm^2]**	**3x70**
approx conductor diameter	[mm]	9.8
insulation thickness	[mm]	5.5
max outer diameter	[mm]	67
approx weight	[kg/km]	3000
min bending radius	[mm]	720
underground installation ρ=1^o Cm/W	[A]	200

Table A1.10.b: *Cable ARG7H1RX 12/20 kV 3x70 mm^2: coefficients a_0, a_1, a_2, a_3 for different pitch values.*

helix radius α [m]	**helix pitch *p* [m]**	**coefficient a_0**	**coefficient a_1**	**coefficient a_2**	**coefficient a_3**
0.018	**1.0**	-0.6189	-6.6444	0.1	1.69
0.018	**1.2**	-0.5004	-5.6066	0.1	1.75
0.018	**1.4**	-0.3949	-4.8682	0.1	1.80
0.018	**1.6**	-0.2991	-4.3169	0.1	1.85
0.018	**1.8**	-0.2106	-3.8904	0.1	1.89
0.018	**2.0**	-0.1279	-3.5513	0.1	1.93

Table A1.11.a: *Cable ARG7H1RX 12/20 kV 3x120 mm^2: construction and electrical characteristics.*

conductor cross-section	**[mm^2]**	**3x120**
approx conductor diameter	[mm]	13.1
insulation thickness	[mm]	5.5
max outer diameter	[mm]	74
approx weight	[kg/km]	4000
min bending radius	[mm]	790
underground installation ρ=1^o Cm/W	[A]	280

Table A1.11.b: *Cable ARG7H1RX 12/20 kV 3x120 mm^2: coefficients a_0, a_1, a_2, a_3 for different pitch values.*

helix radius α [m]	**helix pitch *p* [m]**	**coefficient a_0**	**coefficient a_1**	**coefficient a_2**	**coefficient a_3**
0.020	**1.0**	-0.6178	-6.6444	0.1	1.69
0.020	**1.2**	-0.4996	-5.6066	0.1	1.75
0.020	**1.4**	-0.3944	-4.8682	0.1	1.81
0.020	**1.6**	-0.2987	-4.3169	0.1	1.85
0.020	**1.8**	-0.2102	-3.8904	0.1	1.89
0.020	**2.0**	-0.1276	-3.5513	0.1	1.93

Table A1.12.a: *Cable ARG7H1RX 12/20 kV 3x185 mm^2: construction and electrical characteristics.*

conductor cross-section	[mm^2]	3x185
approx conductor diameter	[mm]	16.1
insulation thickness	[mm]	5.5
max outer diameter	[mm]	81
approx weight	[kg/km]	4800
min bending radius	[mm]	860
underground installation ρ=1° Cm/W	[A]	360

Table A1.12.b: *Cable ARG7H1RX 12/20 kV 3x185 mm^2: coefficients a_0, a_1, a_2, a_3 for different pitch values.*

helix radius α [m]	helix pitch *p* [m]	coefficient a_0	coefficient a_1	coefficient a_2	coefficient a_3
0.022	**1.0**	-0.6166	-6.6444	0.1	1.70
0.022	**1.2**	-0.4987	-5.6066	0.1	1.76
0.022	**1.4**	-0.3937	-4.8682	0.1	1.81
0.022	**1.6**	-0.2982	-4.3169	0.1	1.85
0.022	**1.8**	-0.2098	-3.8904	0.1	1.89
0.022	**2.0**	-0.1272	-3.5513	0.1	1.93

3) RG7H1OR 12/20 kV

Table A1.13.a: *Cable RG7H1OR 12/20 kV 3x25 mm^2: construction and electrical characteristics.*

conductor cross-section	[mm^2]	3x25
approx conductor diameter	[mm]	6.0
insulation thickness	[mm]	5.5
max outer diameter	[mm]	54.5
approx weight	[kg/km]	3550
min bending radius	[mm]	720
open air installation	[A]	153
underground installation ρ=1° Cm/W	[A]	150
underground installation ρ=2° Cm/W	[A]	118

Table A1.13.b: *Cable RG7H1OR 12/20 kV 3x25 mm^2: coefficients a_0, a_1, a_2, a_3 for different pitch values.*

helix radius α [m]	helix pitch *p* [m]	coefficient a_0	coefficient a_1	coefficient a_2	coefficient a_3
0.015	**1.0**	-0.6204	-6.6444	0.1	1.70
0.015	**1.2**	-0.5014	-5.6066	0.1	1.75
0.015	**1.4**	-0.3957	-4.8682	0.1	1.80
0.015	**1.6**	-0.2997	-4.3169	0.1	1.85
0.015	**1.8**	-0.2111	-3.8904	0.1	1.89
0.015	**2.0**	-0.1283	-3.5512	0.1	1.93

Table A1.14.a: *Cable RG7H1OR 12/20 kV 3x35 mm^2: construction and electrical characteristics.*

conductor cross-section	**[mm^2]**	**3x35**
approx conductor diameter	[mm]	7.0
insulation thickness	[mm]	5.5
max outer diameter	[mm]	54.7
approx weight	[kg/km]	3790
min bending radius	[mm]	720
open air installation	[A]	177
underground installation ρ=1° Cm/W	[A]	175
underground installation ρ=2° Cm/W	[A]	138

Table A1.14.b: *Cable RG7H1OR 12/20 kV 3x35 mm^2: coefficients a_0, a_1, a_2, a_3 for different pitch values.*

helix radius α [m]	**helix pitch *p* [m]**	**coefficient a_0**	**coefficient a_1**	**coefficient a_2**	**coefficient a_3**
0.015	**1.0**	-0.6204	-6.6444	0.1	1.70
0.015	**1.2**	-0.5014	-5.6066	0.1	1.75
0.015	**1.4**	-0.3957	-4.8682	0.1	1.80
0.015	**1.6**	-0.2997	-4.3169	0.1	1.85
0.015	**1.8**	-0.2111	-3.8904	0.1	1.89
0.015	**2.0**	-0.1283	-3.5512	0.1	1.93

Table A1.15.a: *Cable RG7H1OR 12/20 kV 3x50 mm^2: construction and electrical characteristics.*

conductor cross-section	**[mm^2]**	**3x50**
approx conductor diameter	[mm]	8.2
insulation thickness	[mm]	5.5
max outer diameter	[mm]	57.4
approx weight	[kg/km]	4360
min bending radius	[mm]	760
open air installation	[A]	209
underground installation ρ=1° Cm/W	[A]	207
underground installation ρ=2° Cm/W	[A]	162

Table A1.15.b: *Cable RG7H1OR 12/20 kV 3x50 mm^2: coefficients a_0, a_1, a_2, a_3 for different pitch values.*

helix radius α [m]	**helix pitch *p* [m]**	**coefficient a_0**	**coefficient a_1**	**coefficient a_2**	**coefficient a_3**
0.015	**1.0**	-0.6204	-6.6444	0.1	1.70
0.015	**1.2**	-0.5014	-5.6066	0.1	1.75
0.015	**1.4**	-0.3957	-4.8682	0.1	1.80
0.015	**1.6**	-0.2997	-4.3169	0.1	1.85
0.015	**1.8**	-0.2111	-3.8904	0.1	1.89
0.015	**2.0**	-0.1283	-3.5512	0.1	1.93

Table A1.16.a: *Cable RG7H1OR 12/20 kV 3x70 mm^2: construction and electrical characteristics.*

conductor cross-section	**[mm^2]**	**3x70**
approx conductor diameter	[mm]	9.9
insulation thickness	[mm]	5.5
max outer diameter	[mm]	62.0
approx weight	[kg/km]	5390
min bending radius	[mm]	820
open air installation	[A]	260
underground installation ρ=1° Cm/W	[A]	253
underground installation ρ=2° Cm/W	[A]	198

Table A1.16.b: *Cable RG7H1OR 12/20 kV 3x70 mm^2: coefficients a_0, a_1, a_2, a_3 for different pitch values.*

helix radius α [m]	**helix pitch *p* [m]**	**coefficient a_0**	**coefficient a_1**	**coefficient a_2**	**coefficient a_3**
0.017	**1.0**	-0.6194	-6.6444	0.1	1.70
0.017	**1.2**	-0.5008	-5.6066	0.1	1.75
0.017	**1.4**	-0.3952	-4.8682	0.1	1.80
0.017	**1.6**	-0.2993	-4.3169	0.1	1.85
0.017	**1.8**	-0.2108	-3.8904	0.1	1.89
0.017	**2.0**	-0.1280	-3.5513	0.1	1.93

Table A1.17.a: *Cable RG7H1OR 12/20 kV 3x95 mm^2: construction and electrical characteristics.*

conductor cross-section	**[mm^2]**	**3x95**
approx conductor diameter	[mm]	11.6
insulation thickness	[mm]	5.5
max outer diameter	[mm]	65.9
approx weight	[kg/km]	6470
min bending radius	[mm]	870
open air installation	[A]	315
underground installation ρ=1° Cm/W	[A]	300
underground installation ρ=2° Cm/W	[A]	234

Table A1.17.b: *Cable RG7H1OR 12/20 kV 3x95 mm^2: coefficients a_0, a_1, a_2, a_3 for different pitch values.*

helix radius α [m]	**helix pitch *p* [m]**	**coefficient a_0**	**coefficient a_1**	**coefficient a_2**	**coefficient a_3**
0.018	**1.0**	-0.6189	-6.6444	0.1	1.70
0.018	**1.2**	-0.5004	-5.6066	0.1	1.75
0.018	**1.4**	-0.3949	-4.8682	0.1	1.81
0.018	**1.6**	-0.2991	-4.3169	0.1	1.85
0.018	**1.8**	-0.2106	-3.8904	0.1	1.89
0.018	**2.0**	-0.1279	-3.5513	0.1	1.93

Table A1.18.a: *Cable RG7H1OR 12/20 kV 3x120 mm^2: construction and electrical characteristics.*

conductor cross-section	**[mm^2]**	**3x120**
approx conductor diameter	[mm]	13.1
insulation thickness	[mm]	5.5
max outer diameter	[mm]	69.3
approx weight	[kg/km]	7470
min bending radius	[mm]	920
open air installation	[A]	362
underground installation ρ=1° Cm/W	[A]	342
underground installation ρ=2° Cm/W	[A]	266

Table A1.18.b: *Cable RG7H1OR 12/20 kV 3x120 mm^2: coefficients a_0, a_1, a_2, a_3 for different pitch values.*

helix radius α [m]	**helix pitch *p* [m]**	**coefficient a_0**	**coefficient a_1**	**coefficient a_2**	**coefficient a_3**
0.019	**1.0**	-0.6184	-6.6444	0.1	1.70
0.019	**1.2**	-0.5000	-5.6066	0.1	1.76
0.019	**1.4**	-0.3947	-4.8682	0.1	1.81
0.019	**1.6**	-0.2989	-4.3169	0.1	1.85
0.019	**1.8**	-0.2104	-3.8904	0.1	1.89
0.019	**2.0**	-0.1277	-3.5513	0.1	1.93

Table A1.19.a: *Cable RG7H1OR 12/20 kV 3x150 mm^2: construction and electrical characteristics.*

conductor cross-section	**[mm^2]**	**3x150**
approx conductor diameter	[mm]	14.4
insulation thickness	[mm]	5.5
max outer diameter	[mm]	72.6
approx weight	[kg/km]	8540
min bending radius	[mm]	960
open air installation	[A]	408
underground installation ρ=1° Cm/W	[A]	381
underground installation ρ=2° Cm/W	[A]	296

Table A1.19.b: *Cable RG7H1OR 12/20 kV 3x150 mm^2: coefficients a_0, a_1, a_2, a_3 for different pitch values.*

helix radius α [m]	**helix pitch *p* [m]**	**coefficient a_0**	**coefficient a_1**	**coefficient a_2**	**coefficient a_3**
0.019	**1.0**	-0.6184	-6.6444	0.1	1.70
0.019	**1.2**	-0.5000	-5.6066	0.1	1.76
0.019	**1.4**	-0.3947	-4.8682	0.1	1.81
0.019	**1.6**	-0.2989	-4.3169	0.1	1.85
0.019	**1.8**	-0.2104	-3.8904	0.1	1.89
0.019	**2.0**	-0.1277	-3.5513	0.1	1.93

Table A1.20.a: *Cable RG7H1OR 12/20 kV 3x185 mm^2: construction and electrical characteristics.*

conductor cross-section	**[mm^2]**	**3x185**
approx conductor diameter	[mm]	16.1
insulation thickness	[mm]	5.5
max outer diameter	[mm]	76.8
approx weight	[kg/km]	10020
min bending radius	[mm]	1020
open air installation	[A]	468
underground installation ρ=1° Cm/W	[A]	431
underground installation ρ=2° Cm/W	[A]	335

Table A1.20.b: *Cable RG7H1OR 12/20 kV 3x185 mm^2: coefficients a_0, a_1, a_2, a_3 for different pitch values.*

helix radius α [m]	**helix pitch *p* [m]**	**coefficient a_0**	**coefficient a_1**	**coefficient a_2**	**coefficient a_3**
0.021	**1.0**	-0.6172	-6.6444	0.1	1.70
0.021	**1.2**	-0.4992	-5.6066	0.1	1.76
0.021	**1.4**	-0.3941	-4.8682	0.1	1.81
0.021	**1.6**	-0.2984	-4.3169	0.1	1.85
0.021	**1.8**	-0.2100	-3.8904	0.1	1.89
0.021	**2.0**	-0.1274	-3.5513	0.1	1.93

Table A1.21.a: *Cable RG7H1OR 12/20 kV 3x240 mm^2: construction and electrical characteristics.*

conductor cross-section	**[mm^2]**	**3x240**
approx conductor diameter	[mm]	18.5
insulation thickness	[mm]	5.5
max outer diameter	[mm]	82.0
approx weight	[kg/km]	12090
min bending radius	[mm]	1090
open air installation	[A]	550
underground installation ρ=1° Cm/W	[A]	500
underground installation ρ=2° Cm/W	[A]	387

Table A1.21.b: *Cable RG7H1OR 12/20 kV 3x240 mm^2: coefficients a_0, a_1, a_2, a_3 for different pitch values.*

helix radius α [m]	**helix pitch *p* [m]**	**coefficient a_0**	**coefficient a_1**	**coefficient a_2**	**coefficient a_3**
0.022	**1.0**	-0.6166	-6.6444	0.1	1.70
0.022	**1.2**	-0.4987	-5.6066	0.1	1.76
0.022	**1.4**	-0.3937	-4.8682	0.1	1.81
0.022	**1.6**	-0.2982	-4.3169	0.1	1.85
0.022	**1.8**	-0.2098	-3.8904	0.1	1.89
0.022	**2.0**	-0.1272	-3.5513	0.1	1.93

Table A1.22.a: *Cable RG7H1OR 12/20 kV 3x300 mm^2: construction and electrical characteristics.*

conductor cross-section	**[mm^2]**	**3x300**
approx conductor diameter	[mm]	21.1
insulation thickness	[mm]	5.5
max outer diameter	[mm]	88.7
approx weight	[kg/km]	14620
min bending radius	[mm]	1180
open air installation	[A]	630
underground installation ρ=1^o Cm/W	[A]	561
underground installation ρ=2^o Cm/W	[A]	435

Table A1.22.b: *Cable RG7H1OR 12/20 kV 3x300 mm^2: coefficients a_0, a_1, a_2, a_3 for different pitch values.*

helix radius α [m]	**helix pitch *p* [m]**	**coefficient a_0**	**coefficient a_1**	**coefficient a_2**	**coefficient a_3**
0.024	**1.0**	-0.6152	-6.6444	0.1	1.70
0.024	**1.2**	-0.4978	-5.6066	0.1	1.76
0.024	**1.4**	-0.3930	-4.8682	0.1	1.81
0.024	**1.6**	-0.2976	-4.3169	0.1	1.85
0.024	**1.8**	-0.2094	-3.8904	0.1	1.90
0.024	**2.0**	-0.1268	-3.5513	0.1	1.93

APPENDIX 2

MAGNETIC FIELD ISOLINES

In Appendix 2 the magnetic field isolines of 1.0 μT, 3.0 μT (‘quality objective’), 5 μT, 10μT (‘attention value’) and 100 μT (‘exposure limit’) have been calculated and plotted for some frequently used underground cable types, such as ARE4H1RX 12/20 kV [64], ARG7H1RX 12/20 kV [63] and RG7H1OR 12/20 kV [66], in order to provide a human exposure protection map concerning the magnetic fields generated by these cables carrying current equal at their ampacity. The calculation of the magnetic field isolines was implemented in Matlab™ environment and based on the exact formulation (eq. 2.23) discussed in Chapter 2, and on formulas (A1.1), (A1.2) and (A1.3) discussed in Appendix 1.

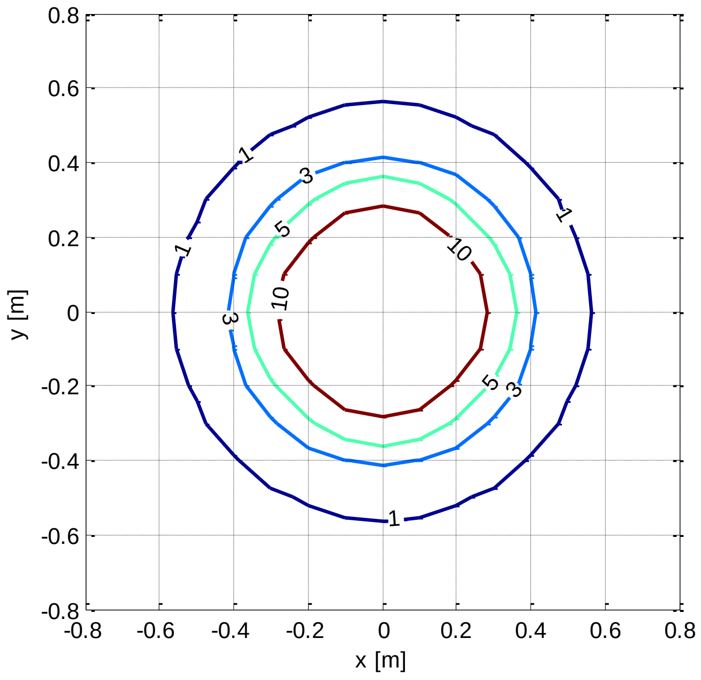

Figure A2.1: *Magnetic field isolines for the cable ARE4H1RX 12/20 kV 3x35 mm^2 (I=147 A)*

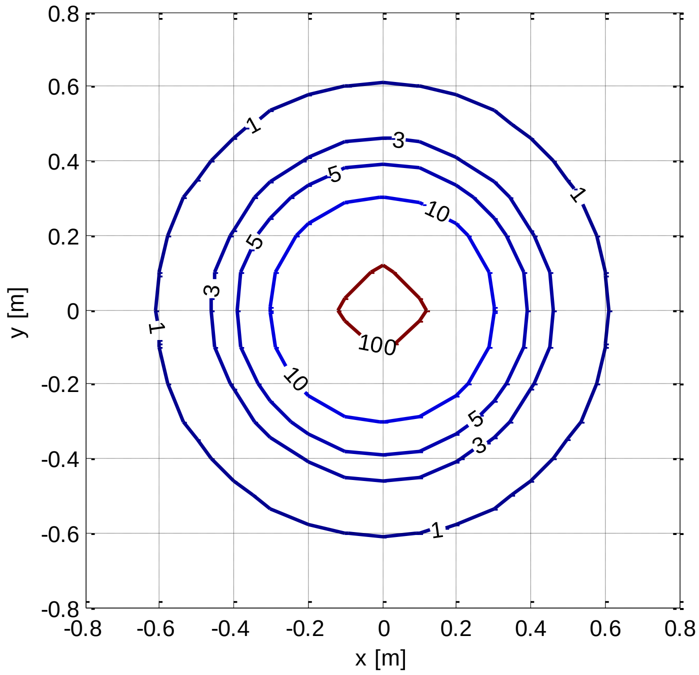

Figure A2.2: *Magnetic field isolines for the cable ARE4H1RX 12/20 kV 3x50 m ^{2} (I=174 A).*

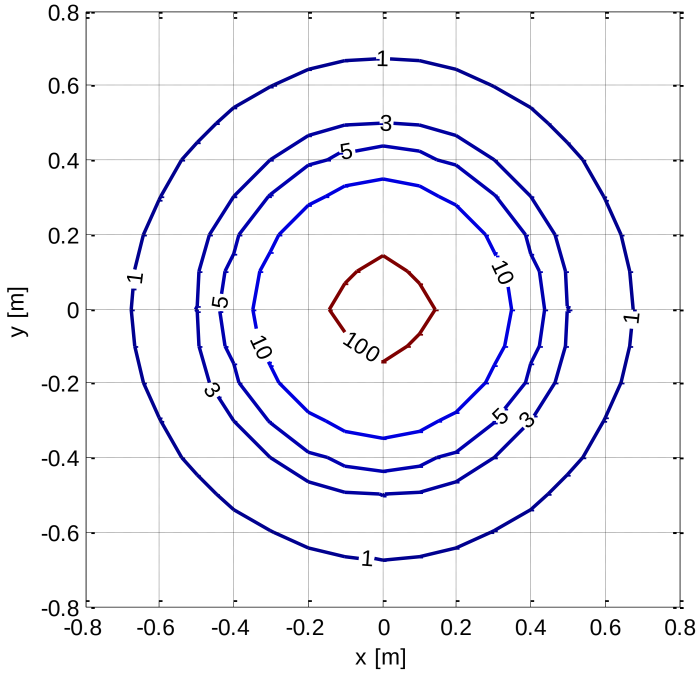

Figure A2.3: *Magnetic field isolines for the cable ARE4H1RX 12/20 kV 3x70 mm^{2} (I=212 A).*

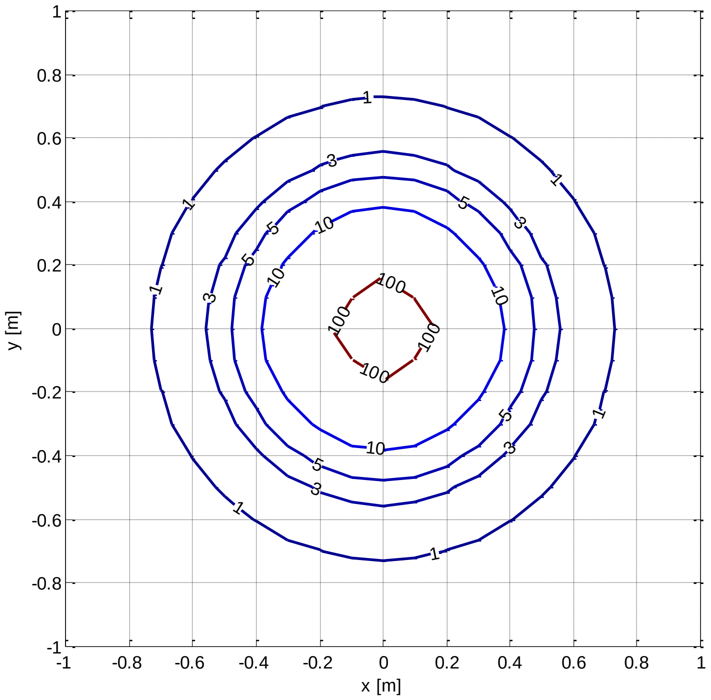

Figure A2.4: *Magnetic field isolines for the cable ARE4H1RX 12/20 kV 3x95 mm^2 (I=253 A).*

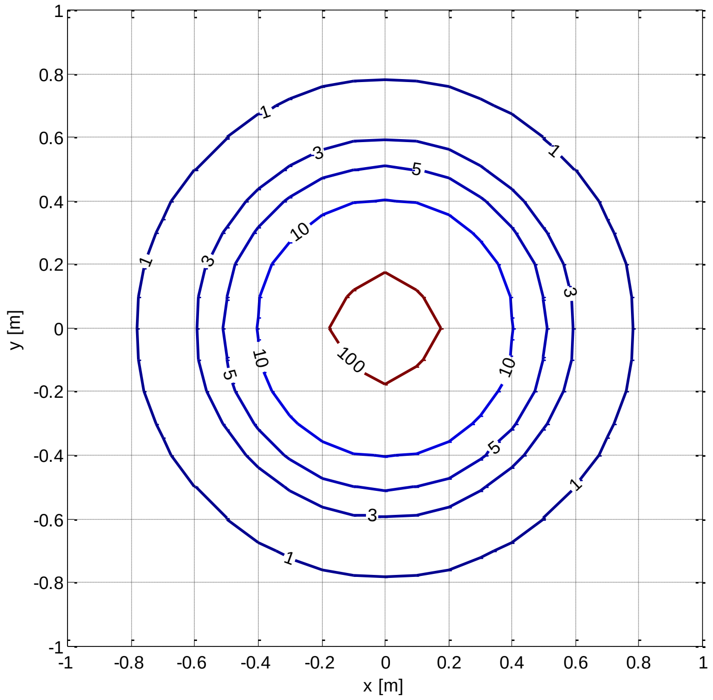

Figure A2.5: *Magnetic field isolines for the cable ARE4H1RX 12/20 kV 3x120 mm^2 (I=288 A).*

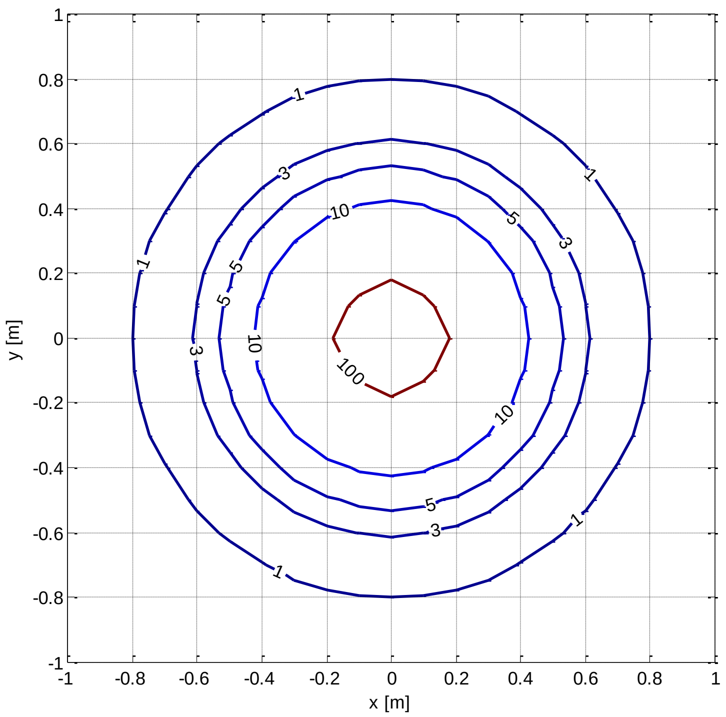

Figure A2.6: *Magnetic field isolines for the cable ARE4H1RX 12/20 kV 3x150 mm^2 (I=322 A).*

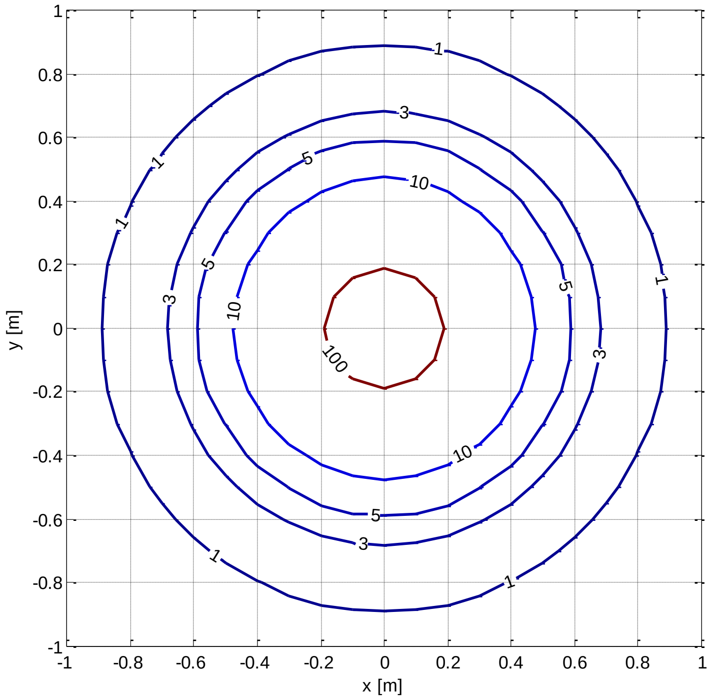

Figure A2.7: *Magnetic field isolines for the cable ARE4H1RX 12/20 kV 3x185 mm^2 (I=365 A).*

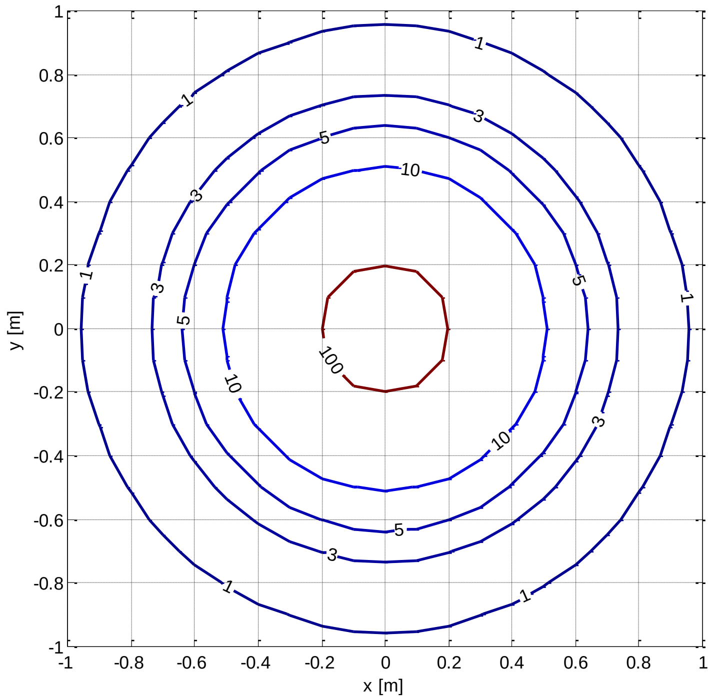

Figure A2.8: *Magnetic field isolines for the cable ARE4H1RX 12/20 kV 3x240 mm^2 (I=423 A).*

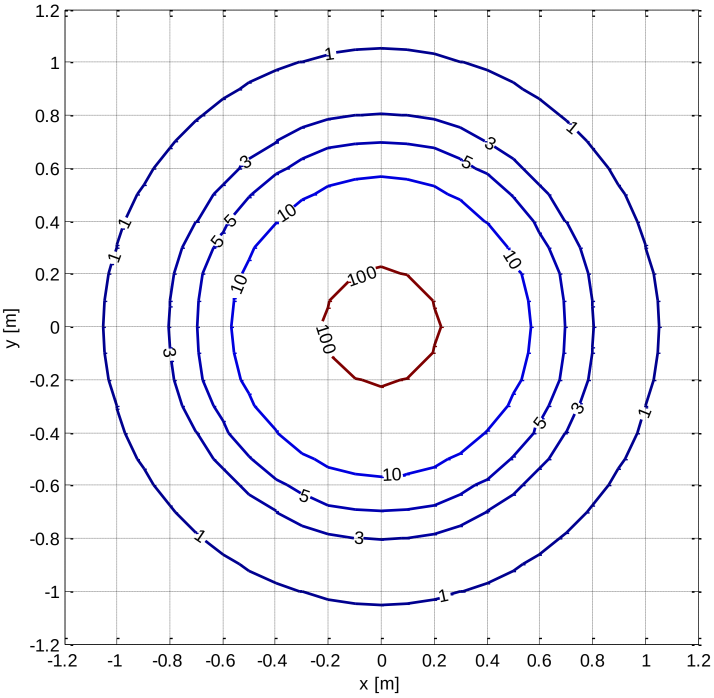

Figure A2.9: *Magnetic field isolines for the cable ARE4H1RX 12/20 kV 3x300 mm^2 (I=478 A).*

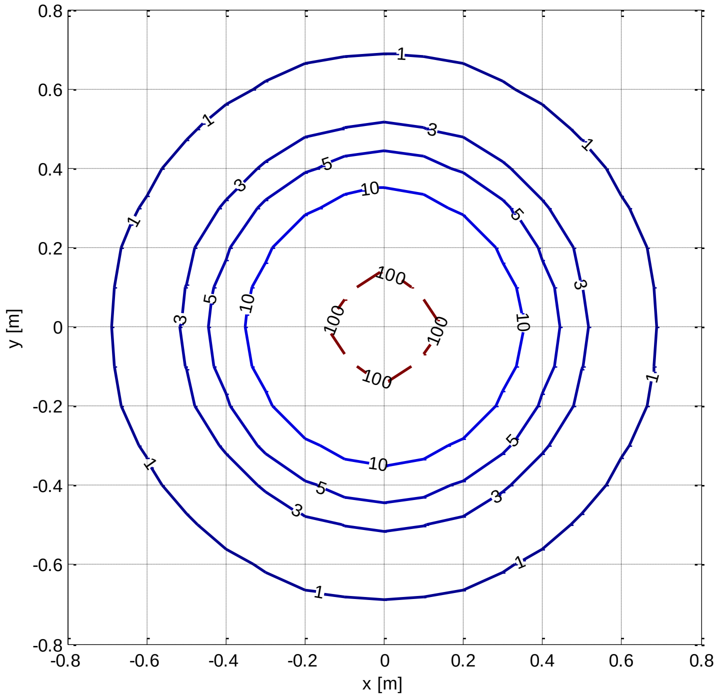

Figure A2.10: *Magnetic field isolines for the cable ARG7H1RX 12/20 kV 3x70 mm^2 (I=200 A).*

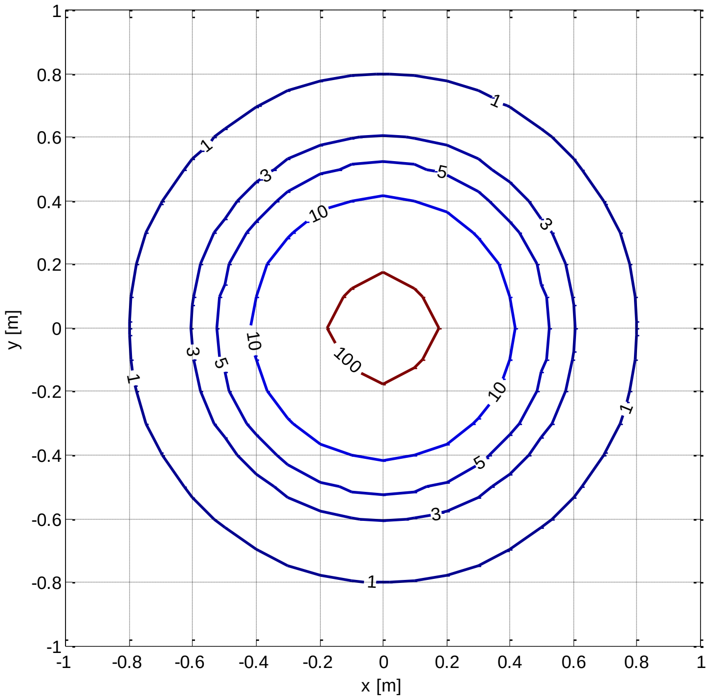

Figure A2.11: *Magnetic field isolines for the cable ARG7H1RX 12/20 kV 3x120 mm^2 (I=280 A).*

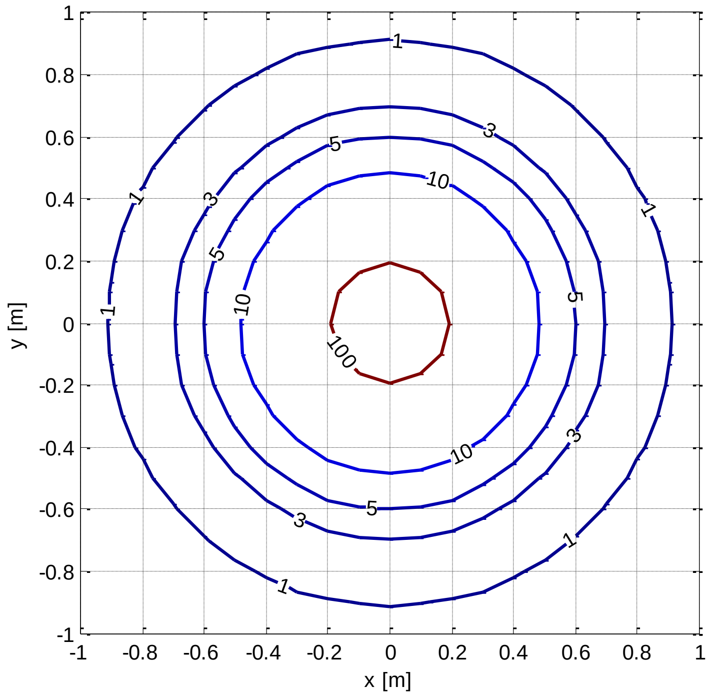

Figure A2.12: Magnetic field isolines for the cable ARG7H1RX 12/20 kV 3x185 mm^2 (I=360 A).

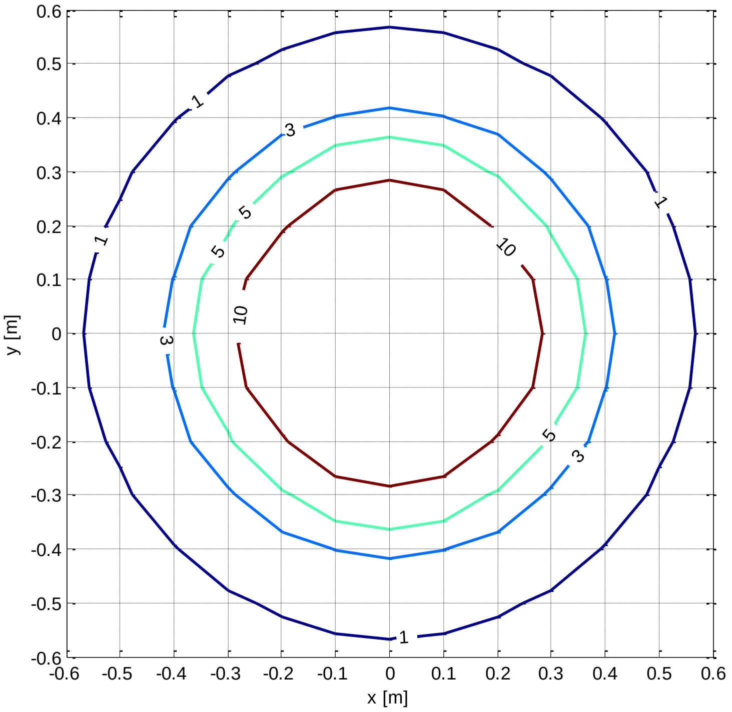

Figure A2.13: Magnetic field isolines for the cable RG7H1OR 12/20 kV 3x25 mm^2 (I=150 A).

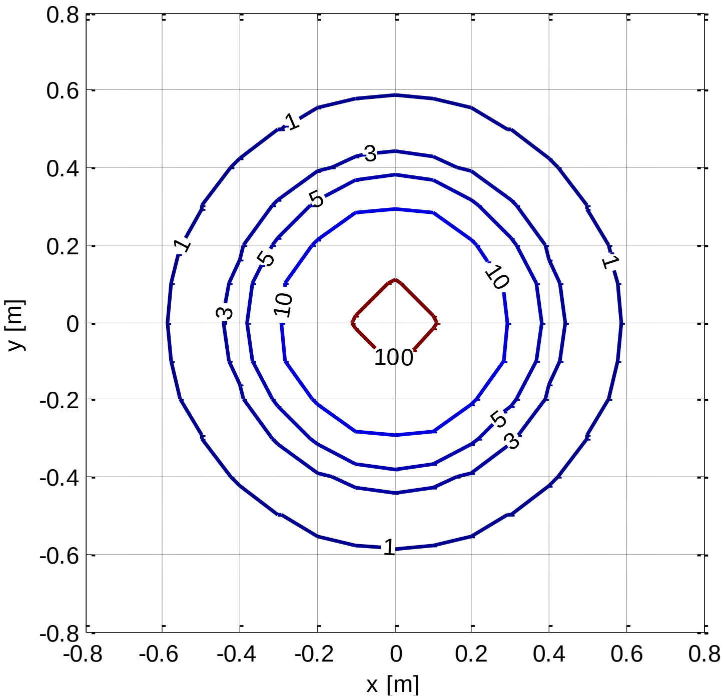

Figure A2.14: *Magnetic field isolines for the cable RG7H1OR 12/20 kV 3x35 mm*^{2} *(I=175 A).*

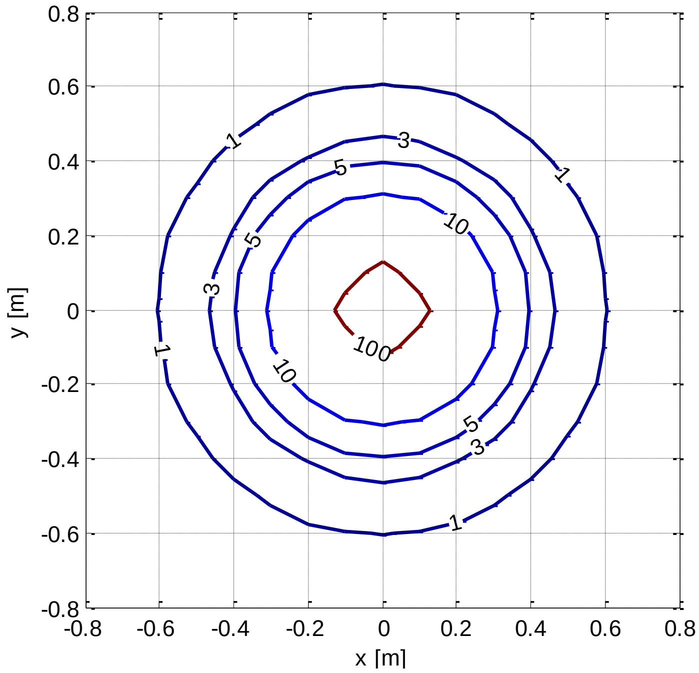

Figure A2.15: *Magnetic field isolines for the cable RG7H1OR 12/20 kV 3x50 mm*^{2} *(I=207 A).*

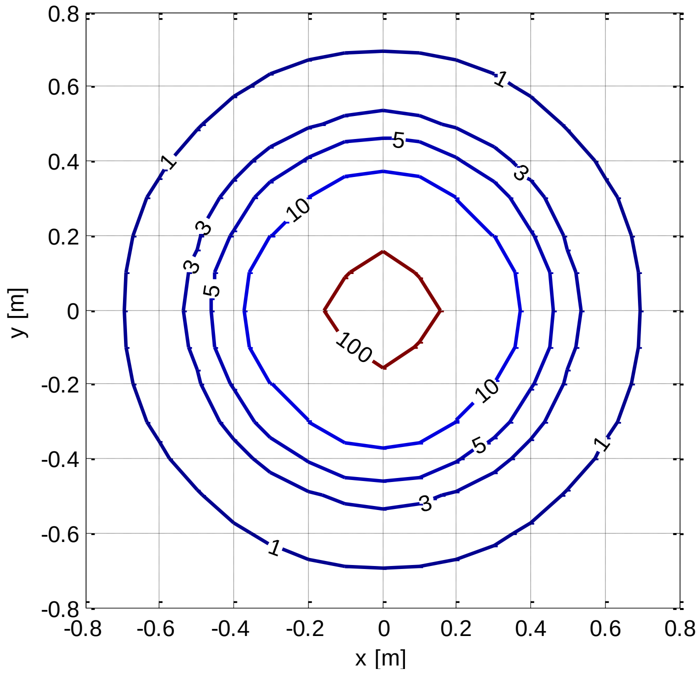

Figure A2.16: *Magnetic field isolines for the cable RG7H1OR 12/20 kV 3x70 mm*^{2} *(I=253 A).*

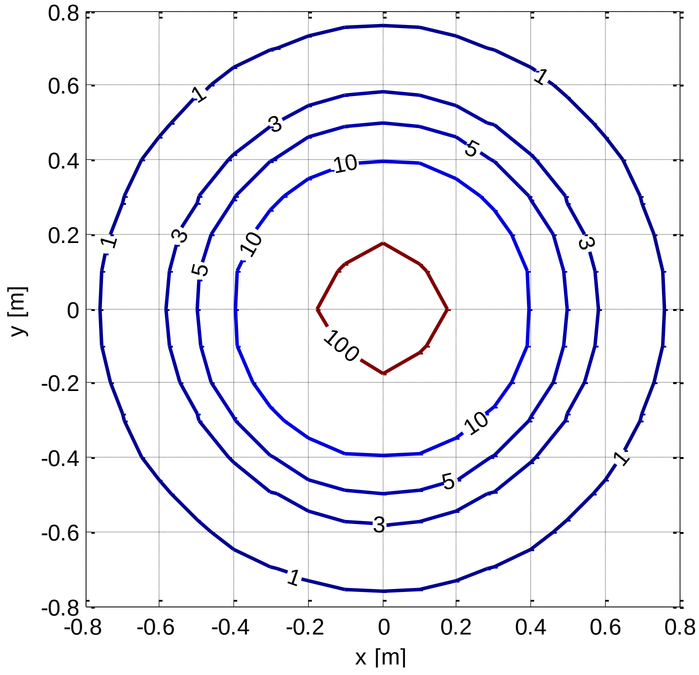

Figure A2.17: *Magnetic field isolines for the cable RG7H1OR 12/20 kV 3x95 mm*^{2} *(I=300 A).*

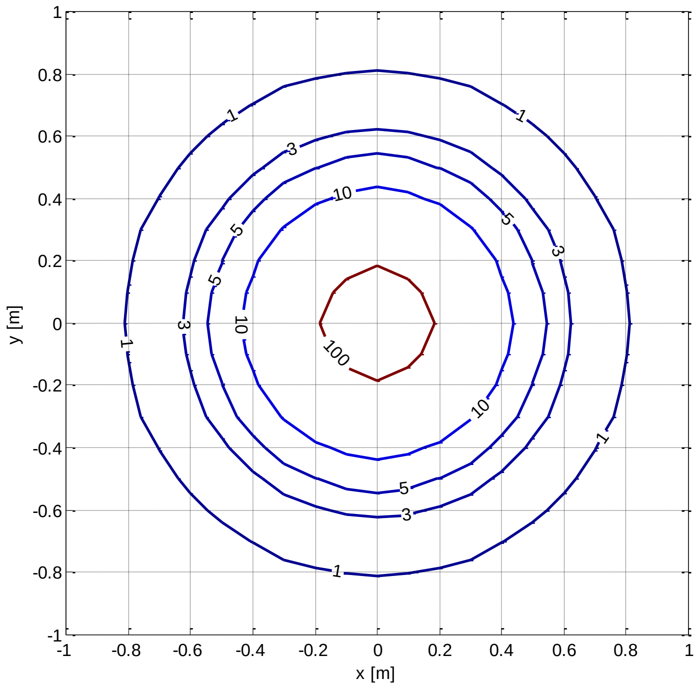

Figure A2.18: *Magnetic field isolines for the cable RG7H1OR 12/20 kV 3x120 mm*^{2} *(I=342 A).*

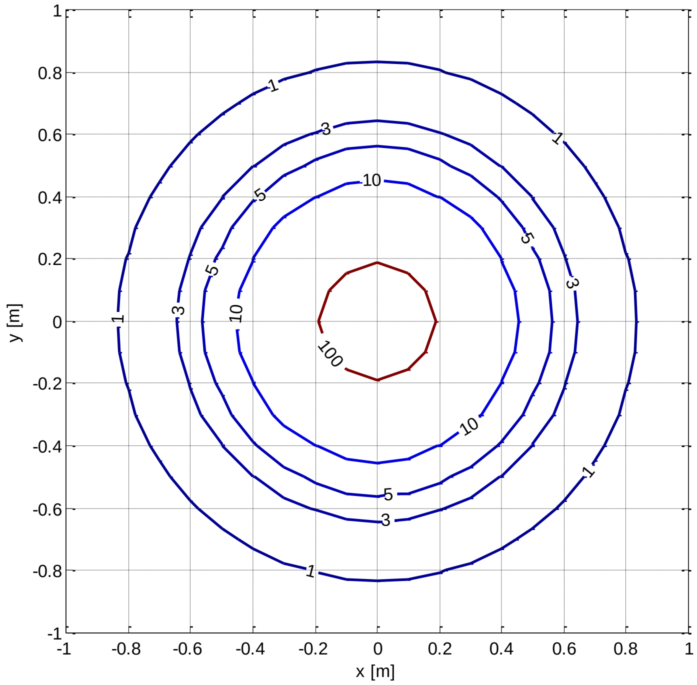

Figure A2.19: *Magnetic field isolines for the cable RG7H1OR 12/20 kV 3x150 mm*^{2} *(I=381 A).*

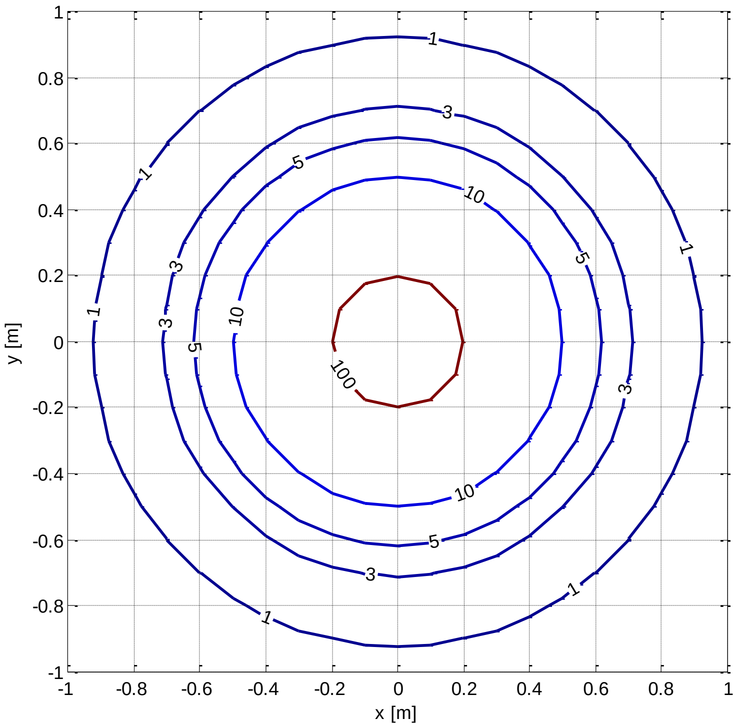

Figure A2.20: *Magnetic field isolines for the cable RG7H1OR 12/20 kV 3x185 mm^2 (I=431 A).*

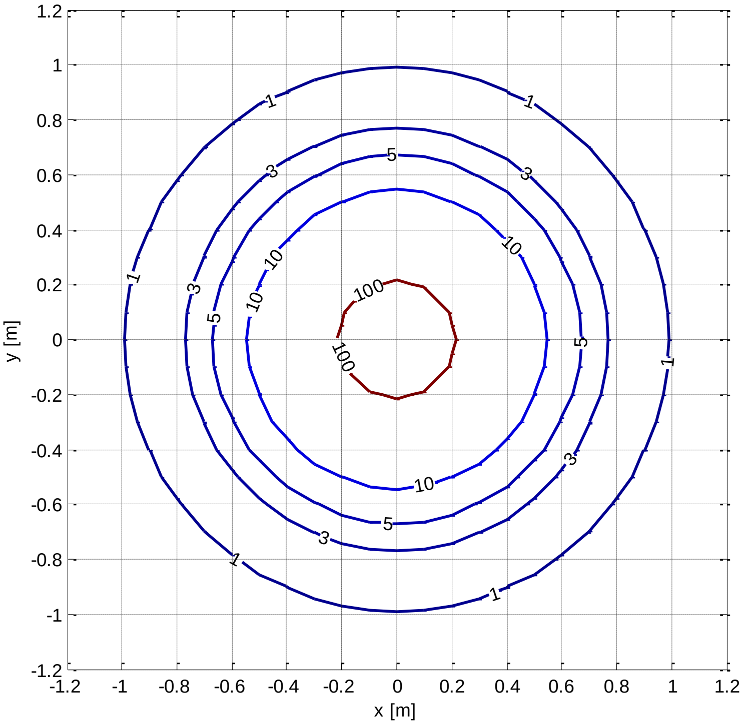

Figure A2.21: *Magnetic field isolines for the cable RG7H1OR 12/20 kV 3x240 mm^2 (I=500 A).*

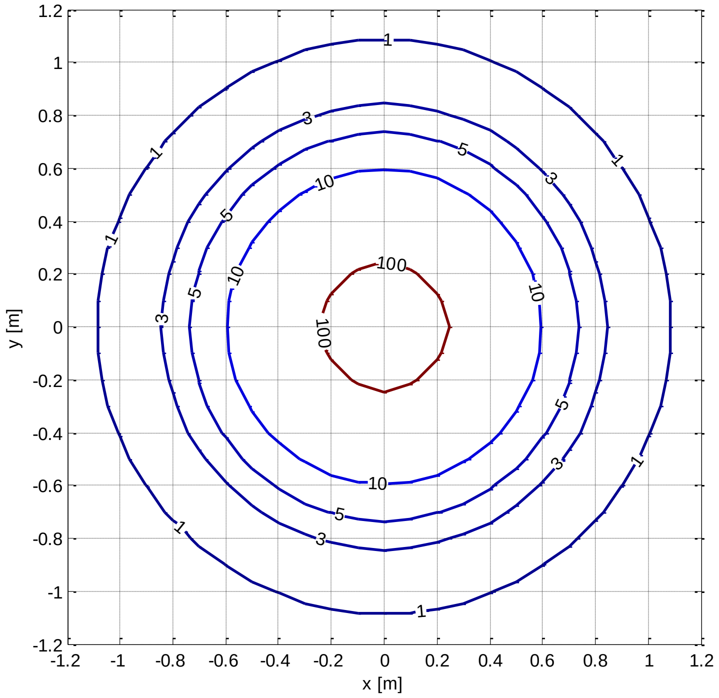

Figure A2.22: *Magnetic field isolines for the cable RG7H1OR 12/20 kV 3x300 mm^2 (I=561 A).*

REFERENCES

[1] ICNIRP Guidelines: "*Guidelines for limiting exposure to time varying electric, magnetic and electromagnetic fields (up to 300 GHz)*", Health Physics, Vol. 74, pp. 494-522, April 1998.

[2] Council Recommendation of 12 July 1999 (1999/519/EC) on the limitation of the exposure of the general public to electromagnetic fields (0 Hz to 300 GHz), Official Journal of the European Communities L 199, pp. 59-70, 30 July 1999.

[3] Directive 2004/40/EC of the European Parliament and of the Council of 29 April 2004: "*On the minimum health and safety requirements regarding the exposure of workers to the risks arising from physical agents (electromagnetic fields) (18th individual Directive within the meaning of Article 16(1) of Directive 89/391/EEC)* ", Official Journal of the European Union L 184, pp. 1-9, 24 May 2004.

[4] DPCM 8 July 2003: "*Fissazione dei limiti di esposizione, dei valori di attenzione e degli obiettivi di qualità per la protezione della popolazione dalle esposizioni ai campi elettrici e magnetici alla frequenza di rete (50 Hz) generati dagli elettrodotti*", Gazzetta Ufficiale No. 200, 29 August 2003 (in Italian).

[5] Standard CEI 106-11: "*Guida per la determinazione delle fasce di rispetto per gli elettrodotti secondo le disposizioni del DPCM 8 luglio 2003 (Art.6) - Parte 1: Linee elettriche aeree e in cavo*", 1st Edition, 2006-02, Dossier 8149, (in Italian).

[6] H. Buchholz: "*Elektrische Stromungsfelder mit Schraubenstruktur*", Elektrische Nachrichten-technik, Band 14, Heft 8, pp.264-280, 1937 (in German).

[7] H. Buchholz: "*Elektrische und Magnetische Potentialfelder*", Chapter 6, Springer-Verlag, Berlid/Gottingenl/Heidelberg, 1957 (in German).

[8] J. R. Moser, R. F. Spencer Jr.: "*Predicting the magnetic fields from a twisted-pair cable*", IEEE Transactions on Electromagnetic Compatibility, Vol. EMC-10, No. 3, pp. 324-329, September 1968.

[9] F. Haber: "*The magnetic field in the vicinity of parallel and twisted three-wire cable carrying balanced three-phased current*", IEEE Transactions on Electromagnetic Compatibility, Vol. EMC-16, No. 2, May 1974.

[10] S. Shenfeld: "*Magnetic fields of twisted-wire pairs*", IEEE Transactions on Electromagnetic Compatibility, Vol. EMC-11, No. 4, pp: 164-169, November 1969.

[11] A.Y. Alksne: "*Magnetic Fields near Twisted Wires*", IEEE Transactions on Space Electronics and Telemetry, Vol. SET 10, pp. 154-158, December 1964.

[12] R. Hagel, L. Gong, R. Unbehauen: "*On the magnetic field of an infinitely long helical line current*", IEEE Trans. on Magnetics, Vol. 30, No. 1, pp. 80-84, January 1994.

[13] M. Ehrich, J. Kuhlmann, D. Netzler: "*Models of a cable bunch formed by twisted three-phase cables*", Proceedings EMC ’97, pp. 463-466, May 1997, Beijing, China.

[14] P. Pettersson, N. Schönborg: "*Predicting the magnetic field from twisted three-phase arrangement*", IEEE International Symposium on Electromagnetic Compatibility, pp. 513-517, 18-22 August 1997, Austin, USA.

[15] P. Pettersson, N. Schönborg: "*Reduction of power system magnetic field by configuration twist*", IEEE Transactions on Power Delivery, Vol. 12, No. 4, pp. 1678-1683, October 1997.

[17] L. Lindberg: "*Reduction of magnetic fields from electric power and installation lines*", IEE Proceedings – Science, Measurement and Technology, Vol. 145, No. 5, pp. 215-221, September 1998.

[18] M. Ehrich, L. O. Fichte: "*Magnetic field reduction of a twisted three-phase power cables of finite length by specific phase mixing*", Proceedings EMC ’99, pp. 448-451, May 1999, Tokyo, Japan.

[19] M. Ehrich, L. O. Fichte, M. Lüer: "*The influence of manufacturing tolerances on the magnetic field of compensated three-phase power cables*", Proceedings EMC ’02, pp. 362-365, May 2002, Beijing, China.

[20] M. Ehrich, L. O. Fichte, S. Kurz, M. Lüer: "*Properties of a field-reduced twisted three-phase power cable of finite length*", Proceedings CEEM ’03, pp. 13-16, November 2003, Hangzhou, China.

[21] T. Tominaka: "*Analytical field calculations for various helical conductors*", IEEE Transactions on Applied Superconductivity, Vol. 14, No. 2, pp. 1838-1841, June 2004.

[22] G. G. Karady, K. E. Holbert, S. G. Adhikari, M. L. Dyer: "*Survey of underground cable generated magnetic fields in a residential subdivision*", Proceedings of the Transmission and Distribution Conference and Exposition 2008 (T&D. IEEE/PES), Chicago (IL), U.S.A., 21-24 April 2008.

[23] K. E. Holbert, G. G. Karady, S. G. Adhikari, M. L. Dyer: "*Magnetic fields produced by underground residential distribution system*", IEEE Transaction on Power Delivery, Vol. 24, No. 3, pp. 1616-1622, July 2009.

[24] E. Kandia: "*Metodi di Calcolo del Campo Magnetico Generato da Cavi Elicordati per la Distribuzione dell’Energia Elettrica*", Master’s Degree Thesis, a.y. 2008-2009, University of Bologna (in Italian).

[25] E. Kandia, M. Landini, G. Mazzanti: "*Calcolo del campo magnetico generato da cavi elicordati per la distribuzione dell'energia elettrica*", ALMA DL - Research Reports, University of Bologna, Ed. Asterisco, September 2009 (ISBN 978-88-965720-1-6) (in Italian).

[26] G. Mazzanti, M. Landini, E. Kandia: "*Metodo semplificato innovativo per il calcolo del campo magnetico generato da cavi elicordati per la distribuzione dell'energia elettrica*", Proceedings of the National Meeting AEIT 2009 (Federazione Italiana di Elettrotecnica, Elettronica, Automazione, Informatica e Telecomunicazioni), 27-29 September 2009, Catania, Italy (in Italian).

[27] G. Mazzanti, M. Landini, E. Kandia: "*A Simple Innovative Method to Calculate the Magnetic Field Generated by twisted three-phase power cables*", IEEE Transactions on Power Delivery, Vol. 25, No. 4, pp: 2646-2654, October 2010.

[28] G. Mazzanti, M. Landini, E. Kandia, C. Biserni: "*Metodi innovativi per il calcolo del campo magnetico generato da cavi elicordati per la connessione in rete di impianti di produzione dell'energia elettrica da fonti rinnovabili*", Proceedings of the V National Congress AIGE 2011 (Nazionale Associazione Italiana Gestione Energia), 8-9 June 2011, Modena, Italy (in Italian).

[29] G. Mazzanti, M. Landini, E. Kandia: "*Terne singole e doppie di cavi elicordati: un metodo semplificato innovative per il calcolo del campo magnetico*", Proceedings of the National Meeting AEIT 2011 (Federazione Italiana di Elettrotecnica, Elettronica, Automazione, Informatica e Telecomunicazioni), 27-29 June 2011, Milano, Italy (ISBN 9788887237290) (in Italian).

[30] G. Mazzanti, M. Landini, E. Kandia, L. Sandrolini: "*Simple calculation method of the magnetic field from double-circuit twisted three-phase cable as a tool for fault detection*", Proceedings of the 8th IEEE SDEMPED 2011, 5-8 September 2011, Bologna, Italy (ISBN 978-1-4244-9302-9).

[31] G. Mazzanti, M. Landini, E. Kandia: "*Innovative Calculation Methods of the Magnetic Field from Single and Double-Circuit Twisted Three-Phase Cables Used for the Connection of Renewable Sources to the Grid*", International Journal of Heat & Technology, Publ. ETS, Vol. 29, No. 2, pp. 103-110, 2011.

[32] G. Mazzanti, M. Landini, E. Kandia, C. Biserni, M. Marzinotto: "*Innovative calculation methods of the magnetic field from single and double-circuit twisted three-phase cables widely used in MV and LV installations*", Central European Journal of Engineering, Versita Publ. co-published with Springer-Verlag, Volume: 2, Number: 2, pp: 212-223, June 2012.

[33] E. Kandia, G. Mazzanti, M. Landini: "*Innovative magnetic field calculation from multiple-circuit twisted three-phase lines*", Accepted for presentation at IEEE IES IECON 2013, 10-13 November 2013, Vienna, Austria.

[34] IEEE Magnetic Fields Task Force: "*Magnetic fields from electric power lines theory and comparison to measurements*", IEEE Transactions on Power Delivery, Vol. 3, No. 4, pp.2127-2136, October 1988.

[35] J. Swanson: "*Magnetic fields from transmission lines: Comparison of calculations and measurements*", IEE Proceedings Generation, Transmission & Distribution, Vol. 142, pp. 481-486, September 1988.

[36] W. T. Kaune, L. E. Zaffanella: "*Analysis of magnetic fields produced far from electric power lines*" IEEE Trans. Power Delivery, vol. 7, pp. 2082-2091, October 1992.

[37] A. Geri, A. Locatelli, G.M. Veca: "*Magnetic fields generated by power lines*", IEEE Transactions on Magnetics, Vol. 31, No. 3, pp. 1508-1511, May 1995.

[38] R.G. Olsen, S.L. Backus, R.D. Stearns: "*Development and validation of software for predicting ELF magnetic fields near power lines*", IEEE Transactions on Power Delivery, Vol. 10, No. 3, July 1995.

[39] A.V. Mamishev, B.D. Russell: "*Measurements of magnetic fields in the direct proximity of power line conductors*", IEEE Transactions on Power Delivery, Vol. 10, No. 3, pp.1211-1216, July 1995.

[40] K. Hameyer, R. Mertens, R. Belmans: "*Numerical methods to evaluate the electromagnetic fields below overhead transmission lines and their measurement*", Proceedings of the 1st IEEE International Conference on Devices, Circuits and Systems, pp. 32-36, 12-14 December 1995, Caracas, Venezuela.

[41] A.V. Mamishev, R.D. Nevels, B.D. Russell: "*Effects of conductor sag on spatial distribution of power line magnetic field*", IEEE Transactions on Power Delivery, Vol. 11, No. 3, pp.1571-1576, July 1996.

[42] A.R. Memari, W. Janischewskyi: "*Mitigation of magnetic field near power lines*", IEEE Transactions on Power Delivery, Vol. 11, No. 3, pp.1577-1586, July 1996.

[43] A. Albano, R. Benato, R. Turri: "*Predictive analysis of environmental magnetic fields generated by multiple power lines*", Proceedings of the IEEE Bologna Power Tech Conference, 23-26 June 2003, Bologna, Italy.

[44] K. Budnik, W. Machczyński: "*Contribution to studies on calculation of the magnetic field under power lines*", European Transactions on Electrical Power 2006; **16**: 345–364.

[45] G. Mazzanti: "*The role played by current phase shift on magnetic field established by double-circuit overhead transmission lines – Part I: Static analysis*", IEEE Transactions on Power Delivery, Vol. 21, No. 2, pp. 939-942, April 2006

[46] G. Mazzanti: "*The role played by current phase shift on magnetic field established by double-circuit overhead transmission lines – Part II: Dynamic analysis*", IEEE Transactions on Power Delivery, Vol. 21, No. 2, pp. 949-958, April 2006

[47] G. Lucca: "*Magnetic field produced by power lines with complex arrangements*", European Transactions on Electrical Power 2011; **21**: 52-58.

[48] Standard CEI 211-4: "*Guida ai metodi di calcolo dei campi elettrici e magnetici generati da linee e da stazioni elettriche*", 2nd Edition, 2008-09, Dossier 9482, (in Italian).

[49] Standard CEI 11-60, "*Portata al limite termico delle linee aeree esterne con tensione maggiore di 100 kV*", 2nd Edition, 2002-06, Dossier 6507, (in Italian).

[50] Standard CEI 211-6: "*Guida per la misura e la valutazione dei campi elettrici e magnetici nell'intervallo di frequenza 0 Hz - 10 kHz, con riferimento all'esposizione umana*", 1st Edition, 2001-01, Dossier 5908, (in Italian).

[51] D. Andreuccetti: " 'CAMPI' - *Un programma per il calcolo del campo elettrico e del campo magnetico dispersi da elettrodotti ad alta tensione*", IFAC-CNR, Version 4.1, May 2002 (in Italian).

[52] Standard CEI EN 60359: "*Apparecchi di misura elettrici ed elettronici, Espressione delle prestazioni*", 1st Edition, 2002-11, Dossier 6703 (in Italian).

[53] M. Bertocco, A. Selmo, A. Sona: "*Design of a Measurement System for Electric and Magnetic Field Analyses*", IMTC 2005 – Instrumentation and Measurement Technology Conference, Ottawa, Canada, pp. 220-225, 17-19 May 2005.

[54] E. Sieni, M. Bertocco: "*Non-uniform low frequency magnetic field measurements*", IMTC 2006 - Instrumentation and Measurement Technology Conference, pp. 2194-2199, Sorrento, Italy, 24-27 April 2006.

[55] M. Misakian: "*ELF electric and magnetic field measurement methods*", 1993 IEEE International Symposium on Electromagnetic Compatibility, pp. 150-155.

[56] M. Misakian and C. Fenimore: "*Distributions of measurement error for three-axis magnetic field meters during measurements near appliances*", IEEE Transactions on Instrumentation and Measurement, Vol. 45, pp. 244–249, 1996.

[57] M. Landini, G. Mazzanti: "*Misura e valutazione dell'esposizione della popolazione ai campi magnetici generati da elettrodotti aerei a doppia terna*", ALMA DL – Research Reports, University of Bologna, Ed. Asterisco, April 2008, ISBN 978-88-902128-8-8 (in Italian).

[58] M. Landini, G. Mazzanti: "*Procedura innovativa per la verifica dei limiti di esposizione della popolazione al campo magnetico generato da elettrodotti aerei a doppia terna*", Ingegneri Architetti Costruttori (INARCOS), pp. 133-144, year LXIV, vol. 2 March 2009 (in Italian).

[59] M. Landini, G. Mazzanti: "*Esposizione della popolazione ai campi magnetici generati da elettrodotti aerei a doppia terna*", AEIT, pp. 46-57, Vol. 96, n. 6, June 2009 (in Italian).

[60] E. Kandia, M. Landini, G. Mazzanti, G. Pasini: "*A smart measurement and evaluation system for the magnetic-field generated by multiple field sources in complex 3-D arrangements*", Proceedings of the IEEE International Conference on Smart Measurements for Grids (IEEE SMFG 2011), Bologna, Italy, 14-16 November 2011.

[61] E. Kandia, M. Landini, G. Mazzanti, G. Pasini: "*Innovative measurement and evaluation apparatus of magnetic field in complex arrangements of multiple field sources*", Proceedings of the 2012 IEEE PES General Meeting, San Diego (CA), USA, 22-26 July 2012.

[62] Standard CEI-UNEL 35011: "*Cavi per energia e segnalamento. Sigle di designazione*", 2nd Edition, 2000-08, Dossier 5757 (in Italian).

[63] http://tinyurl.com/n3cxxf

[64] http://www.prysmian.it/export/sites/prysmian-itIT/attach/pdf/Cavi_Energia_Terrestri_MT/ARE4H1RX_2011.pdf

[65] http://www.lelettricasrl.com/index.php/prodotti/cavi%20eletttrici%20/media%20tensione/media%20tensione%2012/20kv%20are4h5ex

[66] http://www.prysmian.it/export/sites/prysmian-itIT/attach/pdf/Cavi_Energia_Terrestri_MT/RG7H1OR_EPRO_SETTE_2011.pdf